University of Alberta

Examining the Electronic Structure of Metal Pnictides via X-ray Spectroscopy

by

Peter E.R. Blanchard

A thesis submitted to the Faculty of Graduate Studies and Research
in partial fulfillment of the requirements for the degree of

Doctor of Philosophy

Department of Chemistry

©Peter E.R. Blanchard
Fall, 2011
Edmonton, Alberta

Examining Committee

Prof. Arthur Mar, Chemistry

Prof. Ronald G. Cavell, Chemistry

Prof. Jonathan G.C. Veinot, Chemistry

Prof. Alexander Brown, Chemistry

Prof. Michael J. Serpe, Chemistry

Prof. Zhenghe Xu, Chemical and Materials Engineering

Prof. Stephanie L. Brock, Chemistry, Wayne State University

Abstract

Given the wide range of properties and applications of intermetallic compounds, it is important to achieve a detailed understanding of their structure and bonding. X-ray photoelectron spectroscopy (XPS) and X-ray absorption near-edge spectroscopy (XANES) were used to study the electronic structure of several types of pnictides (compounds containing Pn = P, As).

$ZrAs_2$, forming a $PbCl_2$-type structure, has been established to be a genuine binary phase that is strictly stoichiometric. At 900 °C, it supports extensive solubility of Ge to form the ternary extension $Zr(Ge_xAs_{1-x})As$ ($0 \leq x \leq 0.4$). XPS analysis and band structure calculations confirmed that the Ge and As atoms are anionic in character and that the substitution of Ge for As is driven by a depopulation of anion–anion antibonding states.

ZrCuSiPn and REMAsO are important representatives of ZrCuSiAs-type materials. The small magnitudes of the binding energy shifts in the XPS spectra of ZrCuSiPn suggest significant covalent character in the Zr–Si, Zr–Pn, and Cu–Pn bonds, consistent with a three-dimensional structure. On progressing from ZrCuSiP to ZrCuSiAs, the charge transfer from metal to Pn atoms becomes less pronounced, as indicated by changes in the intensity of the Cu K-edge and Zr K, L-edge XANES spectra. Binding energy shifts and satellite features of the XPS spectra of REMAsO indicated that bonding in the [REO] layer is ionic, whereas bonding in the [MAs] layer is strongly covalent. Altering the electronic structure of one layer (by M or RE substitution) does not affect the electronic structure of the other layer, consistent with a two-dimensional structure in REMAsO.

Metal-rich phosphides M_2P (forming Cr_2P-, Fe_2P-, and Co_2P-type structures) and M_3P (forming Ni_3P-type structures) were examined by XPS and XANES. The P $2p_{3/2}$ binding and P K-edge absorption energies decrease with greater ionic character of the $M-P$ bonding and indicate the presence of anionic phosphorus. Interatomic effects play a more important role in affecting the energy shifts in these metal-rich phosphides than in the monophosphides, becoming more pronounced with higher metal concentration. Surprisingly, intraatomic effects dominate in mixed-metal phosphides $(Ni_{1-x}M_x)_2P$ despite evidence of metal-to-metal charge transfer from the Ni XANES spectra and Ni 2p XPS satellite features.

Acknowledgements

Throughout my Ph.D. studies I have been honoured to have work with some extraordinary people. First and foremost, I would like to thank my supervisors Professor Arthur Mar and Professor Ronald G. Cavell for their guidance and encouragement over the years. I am grateful to have had the opportunity to work for both of them. Aside from their rich knowledge of solid state chemistry and X-ray spectroscopy, both professors were also editors on the work presented in this thesis. Prof. Mar is thanked for helping make me a better writer. I would also like to thank past and current members of the Mar research group for their help in synthesizing and characterizing materials when I started my research. I am particularly grateful to Professor Andrew P. Grosvenor for sharing his knowledge in X-ray spectroscopy and for providing help for some ridiculously long synchrotron trips. I would also like to thank Dr. Haiying Bie and Dr. Stanislav Stoyko for their assistance in analyzing crystallographic, magnetic, and resistivity data.

The Natural Sciences and Engineering Research Council (NSERC) of Canada is thanked for providing Discovery Grants to Profs. Mar and Cavell. Dr. Dimitre Karpuzov and the Alberta Centre for Surface Engineering and Science (ACSES) are thanked for allowing me to access the Kartos AXIS 165XPS spectrometer used in this thesis. ACSES was established with support from the Canada Foundation for Innovation (CFI) and Alberta Innovation and Science. Ms. Christina Barker is thanked for her help with the EDX analysis. Dr. Robert McDonald and Dr. Michael J. Ferguson of the X-ray crystallography laboratory are thanked for collecting X-ray diffraction data. Dr. Ning Chen, Dr. Robert Blyth, Mr. Thomas Regier, Dr. Yongfeng Hu, and Dr. Lucia Zuin are thanked for their assistance with XANES experiements on the PGM (07B2-1), SGM (11-ID.1), and HXMA (06ID-1) beamlines at the Canadian Light Source (CLS), which

Table of Contents

List of Tables

List of Figures

List of Symbols and Abbreviations

$2c–2e^-$	2 centre – 2 electron bond
$2c–1e^-$	2 centre – 1 electron bond
Å	Angstrom
$\hbar$	Reduced Planck's constant
$\Delta\chi$	Difference in electronegativity (χ)
$\Delta\mu_o(E)$	Absorption edge height
ΔE_i	Shift in binding energy (BE)
Δl	Change in angular momentum (l)
ΔS	Change in entropy
ΔT	Change in temperature
ε	emittance
η	Exchange energy; Spin-orbit splitting energy
θ	Angle of reflection; Take-off angle
λ	Wavelength; Inelastic mean free path (IMFP)
λ_{id}	Magnetic period
μ	Absorption coefficient
$\mu(E)$	Energy-dependent absorption coefficient
$\mu_o(E)$	Background function describing what X-ray absorption would look like for an isolated atom.
ρ	Concentration of a particular element; Radius of curvature of an electron; Sample density; Resistivity
σ	Photoelectron cross-section; standard deviation of electron beam
σ'	Divergence of the electron beam

φ	Work function
χ_n	Basis function
$\chi(E)$	EXAFS function
ψ	Wave function
A	Atomic mass
a,b,c	unit cell parameters
APS	Advaned Photon Source
ARXPS	Angle-resolved X-ray photoelectron spectroscopy
ASA	Atomic sphere approximation
B_o	Magnetic field of the insertion device
BE	Binding energy
C	Atom concentration
Ch	Chalogen
CHA	Concentric hemispherical analyser
CLS	Canadian Light Source
CN	Coordination number
COHP	Crystal orbital Hamilton population
COOP	Crystal orbital overlap population
cps	Counts per second
d	Analysis depth
d_{hkl}	d-spacing
DFT	Density functional theory
DOS	Density of states

E	Energy of an electron; X-ray energy; Absorption energy
E_o	Absorption edge energy
E_F	Fermi level; Fermi edge
E_{Final}	Energy of the final state
E_{Ground}	Energy of the ground state
E_i	Binding energy of the atom of interest
E_i^o	Reference binding energy
E_V	Vacuum energy
EDX	energy-dispersive X-ray
ESCA	Electron spectroscopy for chemical analysis
EXAFS	Extended X-ray absorption fine-structure
e^-	Electron
F_o	Structure factor
FLY	Fluorescence yield
FWHM	Full width at half maximum
G/L	Gaussian/Lorentzian function
H	Planck's constant
H	Hamiltonian
$h\upsilon$	Excitation energy
HDC	Hydrodechlorination
HDN	Hydrodenitrogenation
HDS	Hydrodesulfurization
hkl	Millar indices

HXMA	Hard X-ray microanalysis
I	Peak intensity from a XPS spectrum; Intensity of transmitted radiation
I_o	Intensity of exciting radiation
I_f	Intensity of radiation produced by fluorescene
I_{Ref}	Intensity of radiation transmitted through a reference sample
ICOHP	Integrated crystal orbital Hamilton population (COHP)
J	Photon flux
j	Coupled angular momentum and spin quantum number
k	Wave vector
K	XPS spectrometer related peak intensity correction factors
K_{id}	Deflection parameter
k	Factor describing the interaction between valence and core electrons
KE	Kinetic energy
L	Ligand
l	Angular orbital momentum
LDA	Local density approximation
M	Metal
m	Mass
MEC	Magnetocaloric effect
MO	Molecular Orbital
MSR	Multiple scattering resonance
N	Volume density of a particular element in a material; Number of pairs of magnets
n	Order of reflection; Principle quantum number

PES	Photoemission spectroscopy
Pn	Pnicogen
PNC/XOR-CAT	Pacific Northwest Consortium / X-ray Operations and Research Collaborative Access Team
$q_{i(j)}$	Charge of atom i (or j)
R	Residual
r_{ij}	Distance between i and j
$R_W(F_o^2)$	Residual that is weighted by the square of the structure factor (F_o)
r	Radius of an atom
RE	Rare-earth
REELS	Reflective electron energy loss spectroscopy
RF	Radio frequency
S	Goodness-of-fit; Entropy
s	Spin quantum number
SGM	Spherical grating monochromator
SXRMB	Soft X-ray microcharacterization beamline
T	Temperature
T_C	Critcal temperature; Curie temperature
T_N	Néel temperature
t	Sample thickness
TB-LMTO	Tight-binding linear muffin-tin orbital
TEY	Total electron yield
Tl	Tetral
U_{eq}	Equivalent isotropic displacement parameters

UHV	Ultra-high vacuum
UPS	Ultraviolet photoelectron spectroscopy
V	Volume of unit cell
vec	Valence electron concentration
VLS PGM	Variable line spacing plane grating monochromator
x,y,z	Atomic coordinates
XAFS	X-ray absorption fine-structure
XANES	X-ray absorption near-edge spectroscopy
XAS	X-ray absorption spectroscopy
XMCD	X-ray magnetic circular dichroism
XPS	X-ray photoelectron spectroscopy
XRD	X-ray diffraction
Z	Atomic number; Number of formula units per unit cell

Chapter 1

Introduction

1.1 Introduction

Most chemists are familiar with the covalent bonding that occurs in molecular substances (typically organic or organometallic), which follow simple electron-counting rules, such as the octet rule or the 18-electron rule. The basis behind these rules is generally well-understood, when molecular orbital theory is applied. In contrast, solid-state extended structures are often assumed to exhibit mostly ionic bonding, with the formation of cations and anions taking place when electrons are completely transferred from the electropositive to the electronegative component. Sadly, this assumption is quite erroneous. Even in a compound like CsF, with the largest possible difference in electronegativity, the bonding consists of 92 % ionic character (based on the Pauling scale).[1] In reality, solid-state compounds exhibit a diversity of bonding character with some combination of ionic, covalent, and metallic character. Nevertheless, the assumption works well to account for the familiar structures of many oxides and halides (such as TiO_2 or NaCl), in which atoms strive to attain filled-shell electron configurations (i.e., octet rule, 18 e^- rule).

When the difference in electronegativity is less pronounced, as in intermetallics, no simple bonding models are applicable. Intermetallic compounds are defined as alloys consisting of two or more metals or metalloids in a definitive composition and having a crystal structure

that differs from the other constituents (this definition is often extended to include phosphides or silicides).[2] Because of the small difference in electronegativity of the component elements, bonding in intermetallics is mostly polar covalent or metallic. For simple intermetallic compounds (i.e., binary alloys), electron counting schemes such as the Hume-Rothery rules and pseudoatom concepts have been developed. However, most intermetallics do not obey these rules often because of electron delocalization associated with metal-metal bonding. Theoretical methods based on solving the Schrödinger equation for periodic structures (i.e., band structure calculations) have also been successful in explaining bonding in these materials. Despite the progress that has been made in understanding intermetallics, researchers have relatively few experimental methods at their disposal for examining the nature of bonding in these fascinating materials.

The electronic structure of solids can be probed directly by X-ray spectroscopic techniques. Although X-ray photoelectron spectroscopy (XPS) and X-ray absorption spectroscopy (XAS) can be applied, in principle, to intermetallic compounds, the poor resolution of earlier instruments made it difficult or impossible to detect small energy shifts. The much improved resolution of modern instruments has now allowed these powerful techniques to be applied to intermetallics, particularly the pnictides.[3] Pnictides (compounds of P, As, Sb, Bi) show a wide range of bonding character. For example, the Fe-P phase diagram contains compounds that exhibit strong covalent bonding (FeP_4)[4] and those that exhibit primarily metallic bonding (Fe_3P).[5] Progress has been made to identify subtle electronic effects (e.g. next-nearest neighbour effects) in the XPS and XAS spectra of model compounds (MP,[6] $M_{1-x}M'_xP$,[7] MAs_yP_{1-y}[8]) when the metal or pnicogen atoms are substituted. These concepts will be used to study bonding in more complicated materials such as metal-rich phosphides (M_2P, $(M_{1-x}M'_x)_2P$, M_3P)

and mixed-cation/mixed-anion pnictides (ZrCuSi*Pn*, *REM*AsO). In the following sections, the bonding models in metal-poor and metal-rich intermetallics are introduced, and the significant applications and properties of these materials are discussed.

1.2 Electron counting schemes

1.2.1 Hume-Rothery rules

William Hume-Rothery was one of the first to correlate crystal structure to electronic structure. He devised simple rules that were originally used to explain bonding in the brass (Cu-Zn) alloys and later extended to alloys containing other elements of similar size and electronegativity (Ag, Sn, Al).[9,10] According to these rules, different combinations of elements form a specific structure based on their average valence electron concentration (*vec*), which is the ratio of the number of valence electrons to the number of atoms. In general, there are six common brass structure types with known *vec* values that are listed in Table 1-1.[9] Structural changes occur with increasing *vec* when antibonding states begin to be filled, resulting in a transformation to a more energically favourable structure.

1.2.2 Zintl-Klemm concept

Although the Hume-Rothery rules seemed to work well for a small subset of alloys, they could not be extended to other intermetallics. Even some binary phases with a given *vec* did not always form the predicted structure. For example, Ag_3Al and Au_3Al have a *vec* of 1.50 but form the β-Mn-type instead of the β-brass structure.[10] The rules fail when the electronegativity difference between atoms is larger. Eduard Zintl was interested in these types of intermetallics,

particularly those containing an electropositive metal (alkali and alkaline earth metals) and a metametal (group 13, 14, or 15). He and Wilhelm Klemm proposed a straightforward principle, now known as the Zintl-Klemm concept, to account for the bonding in these more polar intermetallics. Instead of focusing on the *vec*, with all components treated equally, it was assumed that the more electropositive atom donates electrons to the more electronegative atom so that the octet rule is satisfied.[10] If the number of electrons transferred to the anion is not equal to 8, Klemm proposed the pseudoatom concept to explain how the charges rearrange within a structure. If not enough electrons are transferred to the anion (8-*N*), an extended covalent anionic substructure (i.e., a polyanion) must exist.[10] If there are more than 8 electrons available to be transferred, then the excess electrons must form an extended covalent cationic substructure (i.e., a polycation).[10] Intermetallic compounds that conform to these rules are collectively known as the Zintl phases.[10]

Table 1-1 A survey of the different brass phases including composition and *vec*.[9]

Brass Phase	Composition	*vec*
α	$Cu_{1-x}Zn_x$ $(0 \leq x \leq 0.38)$	$1 - 1.38$
β	$CuZn$	1.5
γ	Cu_5Zn_8	1.62
ε	$CuZn_3$	1.75
η	$Cu_{1-x}Zn_x$ $(0.98 \leq x \leq 1)$	$1.98 - 2$

1.2.3 Polyanionic substructures

Over the years, the Zintl-Klemm concept has been applied to many intermetallics. Here, this concept will be used to illustrate bonding in two intermetallic compounds: $Zr(Si_xAs_{1-x})As$ and ZrCuSiAs. Although their full structures will be discussed later, this section will focus on their anionic substructures.

$Zr(Si_xAs_{1-x})As$ adopts the $PbCl_2$-type structure, which features a three-dimensional network containing four-atom-wide anionic ribbons of As and Si atoms (Figure 1-1a).[11] Of the two possible anionic sites, Si prefers to occupy the interior site (As1/Si1). The As1/Si1-As1/Si1 bond is shorter than As1/Si1-As2 bonds. If the Zintl-Klemm concept is applied, it can assumed that the more electropositive Zr atoms transfer their valence electrons to the more electronegative Si and As atoms.[10,12] The As2-As1/Si1 (2.837Å) bonds, which are longer than the sum of the Pauling metallic radii (As-As 2.48 Å; As-Si 2.41 Å; Si-Si 2.34 Å), are assumed to be weak two-centre-one-electron (2c-1e⁻) bonds.[1,11] The shorter As1/Si1- As1/Si1 bonds (2.482Å) are similar to those predicted from Pauli radii and are assumed to be two-centre-two-electron (2c-2e⁻) bonds.[1,11] With these assumptions, the electron counts are 5e⁻ for As1/Si1 and 7e⁻ for As2. As such, the As atoms have a charge of either 0 (As1) or 2- (As2), and Si atoms have a charge of 1-.

The ZrCuSiAs-type structure is often viewed as a filled variant of the PbFCl-type structure[13] (adopted by phases in the $ZrSi_2$ – $ZrAs_2$ system).[11] Si atoms form a square net with Si-Si bonds of ~2.8 Å (Figure 1-1b).[13] As with the assignments above, these bonds are 2c-1e⁻ bonds with each Si atom having 6 electrons and a formal charge of 2-.
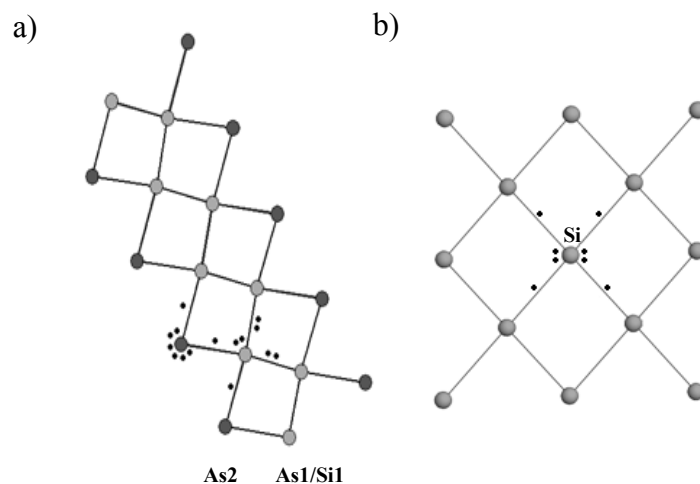
Figure 1-1 The anionic Si/As substructures showing the electron counting scheme for (a) $Zr(Si_{1-x}As_x)As$ and (b) ZrCuSiAs.

1.3 Bonding in metal-rich phases

Although the Zintl-Klemm concept can be extended to explain the bonding in metal-rich phases, through the introduction of polycationic substructures, a more rigorous approach is desirable. In this section, we describe how band structure calculations are applied to intermetallic compounds.

1.3.1 Band structure

The nature of orbital interactions in extended solids can be extrapolated from molecular systems. Many of the intermetallic compounds treated in this thesis contain Ni atoms in tetrahedral coordination environments. Molecular complexes of Ni atoms also adopt tetrahedral geometry, although this is less common than square planar geometry. In molecular orbital (MO) theory, the σ-bonding framework is derived from linear combinations of metal (Ni^{2+}) and groups of ligand (L) atomic orbitals that transform as the same symmetry within the T_d point group (Figure 1-2).[14] The result is familiar: four $M–L$ bonding levels (t_2, a_1) that are fully occupied with electrons, four $M–L$ antibonding levels (a_1^*, t_2^*) that are empty, and five more metal-based
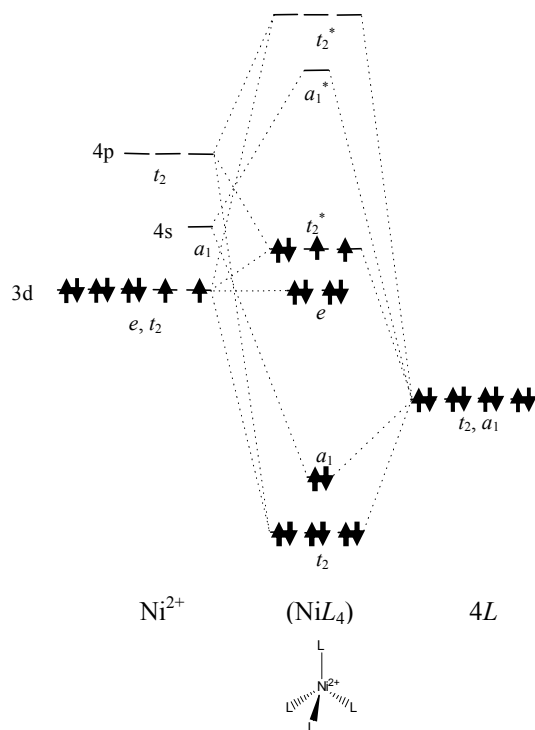
Figure 1-2 Molecular orbital diagram of a tetrahedral $(NiL_4)^{2+}$ complex. Diagram was constructed using information from reference 14.

levels split into a nonbonding e ($3d_{z^2}$, $3d_{x^2-y^2}$) and antibonding t_2 ($3d_{xy}$, $3d_{xz}$, $3d_{yz}$) sets of MOs that are partially filled with electrons.

In an extended solid, there are an infinite number of atoms, and thus orbitals, to combine. Moreover, intermetallic phases may be subject to partial disorder of different atoms in one site. Nevertheless, it is often possible to visualize the structures of intermetallic phases as being built from molecular fragments. For example, metal-centred tetrahedra could be connected to form three-dimensional framework by sharing corners (Figure 1-3a) or edges (Figure 1-3b). In the latter case, metal atoms are brought close enough to each other that orbital overlap may occur to form metal-metal bonding. The occurrence of both *ML* and *MM* bonding creates the interesting mix of polar covalent and metallic character that ultimately influences the properties of intermetallics.

a)   b)

$$M–M = 2X$$ $$M–M = 1.16X$$
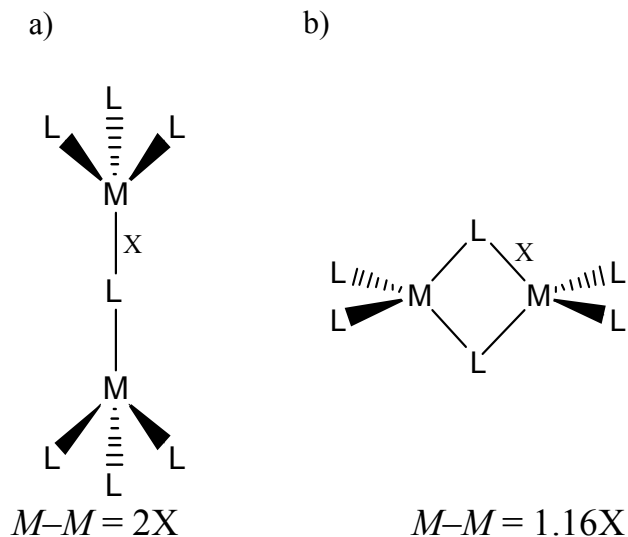
Figure 1-3 (a) Corner-sharing and (b) edge-sharing tetrahedrons with *M–M* separations noted.

Determining the electronic structure of an extended solid takes advantage of the inherent periodicity of the crystal structure, but the general approach, taking linear combinations of atomic orbitals, is the same as for molecules.[15] Consider a one-dimensional chain of Ni atoms separated by a constant spacing *a* (Figure 1-4a). Associated with each atom is a basis function (e.g. a 3*d* orbital), χ_n. The permitted linear combinations of these basis functions that conform to the translational symmetry of this infinite chain are restricted to:

$$\psi_k = \sum_n e^{ikna} \chi_n \qquad\qquad (1\text{-}1)$$

where the wavevector, *k*, is quantized and is restricted to unique values in the range $-\dfrac{\pi}{a} \le k \le \dfrac{\pi}{a}$.

These linear combinations are called *Bloch functions* (an "infinite" molecular orbital, in a sense, or a "crystal orbital") and the range of *k* is called the *first Brillouin zone* (a unit cell in reciprocal space).[15]

Two important Bloch functions that can be easily visualized are at $k = 0$ and $k = \dfrac{\pi}{a}$.

$$\psi_0 = \sum_n e^0 \chi_n = \sum_n \chi_n = \chi_0 + \chi_1 + \chi_2 + \chi_3 + \ldots \qquad (1\text{-}2)$$

$$\psi_{\frac{\pi}{a}} = \sum_n e^{\pi i n} \chi_n = \sum_n (-1)^n \chi_n = \chi_0 - \chi_1 + \chi_2 - \chi_3 + \ldots \qquad (1\text{-}3)$$

In other words, ψ_0 represents the all-in-phase combination of atomic orbitals, whereas $\psi_{\frac{\pi}{a}}$ represents the all-out-of-phase combination. Whether these are bonding or antibonding interactions depends on the type of orbitals being combined. A plot of the energies of ψ_k vs. k is called a *band dispersion diagram* (Figure 1-4b); note that it is sufficient to plot in the range $-\frac{\pi}{a} \leq k \leq \frac{\pi}{a}$ because the energy bands are always symmetric about the centre of the Brillouin zone.[15] Although there are a finite number of states (because k is quantized) they are located so closely in energy that the plot is quasi-continuous and it becomes convenient to connect these discrete states by lines (energy bands). The number of states per energy increment, called the *density of states* (DOS), is a transformation of this reciprocal space picture to one in real space; it is inversely proportional to the slope of E_k vs. k (Figure 1-4b).[15] For metallic systems, like the compounds discussed in this thesis, the Fermi energy (E_F) cuts the DOS. For semiconductors and insulators, E_F will fall between a filled valence band and an empty conduction band.

In the same way as for molecular orbital calculations, it is possible to perform an overlap population analysis to evaluate the bonding character of these Bloch functions for a specified type of interaction. For a solid, this is called a *crystal orbital overlap population* (COOP), (Figure 1-4d), which results from multiplying the DOS by the matrix elements of the overlap integral.[15] The interpretation is that states can be evaluated as being bonding (positive), nonbonding (zero), or antibonding (negative) with respect to a specified interaction by inspecting the sign of the COOP.

a)

$$\psi_k = \sum_n e^{ikna} \chi_n$$

$\chi_0 \quad \chi_1 \quad \chi_2 \quad \chi_3$

E

b)

E_f

$k_0 \quad\quad k_{\frac{\pi}{2}}$

k →

c)

E_f

DOS →

d)

E_f

- 0 +
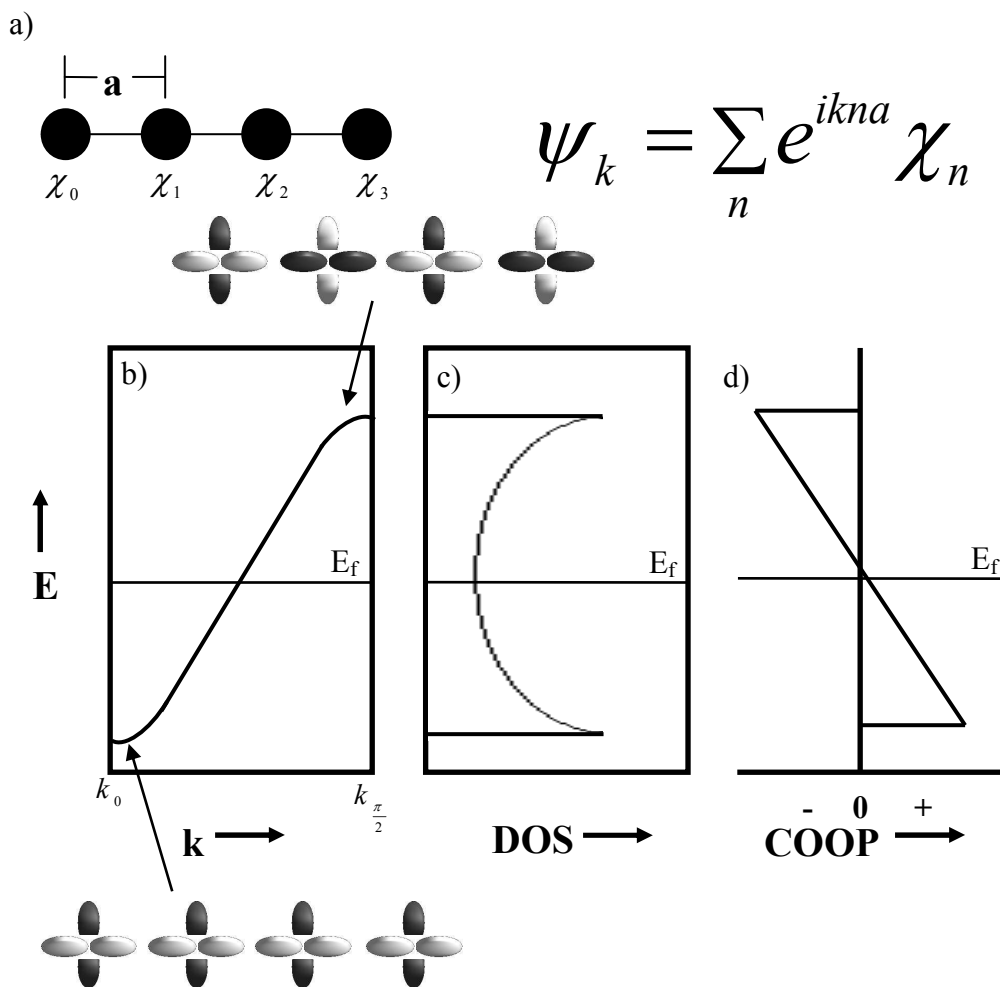
COOP →

Figure 1-4 (a) A 1-D chain of Ni atoms separated by a distance *a*. (b) The band structure, (c) density of state (DOS), and (d) crystal orbital overlap population (COOP) curves for the Bloch functions of Ni $3d_{x^2-y^2}$ orbitals.

It is important to realize that applying the Schrödinger equation to a solid with an infinite number of atoms is a very challenging problem, involving the consideration of the Coulomb potential of nuclei, the Hartree potential, and exchange-correlation potential. An attractive approach to treat this problem is *density functional theory* (DFT), which reduces the many-electron problem to one in which the potentials can be evaluated through the one-electron Kohn-Sham equation.[16] A standard DFT method applied to band structure calculations makes use of the Stuttgart *tight-binding linear muffin-tin orbital* (TB-LMTO) program, within the *local*

density approximation (LDA) and *atomic sphere approximation* (ASA).[17] Potential functions are

characterized by "muffin-tin" spheres whose radii depend on the type of atom and by empty

spheres of zero potential energy to model void space within the unit cell. In DFT techniques, the

COOP curve is replaced by a crystal orbital Hamilton population (COHP) curve, in which the

DOS is now weighted by matrix elements of the Hamiltonian instead of the overlap integral.

Unlike the COOP curve, which is calculated as an average over all bonds within the unit cell, the

COHP curve involves the summation of bonds within the unit cell.[16]

1.3.2 Bonding in Ni_2P

The metal-rich compound Ni_2P serves as a good illustration of how the electronic

structure of a solid is described. Ni_2P forms the Fe_2P-type structure (Figure 1-5a) with Ni atoms

occupying two coordination sites: tetrahedral (surrounded by four P atoms) and square pyramidal

(surrounded by five P atoms).[18] The Ni atoms form an extensive metal-metal bonding network

(not evident from the figure), which prevents full electron transfer to the P atoms. The DOS

curve (Figure 1-5b) can be interpreted as follows: Because the Fermi level cuts through a finite

DOS, Ni_2P is metallic, in agreement with expectation. Inspection of the partial DOS of the P

atoms reveals that there are unoccupied states, implying that P atoms have an incomplete octet.

The partial DOS of the tetrahedrally coordinated Ni atoms encompasses two broad regions,

representing the e and t_2 states, but these are broadened in energy because of additional Ni–Ni

interactions.

a) Ni$_2$P-type Structure

b)
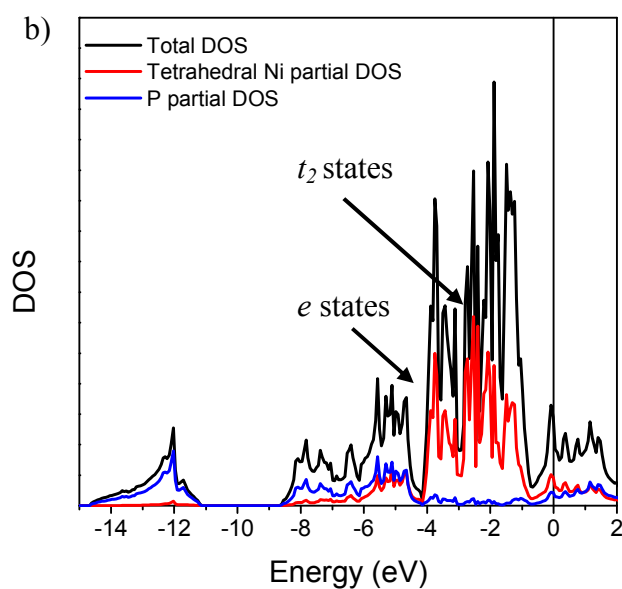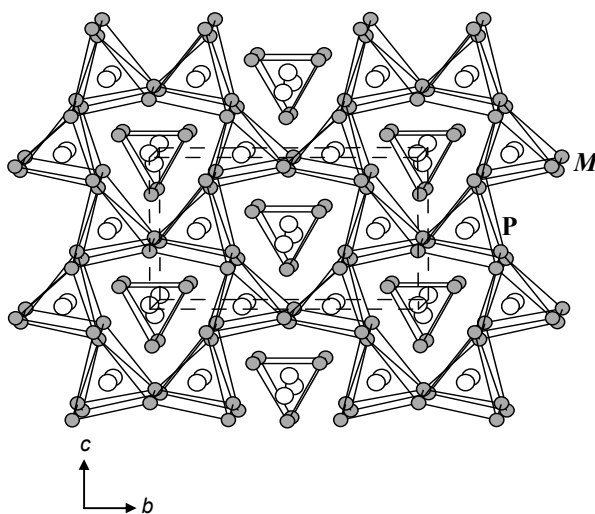
Figure 1-5 (a) The structure of Ni$_2$P forming the Fe$_2$P-type structure. (b) The density of states (DOS) curve of Ni$_2$P highlighting the total DOS (Black line), and the partial DOS for the tetrahedral Ni (Red line) and P (Blue line).

1.4 X-ray Diffraction

The traditional methods which work so well for determining the structures of molecular substances fail for most extended solids, especially intermetallic compounds (e.g., the lines in

NMR spectra are severely broadened because of unpaired electrons in transition-metal and rare-earth atoms). Instead, X-ray diffraction (XRD) is the most important method for structure determination. The principle of XRD is that when X-rays are scattered by a periodic arrangement of atoms in a crystalline solid, they undergo constructive and destructive interference.[19] The resulting diffraction pattern can be modeled as if X-rays are reflected off sets of lattice planes (described by Miller indices (*hkl*)) at specific angles, according to Bragg's law (Figure 1-6):[19]

$$2d_{hkl} \sin \theta_{hkl} = n\lambda \tag{1-4}$$

where λ is the wavelength of the radiation source (typically Cu Kα (Å) or Mo Kα (Å)), d_{hkl} is the spacing between adjacent lattice planes, θ is the angle of reflection, and *n* the order of reflection. Because reflections of higher order *n* are equivalent to first-order reflections of planes (*nh, nk, nl*), this can be simplified and rearranged to:

$$\sin \theta_{hkl} = \frac{\lambda}{2d_{hkl}} \tag{1-5}$$

The diffraction angles (usually expressed as 2θ, which is the angle between the incident and diffracted beam) depend on the unit cell parameters, whereas the intensities of the diffraction peaks depend on the type and positions of atoms within the unit cell.
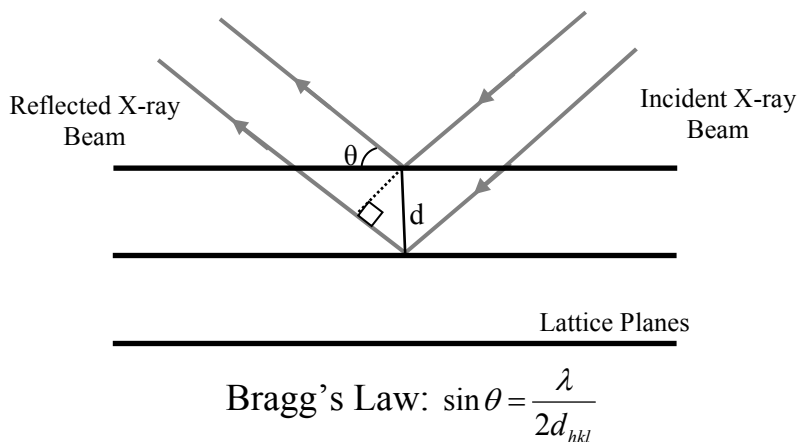
Figure 1-6 The derivation of Bragg's equation.

X-ray diffraction studies are best performed on single-crystal samples. There are typically three stages to solving a crystal structure: i) data collection, ii) finding a trial structure, and iii) refinement of the trial structure.[20] A single crystal is mounted onto a glass fiber and diffraction angles are analyzed to determine the lattice symmetry and unit cell dimensions. From the measured intensities of thousands of reflections, a structure-solving program, such as SHELXTL,[21] makes use of probabilistic theories (direct methods) to propose a trial structure. For compounds of a known structure type, such as those discussed in this thesis, atomic positions can also be easily estimated from known compounds. Least-square refinements are performed to minimize the sum of the deviations between the squares of the observed and calculated intensities. A structure refinement is generally considered to be acceptable when the residual (R-value) is less than 0.10 and the goodness-of-fit (S) is close to 1.[20,22]

In some cases, it is not possible to grow good single crystals, perhaps because they are too small or suffer from twinning. In these situations, XRD data can be collected on powder (microcrystalline) samples. Since a powder contains crystallites in random orientation, only averages of all peaks are collected when the sample is irradiated.[22] The intensities of reflections are measured over a wide range of 2θ (0-100°). Powder XRD is a powerful technique for qualitative phase analysis through matching of experimental powder patterns to model compounds (as illustrated for Ni_2P in Figure 1-7). For new compounds of unknown structures, it is difficult to determine the structure from the powder diffraction pattern. If the structure is known, it is possible to fully refine it using the Rietveld method, in which the entire powder pattern is fitted in small steps.[23] Full profile Rietveld refinement can be performed using a number of software packages, such as Fullprof[24] and LHPM-Rietica.[25]
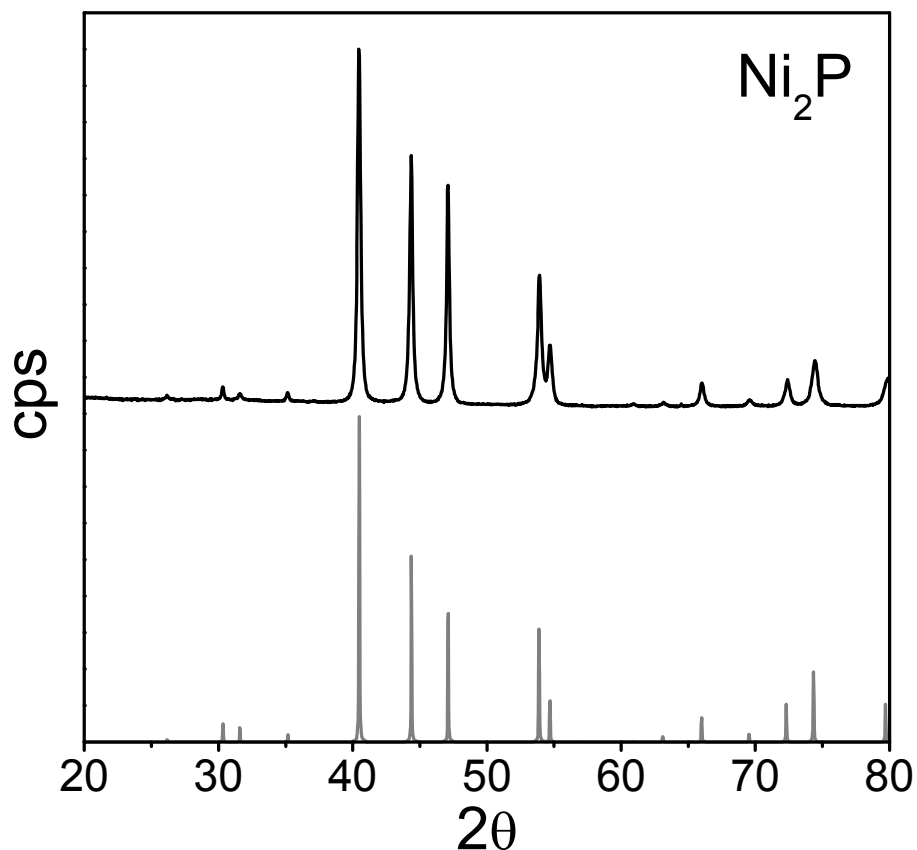
Figure 1-7 The experimental (black line) and theoretical (gray line) powder XRD patterns of Ni_2P. This diffraction pattern was collected on an Inel powder X-ray diffractometer using a Cu Kα X-ray source.

1.5 Properties and applications

1.5.1 Rare-earth transition metal pnictide oxides *REMPn*O

First discovered 20 years ago and originally mistaken as ternary pnictides, the quaternary rare-earth transition-metal pnictide oxides (or "oxypnictides"), *REMPn*O (*RE* = rare-earth, *M* = transition metal), show promise as a new series of materials with varied physical properties.[26,27]

They range from metals,[27] magnetic semiconductors,[28,29] antiferromagnets,[30] and, most extraordinarily, superconductors at relatively high critical temperatures (T_C).[31] These properties are derived from the occurrence of alternating [*REO*] and [*MPn*] layers in the ZrCuSiAs-type structure, an important type that will be detailed later.

A superconductor exhibits zero electrical resistance below a critical temperature T_C.[32] Three parent pnictide oxides are superconducting at modest temperatures: LaFePO ($T_C = 7$ K),[28] LaNiPO ($T_C = 4$ K),[33] and LaNiAsO ($T_C = 2.4$ K).[34] However, T_C can be raised dramatically through appropriate doping, most commonly by electron doping through substitution of O^{2-} with F^-, or RE^{3+} with Th^{4+},[35] and less commonly by hole doping through substitution of RE^{3+} with Sr^{2+}.[36] Various doping methods have lead to the discovery of a large number of superconductors. Some of the more notable examples are listed in Table 1-2.

Table 1-2 The critical temperature (T_C) of various rare-earth transition-metal arsenide oxides.

Compounds	Critical Temperature (T_C)
$Gd_{1-x}Th_xFeAsO$[35]	56 K
$SmFeAsO_{1-x}F_x$[48]	54.6 K
$PrFeAsO_{1-x}F_x$[49]	52 K
$NdFeAsO_{1-x}F_x$[50]	51 K
$LaFeAsO_{1-x}F_x$[31]	43 K
$GdFeAsO_{1-x}F_x$[51]	36 K
$Pr_{1-x}Sr_xFeAsO$[36]	25 K
$LaFe_{1-x}Co_xAsO$[52]	13K

The occurrence of superconductivity in these compounds is puzzling and mysterious, most notably because the presence of magnetic ions like Fe^{2+} is normally incompatible with superconductivity. According to BCS theory (named after Bardeen, Cooper, and Schrieffer), conventional superconductivity arises from the formation of electron pairs through strong electron-phonon coupling.[37] However, BCS theory fails to explain high-T_C superconductivity where electron-phonon interactions would be too disrupted by thermal fluctuations.[38] The pnictide oxides show intriguing similarities to the high-T_C cuprates, which were first discovered in 1986 and now have T_C's as high as 150 K.[39,40] Both adopt layered structures with the conduction along [CuO] planes being analogous to that along [*MPn*] layers. This two-dimensionality is believed to be the key feature of high-T_C superconductivity.[39,41]

In the cuprates, a temperature-dependent pseudogap (a region near E_F that contains very few energy states) opens up below T_C, which allows electrons to move along the surface of the [CuO] planes.[42] Evidence for a similar pseudogap, consisting of mostly Fe 3d orbitals, has now been reported in the pnictide oxides. This suggests that electrons in the [*MPn*] layer may be involved in superconductivity.[43-45] However, a recent study on single crystal LaFePO has suggested that the pseudogap is an artifact of previous studies using polycrystalline samples.[46] A more controversial explanation is that antiferromagnetic spin fluctuations are the cause of superconductivity.[47]

1.5.2   *M*₂P and *M*₃P phosphides

Metal-rich phosphides M_2P exhibit a wide range of magnetic properties, by virtue of the unpaired electrons provided by the transition metal (*M* = Mn, Fe, Co, Ni). Mn₂P exhibits antiferromagnetic behaviour, in which the magnetic moments are aligned in an antiparallel

fashion below a Néel temperature (T_N) of 103 K.[53] Fe_2P exhibits ferromagnetic behaviour, in which the magnetic moments are aligned in a parallel fashion below a Curie temperature (T_C), variously reported to be 266 K (Bailey and Meyer),[54,55] 306 K (Chiba),[56] and 209 K (Fujii).[57] Neutron diffraction studies have shown that the two Fe centres have different magnetic moments, with the 4-coordinate Fe atoms having the smaller magnetic moment.[58] Co_2P and Ni_2P exhibit Pauli paramagnetic behaviour in which the delocalized conduction electrons of these metallic solids split in energy such that there is a slightly greater population of spins parallel instead of antiparallel to the external magnetic field, resulting in a small, positive, and temperature-independent magnetic susceptibility.[59]

The properties of solid solutions based on M_2P have also been investigated. Mixed-metal phosphides $(M_{1-x}M'_x)_2P$ (where M' is the more electronegative) undergo magnetic phase transition with metal substitution. For example, $(Mn_{1-x}Fe_x)_2P$ changes from antiferromagnetic to ferromagnetic when x exceeds 0.98.[60] $(Fe_{1-x}Ni_x)_2P$ is ferromagnetic with T_C at a maximum of 342 K at $x = 0.1$, diminishing to 100 K as x increases before reverting to Pauli paramagnetic behaviour at $x = 0.8$.[61] $MnFeTt_yP_{1-y}$ (Tt = Si, Ge) is ferromagnetic, with T_C increasing as both y and the c/a ratio increase.[62]

Perhaps the most attractive application of these mixed-metal phosphides $(M_{1-x}M'_x)_2P$ is as potential candidates for magnetic refrigeration. Compared to vapour-cycle refrigeration, magnetic refrigeration is more environmentally friendly and energy efficient.[63] It is based on the magnetocaloric effect (MCE), a phenomenon first observed in iron metal in which a change in temperature is induced upon exposure to an external magnetic field because of the onset of magnetic ordering.[64] In the magnetic refrigeration cycle (Figure 1-8), a magnetic material is initially isolated from the system to be cooled. When an external magnetic field is applied,

randomly oriented magnetic moments suddenly align, this ordering decreasing the overall magnetic entropy (ΔS). Under adiabatic conditions, there is an equal but opposite change in the entropy of the lattice, which is manifested by an increase in temperature (ΔT).[64,65] This change in temperature can be determined by the Maxwell relation:[64,65]

$$\left(\frac{\partial S}{\partial B}\right)_T = \left(\frac{\partial M}{\partial T}\right)_B \qquad (1\text{-}6)$$
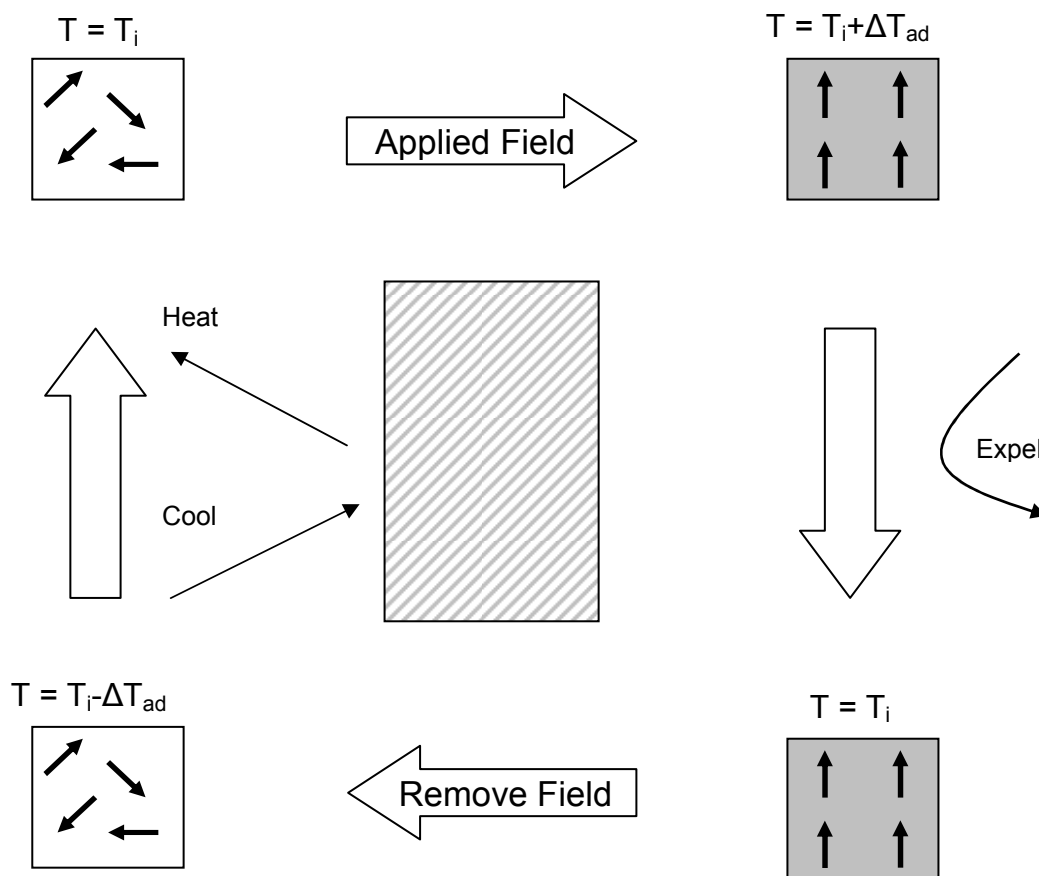
Figure 1-8 A schematic representing of the magnetic-refrigeration cycle constructed using information from reference 65.

where M is the magnetization of the magnetic material in the external magnetic field B. At this point, a heat transfer fluid (either a liquid or gas) is put in contact with the magnetized system

and removes the excess heat. When the external magnetic field is then reduced to zero, the magnetic ordering is disrupted and the magnetic moments are once again randomized. This disordering causes a sudden increase in ΔS and the temperature is decreased by ΔT. The magnetic material is returned to its initial temperature (T_i) by withdrawing heat from the material to be cooled so that the process can be repeated. The most viable magnetocaloric materials for magnetic refrigeration are ferromagnets that order near or above room temperature and induce a large ΔS.[63,64] Competing with the "giant MCE" material $Gd_5Ge_2Si_2$ ($\Delta S = 14.5$ $J \cdot kg^{-1} \cdot K^{-1}$),[66] the transition-metal pnictide $MnFeP_{0.45}As_{0.55}$ (Fe_2P-type) has, coincidentally, a maximum ΔS of 14.5 $J \cdot kg^{-1} \cdot K^{-1}$ under an external field of 2 T above 300 K.[63] Despite a lower ΔS of 2.0 $J \cdot kg^{-1} \cdot K^{-1}$ (under 2T), $(Fe_{0.975}Ni_{0.025})_2P$ is also a promising candidate because its T_C is above 300 K.[67] Work is in progress to improve ΔS in Fe_2P-type materials by fine-tuning their composition.

The phosphides M_2P have also been identified as catalysts for hydrodesulfurization (HDS),[68] hydrodenitrogenation (HDN),[68] and hydrodechlorination (HDC) processes,[69] which remove S, N, and Cl, respectively, from hydrocarbons. The catalytic activity increases in the order $Fe_2P < Co_2P < Ni_2P$.[68,70-72] Ni_2P supported on SiO_2 is more active than the commercial catalyst Ni-Mo-S/SiO_2 (HDS 98% vs. 78%; HDN 80% vs. 43%).[68] Backbonding from P to Ni atoms is believed to stabilize the Ni 3d states, enhancing the ability of the Ni sites to be adsorbed with S- and N-containing compounds on the metal-rich (001) surface of Ni_2P.[73] Evidence to support this proposal comes from the observation that doping Ni_2P with Co enhances the activity, showing that occupation of metal 3d states is important.[74] However, the catalyst support also plays a role since Si-based supports tend to perform better than alumina supports (which bond too strongly to P atoms of Ni_2P, but carbon-coating partly mitigates against this

problem).[75,76]   Finally, new efforts are being made to increase surface area by developing nanoparticles of Ni_2P.[77,78]

Although not as well investigated as M_2P, the even more metal-rich phosphide Ni_3P also exhibits catalytic activity in HDC, HDS and HDN processes.[69,79-81] Ni_3P is a potential industrial coating stable up to 400 ^0C and has been identified as a major component in meteorites.[82-84] Applications of other related phases have not been investigated. In terms of magnetic behaviour, Fe_3P is ferromagnetic (T_C = 716 K),[54] Mn_3P is antiferromagnetic (T_N = 115 K),[55] and Ni_3P and Cr_3P are Pauli paramagnetic.[85]

1.6 Studying the electronic structure of metal pnictides via X-ray spectroscopy

Despite the importance of many of these metal pnictides, their electronic structures have not been well investigated by experimental means. The goal of this thesis is to apply XPS and XAS to understand their electronic structures. Chapter 3 describes the $ZrGe_2$-$ZrAs_2$ phase diagram and an XPS study of $ZrAs_2$ and $Zr(Ge_{1-x}As_x)As$. Chapter 4 discusses the electronic structure of ZrCuSi*Pn* phases. Chapters 5 and 6 discusses the electronic effects of altering the [*M*As] and [*RE*O] layers, respectively, in *REM*AsO. Chapters 7 and 8 discuss the electronic structures of the metal-rich binary (M_2P, M_3P) and ternary (($Ni_{1-x}M_x)_2P$), respectively, as a extension of the studies of *M*P and $M_{1-x}M'_xP$ phosphides. In the next chapter, XPS and XAS are described in detail, and their applications and interpretation are discussed.

Chapter 2

X-ray spectroscopy

2.1 Introduction

In this thesis, X-ray photoelectron spectroscopy (XPS) and X-ray absorption spectroscopy (XAS) are applied to study the electronic structure of intermetallics. By analyzing shifts in energy and spectral features, we can infer information about bonding, oxidation states, and coordination environment. XPS can be performed in-house in a laboratory setting, whereas XAS requires the use of synchrotron radiation available only in large-scale facilities like the Canadian Light Source (CLS) and Advanced Photon Source (APS).

2.2 X-ray photoelectron spectroscopy

XPS is a powerful technique normally used to examine the electronic structure of surfaces, but with appropriate sample preparation, bulk solids can be examined as well. Also known as electron spectroscopy for chemical analysis (ESCA),[86] XPS is capable of detecting all elements except H and He.[87-89] First developed by Siegbahn in 1954, XPS makes use of the photoelectric effect, a phenomenon discovered by Hertz in 1887 and later explained by Einstein in 1907.[86] When an atom M absorbs electromagnetic radiation (such as X-rays), an electron (called a photoelectron) is ejected:

$$M \xrightarrow{\;h\upsilon\;} M^+ + e^-$$

(2-1)

Properly formulated, the binding energy (BE) of this electron is the difference in energy between the final state (E_{final}), represented by M^+ with N-1 electrons, and the ground state (E_{ground}), represented by M with N electrons.[86,88] In the XPS experiment (Figure 2-1), electrons emanating from different orbitals are successively ejected with specific kinetic energies (KE). The energy of the absorbed X-ray photon is equal to the energy needed (BE) to bring an electron from its ground state to the Fermi edge (E_F), the energy needed (called the work function φ) to bring it to the vacuum (E_V), and finally its KE when it is ejected:[86,88]

$$h\upsilon = KE + BE + \varphi \qquad (2\text{-}2)$$

Although φ depends on the spectrometer and the sample, it can be fixed to a constant value by grounding the sample, which pins the Fermi edge of the sample and spectrometer to the same energy.

Photoelectric Effect
BE = *hv* – KE - *φ*

Ni metal
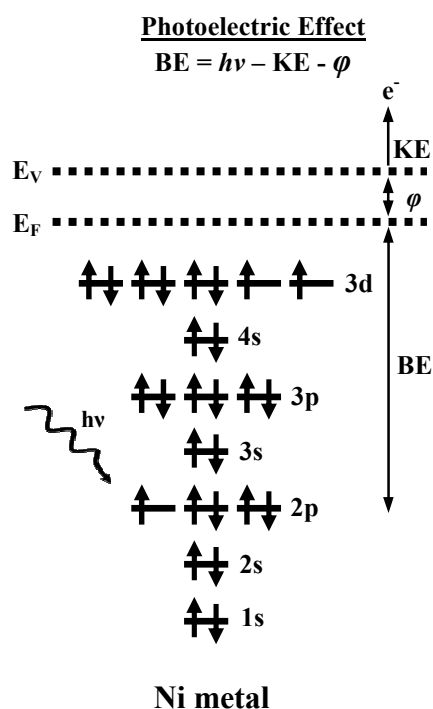
Figure 2-1 The ejection of a 2p electron from a Ni atom bombarded by X-ray energy.

In the early development of XPS, the ejection of a photoelectron was viewed as an ionization event in which the BE was interpreted as the first ionization energy from a given orbital.[86,88] This assumption that one-electron wavefunctions can be considered in isolation, known as Koopmans' theorem, worked well for s orbitals, which have zero orbital angular momentum ($l = 0$).[86,88] However, as instrument resolution improved, it could not account for the two peaks observed for p, d, and f orbitals, which have non-zero orbital angular momentum (Figure 2-2). These two peaks arise because the unpaired core electron remaining after photoionization can be in a spin-up or spin-down final state.[86,88] They are labelled nl_j (where n is the principal quantum number, l is the orbital angular momentum quantum number, and j is the Russell-Saunders coupled (orbital, l, and spin, s) angular momentum, with allowed values ranging from $l+s$ to $|l–s|$), as shown for the $2p_{3/2}$ and $2p_{1/2}$ peaks in the Ni 2p core-line spectra. The relative intensities of these peaks are proportional to the degeneracy of these final states, which is equal to $2j+1$.[86,88] The energy difference between the two final states, known as the exchange energy η or spin-orbit splitting energy, depends on l and scales with the atomic number Z and the inverse cube of the atomic radius $1/r^3$, with the spin-up state being lower in energy.[85] The line-width of each peak depends on thermal scattering within the solid, the lifetime of the final state, the X-ray source, and the energy resolution of the analyzer.[87] In general, the spin-down final state has a shorter life time than the spin-up final state and will have a slightly larger full-width-at-half-maximum (FWHM).[87]

A schematic of a modern day XPS instrument is shown in Figure 2-3. XPS experiments are performed under ultra-high vacuum (UHV) at pressures ranging between 10^{-8} and 10^{-10} torr to prevent residual gas molecules from scattering low-energy electrons, decreasing the signal-to-
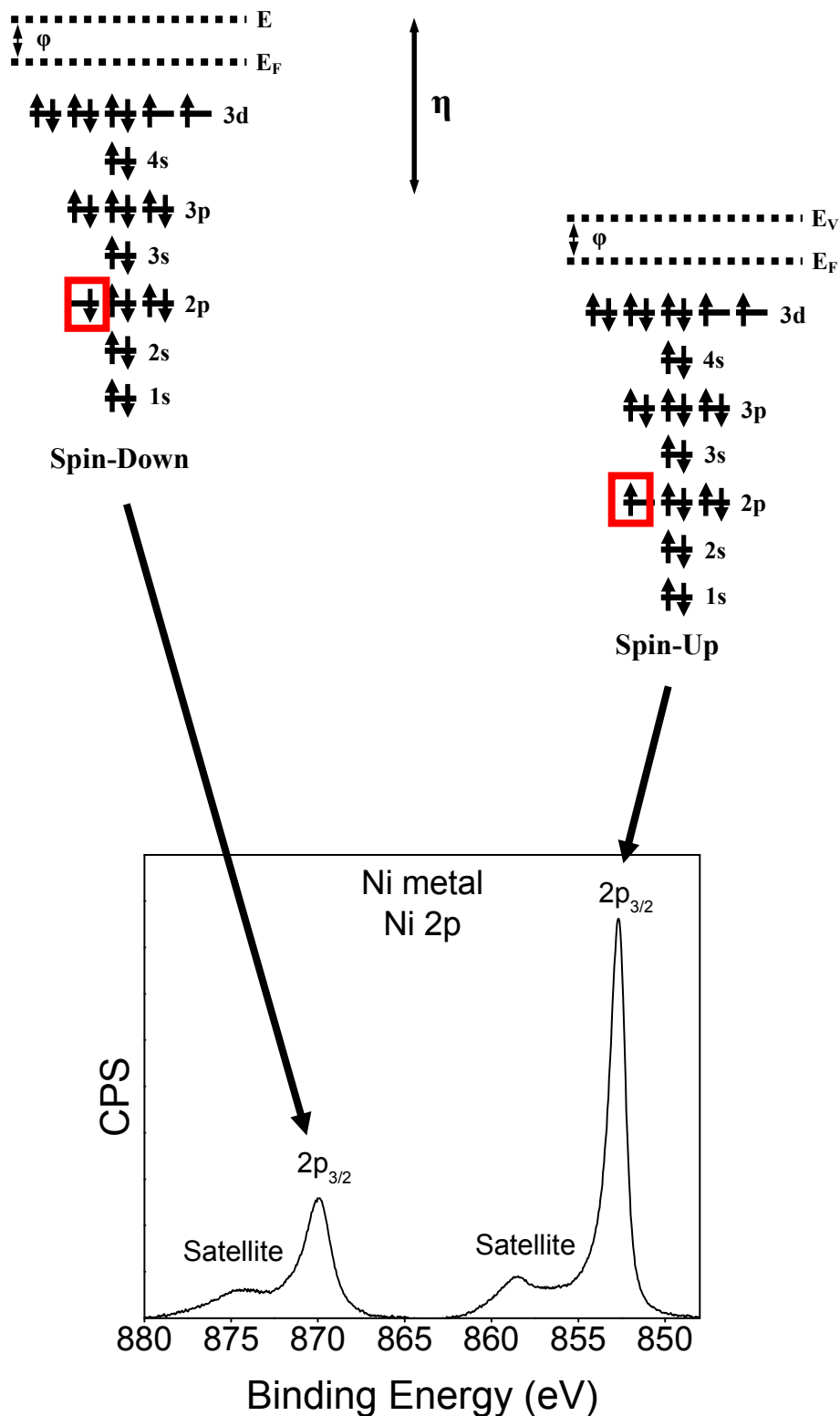
Figure 2-2 The spin-up ($2p_{3/2}$) and spin-down ($2p_{1/2}$) final states of the Ni 2p XPS spectrum. The Ni 2p XPS spectrum was collected on a Kratos AXIS 165 XPS spectrometer using an Al Kα X-ray source (1486.7 eV).

noise ratio.[87] UHV conditions are achieved using an ion pump. All XPS instruments are equipped with an X-ray source, the most common being monochromatic Al Kα.[87] Monochromatization is achieved by selective diffraction from a known surface of a quartz crystal.[87] Monochromatic sources are often preferred over achromatic ones because of their higher resolution.[87] However, an achromatic Mg Kα X-ray source is used when core-line peaks are obscured by Auger peaks, which arise when a second electron (Auger electron) is emitted with a specific KE (and hence BE) as another possible relaxation mechanism after photoionization of the core electron takes place.[86,90,91] However, unlike photoelectrons which have a fixed BE, it is the KE of an Auger peak that is fixed. An Auger peak can thus be identified because its BE will vary if the excitation source is altered. In photoemission spectroscopy (PES), the variable wavelengths that can be tuned with a synchrotron source are used to measure multiple spectra to gain additional information such as the experimental DOS.[86,92] Although not used in this thesis, ultraviolet photoelectron spectroscopy (UPS) makes use of the low excitation energy of a He discharge lamp (21.2 eV) to improve surface sensitivity over an X-ray source.[86,93]

Once a photoelectron is emitted from a sample, it enters a detector system consisting of a transfer lens, an electron energy analyser, and a detector. The angle between the detector system and the X-ray source is fixed at 54.7° to minimize the orbital angular dependence of the photoelectrons.[86] Photoelectrons in the vacuum are focused on the electron lens via electrostatic and magnetic fields. At the entrance slit of the transfer lens, the KE of the photoelectrons is reduced so that all electrons have the same energy. This retarding energy is known as the pass energy; the lower the pass energy, the higher the resolution.[86,87] Exiting the transfer lens at the same energy, the photoelectrons next enter the electron energy analyzer. In the Kratos AXIS 165
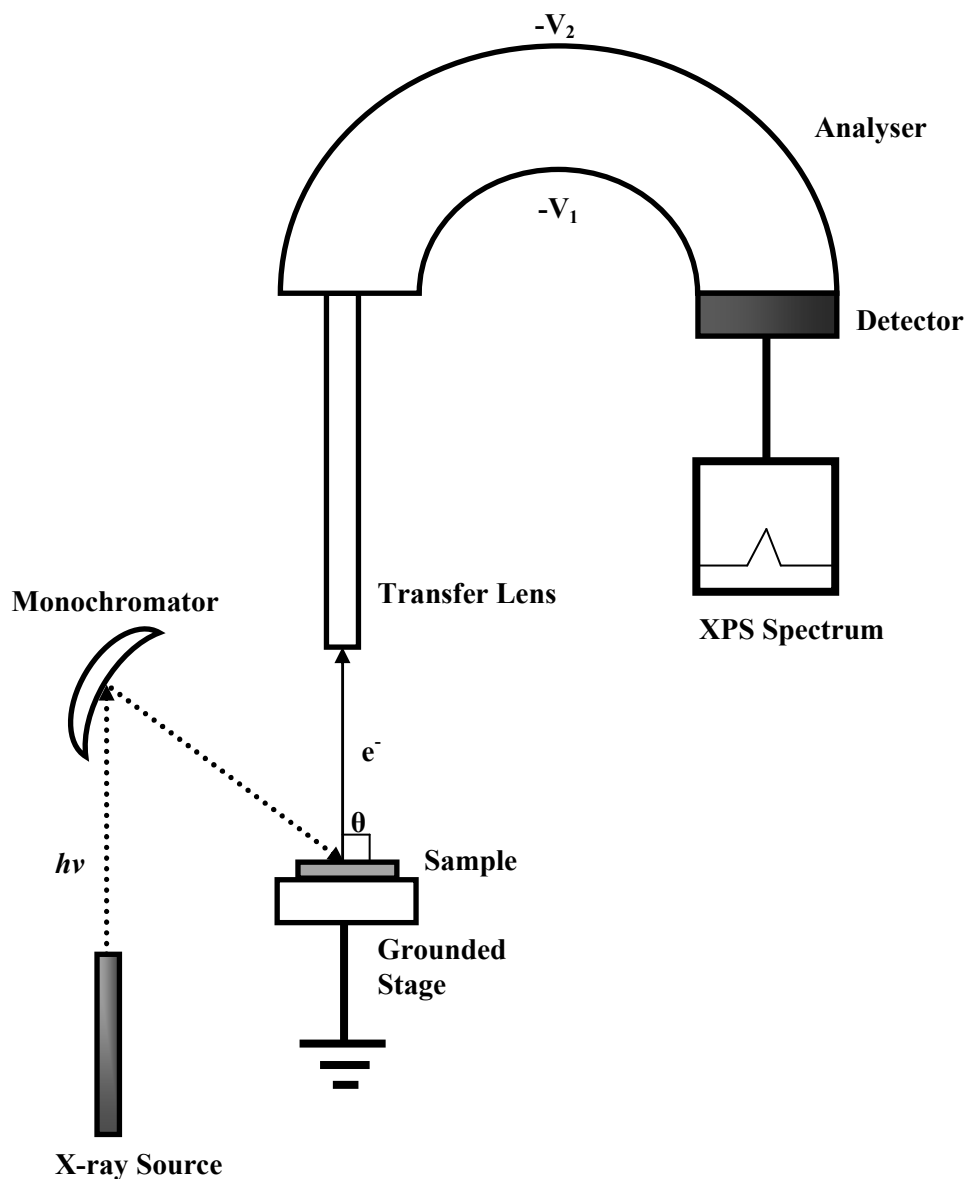
Figure 2-3 Schematic of an X-ray photoelectron spectrometer.

spectrometer, photoelectrons encounter opposing potentials along the walls of a concentric hemispherical analyser (CHA), with the upper hemisphere having the higher potential, such that only those photoelectrons with KE equal to the pass energy reach the detector while others are absorbed by the walls. The most common detector is an electron multiplier tube, which counts every electron as an independent event.[86,87] Here, a system of 8 channeltron detectors, each made of glass impregnated with metal (often lead or vanadium), allows for parallel data

acquisition. The XPS spectrum is constructed from a plot of intensity (cps) for each BE, calculated from equation 2-2 from the KE measured in the transfer lens before the photoelectron is retarded to the pass energy.

Two types of spectra can be obtained depending on the pass energy.[86,88] A survey spectrum is collected over a wide BE range (1100–0 eV) with a high pass energy (typically 160 eV) to identify the elemental composition in the sample (Figure 2-4). A high resolution spectrum is collected over a narrow BE range (<100 eV) with a low pass energy (typically 20 eV) to observe detailed spectral features and to obtain accurate BE values. The intensity of a core-line peak depends on many factors:[88]

$$I = J\rho\sigma K\lambda \tag{2-3}$$

where J is the photon flux, ρ is the concentration of a particular element, σ is the photoelectron cross-section, K is a constant term combining all instrumental factors, and λ is the inelastic mean free path (IMFP). The concentration of a given element is proportional to the relative intensity of a chosen core-line peak:[88]

$$C_i = \frac{I_i/\sigma_i\lambda_i}{\sum_j^n I_j/\sigma_j\lambda_j} \tag{2-4}$$

The cross-section, σ, represents the probability of a given photoelectron to be emitted, and depends on the type of element and the excitation energy.[94,95] The IMFP describes the average distance that a photoelectron travels before it is scattered when it collides with other electrons in the material.[88] Scattering is more pronounced at high BE, resulting in a stepped background in the spectrum. When a path length of 3λ is traversed, the probability of scattering is 95%.[88] Typical values of λ are 10-30 Å.[96] The analysis depth, or how far a photoelectron travels
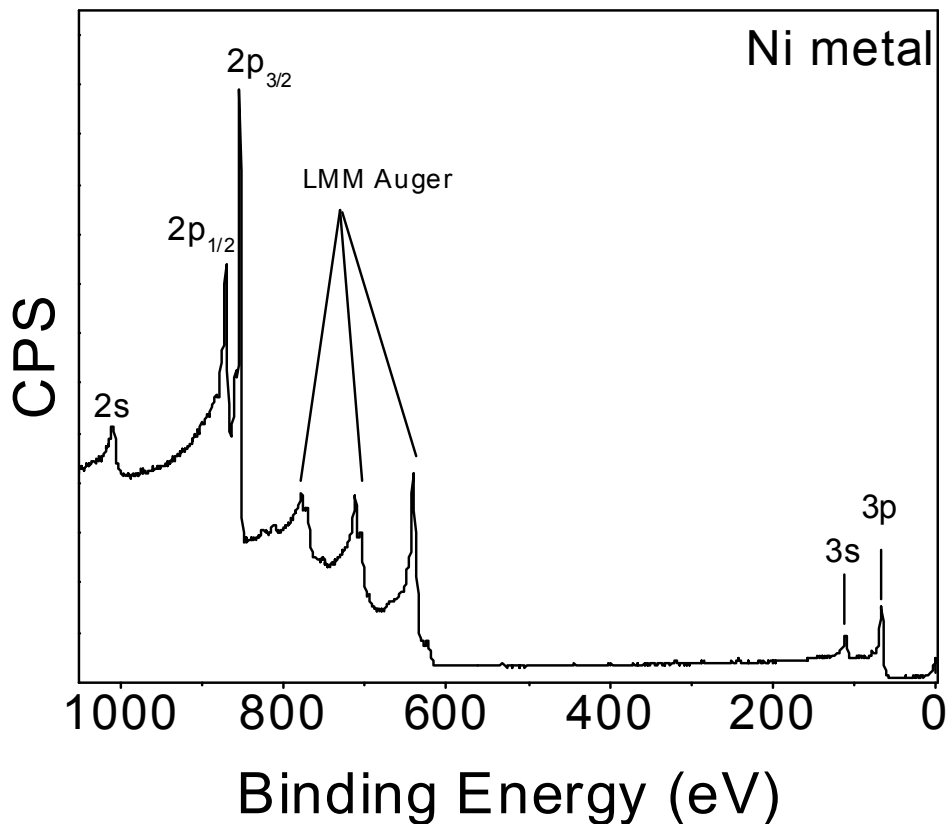
Figure 2-4 XPS survey spectrum of Ni metal. This spectrum was collected on an Kratos AXIS 165 XPS spectrometer using an Al Kα X-ray source (1486.7 eV).

through a sample, depends strongly on the take-off angle, θ, between the surface and the detector:[88]

$$d = 3\lambda \sin \theta \qquad (2\text{-}5)$$

The maximum depth is 3λ (at 90°), corresponding to typical values of 30–90 Å, which may be considered to be representative of the bulk solid. However, as θ is decreased to 0°, only photoelectrons near the surface can be ejected, which accounts for the exquisite surface sensitivity of XPS. Studies of photoelectron intensity as a function of θ form the basis of angle-resolved XPS (ARXPS).[97]

In high-resolution XPS spectra, the fine structure of core-line peaks is very informative. The background is first removed by fitting to a Shirley-type function (which best models the energy-loss behaviour).[98] Core-line peaks for atoms of main-group elements are commonly fitted to a symmetrical lineshape, combining Gaussian and Lorentzian functions.[99] In contrast, core-line peaks for atoms with unpaired electrons (i.e., transition metals with partly filled d and f configurations) are subject to multiplet splitting arising from the occurrence of non-degenerate final states.[86] This phenomenon can be exploited to distinguish between high- vs. low-spin configurations in octahedral complexes, such as those of Fe^{2+} ($3d^6$). The Fe 2p core-line peaks are asymmetrical in high-spin $FeBr_2$ (t_{2g}^4 e_g^2) but symmetrical in low-spin $K_4Fe(CN)_6$ (t_{2g}^6 e_g^0).[100] Asymmetric lineshapes skewed towards higher BEs are also seen in metallic solids, discussed later. Satellite peaks can be observed because of final state effects, such as the occurrence of plasmons when a photoelectron is scattered by valence electrons (as seen in the Ni metal, Figure 2-2).

The most useful feature of high-resolution XPS spectra is the sensitivity of the BEs of the core-line peaks to changes in oxidation state, which alter the degree of nuclear screening. Cations have fewer valence electrons, making photoelectrons harder to remove and shifting the core-line peak to higher BE. Anions have more valence electrons, making photoelectrons easier to remove and shifting the core-line peak to lower BE. However, surrounding atoms also affect the BE. For example, the nickel(II) halides have different Ni $2p_{3/2}$ BEs (NiF_2, 857.8 eV; $NiCl_2$, 856.6 eV; $NiBr_2$, 855.3 eV) despite a common oxidation state of +2, illustrating a ligand effect.[100] Bonds to less electronegative ligands are more covalent, resulting in more shared electrons screening the nuclear charge, thus lowering the BE, as seen in $NiBr_2$. Bonds to more electronegative ligands are more ionic, resulting in fewer electrons screening the nuclear charge,

thus increasing the BE, as seen in NiF_2. The number of surrounding ligands and their distance from the absorbing atom also affect the BE. These interatomic effects will be discussed in later chapters.

A secondary feature of high-resolution XPS spectra in the region of low BE (20–0 eV) corresponds to the valence band. In the past, valence band analysis was normally performed with UPS.[88] However, because of the low excitation energy used in UPS, such spectra were only representative of the surface and not the bulk of the solid.[88] As the name implies, valence band spectra examine the states directly involved in bonding. They are often compared to calculated DOS curves. Oxidation states can also be determined by fitting the valence band, in a procedure detailed later. The shape of the valence band near the Fermi edge depends on the electronic properties of the solid. Metals (such as Ni metal, Figure 2-5) show a sharp cut-off at 0 eV, as the Fermi edge cuts a partially filled band.[86] Semiconductors and insulators show a drop-off below 0 eV, as the Fermi edge falls at the top of a filled valence band.
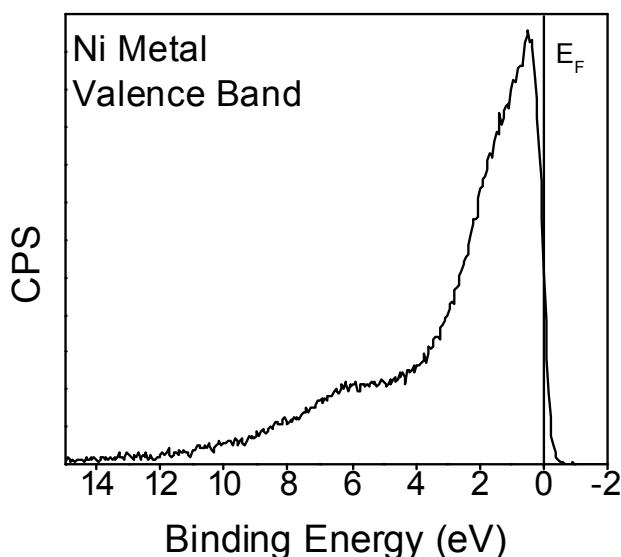
Figure 2-5 Valence band spectrum of Ni metal. The vertical line at 0 eV represents the Fermi edge (E_F). This spectrum was collected on a Kratos AXIS 165 XPS spectrometer using an Al Kα Kα X-ray source (1486.7 eV).

The electrical properties must be considered in the XPS experiment. Because electrons are emitted from the sample, the surface becomes positively charged, so that the photoelectrons may appear to have lower KE (higher BE) than expected. This charging can be easily eliminated in metals, which are conductors, by grounding to the sample holder so that electrons are replenished.[86] However, charging is a serious problem in insulators, causing not only an artificial BE shift, but also line broadening and peak splitting (if there is differential charging on the surface).[86] A common method to rectify this problem is to apply a charge neutralization, by bathing the surface with electrons emitted from a tungsten filament, as done in the AXIS 165 spectrometer.[86] Another method is to calibrate spectra to the adventitious carbon present on all surfaces, with the C 1s line set to 284.8 ± 0.2 eV (all XPS spectra in this thesis are referenced to the C 1s line set to 284.8 eV).[86] For metals, a secondary calibration method is to set the maximum of first derivative of the valence band to 0 eV.[86]

To probe the electronic properties of the bulk solid, it is important to remove any surface oxides, which are not representative of the bulk. Ideally, it is desirable to analyze a large single crystal that has been freshly cleaved. A process called ion sputtering makes use of an Ar^+ beam to physically remove atoms from the surface (Figure 2-6).[88] Although a destructive technique, ion sputtering enables profiling at further depths than achievable by ARXPS. Care must be taken in ion sputtering because there may be unintended consequences: (i) light atoms may be preferentially removed, (ii) ion-induced reactions may occur (such as the reduction of Mn^{2+} and Ce^{3+}),[102,103] (iii) prolonged ion-beam exposure may increase the roughness of the surface leading to poorer resolution.
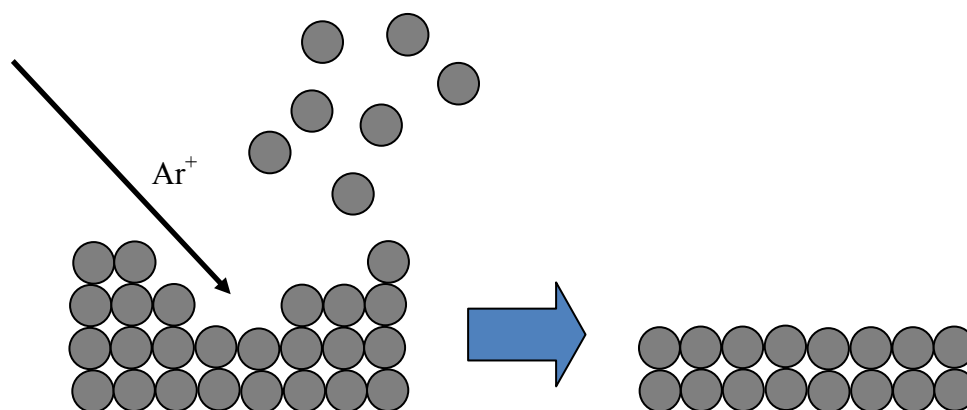
Figure 2-6 Schematic for the removal of surface atoms by Ar$^+$ ion bombardment.

2.3 X-ray absorption spectroscopy

2.3.1 Synchrotron radiation

In 1947, researchers at General Electric Research Laboratory in Schenectady, New York observed that electrons travelling at relativistic speeds (near the speed of light) and bent by an external magnetic field in a particle accelerator lose their energy in the form of electromagnetic radiation.[104-106] The energy of this synchrotron radiation corresponds to the energy loss of the electrons:[105]

$$\Delta E = 88.5 \frac{E^4}{\rho} \tag{2-6}$$

where ρ is the radius of curvature (28 m in the Canadian Light Source (CLS) and 176 m in the Advanced Photon Source) and E is the energy of the electron (typically 2-8 GeV depending on the facility).[105] Synchrotron radiation has several advantages over traditional X-ray sources, providing a higher flux (number of photons per second), brightness (flux per vertical angle), and brilliance (brightness per source area).[105]

Because first-generation facilities were often parasitic operations on existing high-energy physics facilities, the output of synchrotron radiation was limited.[107] A huge advancement in second-generation facilities was the development of an ultra-high vacuum storage ring (Figure 2-7).[105] Electrons produced in a linear particle accelerator are transported to a booster ring where they are accelerated to the desired energy before being injected into the storage ring.[108] Bending magnets around the circumference of the storage ring accelerate the electrons through Lorentz forces, producing a fan of X-rays (Figure 2-8a).[105] The dimensions of the electron beam are specified by the emittance (ε), which is the product of the standard deviation (σ) and divergence (σ') of the beam in the horizontal and vertical positions.[105] Normally, the horizontal emittance is greater than the vertical emittance, resulting in horizontal polarization.[105]

In third-generation facilities, insertion devices are added to the straight sections of the storage ring to produce an electron beam of even greater brightness and brilliance.[105,107] These insertion devices consist of arrays of N pairs of magnets that alternate in polarity, causing electrons to follow a sinusoidal path, characterized by a deflection parameter K_{id}:[105]

$$K_{id} = 0.934 \lambda_{id} B_o \qquad\qquad (2\text{-}7)$$

where λ_{id} is the magnetic period and B_o is the magnetic field of the insertion device. Two types of insertion devices are wigglers (Figure 2-8b) and undulators (Figure 2-8c). Wigglers have a larger K_{id} with a magnetic field often greater than that of the bending magnet (e.g. a wiggler with N magnetic periods is the equivalent to $2N$ bending magnets) and a relatively long λ_{id}.[105] Undulators typically have smaller magnetic fields and shorter λ_{id} so that K_{id} is close to 1.[105] They produce pulses of radiation that are out-of-phase with the next pulse so that the white spectrum of radiation produced from the bending magnet is replaced by harmonic radiation. This lowers the overall mean energy of the electron but enhances the brightness and brilliance.[105] Moreover,

unlike bending magnets and wigglers, which produce horizontal polarized radiation, the orientation of the magnetic field of the undulator can be changed allowing for control of the polarization and enabling the study of magnetic materials using a technique known as X-ray magnetic circular dichroism (XMCD).[108]
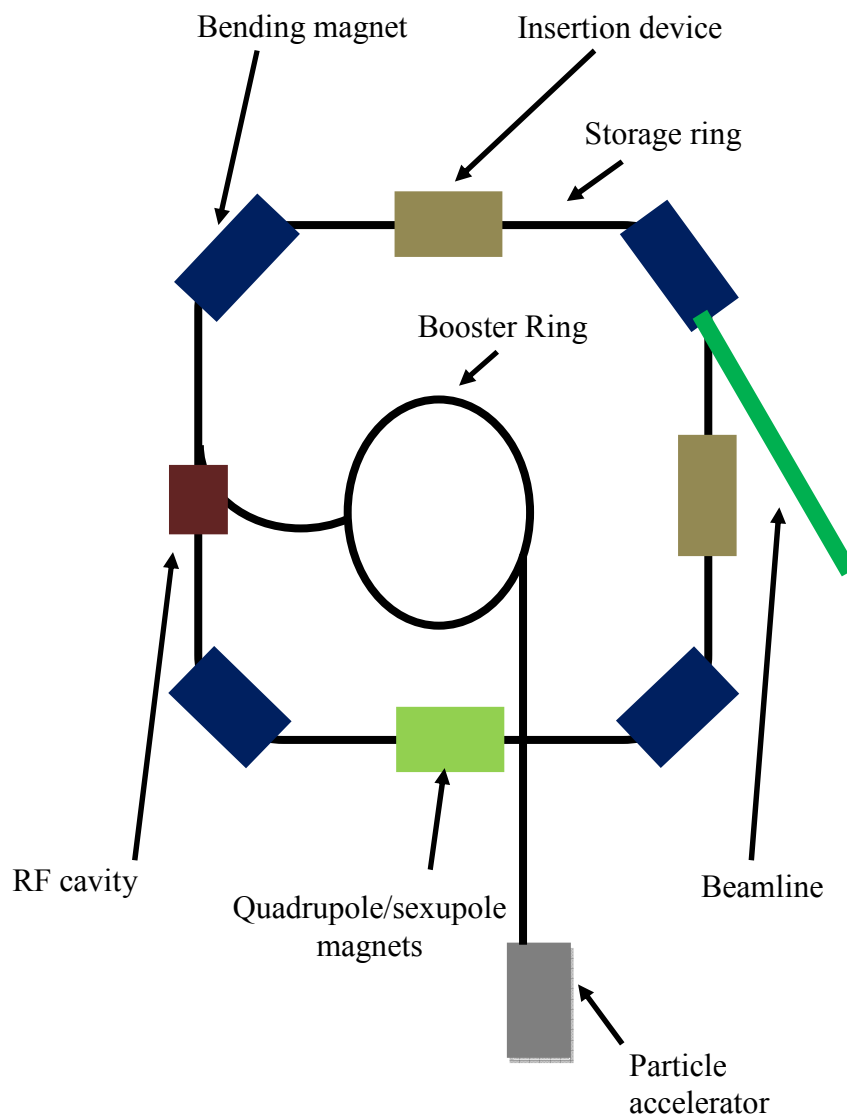
Figure 2-7 Schematic for a synchrotron storage ring.

a) Bending Magnet

Electron beam   Radiation Fan

Bending magnet

b) Wiggler

$\lambda_{wiggler}$ K > 1

N   S   N   S   N

S   N   S   N   S

c) Undulator

$\lambda_{undulator}$ K ≈ 1

N S N S N S N S N S

S N S N S N S N S N
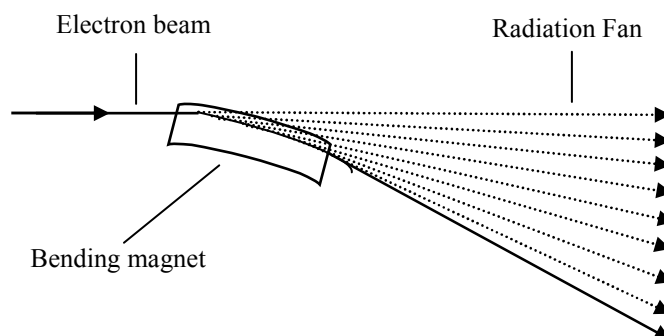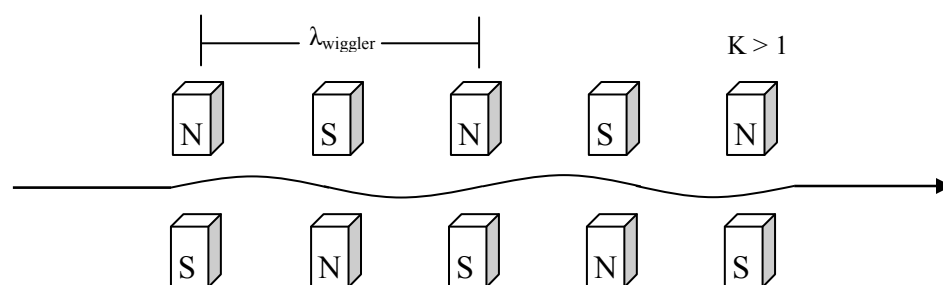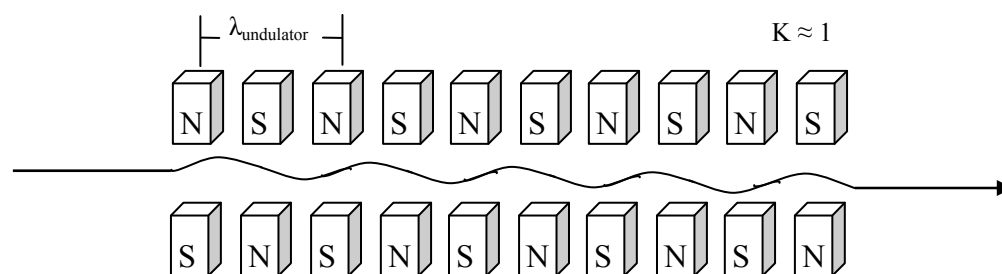
Figure 2-8 Schematics representing a) bending magnet, b) wiggler, and c) undulator.

Other components of the storage ring play important roles in maintaining the energy and path of the electron beam. To focus the electron beam, quadrupole and sextupole magnets are placed at various positions around the ring.[105,108] To prevent the electrons from losing energy,

radio frequency (RF) cavities are placed in the straight sections of the storage ring.[105,108] RF radiation bunches electrons together, increasing the overall brightness and lowering the emittance.

The X-rays produced from a bending magnet are polychromatic, with energy ranging from the soft (less than 2000 eV) to the hard X-ray region (greater than 2000 eV). For an XAS experiment, a specific region is selected by directing X-rays down a beamline that is tangent to the electron beam circumference. A beamline consists of three components: a front end, beamline optics, and experimental endstation.[105] At the front end, X-rays enter a vacuum pipe consisting of monochromators, focusing mirrors, and diffraction gradients that are used to focus the X-rays to a specific energy.[105] The XAS experiment is performed at an endstation.

2.3.2 X-ray absorption near-edge spectroscopy

In an XAS experiment, a sample absorbs X-rays (generated by a synchrotron) according to Beer's law:[109]

$$I = I_o e^{-\mu t} \tag{2-8}$$

where I_o is the incident X-ray intensity, I is the transmitted intensity, t is the thickness of the sample, and μ is the absorption coefficient. The quantity of interest, μ, depends on several factors:[109]

$$\mu \approx \frac{\rho Z^4}{A E^3} \tag{2-9}$$

where E is the X-ray energy, A is the atomic mass, and ρ is the sample density. A typical X-ray absorption spectrum (Figure 2-9) can be divided into two regions: X-ray absorption near-edge spectroscopy (XANES) and extended X-ray absorption fine-structure (EXAFS). In XANES, a sharp increase in μ, known as the absorption edge, is observed when an atom absorbs sufficient

energy to excite an electron to the first conduction state above E_F (Figure 2-10a).[109,110] For a metal, of course, the absorption edge energy corresponds to the BE. Similar to BE values, the absorption edge energy depends on the oxidation state of the absorbing atom. The fine structure found at 0–30 eV beyond the absorption edge results when core electrons are excited but remain bound in empty conduction states above E_F.[109,111] This fine structure can provide information about the coordination environment of the absorbing atom. The transition of an excited electron to conduction states follows the dipole selection rule ($\Delta l = \pm 1$). For example, the Ni K-edge results from a transition of an electron from the 1s ($l = 0$) to 2p ($l = 1$) state. When there is mixing of states, it is often possible to observe quadrupolar transitions ($\Delta l = \pm 2$), such as that from the 1s to 3d (which are mixed significantly with 4p) states in the Ni K-edge spectrum shown.[111] These quadrupolar transitions typically occur at lower energy than dipolar transitions and are often referred to as pre-edge peaks.[111]
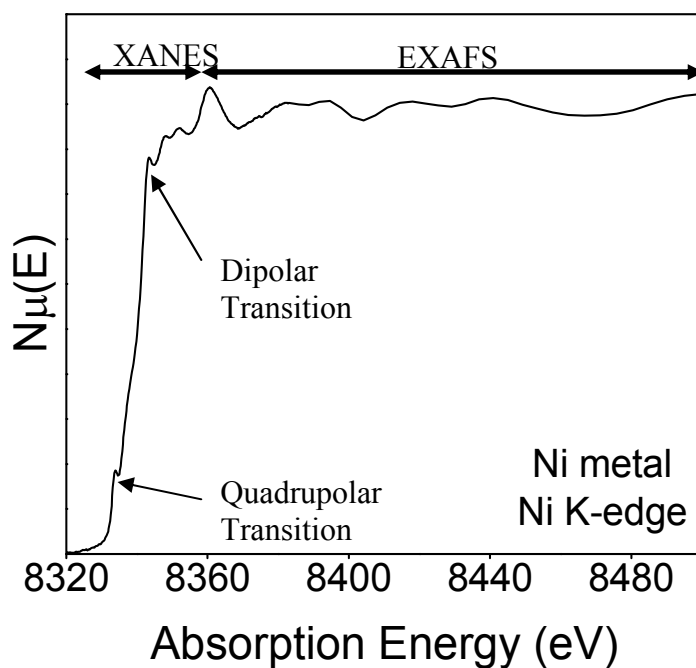
Figure 2-9 The normalized Ni K-edge XAS spectrum for Ni metal measured in transmission mode.

An alternative explanation for the fine structure seen in XANES involves the excited core electron being ejected from the absorbing atom as a photoelectron.[109,112,113] If the outgoing photoelectron is treated as a wave, it can interact with surrounding atoms and be scattered back to the absorbing atom. If the excitation energy is close to the absorption edge, the photoelectron has little KE and the backscattering can follow multiple pathways (Figure 2-10b). The constructive and destructive interference of these photoelectron waves results in broad peaks near the absorption edge known as multiple scattering resonance (MSR) peaks.[109,112,113] These peaks depend on the coordination environment, but theoretical modeling is required to extract this information.[113] At X-ray energies well above the absorption edge (>30 eV), the photoelectron has sufficient KE to be scattered and backscattered along a single path (Figure 2-10c), resulting in the oscillating pattern observed in the EXAFS region (Because this thesis focuses on the XANES portion of XAS, EXAFS will only be briefly discussed here).[109] EXAFS is defined as the oscillatory part, $\chi(E)$, of the total absorption coefficient and is evaluated as:[109]

$$\chi(E) = \frac{\mu(E) - \mu_o(E)}{\Delta\mu_o(E)} \tag{2-10}$$

where $\mu(E)$ is the energy-dependent absorption coefficient, $\mu_o(E)$ is the background spectrum for a single absorbing atom, and $\Delta\mu_o(E)$ is the absorption edge height. $\chi(E)$ is plotted as a function of the wavevector, k, of the photoelectron:[109]

$$k = \sqrt{\frac{2m(E - E_o)}{\hbar^2}} \tag{2-11}$$

where m is the mass of the electron, E is the absorption energy, E_o is the absorption edge energy, and $\hbar$ is the reduced Planck's constant. A Fourier transform produces a plot dependent on the scattering path length, R, from which atom-atom distances (R) and coordination environment (peak intensity) can be inferred.[109,113]
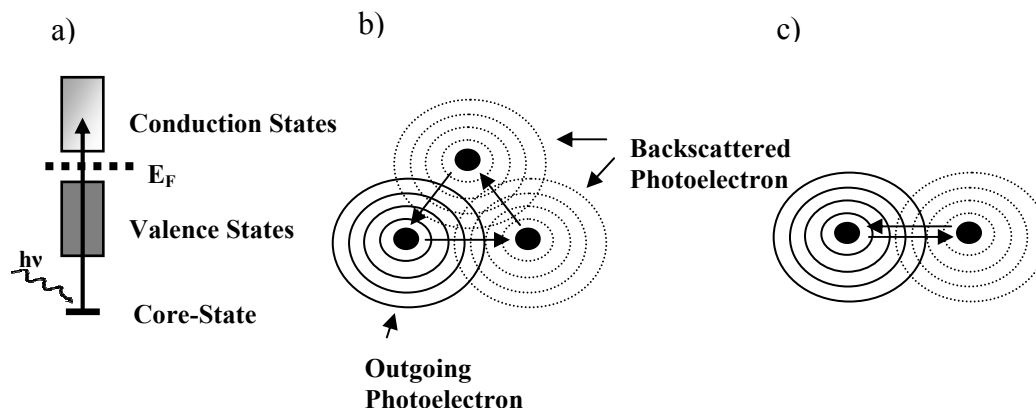
Figure 2-10 Representations of a) an electron excited to conduction states causing XANES, b) a multiple scattering event that causes the MSR phenomenon, and c) the single scattering event causing EXAFS.

There are three main methods for detecting the absorption event. The simplest is transmission of X-rays through a thin uniform sample (Figure 2-11). If the thickness is neglected, $\mu(E)$ is evaluated as:[109]

$$\mu(E) = \log \frac{I_0}{I} \qquad (2\text{-}12)$$

The intensities of the incoming and outgoing X-ray beam are measured with gas-filled ion chambers, which typically consist of parallel-plate capacitors filled with inert gas to detect the ionization current.[109,113] A reference sample with a known absorption edge energy is often placed behind the I ionization chamber where its transmission intensity (I_{Ref}) is measured.[109,113] The other two detection methods are based on decay processes of the excited state produced from photoionization. When a high-energy core electron fills a deep core hole, X-ray fluorescence occurs at a well-defined energy that is characteristic of the absorbing atom. Fluorescence yield (FLY) detectors are placed at 90° to the incident X-ray beam with the sample tilted at 45° (Figure 2-11).[109] Because the number of fluorescent photons generated is

proportional to the cross-section for the photoionization of the core electron, the absorption energy can be determined from:[109]

$$\mu(E) \approx \frac{I_f}{I_o} \qquad\qquad (2\text{-}13)$$

The decay of the excited state may also lead to emission of secondary electrons, Auger electrons, and sometimes photoelectrons.[109,114] Collectively, all of these electron signals can be measured to give the total electron yield (TEY).[114] Unlike X-ray fluorescence, which has a depth penetration of few micrometers, TEY is surface-sensitive (probing up to 20-100 Å).[114] Because the TEY signal decreases with increasing atomic number, this is the preferred detection method for light elements.[109,114] Both FLY and TEY detection are employed in the soft X-ray region where X-rays are not well transmitted.[109,114]
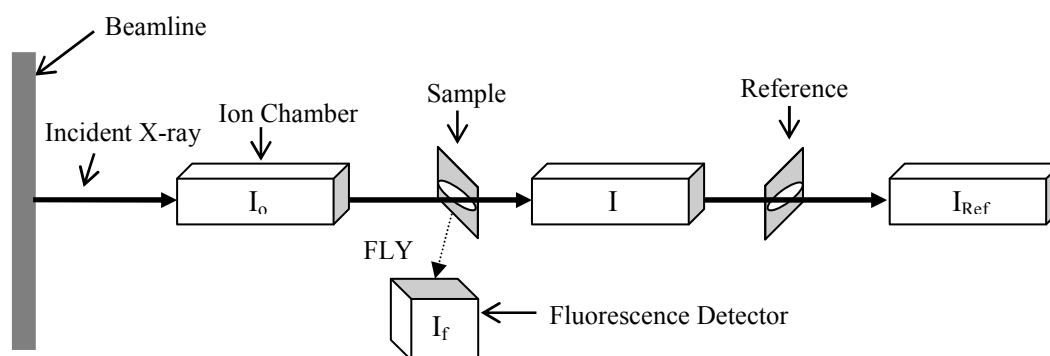
Figure 2-11 Typical set-up for a XAS experiment.

2.3 Metal pnictides

Many of the metal pnictides investigated in this thesis have been known for over 60 years. However, earlier XPS studies, such as those on *M*P and *M*$_2$P, were hampered by poor instrumental resolution and contamination with surface oxides.[115] For Ni$_2$P, extensive catalytic studies have been performed but only the EXAFS portion of the XAS spectra has been measured,

effectively neglecting important information about the electronic structure.[116-118] With state-of-the-art instrumentation and techniques, detailed XPS and XAS measurements have been made on transition-metal pnictides MPn (M = Cr-Co; Pn = P, As), providing new insight on the electronic effects of metal and pnictide substitutions. In the series of transition-metal phosphides MP (M = Cr-Co), the P 2p BE and P K-edge absorption edge shift to lower energy (by up to 0.4 eV) as M becomes more electropositive, consistent with greater M-to-P charge transfer.[6] In the mixed-metal $M_{1-x}M'_xP$ and mixed-pnictide $MAs_{1-y}P_y$ systems, it has been possible to detect BE shifts as small as 0.1 eV that originate from next-nearest neighbour effects through careful statistical analysis of multiple samples.[7,8] Further evidence for these next-nearest neighbour effects was seen through the occurrence of M-to-M' charge transfer in the metal L- and K-edge XANES spectra, for which the metal-bound 3d conduction states can be probed. More complex phosphides ($LaFe_4P_{12}$, $CeFe_4P_{12}$, CoP_3),[119,120] arsenides ($Hf(Si_{0.5}As_{0.5})As$),[121] and antimonides ($LaFe_4Sb_{12}$, $CeFe_4Sb_{12}$)[120] have also been examined by XPS to determine oxidation states in these materials.

Chapter 3

On the existence of ZrAs$_2$ and ternary extension Zr(Ge$_x$As$_{1-x}$)As (0 ≤ x ≤ 0.4)[*]

3.1 Introduction

Among the ternary M–Tt–Pn (M = Ti, Zr, Hf; Tt (tetrel) = Si, Ge, Sn; Pn =P, As, Sb, Bi) systems, the antimonides are now relatively well studied whereas the other pnictides are not. One interesting outcome from these investigations has been the proposal that "β-ZrSb$_2$" does not exist as a true binary but rather as a Si-stabilized ternary phase, Zr(Si$_x$Sb$_{1-x}$)Sb, with a small phase width (0.07 ≤ x ≤ 0.12) adopting the orthorhombic PbCl$_2$-type structure.[122] With higher Si content, ZrSi$_{0.7}$Sb$_{1.3}$ adopts the tetragonal PbFCl-type structure.[123] In both cases, the source of Si is believed to originate from the use of fused-silica tubes as the container material. Mixing of other Tt atoms (such as Ge and Sn) is also possible in these antimonides.[122,123] Similar doubts might be cast on the analogous binary PbCl$_2$-type zirconium arsenide, ZrAs$_2$, which was prepared in fused-silica tubes as well.[124,125] In an early structure determination, the possibility of an As-deficient formula, ZrAs$_{2-x}$, could not be excluded.[125] In more recent investigations, we have established that, like the antimonides, the ternary arsenides Zr(Si$_x$As$_{1-x}$)As form partially ordered solid solutions with a PbCl$_2$-type phase forming at lower Si content (0 ≤ x ≤ 0.4) (on the assumption that ZrAs$_2$ does exist) and a PbFCl-type phase forming at higher Si content (x = 0.6).[11]

Herein, we perform further experiments to determine if $ZrAs_2$ is indeed a true binary phase and to identify the phases formed in the As-rich portion of the ternary germanium-containing $Zr(Ge_xAs_{1-x})As$ system through X-ray diffraction analysis. As well, X-ray photoelectron spectroscopy (XPS), band structure calculations, and physical property measurements were carried out to characterize the electronic structures.

3.2 Experimental

3.2.1 Synthesis

Starting materials were Zr powder (99.9%), Ge pieces (99.99%), and As pieces (99.9998%), all from Alfa-Aesar. Products were analyzed by powder X-ray diffraction (XRD) patterns obtained on an Inel diffractometer equipped with a CPS 120 detector. Reactions with nominal loading composition "$ZrAs_2$" were carried out either directly in sealed fused-silica tubes or in alumina tubes jacketed by fused-silica tubes, with or without a small grain of I_2 (Anachemia) added to promote crystal growth, as summarized in Table 3-1. The tubes were evacuated, sealed, and placed in a furnace where they were heated to 850 °C over 2 days, kept at that temperature for 1 week, and cooled to room temperature over 1 days. Similarly, reactions with loading compositions "$Zr(Ge_xAs_{1-x})As$" ($0 \leq x \leq 1$ at increments of 0.1–0.2) were carried out in alumina tubes jacketed by fused-silica tubes, which were evacuated and sealed. The tubes were heated at 500 °C for 1 d and 900 °C for 1 week, and then cooled to room temperature. The samples were ground and placed in new containers which were heated at 900 °C for 1 week. A few additional reactions were conducted at 1050 °C in attempts to prepare a PbFCl-type phase, to no avail.

Table 3-1 Reaction conditions and unit cell parameters for ZrAs$_2$.

Reaction condition	Products	a (Å)	b (Å)	c (Å)	V (Å)
Sealed tube	ZrAs$_2$	6.800(2)	3.687(1)	9.036(2)	226.3(2)
Sealed tube, with I$_2$	ZrAs$_2$	6.792(2)	3.694(2)	9.026(4)	226.4 (1)
Alumina tube	ZrAs$_2$	6.795(4)	3.690(4)	9.028(4)	226.4(2)
Alumina tube, with I$_2$	ZrAs$_2$	6.801(3)	3.687(2)	9.039(4)	226.6(2)

3.2.2 Structure determination

Single-crystal X-ray diffraction data were collected on a Bruker Platform / SMART 1000 CCD diffractometer at 23 °C using ω scans. Structure solution and refinement were carried out with use of the SHELXTL (version 6.12) program package.[21] Face-indexed numerical absorption corrections were applied.

A needle-shaped single crystal was selected from the ZrAs$_2$ sample prepared in the silica-jacketed alumina tube in the presence of I$_2$. Although energy-dispersive X-ray (EDX) analysis performed on a Hitachi S-2700 scanning electron microscope indicated the presence of Zr and As, the absence of Si could not be directly ruled out because of the partial overlap of Zr L- and Si K-emission lines. From the intensity data, the orthorhombic space group *Pnma* was chosen and the initial atomic positions were located by direct methods. As an indirect test for the absence of Si, refinements were performed in which the two possible nonmetal sites were allowed to be occupied by a mixture of Si and As atoms, with no constraints over their ratio. The occupancies converged to 1(1)% Si and 99(1)% As on the first site (0.12, ¼, 0.04), and 0(1)% Si and 100(1)% As on the second site (0.08, ¼, 0.65), lending strong support for the absence of Si. In the final refinement, only As atoms were assumed to fully occupy these sites.

A needle-shaped single crystal was obtained from a reaction with nominal composition "Zr(Ge$_{0.4}$As$_{0.6}$)As" prepared in the presence of I$_2$. Because the similar X-ray scattering factors of Ge and As posed a challenge in determining their site distribution, several models were tested. Placing Ge atoms entirely within the first site (0.12, ¼, 0.04) and As atoms within the second site (0.08, ¼, 0.65) resulted in equivalent isotropic displacement parameters, U_{eq}, of 0.0064(1) and 0.0073(1) Å^2, respectively, and agreement factors of $R(F) = 0.015$ and $R_w(F_o^2) = 0.034$. Reversing this site distribution gave U_{eq} values of 0.0081(1) Å^2 for the first site and 0.0052(1) Å^2 for the second site, and slightly worse agreement factors of $R(F) = 0.016$ and $R_w(F_o^2) = 0.039$. Finally, a similar treatment as above in which Ge and As atoms were allowed to disorder over both sites was successful in resolving a preferential occupation of 37(8)% Ge and 63(8)% As on the first site, and 8(9)% Ge and 91(9)% As on the second site. Taking into account the large uncertainties in these occupancies, we assumed that only the first site was disordered with Ge and As atoms, whereas the second site was occupied exclusively by As atoms, in accordance with related structures such as Zr(Ge$_{0.2}$Sb$_{0.8}$)Sb and Zr(Si$_{0.4}$As$_{0.6}$)As in which the Tt atom enters only one of the two anion sites.[11,122] The final refinement led to a formula of "Zr(Ge$_{0.33(6)}$As$_{0.67}$)As", which we simplify to Zr(Ge$_{0.3}$As$_{0.7}$)As in subsequent discussion.

Atomic positions were standardized with the program STRUCTURE TIDY.[126] Crystal data and further details of the data collection are given in Table 3-2. Final values of the positional and displacement parameters are given in Table 3-3. Selected interatomic distances are listed in Table 3-4. Further data, in CIF format, have been sent to Fachinformationszentrum Karlsruhe, Abt. PROKA, 76344 Eggenstein-Leopoldshafen, Germany, as supplementary material No. CSD-421869 (ZrAs$_2$) and CSD-421870 (Zr(Ge$_{0.3}$As$_{0.7}$)As) and can be obtained by contacting FIZ (quoting the article details and the corresponding CSD numbers).

Table 3-2 Crystallographic data for ZrAs$_2$ and Zr(Ge$_{0.3}$As$_{0.7}$)As.

Formula	ZrAs$_2$	Zr(Ge$_{0.33(6)}$As$_{0.67}$)As
Formula mass (amu)	241.06	240.30
Space group	*Pnma* (No. 62)	*Pnma* (No. 62)
a (Å)	6.8006(3)	6.7380(4)
b (Å)	3.6883(2)	3.6680(2)
c (Å)	9.0328(4)	9.1202(5)
V (Å^3)	226.57(3)	225.41(2)
Z	4	4
ρ (g cm^{-3})	7.067	7.081
Crystal dimensions (mm)	0.066 × 0.084 × 0.662	0.25 × 0.03 × 0.03
μ (Mo Kα) (mm^{-1})	33.38	33.07
Transmission factors	0.0235-0.1983	0.1123-0.5751
2θ limit (deg.)	7.50-66.24	7.52-66.04
No. of data collected	2922	2882
No. of unique data including $F_o^2 < 0$	479 (R_{int} − 0.037)	476 (R_{int} − 0.024)
No. of unique data, with $F_o^2 > 2\sigma(F_o^2)$	473	422
No. of variables	20	21
$R(F)$ for $F_o^2 > 2\sigma(F_o^2)$[a]	0.027	0.015
$R_w(F_o^2)$[b]	0.059	0.030
Goodness of fit	1.307	1.053
$(\Delta\rho)_{max}$, $(\Delta\rho)_{min}$ (e Å^{-3})	2.29, -3.37	0.7, -0.94

[a] $R(F) = \sum \lVert F_0 \rvert - \lvert F_c \rVert / \sum \lvert F_o \rvert$.

[b] $R_W(F_o^2) = \left[\sum \left[w(F_o^2 - F_c^2)^2 \right] / \sum wF_o^4 \right]^{1/2}$; $w^{-1} = \left[\sigma^2(F_o^2) + (Ap)^2 + Bp \right]$, where $p = \left[\max(F_o^2) + 2F_c^2 \right]/3$.

Table 3-3 Atomic coordinates and equivalent isotropic displacement parameters for $ZrAs_2$ and $Zr(Ge_{0.3}As_{0.7})As$.

Atom	Wyckoff position	Occupancy	$\underline{x}$	y	z
$ZrAs_2$					
Zr	$4c$	1	0.22644(5)	¼	0.33804(3)
As1	$4c$	1	0.11820(5)	¼	0.04210(4)
As2	$4c$	1	0.08332(5)	¼	0.64704(3)
$Zr(Ge_{0.3}As_{0.7})As$					
Zr	$4c$	1	0.22731(4)	¼	0.33785(3)
Ge/As1	$4c$	0.33(6)/0.67	0.11971(4)	¼	0.04266(3)
As2	$4c$	1	0.08873(4)	¼	0.64771(3)

[a] U_{eq} is defined as one-third of the trace of the orthogonalized U_{ij} tensor.

Table 3-4 Selected interatomic distances (Å) in $ZrAs_2$ and $Zr(Ge_{0.3}As_{0.7})As$.

	$ZrAs_2$	$Zr(Ge_{0.3}As_{0.7})As$
Zr–$X1$	2.7727(4)	2.7882(4)
Zr–As2 (×2)	2.8030(3)	2.8120(3)
Zr–$X1$ (×2)	2.8133(3)	2.8134(3)
Zr–As2 (×2)	2.8374(3)	2.8135(3)
Zr–$X1$	2.8759(5)	2.8598(4)
Zr–As2	2.9560(4)	2.9762(4)
$X1$–$X1$ (×2)	2.5620(4)	2.5635(4)
$X1$–As2 (×2)	2.9017(4)	2.8532(3)

[a]Site $X1$ is occupied by As atoms in $ZrAs_2$ or by 0.3 Ge and 0.7 As in $Zr(Ge_{0.3}As_{0.7})As$.

3.2.3 Band structure calculations

Tight-binding linear muffin tin orbital (TB-LMTO) band structure calculations were performed on $ZrAs_2$ and hypothetical $Zr(Ge_{0.5}As_{0.5})As$ within the local density and atomic

spheres approximations using the Stuttgart TB-LMTO program.[127] Cell parameters and atomic positions were taken from the crystal structures of $ZrAs_2$ and $Zr(Ge_{0.3}As_{0.7})As$. The ordered $Zr(Ge_{0.5}As_{0.5})As$ model (in space group *Pmc21*), based on one previously considered for $Zr(Si_{0.5}As_{0.5})As$ forming a $PbCl_2$-type structure, involves an alternation of Ge and As atoms within zigzag chains parallel to *b*.[11] The basis sets consisted of Zr 5s/5p/4d/4f, Ge 4s/4p/4d, and As 4s/4p/4d orbitals, with the Zr 4f, Ge 4d, and As 4d orbitals being downfolded. Integrations in reciprocal space were carried out with an improved tetrahedron method with 105 ($ZrAs_2$) or 168 ($Zr(Ge_{0.5}As_{0.5})As$) irreducible *k* points within the first Brillouin zone.

3.2.4 X-ray photoelectron spectroscopy

XPS spectra were measured on a Kratos AXIS 165 spectrometer equipped with a monochromatic Al Kα X-ray source (15 kV, 14 mA) and a hybrid lens with a spot size of 700 μm × 400 μm. Crystals of $ZrAs_2$ or $Zr(Ge_{0.3}As_{0.7})As$ were ground into fine powder, pressed onto In foil, and mounted on a Cu sample holder. Although they did not appear to be air-sensitive, the samples were handled in a glove box and transferred within a sealed container to the XPS instrument. The pressure inside the analysis chamber was maintained at 10^{-7} to 10^{-9} Pa. The samples were sputter-cleaned with an Ar^+ ion beam (4 kV, 10 mA) until all surface oxides were removed. A slight reduction of As, caused by the sputtering procedure, does not detract from analysis of the As 3d spectra.

Survey spectra, which were collected with a binding energy (BE) range of 0–1100 eV, a pass energy of 160 eV, a step size of 0.7 eV, and a sweep time of 180 s, confirmed the expected compositions and, importantly, did not reveal the presence of Si in the samples. High-resolution core-line spectra were collected with an energy envelope of 60 eV (Zr 3d peak) or 20 eV (Ge 3d

and As 3d peaks), a pass energy of 20 eV, a step size of 0.05 eV, and a sweep time of 180 s. The number of scans collected varied depending on the sample. No charge correction was applied because these samples are good conductors. All spectra were calibrated against the C 1s line at 284.8 eV arising from adventitious C. Although the C 1s signal overlaps with an As Auger signal, an acceptable method for checking the calibration in metallic systems such as these is to set the Fermi edge, located from the maximum of the first derivative of the valence band spectrum, to 0 eV.[87] The spectra were analyzed with use of the CasaXPS software package.[128] The background arising from energy loss was removed by applying a Shirley-type function and the peaks were fitted to pseudo-Voigt (70% Gaussian and 30% Lorentzian) line profiles. On the basis of previous measurements made on the same spectrometer, the BE values are estimated to have a precision better than ±0.1 eV.

3.2.5 Electrical resistivity and magnetic susceptibility

A needle-shaped crystal of $Zr(Ge_{0.3}As_{0.7})As$ with dimensions of 0.60 mm $\times$ 0.015 mm $\times$ 0.015 mm was mounted for standard four-probe electrical resistivity measurements on a Quantum Design PPMS system equipped with an ac transport controller (Model 7100). The current was 100 μA and the frequency was 16 Hz. The resistivity was measured along the needle axis, which corresponds to the crystallographic b axis, between 2 and 300 K.

Magnetic susceptibility measurements were made on a 100-mg ground sample of $Zr(Ge_{0.3}As_{0.7})As$ between 2 and 300 K on a Quantum Design 9T–PPMS dc magnetometer / ac susceptometer. The susceptibility was corrected for contributions from the holder and underlying sample diamagnetism.

3.3 Results and discussion

3.3.1 Is ZrAs$_2$ a true binary phase?

Reactions at 850 °C were carried out to prepare ZrAs$_2$ within different containers, in the presence or absence of I$_2$. Although EDX analyses on single crystals could not definitively rule out the absence of Si (because of the overlap of Zr and Si X-ray emission lines), the XPS survey spectra showed no evidence for Si. Powder X-ray diffraction revealed that the products of all these reactions were phase-pure (i.e., no impurities; Figure A1-1 in Appendix 1). The refined cell parameters for the samples prepared within alumina tubes were within 3σ from those prepared within silica tubes (Table 3-1). Single-crystal X-ray diffraction analysis indicated that the two anion sites are fully occupied by As atoms, with unremarkable displacement parameters. XPS analysis also showed no evidence of Si. This body of evidence strongly supports the existence of ZrAs$_2$ as a strictly stoichiometric, true binary phase, and not an impurity-stabilized one, as has been proposed for "β-ZrSb$_2$".[122]

The structure of ZrAs$_2$ reported here ($R(F)$ = 0.027) supersedes the earlier determination based on Weissenberg photographic data ($R(F)$ = 0.276).[125]   The Zr atoms reside in approximately monocapped square antiprismatic polyhedra (CN9; Zr–As, 2.7727(4)–2.9560(4) Å), which are connected to form a three-dimensional network containing four-atom-wide anionic ribbons of As atom (similar to the Si/As substructure discussed in section 1.2.3 in Chapter 1) extending along the b direction (Figure 3-1). Within these ribbons, the bonds within the interior (As1–As1, 2.5620(4) Å) are significantly shorter than those to the terminal atoms (As1–As2, 2.9017(4) Å).
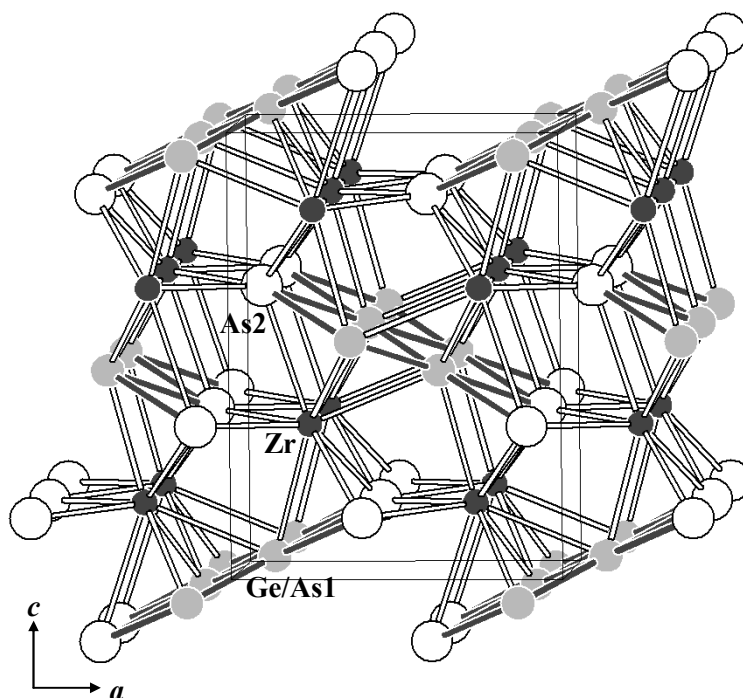
Figure 3-1 PbCl$_2$-type structure of ZrAs$_2$ or Zr(Ge$_{0.3}$As$_{0.7}$)As. The Ge atoms preferentially occupy only one of the two possible anion sites.

3.3.2 Ternary extension Zr(Ge$_x$As$_{1-x}$)As

The reactions performed at 900 °C indicated that the solid solution Zr(Ge$_x$As$_{1-x}$)As forms for $0 \leq x \leq 0.4$. Powder X-ray diffraction patterns revealed phase-pure products up to $x = {\sim}0.4$ (Table A1-1 and Figure A1-2 in Appendix 1). A crystal obtained from a reaction with nominal composition "Zr(Ge$_{0.4}$As$_{0.6}$)As" was found from the single-crystal structure determination to have a formula of Zr(Ge$_{0.33(6)}$As$_{0.67}$)As, with the Ge atoms preferentially entering the interior sites of the four-atom-wide anionic ribbons. The uncertainties in the occupancies are large enough that the upper limit of Ge solubility into ZrAs$_2$ can be estimated to be no higher than $x = 0.4$. Above this point, multiphase mixtures consisting of PbCl$_2$-type Zr(Ge$_x$As$_{1-x}$)As, ZrAs, and elemental Ge were observed. A Ge-rich phase of approximate composition "ZrGe$_{1.3}$As$_{0.7}$" was

identified which probably lies off the $ZrAs_2$–$ZrGe_2$ join in the ternary phase diagram; further investigation of this phase was hampered by lack of suitable crystals for structure determination.

On most scales of atomic radii, Ge is slightly larger than As (e.g., Pauling metallic radii R_1 of 1.24 Å for Ge and 1.21 Å for As).[1] At first glance, it is somewhat surprising, then, to observe that the unit cell volume contracts slightly (by 1 Å^3) on progressing from $ZrAs_2$ to $Zr(Ge_{0.4}As_{0.6})As$ (Figure 3-2). The small change in unit cell volume results from the trends of decreasing a and b opposing the trend of increasing c. These trends cannot be easily explained by geometrical considerations. An argument based on size effects would also need to take into account that the Ge and As atoms are anionic but with differing charges. The Zr–$X1$ (where $X1$ is the disordered site) and Zr–As2 distances change irregularly as Ge partially substitutes for As (Table 3-4), such that the average bond lengths around the Zr atom remain unchanged at 2.83 Å. Within the four-atom-wide anionic ribbons (As2–$X1$–$X1$–As2), the $X1$–$X1$ distances remain the same whereas the $X1$–As2 distances shorten. In TiNiSi-type structures, which are ternary variants of the Co_2Si-type (anti-$PbCl_2$-type) structure, the interior sites of these ribbons tend to be occupied by smaller atoms.[129] If the same argument is applied to $Zr(Ge_{0.4}As_{0.6})As$, then the preference for Ge atoms to enter the interior $X1$ sites implies that the Ge atoms are smaller and less negatively charged than the As atoms, thereby accounting for the cell contraction.

3.3.3 Electronic structure and physical properties

Because the trends in bond lengths suggest that electronic effects are at play, the band structures for $ZrAs_2$ and a hypothetically ordered model of $Zr(Ge_{0.5}As_{0.5})As$ were examined. The
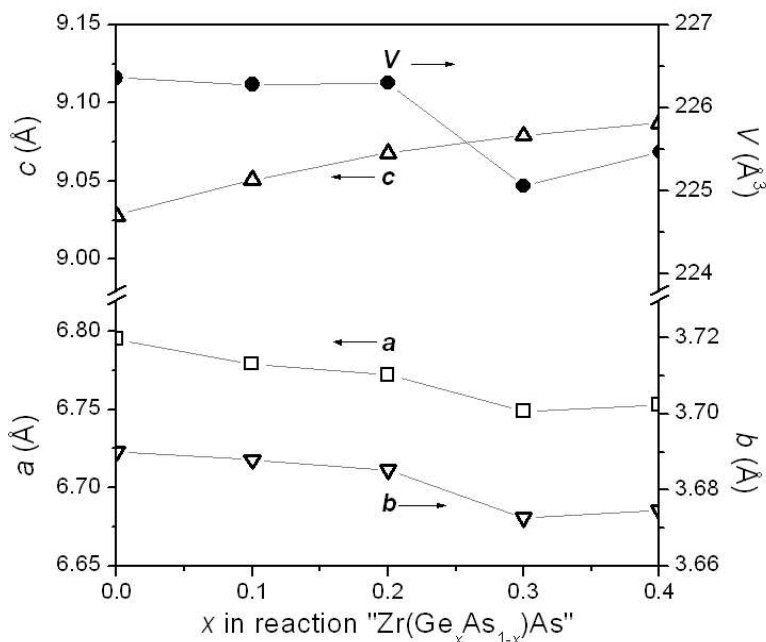
Figure 3-2 Plot of cell parameters vs. x for $Zr(Ge_xAs_{1-x})As$ forming the $PbCl_2$-type structure. The lines are shown only to guide the eye.

lowest energy block (from -14.5 to -9 eV) in $ZrAs_2$ splits into two subbands upon the ordered substitution of Ge into one of the As sites in $Zr(Ge_{0.5}As_{0.5})As$ (Figure 3-3). At higher energy, the density of states (DOS) curves are similar except that the Fermi level is shifted from its position at a pseudogap in $ZrAs_2$ to just slightly below (by 1 eV) in $Zr(Ge_{0.5}As_{0.5})As$, a consequence of the reduced electron count. Inspection of the crystal orbital Hamilton population (COHP) curves in $ZrAs_2$ reveals that Zr–As bonding is optimized but As–As bonding is not because some antibonding levels are occupied (Figure 3-3). Lowering the Fermi level in $Zr(Ge_{0.5}As_{0.5})As$ depopulates these anion-anion antibonding states. As judged from the integrated COHP values ($-$ICOHP), this has little effect on the $X1$–$X1$ bonds (1.8 eV in both $ZrAs_2$ and $Zr(Ge_{0.5}As_{0.5})As$) but strengthens the $X1$–As2 bonds (0.4 eV in $ZrAs_2$ vs. 0.6 eV in $Zr(Ge_{0.5}As_{0.5})As$). This stabilization of anion-anion bonding competes with the destabilization of Zr–anion bonding, setting a limit on how much Ge can substitute for As. In $Zr(Ge_{0.5}As_{0.5})As$, the Zr–anion bonding
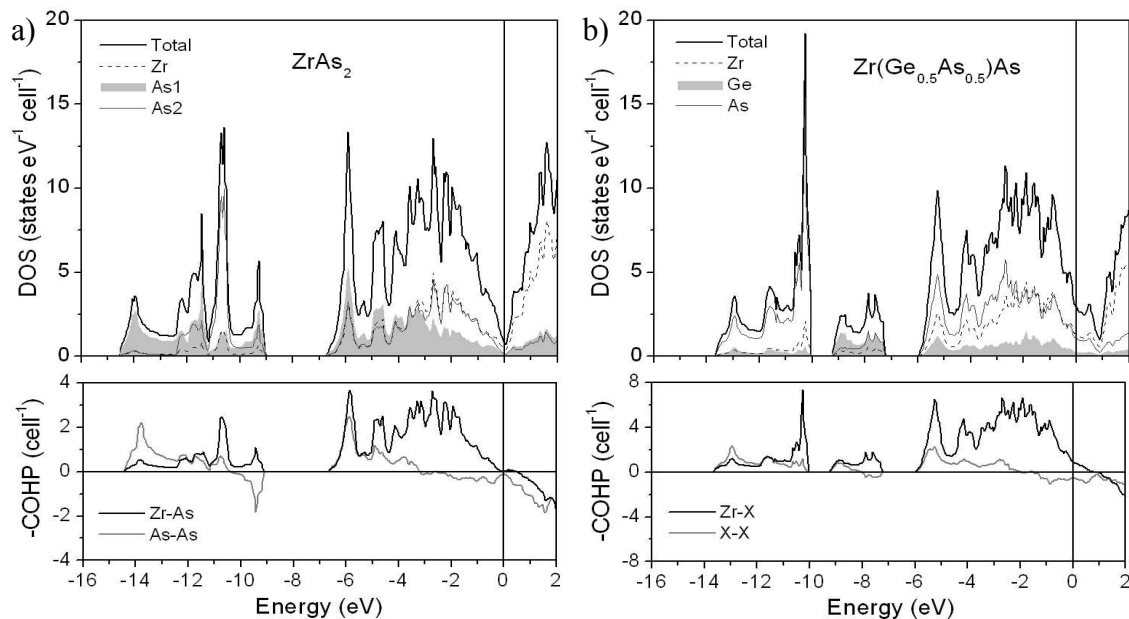
Figure 3-3 Band structures for (a) ZrAs$_2$ and (b) hypothetically ordered "Zr(Ge$_{0.5}$As$_{0.5}$)As". The top panels show the density of states (DOS) and atomic projections. The bottom panels show the crystal orbital Hamilton population (–COHP) curves.

interactions near the Fermi level are quite weak, such that the –ICOHP value remains essentially unchanged (1.5 eV) from that in ZrAs$_2$.

The electronic character of these compounds was further examined through XPS analysis. Because the Ge 3d and Zr 4p peaks overlap, we present only the Zr 3d and As 3d XPS spectra for ZrAs$_2$ and Zr(Ge$_{0.3}$As$_{0.7}$)As. In both compounds, the Zr 3d spectra were fitted to two peaks corresponding to the 3d$_{5/2}$ and 3d$_{3/2}$ spin-orbit-coupled final states, with an intensity ratio of 3:2 (Figure 3-4a). The shoulder at high BE, quite prominent in Zr(Ge$_{0.3}$As$_{0.7}$)As, is attributed to surface oxides. The asymmetric lineshapes are a signature of electronic delocalization common in transition metals and have been previously observed in Zr(Si$_{0.6}$As$_{0.4}$)As.[11] First described by Doniach and Šunjić, this asymmetry originates from the excitation of valence electrons, interacting with the core-hole produced after photoionization, into empty conduction states above

the Fermi edge.[130] Since there is a continuum of states above the Fermi edge in metallic systems, an asymmetric tail is observed.

The Zr $3d_{5/2}$ BE of 179.9(1) eV, identical for $ZrAs_2$ and $Zr(Ge_{0.3}As_{0.7})As$, falls between those for Zr metal (178.9(3) e V) and ZrO_2 (182.7(6) eV), indicating the presence of cationic Zr species with an intermediate oxidation state consistent with partially filled Zr 3d states found in the DOS curves.[101] The As 3d spectra suffer from a slight reduction, common in the spectra for other transition-metal monoarsenides, caused by Ar^+ sputtering giving rise to the shoulders at low BE; surface oxides probably give rise to the shoulders at high BE (Figure 3-4b).[8,131] These spectra were fitted to two component peaks corresponding to the $3d_{5/2}$ and $3d_{3/2}$ spin-orbit-coupled final states separated by 0.7 eV, each with a FWHM of 1.0 eV and in an intensity ratio of 3:2. The As $3d_{5/2}$ BE (41.2(1) eV for $ZrAs_2$ and 41.0(1) eV for $Zr(Ge_{0.3}As_{0.7})As$) is lower than in elemental As (41.7(2) eV), indicating the presence of anionic As species with a charge close to 1−, as deduced by comparison to the spectra of related compounds.[101] The BE is slightly lower in $Zr(Ge_{0.3}As_{0.7})As$ than in $ZrAs_2$, which would be consistent with the expectation of more negatively charged As atoms induced by the greater polarity of Ge–As bonds, but we cannot rule out the possibility that the small shift may be spurious, perhaps caused by the Ar^+ sputtering.

Consistent with the band structure, $Zr(Ge_{0.3}As_{0.7})As$ exhibits weakly metallic behaviour. The high electrical resistivity and the low residual resistivity ratio ($\rho_2/\rho_{300} = 0.9$) stem from the disorder in this compound (Figure 3-5a). The magnetic susceptibility curve indicates temperature-independent Pauli paramagnetism, with a small Curie tail presumably due to trace impurities (Figure 3-5b).
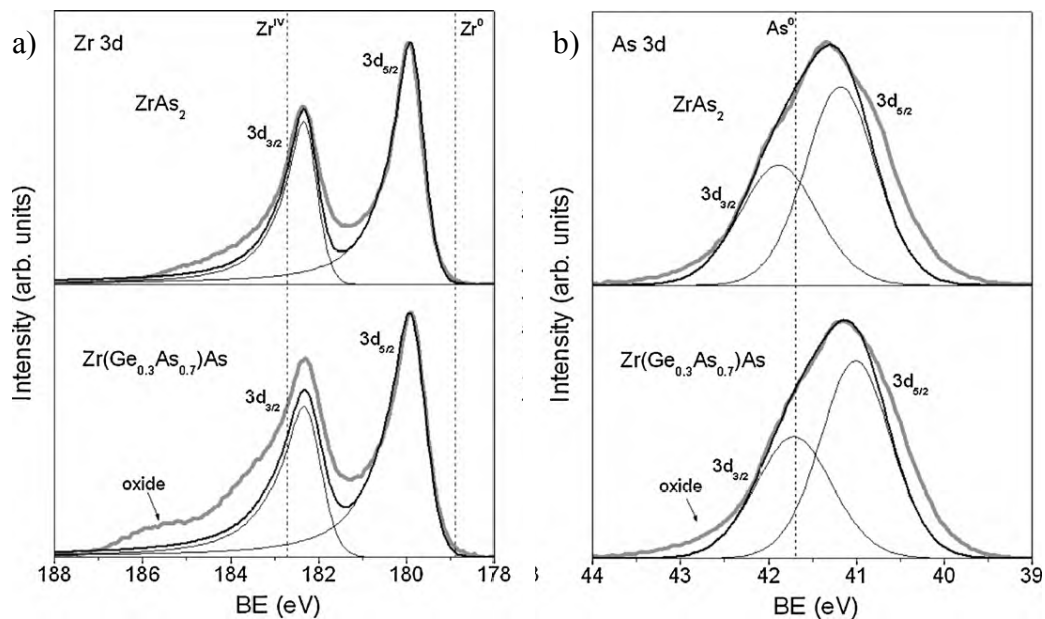
Figure 3-4 (a) Zr 3d and (b) As 3d XPS spectra for ZrAs$_2$ (top panels) and Zr(Ge$_{0.3}$As$_{0.7}$)As (bottom panels). The experimental spectra (thick grey lines) are fitted with component peaks (thin lines) to give the combined envelope (black lines). The dashed vertical lines mark the Zr 3d$_{5/2}$ and As 3d$_{5/2}$ BEs expected for the indicated charges.
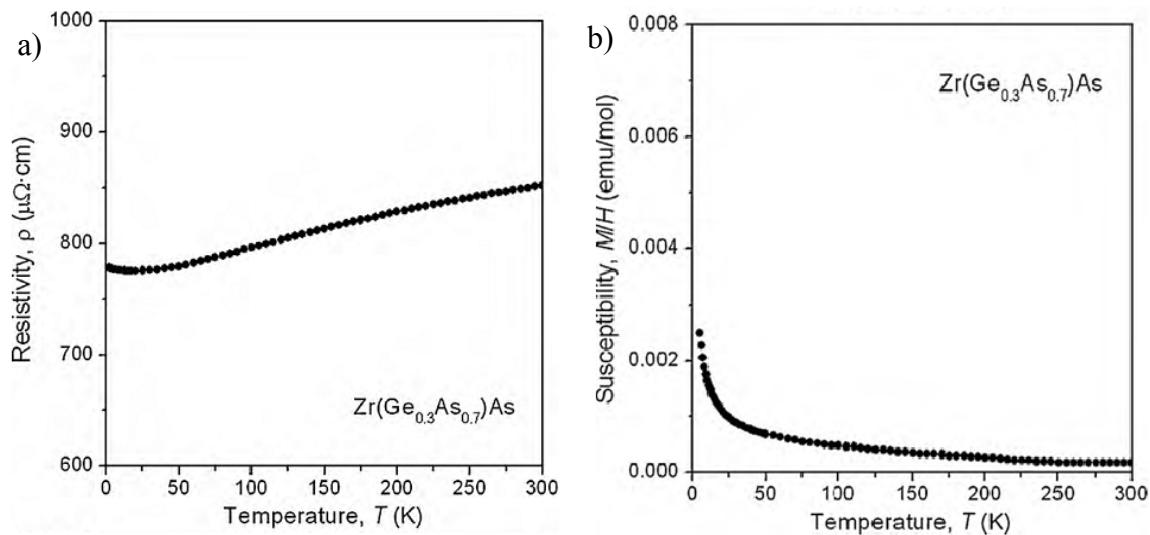
Figure 3-5 (a) Electrical resistivity and (b) magnetic susceptibility for Zr(Ge$_{0.3}$As$_{0.7}$)As.

3.4 Conclusions

Unlike the antimonide "β-ZrSb$_2$", which is impurity-stabilized, the arsenide ZrAs$_2$ is a true binary phase adopting the PbCl$_2$-type structure. The ternary extension Zr(Ge$_x$As$_{1-x}$)As forms up to $x = \sim0.4$, with Ge atoms entering preferentially into the interior sites of four-atom wide anionic ribbons in this structure. This solid solution range is similar as observed previously in Zr(Si$_x$As$_{1-x}$)As but is much wider than in Zr(Si$_x$Sb$_{1-x}$)Sb.[11,122] Although the substitution of Si or Ge into ZrAs$_2$ seems to originate for the same reasons (strengthened anion-anion bonding) as for the impurity stabilization of "β-ZrSb$_2$", there are subtle differences in these systems that may need to be explored further. For example, a PbFCl-type phase was not observed in Zr(Ge$_x$As$_{1-x}$)As with higher values of x, unlike Zr(Si$_x$As$_{1-x}$)As or Zr(Si$_x$Sb$_{1-x}$)Sb, at least under the temperatures studied (from 900 to 1050 $^{\circ}$C). The band structure of ZrAs$_2$ reveals a pseudogap at the Fermi level and the electrical resistivity of Zr(Ge$_{0.3}$As$_{0.7}$)As is quite high, characteristic of a poor metal. ZrAs$_2$ or related pnictides may be worthwhile investigating towards potential applications in thermoelectric materials, for which small band gaps, the presence of heavy atoms, and low thermal conductivity are required.

Chapter 4

Electronic structure of ZrCuSiAs and ZrCuSiP by X-ray photoelectron and absorption spectroscopy[*]

4.1 Introduction

The tetragonal structure of ZrCuSiAs (space group $P4/nmm$ (no. 129)) serves as the prototype for numerous compounds, including the superconducting rare-earth transition-metal pnictide oxides *REMPn*O discussed in Chapter 1.[27]   It has been fashionable to portray the structure of the pnictide oxides in terms of a stacking of alternating [*RE*O] and [*MPn*] layers, with both O and *M* atoms in tetrahedral coordination geometries (Figure 4-1a). Although over one hundred pnictide oxides are known to form the ZrCuSiAs-type structure, there are only three examples of quaternary silicon pnictides known to date: ZrCuSiAs itself,[13] HfCuSiAs,[13] and ZrCuSiP.[132]   Ostensibly the structure of ZrCuSiAs can also be described in terms of layers, [ZrSi] and [CuAs], with Si and Cu atoms in the tetrahedral sites (Figure 4-1b). The c/a ratio is 2.0–2.3 for all the oxide representatives of this structure type, but 2.6 for the three quaternary silicon pnictides.[133]   Paradoxically, this expanded c/a ratio does not mean that the layers are further apart in ZrCuSiAs! The reasons seem evident even from just casual inspection of the figures. Within individual layers, the tetrahedra are highly compressed along the *c*-direction in *REMPn*O, but highly elongated in ZrCuSiAs. This distortion causes the Zr atoms in the [ZrSi]

---

layer to approach the As atoms in the [CuAs] layer quite closely (2.8 Å).[13] The electron-precise

formulations $[RE^{3+}O^{2-}][M^{2+}Pn^{3-}]$ and $[Zr^{4+}Si^{2-}][Cu^{1+}As^{3-}]$, deduced upon the assumption of full

electron transfer, seem to provide a tidy explanation for the origin behind this distortion. Apart

from the transition-metal atoms which can support partially filled d-states, all atoms in *REMPnO*

attain filled-shell electron configurations; thus, *REMPnO* (and the other oxides) are classified as

"normal valence" compounds. On the other hand, as discussed in section 1.2.3 of Chapter 1, the

Si atoms in ZrSiCuAs are deficient with respect to the 8–*n* rule and must then form Si–Si bonds;

that is, ZrCuSiAs should be considered a polyanionic compound. The formation of these Si–Si

bonds contracts the structure within the *ab* plane, concomitant with an expansion along the *c*-

direction.
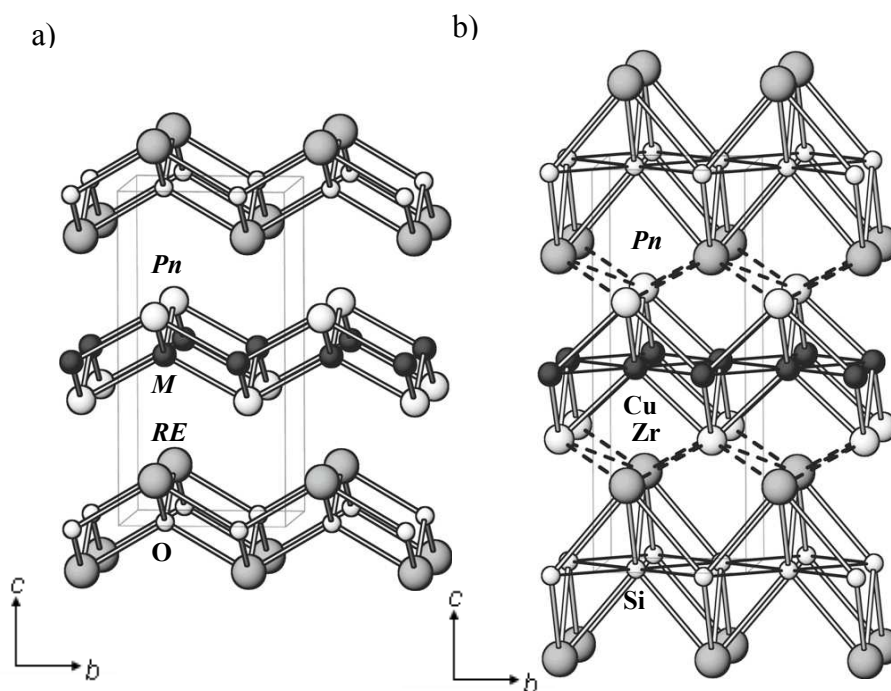
Figure 4-1 Crystal structure of (a) *REMPnO* showing non-interacting [*RE*O] and [*MPn*] layers and (b) ZrCuSi*Pn* (*Pn* = P, As) showing interacting [ZrSi] and [Cu*Pn*] layers, stacked along the *c*-direction.

Herein, we will investigate the electronic structure and bonding in ZrCuSiAs, as well as its phosphide analogue ZrCuSiP. We take primarily an experimental approach, applying X-ray photoelectron spectroscopy (XPS) and X-ray absorption near-edge spectroscopy (XANES) to probe energy differences in core-level atomic states, supplemented by band structure calculations to examine the bonding character in these compounds. The results from the band structure study will be compared with LaNiAsO, a representative member of rare-earth arsenide oxides that will be discussed in detail in Chapters 5 and 6. Many theoretical calculations have now been performed on the electronic structure of these pnictide oxides.[41,46,134-145] However, there has been no study that directly compares the pncitide oxides to the silicide pnictides.

4.2 Experimental

4.2.1 Synthesis

ZrCuSiAs and ZrCuSiP were prepared according to literature procedures.[13,132] Reagents were Zr wire (99.9%, A. D. Mackay), Cu powder (99.9999%, Cerac), Si pieces (99.99999%, Alfa-Aesar), As powder (99.5%, Cerac), and red P powder (99.995%, Cerac). For ZrCuSiAs, a stoichiometric mixture of "ZrSi" (previously prepared by arc-melting), Cu, and As powders was placed within an evacuated sealed fused-silica tube, which was heated to 873 K over 1 day, kept at that temperature for 2 days, heated to 1173 K over 1 day, kept at that temperature for 2 days, and water-quenched. The product was reground and reheated at 1073 K for 4 days; this procedure was repeated three times. For ZrCuSiP, a stoichiometric mixture of "ZrCuSi" (previously prepared by arc-melting) and P was placed within an evacuated sealed fused-silica tube, which was heated to 873 K over 1 day, kept at that temperature for 1 day, heated to 1123 K

over 1 day, kept at that temperature for 2 days, and water-quenched. The product was reground and reheated at 1123 K for 4 days; this procedure was repeated three times. The products were judged to be single-phase from their powder X-ray diffraction patterns collected on an Inel powder diffractometer (Figure A2-1 in Appendix 2). The unit cell parameters are $a = 3.6608(8)$ Å and $c = 9.604(2)$ Å for ZrCuSiAs, and $a = 3.5663(8)$ Å and $c = 9.421(2)$ Å for ZrCuSiP, which are comparable to previously reported values ($a = 3.6736(2)$ Å and $c = 9.5712(9)$ Å for ZrCuSiAs;[13] $a = 3.5671(1)$ Å and $c = 9.4460(4)$ Å for ZrCuSiP[132]).

4.2.2 XPS analysis

XPS spectra for ZrCuSiAs and ZrCuSiP were measured on a Kratos 165 spectrometer equipped with a monochromatic Al Kα X-ray source (14 mA, 15 kV) and a hybrid lens with a spot size of 700×400 μm^2. The samples are air-stable but to minimize exposure to air, they were handled in an Ar-filled glove box where they were finely ground, pressed into In foil, mounted on a Cu sample holder, and placed in a sealed container for transfer to the analysis chamber of the spectrometer. The pressure inside the XPS instrument was maintained between 10^{-7} and 10^{-9} Pa. Samples were sputter-cleaned with an Ar$^+$ ion beam (4 kV, 10 mA) until core-line peaks associated with surface oxides were no longer observed in the XPS spectra. A small shoulder in the As 3d XPS spectra indicated that a slight reduction of As occurred in ZrCuSiAs; however, the binding energies (BEs) in these and other spectra were, within standard uncertainties, the same before and after the sputtering procedure.

Survey spectra, collected with a BE range of 0–1100 eV, a pass energy of 160 eV, a step size of 0.7 eV, and a sweep time of 180 s, confirmed the expected chemical compositions (Zr:Cu:Si:Pn = 1:1:1:1) for the samples examined. High-resolution core-line spectra were

collected with an energy envelope of appropriate range (50 eV for Zr 3d; 60 eV for Cu 2p; 20 eV

for Si 2p, As 3d, and P 2p), a pass energy of 20 eV, a step size of 0.05 eV, and a sweep time of

180 s. No charge correction was required because the samples are good conductors. The spectra

were calibrated to the C 1s line at 284.8 eV arising from adventitious carbon. As a check, the

first derivative of the edge onset of the valence band was set to 0 eV (a suitable calibration

technique for metallic samples).[87] The spectra were analyzed with use of the CasaXPS software

package.[128] The background arising from energy loss was removed by applying a Shirley-type

function and the peaks were fitted to pseudo-Voigt (70% Gaussian and 30% Lorentzian) line

profiles to take into account spectrometer and lifetime broadening effects. Table 4-1 lists

average BE values expressed to two decimal places, with uncertainties estimated at better than

±0.10 eV, as established by collecting multiple spectra (Table A2-1 in Appendix 2).

Table 4-1 Core-line BEs (eV) for ZrCuSiAs and ZrCuSiP.

	ZrCuSiAs	ZrCuSiP
Zr $3d_{5/2}$ [a]	179.64(2)	179.66(5)
Cu $2p_{3/2}$ [a]	933.68(3)	933.70(6)
Si $2p_{1/2}$	99.41(4)	99.40(5)
As $3d_{5/2}$ or P $2p_{3/2}$	41.13(6)	128.82(6)

[a] For comparison, the Zr $3d_{5/2}$ BE is 178.91(3) eV in Zr metal and the Cu $2p_{3/2}$ BE is 932.86(4) eV in Cu metal.

4.2.3 XANES analysis

X-ray absorption spectra were measured at the Canadian Light Source (CLS) in

Saskatoon, Saskatchewan. The bending magnet soft X-ray microcharacterization beamline

(SXRMB, 06B1-1) was used for Zr L-edge spectra, the high-resolution spherical grating

monochromator beamline (SGM, 11ID-1) for Cu L-edge spectra, and the variable line spacing plane grating monochromator beamline (VLS PGM, 11ID-2) for Si L-edge spectra. The SXRMB beamline is equipped with an InSb (111) double crystal monochromator which provided a photon flux of $\sim 10^{11}$ photons/s, with a resolution of 3.3 eV at 10 keV and a beamsize of approximately $300 \times 300 \ \mu m^2$. Finely ground samples were mounted on carbon tape and inserted into the vacuum chamber via a load lock. Multiple scans of the Cu and Si L-edge XANES spectra were collected for each sample, giving an estimated accuracy of ± 0.1 eV for the absorption energies. Spectra were collected in total electron yield (TEY) and X-ray fluoresence yield (FLY) modes, with a step size of 0.1 eV through the edge over various energy ranges (Zr L-edge, ~50 eV below to ~500 eV above the edge; Cu L-edge, ~20 eV below to ~65 eV above; Si L-edge, ~30 eV below to ~30 eV above). The Zr spectra were calibrated against a standard of $FePO_4$, with the maximum of the first derivative of the P K-edge set to 2153.0 eV;[146] the Cu and Si spectra were calibrated against standards of the elemental metals, with the maxima in the first derivatives of the L_3-edges set to 932.7 eV for Cu and 99.2 eV for Si.[147] Uncertainties of ± 0.1 eV for the absorption edge energies were estimated by collecting multiple scans for each sample.

The Pacific Northwest Consortium / X-ray Operations and Research Collaborative Access Team (PNC/XOR-CAT), Sector 20 bending magnet beamline (20BM), at the Advanced Photon Source (APS) at Argonne National Laboratory was used to measure Zr and Cu K-edge XANES spectra. The silicon (111) double crystal monochromator on this beamline provided a photon flux of $\sim 10^{11}$ photons/sec with a resolution of 1.4 eV at 10 keV and a beam size of approximately 1×4.5 mm. Finely ground samples were sandwiched between Kapton tape and positioned at 45° to the X-ray beam. Spectra were measured in transmission mode with an ionization detector (filled with a 50:50 mixture of He and N_2 in the ionization chamber) and in

fluorescence mode with a Canberra 13-element fluorescence detector. The step size was 0.1 eV through the absorption edge. Standards of Zr or Cu metal were placed in a second position downstream of the samples and measured in transmission mode concurrently with the samples. The maxima in the first derivatives of the K-edges were set to 17998 eV for Zr and 8979 eV for Cu.[147] All XANES spectra were analyzed with use of the Athena software program.[147]

4.2.4 Band structure calculations

Tight-binding linear muffin tin orbital (TB-LMTO) band structure calculations were performed on ZrCuSiAs within the local density and atomic spheres approximations using the Stuttgart TB-LMTO program.[127] The basis sets consisted of Zr 5s/5p/4d/4f, Cu 4s/4p/3d, Si 3s/3p/3d, and As 4s/4p/4d orbitals, with the Zr 4f, Si 3d, and As 4d orbitals being downfolded. Integrations in reciprocal space were carried out with an improved tetrahedron method over 84 independent k points within the first Brillouin zone. For comparison, the band structure of LaNiAsO was also calculated in a similar manner.

4.3 Results and discussion

To parallel the approach taken to analyze the electronic structure of the rare-earth arsenide oxides *REM*AsO, to be discussed in a later chapter, we first break down the structure of ZrCuSi*Pn* (*Pn* = P, As) into its nominally separate "layers", [ZrSi] and [Cu*Pn*]. Then we examine the question of whether the layers interact by probing to what extent charge transfer occurs within and between these layers.

4.3.1 [ZrSi] layer

The Zr 3d XPS spectra for ZrCuSiAs and ZrCuSiP were fitted to two peaks corresponding to the spin-orbit-split $3d_{5/2}$ and $3d_{3/2}$ final states, in an intensity ratio of 3:2 (Figure 4-2). The weak shoulder found at high BE in all spectra is interpreted as a surface oxide. The Zr $3d_{5/2}$ BEs in ZrCuSiAs (179.64(2) eV) and ZrCuSiP (179.66(5) eV) are higher than in Zr metal (178.91(3) eV), indicating the presence of cationic Zr atoms, but they are much lower than in ZrO_2 (182.7(6) eV), indicating that the charge is nowhere as extreme as 4+ which would be expected if full electron transfer were to occur.[101] Indeed, a signature for electronic delocalization is already evident in the asymmetric lineshapes of these peaks, skewed towards higher BE. Common in the spectra of many elemental transition metals, including Zr, this asymmetry arises from the Doniach-Šunjić process described in Chapter 3 (Section 3.3.3). This asymmetry arises when valence electrons, interacting with the core-hole formed after photoionization, are excited into the continuum of empty conduction states above the Fermi edge.[130] In this way, the core electrons experience substantial nuclear screening to the extent that the Zr 3d BEs in ZrCuSiAs and ZrCuSiP do not shift much from that in Zr metal. Further evidence for this electronic delocalization is provided by resistivity measurements, which show semimetallic behaviour for ZrCuSiP, and band structure calculations, which show a pseudogap at the Fermi level (vide infra).[132]

The Si 2p XPS spectra were fitted to two components representing the $2p_{3/2}$ and $2p_{1/2}$ spin-orbit-split final states, in an intensity ratio of 2:1, FWHM of 0.9 eV, and an energy splitting of 0.6 eV (Figure 4-3a). The second set of peaks at higher BE is assigned to surface silicon suboxides.[11,121] Surprisingly, the Si $2p_{3/2}$ BEs in ZrCuSiAs (99.41(4) eV) and ZrCuSiP (99.40(5) eV) are, within standard uncertainty, the same as in elemental Si (99.5(2) eV), even though the
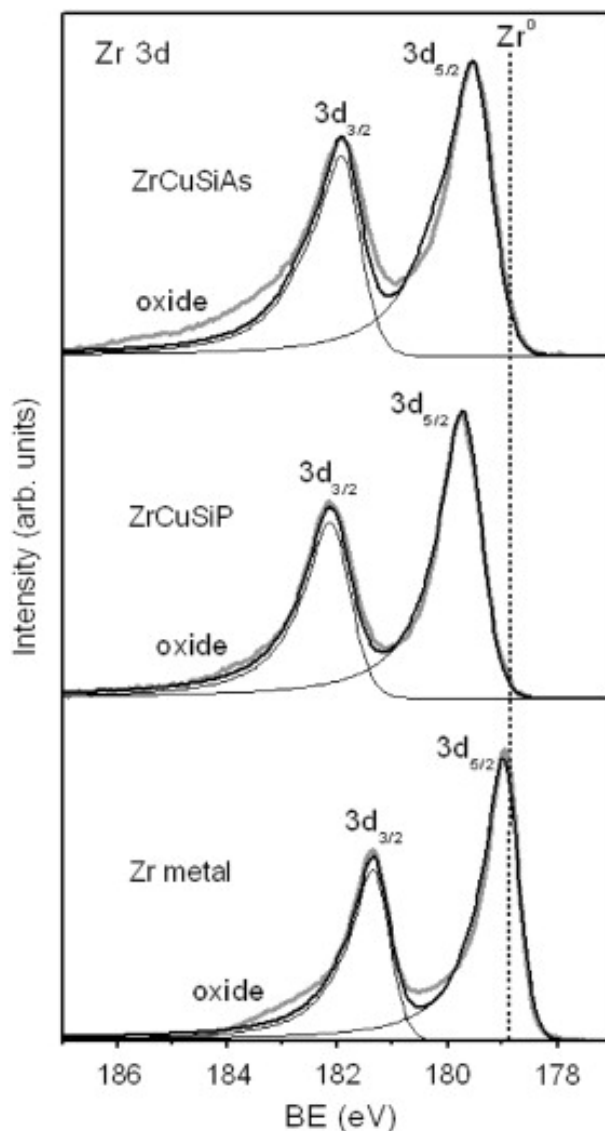
Figure 4-2 Zr 3d XPS spectra, fitted with $3d_{5/2}$ and $3d_{3/2}$ components, for ZrCuSiAs, ZrCuSiP, and Zr metal. The vertical dashed line marks the $3d_{5/2}$ BE for Zr metal.

formal charge is 2–.[101,121] A closely related case is $Zr(As_{0.6}Si_{0.4})As$, in which the more perceptibly shifted Si $2p_{3/2}$ BE (98.9 eV) is correlated with an approximate negative charge of 1-.[11] The implication is that the Zr-to-Si charge transfer is less pronounced and that the Zr–Si bonds are even more highly covalent in ZrCuSiAs and ZrCuSiP than in $Zr(As_{0.6}Si_{0.4})As$. The absence of a BE shift would also be consistent with the occurrence of strong Si–Si bonding
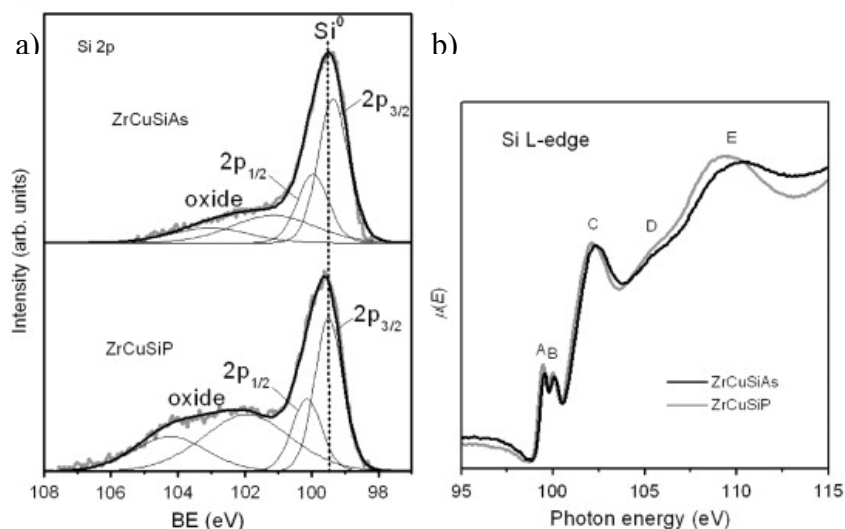
Figure 4-3 (a) Si 2p XPS spectra, fitted with $2p_{3/2}$ and $2p_{1/2}$ components, and (b) Si L-edge XANES spectra (FLY mode) for ZrCuSiAs and ZrCuSiP. The vertical dashed line in (a) marks the $2p_{3/2}$ BE for elemental Si. Features A–E in (b) are discussed in section 4.3.1.

within square nets in the structure, supporting the presence of an extended polyanionic Si network. The identical BEs in ZrCuSiAs and ZrCuSiP suggest that the Si charges are independent of the nature of the pnicogen. To confirm this point, the Si L-edge XANES spectra, which are less sensitive to final state effects than are XPS spectra, were analyzed (Figure 4-3b).[148] The features (A to E) in these spectra arise from dipole-allowed transitions of 2p electrons into unoccupied s and d states ($\Delta l = \pm 1$) and are characteristic of tetrahedrally coordinated Si (such as in α-quartz).[149] Peaks A and B correspond to transitions from 2p to 3s states (with a_1 symmetry); they are split 0.6 eV apart from spin-orbit-coupling into $2p_{3/2}$ (L_3-edge) and $2p_{1/2}$ states.[149] As anticipated, the L-edge absorption energies are essentially identical for both ZrCuSiAs and ZrCuSiP. Peak C is assigned to a $t_2 \rightarrow t_2^*$ (2p to strongly hybridized s-p states) transition, peak D to multiple scattering resonance (MSR), and peak E to a $2p \rightarrow 3d$ transition (or possibly a surface oxide).[149,150]

4.3.2 [CuPn] layer

Cu 2p XPS spectra for ZrCuSiAs and ZrCuSiP consist of $2p_{3/2}$ and $2p_{1/2}$ core-line peaks in an intensity ratio of 2:1 (Figure 4-4a). Interestingly, despite the expectation of Cu^{1+}, these spectra exhibit features characteristic of both Cu^{2+} and Cu^{1+} systems. On one hand, the Cu $2p_{3/2}$ BEs in ZrCuSiAs (933.68(3) eV) and ZrCuSiP (933.70(6) eV) are higher than in Cu metal (932.86(4) eV). The occurrence of BE shifts relative to Cu metal is usually diagnostic for compounds containing Cu^{2+} but not Cu^{1+}.[151-154] On the other hand, as gauged by their FWHMs, the Cu $2p_{3/2}$ peaks in ZrCuSiAs and ZrCuSiP (1.0 eV) are much narrower than in CuO (3.2 eV)[155] but closer to those in $CuBr^{156}$ or CuI (1.2 eV).[157] The absence of line broadening is usually diagnostic for compounds containing Cu^{1+} but not Cu^{2+}. Significant line broadening occurs for Cu^{2+} ($3d^9$) where the interaction of unpaired 3d electrons with 2p electrons after photoionization gives rise to multiplet splitting, but not for Cu^{1+} ($3d^{10}$) where no such interaction can occur because of the absence of unpaired electrons.[158] These seeming contradictions can be reconciled upon realization that the bonding in these quaternary pnictides is highly covalent. Thus, the BE correlation may break down, similar to the case of the chalcogenides Cu_2S and CuS, which are indistinguishable by their Cu 2p BEs.[158] Moreover, because these pnictides are expected to be semimetallic, the mechanism for line broadening is different. The Cu $2p_{3/2}$ peaks actually resemble more closely those in Cu metal (FWHM of 0.8 eV; Figure 4-4a), $CeCu_4Al$ (FWHM of 1.0 eV),[159] and other alloys containing Cu^{1+} or Cu^{0},[152] with a small asymmetry to higher BE arising in the same way (Doniach-Šunjić process) as described earlier for the Zr 3d core-line.
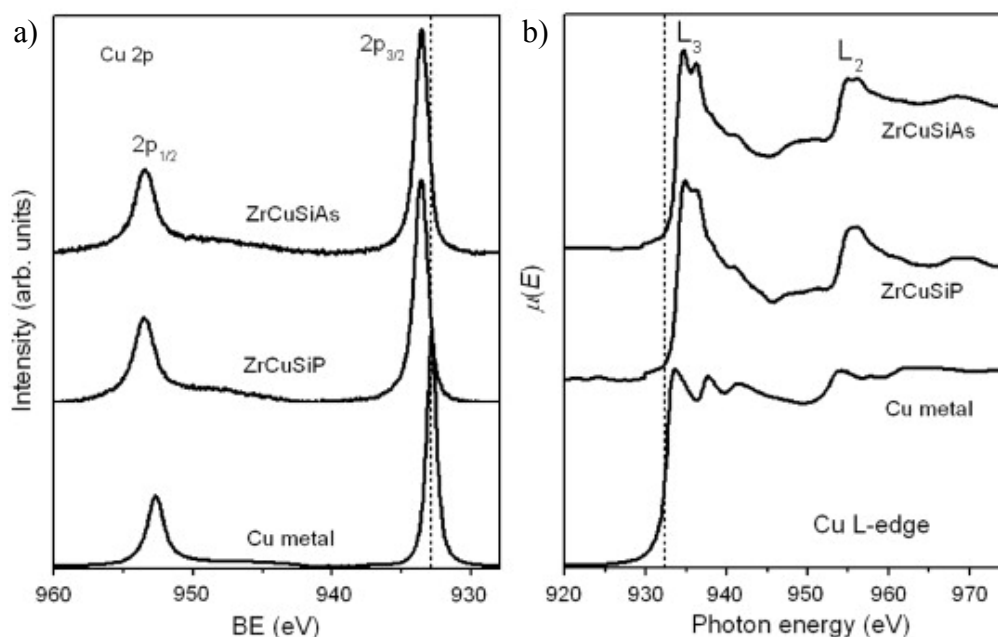
Figure 4-4 (a) Cu 2p XPS spectra and (b) Cu L-edge XANES spectra (FLY mode) for ZrCuSiAs, ZrCuSiP, and Cu metal. The vertical dashed lines mark the Cu $2p_{3/2}$ BE in (a) and the Cu L_3-edge absorption energy in (b) for Cu metal. Spectra are offset for clarity.

Another defining feature that can be examined is an intense satellite above the $2p_{3/2}$ core line at 940–945 eV seen in the Cu 2p XPS spectra for Cu^{2+} but not Cu^{1+} or Cu^0 systems, as has been exploited to identify Cu^{2+} in cuprate superconductors.[151-153,155,158,160-166] The two theories developed (a "shake-up" process in which Cu valence electrons are excited into empty conduction states above the Fermi edge after photoionization,[151] or a "shake-down" process in which ligand electrons relax into empty conduction states after photoionization[158]) both predict that this satellite is only possible in Cu^{2+} systems where empty 3d conduction states are available. The absence of this satellite in ZrCuSiAs and ZrCuSiP thus eliminates the possibility for an assignment of Cu^{2+}.

Further information can be gained from the Cu L-edge XANES spectra, which reveal dipole-allowed transitions from $2p_{3/2}$ (L_3-edge) or $2p_{1/2}$ (L_2-edge) states to unoccupied 4s and 3d

states (Figure 4-4b). The lineshapes are typical of Cu^{1+} compounds. Given the d^{10} configuration

for Cu^{1+} and Cu^0, the 2p → 4s transition is much more probable than the 2p → 3d transition,

whereas the reverse holds for Cu^{2+} ($3d^9$).[167] The correlation between absorption energy and

charge is not so straightforward. Although it is true that the L_3-edge energy for Cu^{1+} is higher

than for Cu^0 because of the greater positive charge, it is actually lower for Cu^{2+} because of the

presence of unfilled 3d states.[167] The L_3-edge absorption energy in ZrCuSiAs and ZrCuSiP (both

934.0 eV) is found to be higher than in Cu metal (932.7 eV), supporting the presence of Cu^{1+}. In

principle, the intensity of the Cu L-edge, which should be proportional to the number of

conduction states, can be analyzed; however, this relationship is not valid here because these

spectra were measured in FLY mode, which is influenced by self-absorption effects.

The As 3d and P 2p XPS spectra each show one broad signal, fitted to the As $3d_{5/2}$ and

$3d_{3/2}$ components (intensity ratio of 3:2, FWHM of 0.9 eV, splitting of 0.7 eV) and P $2p_{3/2}$ and

$2p_{1/2}$ components (intensity ratio of 2:1, FWHM of 0.7 eV, splitting of 0.9 eV), respectively

(Figure 4-5). The As XPS spectrum shows a small asymmetry at higher BE which is attributed

to surface oxides (as seen in the Zr XPS spectrum, as well as in $As_{1-x}Se_x$)[131] or may be caused by

the line-broadening mechanism described earlier involving electronic delocalization in

ZrCuSiAs. The P XPS spectrum includes a minor component which is assigned to the $2p_{1/2}$ core-

line peak of trace amounts of elemental P, with the $2p_{3/2}$ peak presumably buried under the more

intense main peaks for ZrCuSiP. The As $3d_{5/2}$ BE is lower in ZrCuSiAs (41.13(6) eV) than in

elemental As (41.7(2) eV) and the P $2p_{3/2}$ BE is lower in ZrCuSiP (128.82(6) eV) than in

elemental P (130.2(3) eV), indicating the presence of anionic pnicogen atoms in both cases.[101,121]

As in the case for the Si atoms within the [ZrSi] layer, these BE shifts are less extreme than

expected for nominal Pn^{3-} anions within the [CuPn] layer because of the substantial covalent

character in the bonds. The magnitude of these shifts should reflect the degree of electron transfer within the Cu–*Pn* bonds. Interestingly, the BE shifts are less pronounced for the As atoms (ΔBE of 0.6 eV) than for the P atoms (ΔBE of 1.4 eV), implying that As is less electronegative than P. This observation contradicts the relative ordering of the Allred-Rochow electronegativities for As (2.20)[8] and P (2.06),[168] as was previously noted in a comparative XPS study of binary transition-metal phosphides vs. arsenides.
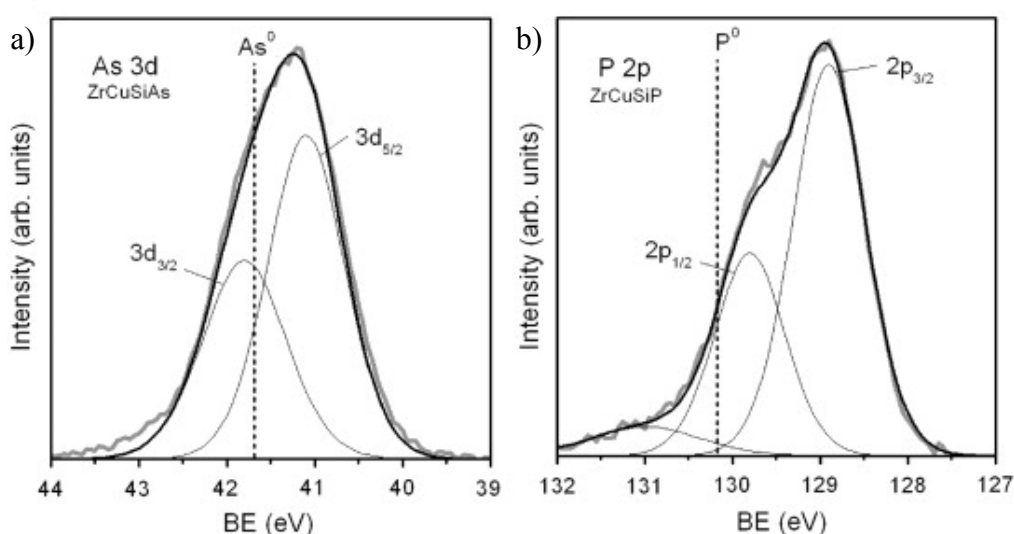
Figure 4-5 (a) As 3d XPS spectrum, fitted with $3d_{5/2}$ and $3d_{3/2}$ components, for ZrCuSiAs, and (b) P 2p XPS spectrum, fitted with $2p_{3/2}$ and $2p_{1/2}$ components, for ZrCuSiP. The vertical dashed lines mark the As $3d_{5/2}$ BE for elemental As and the P $2p_{3/2}$ BE for elemental P.

4.3.3. Charge transfer within and between [ZrSi] and [Cu*Pn*] layers

It is useful to summarize the conclusions reached so far. The [ZrSi] layer contains Zr cations and Si anions, but the charges are not extreme (as implied by little or even no energy shifts relative to the element) and there is evidence for electronic delocalization. The [Cu*Pn*] layer contains Cu^{1+} cations and *Pn* anions, with more pronounced energy shifts, consistent with a greater ionic character in the Cu–*Pn* bonds than in the Zr–Si bonds. Of the remaining questions,

the most important is whether the separate layers interact; that is, we want to address the possibility that the *Pn* atoms are bonded not only to the Cu atoms, but also to the Zr atoms (Figure 4-1b). If so, then it is of interest to determine how the extent of Zr-to-*Pn* or Cu-to-*Pn* charge transfer is altered in ZrCuSiAs vs. ZrCuSiP. Because transitions in Zr and Cu XANES spectra can reflect changes in the occupancy of specific states within atoms, they provide a way to answer these questions.

The Zr K-edge spectra reveal transitions of 1s electrons into unoccupied p states (Figure 4-6a). The immediate observation that the spectra differ for ZrCuSiAs and ZrCuSiP implies that the Zr and *Pn* atoms do interact. We use the calculated conduction band for ZrCuSiAs (Figure 4-7) to aid in the interpretation of these spectra by identifying qualitatively what orbital contributions are likely in the final states of these transitions. (The calculated conduction band for ZrCuSiP is similar and not shown here.) Peak A is assigned as a transition from Zr 1s to Zr 5p states that are hybridized with p states of Si and *Pn* atoms. This peak is more intense in ZrCuSiAs than in ZrCuSiP, which indicates that there are more pnicogen-based conduction states available in the former, consistent with the earlier assertion that As is less electronegative than P and thus that charge transfer is less from Zr to As than to P atoms. (An alternative assignment, an MSR phenomenon in which the peak becomes more intense with larger next-nearest neighbour atoms, can be dismissed because the second coordination sphere around Zr is the same in both compounds.[169]) Peak B is assigned either as a transition from Zr 1s to Zr 5p states that are hybridized with Cu 4p states, or possibly an MSR process.[169] More convincing evidence for the interaction of Zr and *Pn* atoms is provided by the Zr L-edge spectra, which probe the Zr 4d states directly involved in bonding. Here, the spectra consist of L_3- and L_2-edges, corresponding to transitions from Zr $2p_{3/2}$ and $2p_{1/2}$ states, respectively, to unoccupied 4d
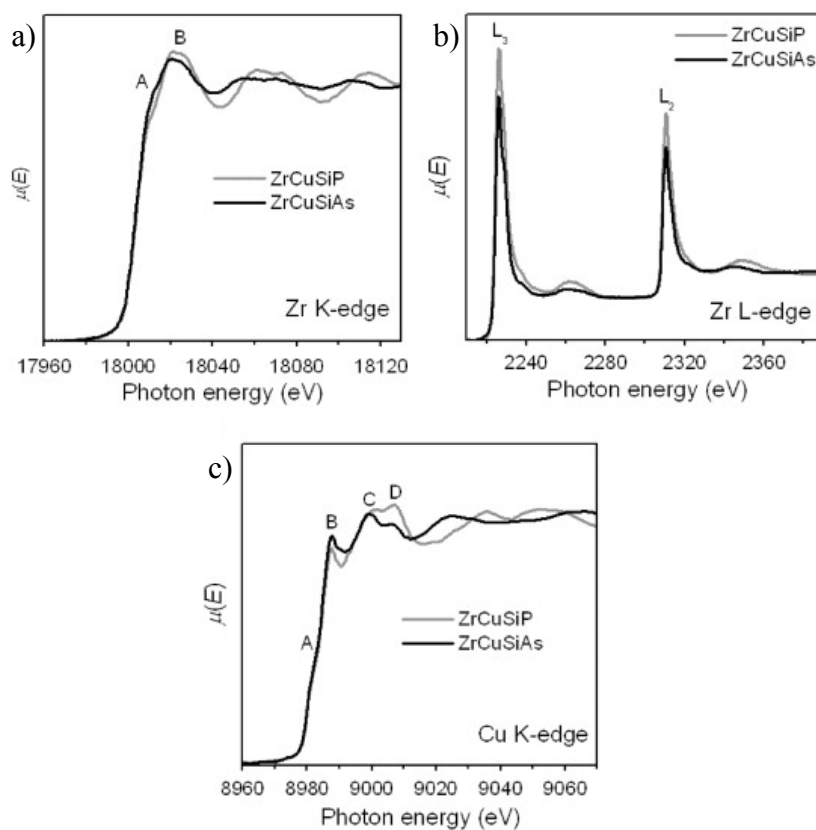
Figure 4-6 Normalized (a) Zr K-edge, (b) Zr L-edge, and (c) Cu K-edge XANES spectra for ZrCuSiAs and ZrCuSiP. Zr and Cu K-edge spectra were measured in transmission mode and Zr L-edge spectra in TEY mode. Marked features are discussed in Section 4.3.3.
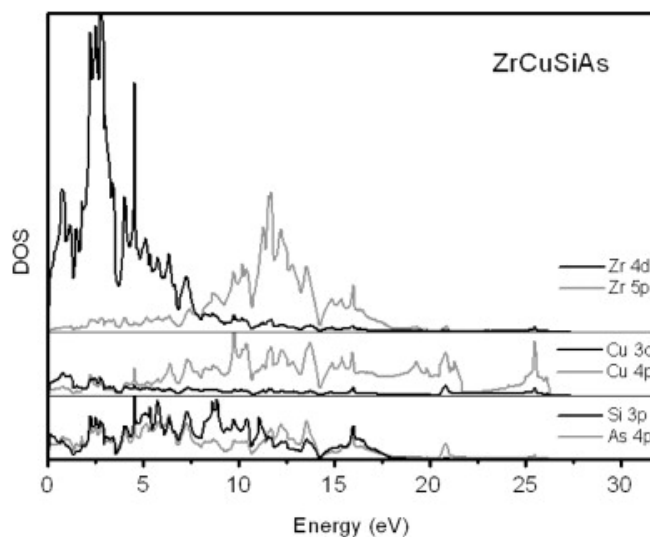
Figure 4-7 Orbital projections of the calculated conduction states for ZrCuSiAs. The projections are offset for clarity but are set on the same scale.

states (Figure 4-6b). Both edges are less prominent in ZrCuSiAs than in ZrCuSiP, indicating that there are fewer Zr-based conduction states in the former.

Complementary information about the extent of metal-to-pnicogen charge transfer can be gained from the Cu K-edge XANES spectra, which reveal transitions of Cu 1s electrons into unoccupied p states (Figure 4-6c). Peak A resembles a pre-edge feature corresponding to a dipole-forbidden 1s $\rightarrow$ 3d transition commonly found for Cu^{2+} species by virtue of their unfilled 3d-based conduction states.[170] Because the possibility of Cu^{2+} was already eliminated from the XPS data, the more likely assignment is a dipole-allowed transition from Cu 1s to strongly hybridized Cu 3d/4p states associated with the tetrahedral coordination geometry around Cu^{1+} species (similar to the case of copper(I) halides).[171] An alternative assignment is a transition from Cu 1s to Cu 4p states that are hybridized with Zr 4d states, as found near the Fermi edge in the conduction band (Figure 4-7). Although the Zr and Cu atoms are more than 3 Å apart, similar types of long-distance interactions have been implicated in the spectra of $Ca_{2-x}Sr_xFe_2O_5$,[172] $LaFeAsO_{1-x}F_x$,[173] and La_2CuO_4.[174] Peak B is assigned as a transition from Cu 1s to Si 3p and *Pn n*p states. With the assumption that the contribution from the Si states is identical (on the basis of the lack of changes in the Si XPS and XANES spectra), the greater intensity of this peak in ZrCuSiAs than in ZrCuSiP confirms that there are more pnicogen-based conduction states in the former. As before, this implies that As is less electronegative than P and that charge transfer is less from Cu to As than to P atoms. The remaining peaks, C and D, are assigned as transitions from Cu 1s to Zr 5p and Cu 4p states (seen in the conduction band), or possibly as MSR phenomena.[113]

4.3.4 Band structure

It is now of interest to see if the conclusions gained from the spectroscopic evidence are supported by the calculated band structure for ZrCuSiAs, in comparison to a representative rare-earth arsenide oxide, LaNiAsO. In common with other rare-earth pnictide oxides, the band structure for LaNiAsO is characterized by a partially filled valence band that comprises a narrow range of La- and O-based states (from –6 to –3 eV) and a wider range of Ni- and As-based states (from –6 eV upwards), with the bands near the Fermi level dominated by Ni 3d states (Figure 4-8a). (The narrow low-energy band centred near –11.5 eV largely comprises As 4s states.) Notwithstanding the usual assumption that the [LaO] layer contains ionic bonds,[31] the mixing of La and O states implies that there is also some covalent character here, as reflected by the modest integrated crystal orbital Hamilton population (–ICOHP) value of 0.65 eV/bond and the occupation of La–O bonding levels in this energy range (Figure 4-8b). The main stabilizing contribution in this structure, however, occurs within the [NiAs] layer, where a large –ICOHP of 1.88 eV/bond for the Ni–As contacts is derived from the occupation of strongly bonding levels. Weak Ni–Ni bonding (–ICOHP of 0.17 eV/bond) is associated with the arrangement of Ni atoms 2.92 Å apart forming square nets within the [NiAs] layer. The corresponding arrangement of O atoms, too far apart at 2.92 Å, within the [LaO] layer leads to no O–O bonding interactions (–ICOHP of 0.02 eV/bond), of course. If the interaction between La and As atoms is interrogated, the small (but non-negligible) –ICOHP value of 0.10 eV/bond indicates that interlayer bonding between the [LaO] and [NiAs] layers is considerably weaker than intralayer bonding; the picture of nearly separate ionic [LaO] and covalent [NiAs] layers holds.
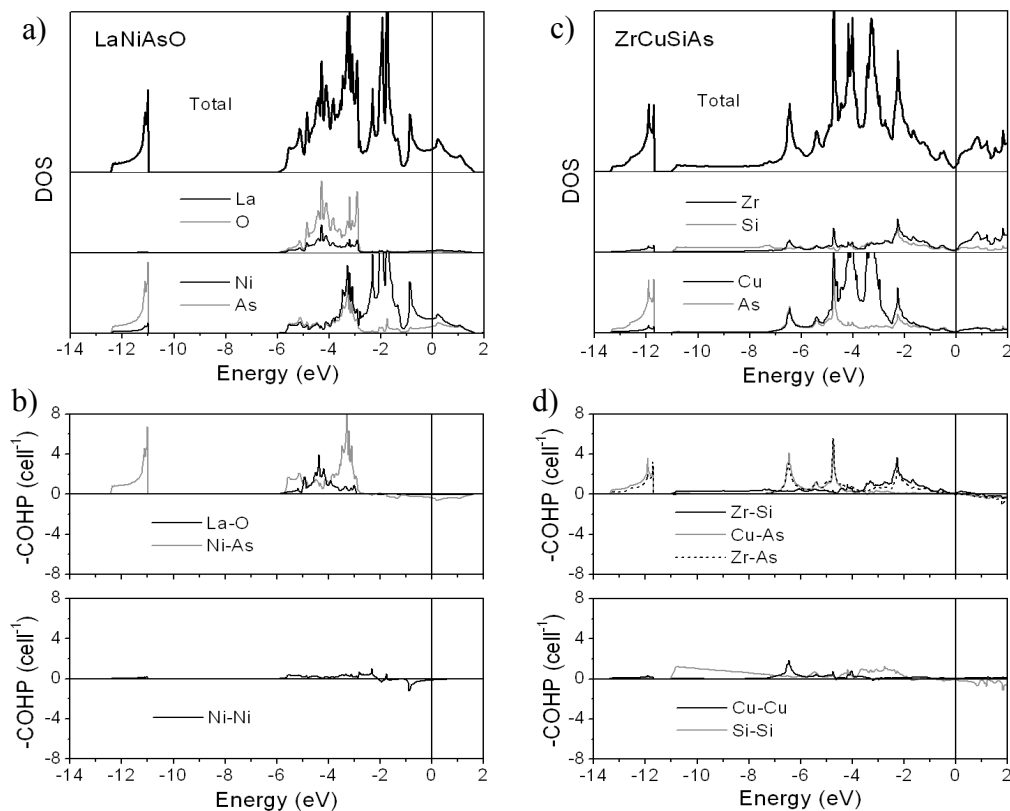
Figure 4-8 Density of states (DOS) with its orbital projections and crystal orbital Hamilton population (COHP) curves for (a–b) LaNiAsO and (c–d) ZrCuSiAs The Fermi level is at 0 eV.

The band structure for ZrCuSiAs reveals some striking differences (Figure 4-8c). The Fermi level falls in a pseudogap, so that semimetallic behaviour is predicted. (Although the properties of ZrCuSiAs have not been measured, the electrical resistivity of ZrCuSiP is quite high, 1.5×10^{-3} $\Omega \cdot$cm at 300 K, and falls only to 1.0×10^{-3} $\Omega \cdot$cm at 5 K.[132]) Unlike the [LaO] layer in LaNiAsO, the [ZrSi] layer gives rise to dramatically wider energy dispersion, consistent with more pronounced covalent bonding character associated with the occupation of Zr–Si bonding levels (–ICOHP of 1.51 eV/bond) (Figure 4-8d). A wide subband extending down to – 11 eV originates from orbital interactions of Si-based states, made possible by the closer 2.60 Å separation of Si atoms within square nets in the [ZrSi] layer. Occupation of Si–Si bonding levels leads to a substantial –ICOHP of 1.41 eV/bond, confirming the presence of strong delocalized

homoatomic bonding within these polyanionic Si square nets. Relative to the [NiAs] layer in LaNiAsO, the compression of the [CuAs] layer in ZrCuSiAs within the *ab* plane does not alter the metal-arsenic bonding too much (–ICOHP of 1.43 eV per Cu–As bond) but does enhance the metal-metal bonding (–ICOHP of 0.49 eV per Cu–Cu bond). Importantly, the occupation of Zr–As bonding levels leads to substantial interlayer bonding (–ICOHP of 1.73 eV/bond) that is of the same magnitude as the intralayer bonding. Consistent with the Zr XANES spectra which show evidence for Zr–As interactions, the picture of interacting [ZrSi] and [CuAs] layers is confirmed.

4.4 Conclusions

The [LaO] and [NiAs] layers in LaNiAsO can be treated independently (as suggested by the insensitivity of the As 3d BEs upon substitution of La with other *RE* elements), but the [ZrSi] and [CuAs] layers in ZrCuSiAs are strongly interacting (as suggested by the visible changes in the Zr K- and L-edge XANES spectra upon substitution of As with P). That is, there exists a real charge transfer from Zr atoms in the [ZrSi] layer to the As atoms in the [CuAs] layer. As inferred from shifts in the Zr K- and L-edge absorption energies, this metal-to-pnicogen charge transfer is enhanced even more in ZrCuSiP, indicating that P is more electronegative than As (in contradiction to tabulated Allred-Rochow values). Band structure calculations confirm that Si–Si and Zr–As interactions are ultimately responsible for the development of a three-dimensional covalent bonding network in ZrCuSiAs.

Chapter 5

Electronic structure of lanthanum transition-metal arsenide oxides LaMAsO (M = Fe, Co, Ni) and LaFe$_{1-x}M'_x$AsO (M' = Co, Ni) by X-ray photoelectron and absorption spectroscopy[*]

5.1 Introduction

In the previous chapter, it was determined from band structure calculations that rare-earth transition metal pnictide oxides (REMAsO) can be viewed having two-dimensional character, with separate ionic [REO] and covalent [MAs] layers. As pointed out in Chapter 1, the layered nature of the structure (tetragonal ZrCuSiAs-type) adopted by these arsenide oxides is believed to be of critical importance in imparting their interesting electronic properties. Within the [MAs] layers, the distortion of metal-centred tetrahedra and the ~2.8 Å separation of the M atoms arranged in square nets are suggestive of metal-metal bonding interactions.[175] Furthermore, for LaFeAsO, Fe Mössbauer spectroscopy has revealed that the tetrahedral Fe centre is in a low-spin state, implying a completely filled set of e states.[135] Simple electron counting, with the assumption of full charge transfer, suggests the formulation [$RE^{3+}O^{2-}$][$M^{2+}Pn^{3-}$]. However, as discussed in the previous chapter, this approximation of the electronic structure may be incorrect as the bonding within each layer is quite different. To what extent charge transfer really occurs and to what degree the bonding is covalent vs. ionic are questions that can be confronted with more prowess.

In Chapter 5, band structure calculations of LaNiAsO revealed that the valence states comprise a lower-energy band derived from O 2p and As 4p states, and a higher-energy band derived from Ni 3d states, with the Fermi level located just above a sharp spike in the Ni d-band. However, it is important to provide experimental evidence. X-ray photoelectron spectroscopy (XPS) and X-ray absorption near-edge spectroscopy (XANES) have been previously applied to show that the silicide pnictides ZrCuSiPn exhibited three-dimensional character. A logical extension of this work would be to explore the electronic structure of the pnictide oxides using these techniques. First we examine the effects of altering the [MAs] layer in a series of arsenide oxides LaMAsO (M = Fe, Co, Ni). Aside from previous investigations focusing on the F-doped samples (e.g., LaFeAsO$_{1-x}$F$_x$), no comparative study of these three systems has yet been reported.[30,46,134,136,173,176-180] High-resolution core-level (La 3d, M 2p, As 3d, and O 1s) and valence band XPS spectra, as well as As K-edge XANES spectra, are analyzed. Metal K- and L-edge XANES spectra for the mixed-metal series LaFe$_{1-x}M'$AsO (M' = Co, Ni) are also presented.

5.2 Experimental

5.2.1 Synthesis

All reagents, obtained from Cerac or Alfa-Aesar with purities better than 99.5%, were handled in an Ar-filled glove box. Starting material LaAs was prepared from stoichiometric reaction of elemental La and As at 1050 °C for 2 days in an evacuated fused silica tube. Binary oxide starting materials Fe$_2$O$_3$, CoO, Co$_3$O$_4$, and NiO were dehydrated by heating at 900 °C for 2 days. The quaternary arsenide oxides LaMAsO were prepared from stoichiometric mixtures of LaAs with Fe / Fe$_2$O$_3$ (for LaFeAsO), CoO (for LaCoAsO), or NiO (for LaNiAsO). The mixed-

metal series LaFe$_{1-x}$$M'_x$AsO ($M'$ = Co, Ni; $0 \leq x \leq 1$) were prepared from stoichiometric mixtures of LaAs, La$_2$O$_3$, Fe$_2$As, and FeAs with either CoO / Co$_3$O$_4$ or NiO. The mixtures were finely ground and loaded into alumina crucibles placed within fused-silica tubes, which were evacuated, sealed, and heated at 1250 °C for 3 days. For the mixed-metal samples, three cycles of grinding and heating were necessary to ensure homogeneity, as judged by powder X-ray diffraction (XRD) patterns collected on an Inel powder diffractometer. Any remaining byproducts (generally binary phases such as La$_2$O$_3$ or MAs) were removed by treating the samples with dilute hydrochloric acid. All samples were deemed to be single-phase and free of impurities, as seen in representative XRD patterns (Figure A3-1 in Appendix 3).

5.2.2 XPS analysis

XPS spectra were measured on a Kratos AXIS 165 spectrometer equipped with a monochromatic Al Kα X-ray source (14 mA, 15 kV) and a hybrid lens with a spot size of 700 × 400 μm^2. The samples are air-stable but to minimize exposure to air, they were handled in an Ar-filled glove box where they were finely ground, pressed into In foil, mounted on a Cu sample holder, and placed in a sealed container for transfer to the analysis chamber of the spectrometer. The pressure inside the XPS instrument was maintained at 10^{-7}–10^{-9} Pa. Samples were sputter-cleaned with an Ar$^+$ ion beam (4 kV, 10 mA) until core-line peaks associated with surface oxides were no longer observed in the XPS spectra. A small shoulder in the As 3d XPS spectra indicated that a slight reduction of As occurred; however, the As 3d$_{5/2}$ BEs for the arsenide oxides were, within standard uncertainties, the same before and after the sputtering procedure (Table A3-1 and Figure A3-2 in Appendix 3).

Survey spectra were collected with a BE range of 0–1100 eV, a pass energy of 160 eV, a step size of 0.7 eV, and a sweep time of 180 s. Analyses of these spectra confirmed the expected chemical compositions (La:M:As:O = 1:1:1:1) for these arsenide oxides. High-resolution core-line spectra were collected with an energy envelope of appropriate range (La 3d, 60 eV; M 2p, 50 eV; As 3d and O 1s, 20 eV), a pass energy of 20 eV, a step size of 0.05 eV, and a sweep time of 180 s. To avoid interference by an Fe Auger peak produced when Al Kα X-rays are used, the Co 2p core-line spectra for LaFe$_{1-x}$Co$_x$AsO were collected with a Mg Kα X-ray source (10 mA, 15 kV). Although no charge correction was required for the arsenide oxide samples, which are good conductors, the spectra were nevertheless calibrated to the C 1s line at 284.8 eV arising from adventitious carbon. Such a correction was needed and used in the case of a insulating La$_2$O$_3$ sample measured as a standard. All high-resolution spectra were analyzed with use of the CasaXPS software package.[128] The background arising from energy loss was removed by applying a Shirley-type function and the peaks were fitted to pseudo-Voigt (70% Gaussian and 30% Lorentzian) line profiles to take into account spectrometer and lifetime broadening effects. Except for La$_2$O$_3$ (which has been reported previously and was measured here only as a standard), multiple spectra of each sample were collected, establishing a BE precision estimated at better than ±0.10 eV (Tables A3-1–A3-3 in Appendix 3).[181] In subsequent discussion, BE values are quoted to two decimal places with this uncertainty implicitly understood. Table 5-1 summarizes the average BE values measured for all core-line XPS spectra.

5.2.3 XANES analysis

Measurements were performed at the Canadian Light Source (CLS) in Saskatoon, Saskatchewan. Metal L-edge XANES spectra were collected on the spherical grating

monochromator (SGM) undulator beamline (11ID-1). Powder samples were mounted on carbon tape and inserted into the vacuum chamber via a load lock. Spectra were collected from ~20 eV below to ~65 eV above the edge using both total electron yield (TEY) and X-ray fluorescence yield (FLY) modes. These spectra were calibrated to the elemental metals, with the maxima in the first derivatives of the L_3-edges set to 706.8 eV (Fe) and 778.1 eV (Co).[147]

Table 5-1 Core-line BEs (eV) for LaMAsO (M = Fe, Co, Ni) and LaFe$_{1-x}M'$AsO (M' = Co, Ni).

Sample	La $3d_{5/2}$	M $2p_{3/2}$	M' $2p_{3/2}$	As $3d_{5/2}$	O 1s
LaFeAsO	834.88	707.11		41.18	529.94
LaCoAsO	834.85	778.55		41.29	529.89
LaNiAsO	834.92	not measured [a]		41.43	529.96
LaFe$_{0.9}$Co$_{0.1}$AsO	834.91	707.07	778.54	41.14	529.93
LaFe$_{0.8}$Co$_{0.2}$AsO	834.81	707.06	778.59	41.18	529.86
LaFe$_{0.4}$Co$_{0.6}$AsO	834.94	707.15	778.42	41.22	529.91
LaFe$_{0.2}$Co$_{0.8}$AsO	834.77	707.18	778.43	41.30	529.93
LaFe$_{0.8}$Ni$_{0.2}$AsO	834.79	707.12	not measured [a]	41.28	529.97
LaFe$_{0.7}$Ni$_{0.3}$AsO	834.95	707.11	not measured [a]	41.31	530.00

[a]The Ni $2p_{3/2}$ core-line peak is obscured by the La $3d_{5/2}$ peak and could not be analyzed.

Arsenic K-edge and metal K-edge XANES spectra were collected on the hard X-ray microanalysis (HXMA) superconducting wiggler beamline (06ID-1). Powder samples were sandwiched between Kapton tape and positioned at 45° to the X-ray beam. A silicon (220) crystal monochromator provided a monochromatic photon flux of ~6 × 10^{11} photons/sec with a resolution of 1 eV at 10 keV and a beam size of 100 × 500 μm^2. Spectra were collected in

transmission mode with an ion chamber detector (filled with a 50:50 mixture of N_2 and Ar) and in fluorescence mode with a Lytle detector.[182] The step size was 0.2 eV on traversing through the absorption edge. These spectra were calibrated to Au, with the maximum in the first derivative of the Au L_3-edge set to 11919 eV.[147] All XANES spectra were analyzed with use of the Athena software program.[147]

5.3 Results and discussion

5.3.1 Fe and Co 2p XPS spectra

High-resolution metal core-line XPS spectra have been measured for LaMAsO (M = Fe, Co, Ni). Unfortunately, the Ni 2p spectra could not be analyzed because the Ni $2p_{3/2}$ peak is obscured by the La $3d_{3/2}$ peak, which coincides in energy. The Fe and Co 2p XPS spectra for LaFeAsO and LaCoAsO, respectively, reveal two peaks corresponding to the $2p_{3/2}$ and $2p_{1/2}$ spin-orbit-coupled final states (Figure 5-1). Normally, the BE depends principally on the valence state of an atom within a solid but it is also influenced by other factors.[183] The Co $2p_{3/2}$ peak in LaCoAsO does shift discernibly to higher BE (778.55 eV) relative to Co metal (778.1 eV),[6] suggesting the presence of positively charged Co atoms in LaCoAsO. However, a similar shift in the Fe $2p_{3/2}$ peak is barely perceptible in LaFeAsO (707.11 eV) relative to Fe metal (707.0 eV).[6] The interpretation is complicated by the asymmetric peak lineshapes, skewed towards higher energy, which is due to the Doniach-Šunjić process described in Chapter 3. This lineshape originates from strong electron delocalization associated with the metal-metal bonding

network found in the pnictide oxides.[130] In solids exhibiting such delocalized bonding or metallic behaviour, the BE shifts can be quite misleading. For example, the Co $2p_{3/2}$ BE in CoAs (777.91 eV)[8] is actually lower than in Co metal,[6] even though the Co atoms are found to be positively charged (close to 1+) when assessed by different means. Thus, another approach is needed to interpret these spectra.
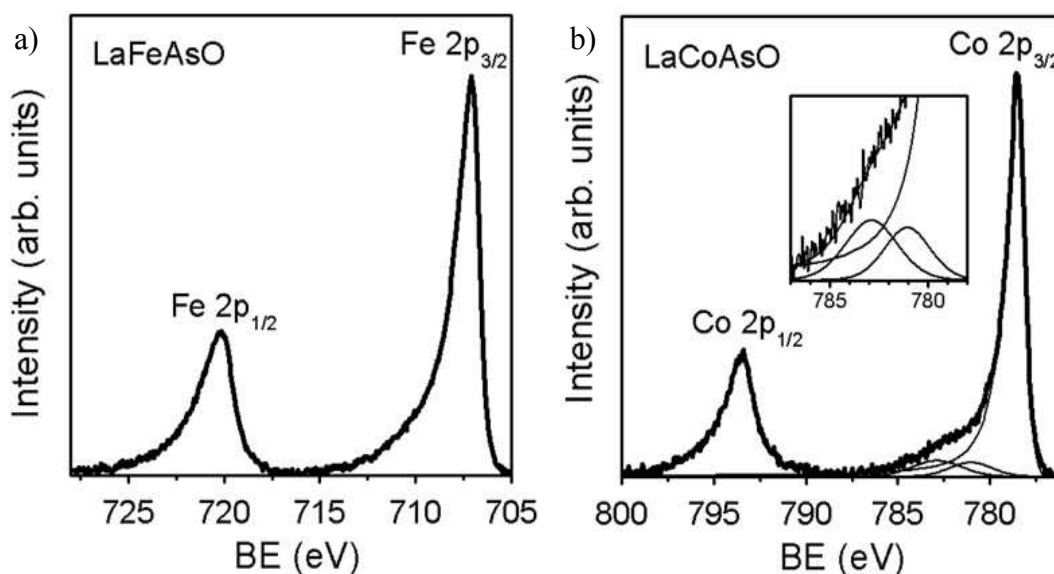
Figure 5-1 (a) Fe 2p XPS spectrum for LaFeAsO and (b) Co 2p XPS spectrum for LaCoAsO. The satellite structure, modeled as two peaks, is enlarged in the inset in (b).

Closer inspection of the Co 2p XPS spectrum reveals a satellite feature at higher BE to the main $2p_{3/2}$ peak (inset of Figure 5-1b), similar to that seen in Co metal,[6] CoAs,[8] and other Co-containing compounds.[119,120] This satellite feature can be accounted for through either a plasmon loss[184] or a two-core-hole model.[185] In the plasmon loss model, the photoelecton loses KE (with an apparent increase in BE) when it interacts with bound valence electrons, which are caused to oscillate.[184] Although this model was the first to be proposed, it was abandoned when no

evidence of a plasmon event was observed in electron energy loss spectra.[185] In the two-core hole theory, a core-hole produced after photoionization effectively acts as a positive charge and pulls conduction states below the Fermi edge.[185] If the conduction states are empty, a satellite peak is observed because the final state contains two holes (one in the core states and one in the valence). If the conduction state pulled below the Fermi edge is full, only one hole occurs in the final state and only the core-line is observed. This model has been the more widely accepted explanation, and has been used to account for the presence of the satellite feature in Co metal.[186] However, recent reflective electron energy loss spectrum (REELS) of Co has shown new evidence for two plasmons (bulk and surface).[6] The energy difference between the plasmon satellites and the main line peak in the REELS spectra is similar to the BE difference between the satellite and the core-line peaks in the Co 2p XPS spectra of these compounds.[6] If the satellite peak was due to a two-core-hole model, satellite peaks should not have been observed in the REELS spectra.

Both models can be used to predict the oxidation state of Co in LaCoAsO. In either model, the intensity of the satellite peak is proportional to the number of valence electrons on the Co atom within the solid.[120] In the plasmon loss model, the cross-section of the plasmon oscillations is proportional to the number of valence electrons (i.e., oscillations will increase if there are more valence electrons). In the two-core-hole model, more valence electrons will stabilize the hole in the valence band increasing the cross-section for the two-core-hole state. The satellite feature shown in Figure 5-1b was interpreted through the plasmon loss model, with the two peaks observed representing the bulk and surface plasmons. Surface plasmons are

typically observed at high BE because the outgoing photoelectron has lower KE as it interacts with valence electrons near the surface. The normalized satellite intensity ($I_{satellite}/I_{core\text{-}line}$) is found to be lower in LaCoAsO (0.20) than in Co metal (0.32),[6] which leads to the conclusion that Co atoms are, in fact, positively charged. Given that the satellite intensity is similar to that in CoAs (0.22), the Co atoms in LaCoAsO are proposed to have a charge closer to 1+ than to 2+.[6] By extrapolation, we propose that the Fe atoms are similarly positively charged (close to 1+) in LaFeAsO.

5.3.2 As 3d XPS and K-edge XANES spectra

The As 3d XPS spectra for LaMAsO (M = Fe, Co, Ni) show one signal (Figure 5-2a), which was fitted to two component peaks corresponding to the 3d$_{3/2}$ and 3d$_{5/2}$ spin-orbit-coupled final states, each with a full-width at half-maximum (FWHM) of 1.2–1.3 eV in an intensity ratio equal to the theoretical value of 3:2. The spectra exhibit a shoulder at low BE that is attributed to a slight reduction of the As atoms caused by the Ar$^+$ ion sputtering procedure. The signal shows a slight asymmetry at high BE, which may be attributed to the formation of suboxides (similar to the case in As$_{1-x}$Se$_x$)[131] or which may be indicative of strong electronic delocalization within the M–As bonds. There are observable shifts in the As 3d$_{5/2}$ BE, which decreases from 41.43 to 41.18 eV on progressing from LaNiAsO to LaFeAsO. These BE values are lower than in elemental As (41.7(2) eV),[101] indicating the presence of anionic As atoms. On the basis of a linear relationship assumed between charge and BE found for other As-containing compounds in the NIST X-ray spectroscopy database, we estimate a charge closer to 1– than 3– for the As

atoms in La*M*AsO.[101] The BE shifts can be correlated with the difference in electronegativity $\Delta\chi$

between *M* and As (Figure 5-2b).[168] This trend can be understood in terms of a ground state

effect in which more pronounced polar character in the *M*–As bond is associated with greater

charge transfer from *M* to As atoms, leading to more negatively charged As atoms and thus

lower BE in the progression from LaNiAsO to LaFeAsO. The same trend is also consistent with

a final state effect in which, as *M* becomes less electronegative, the electrons in the surrounding

M atoms experience greater interatomic relaxation towards the nuclear charge of a central As

atom after production of the core hole, resulting in a lowering of the As final state energy and

thus lower BE in the progression from LaNiAsO to LaFeAsO.[187,188] However, as supported

below by the As K-edge results, we assert that the BE shifts are dominated by ground state

effects.
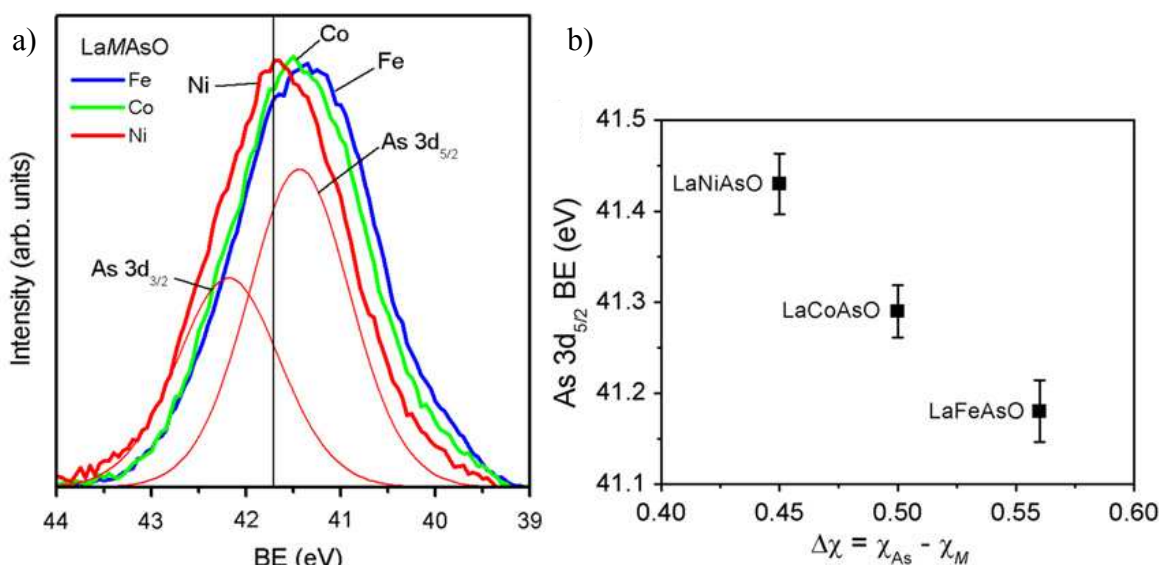
Figure 5-2 (a) As 3d XPS spectra for La*M*AsO (*M* = Fe, Co, Ni). The spectrum for LaNiAsO is fitted with $3d_{3/2}$ and $3d_{5/2}$ component peaks. The vertical line at 41.7 eV marks the $3d_{5/2}$ BE for elemental As. (b) Dependence of As $3d_{5/2}$ BE on the electronegativity difference between As and *M*.

At this stage, the assignment of As^{1-} proposed on the basis of BE shifts presents a problem because the overall charge on the [MAs] layer would not be negative, contrary to expectations. Just as with the metal 2p BEs, it may be misleading to rely on the As 3d BEs to deduce atomic charges when electronic delocalization is important, as is the case here. An alternative means to assess the As charge is to examine the As K-edge XANES spectra, which also offer further evidence for the variation in M-to-As charge transfer in LaMAsO (M = Fe, Co, Ni). Although the absorption edge energy does not show any significant shifts, there are dramatic changes in the intensities and lineshapes of three peaks marked A, B, and C (Figure 5-3), which are quite different in appearance from the previously studied cases of As_2S_3[189] and MAs.[8] The most informative feature, A, is typically assigned to be a white-line pre-edge peak that arises from the dipole-allowed excitation of As 1s electrons into unoccupied As 4p states above the Fermi edge. Peak A does not show resolvable energy shifts that might be expected from M substitution, likely as a result of the interaction of the As 4p states with the M 3d states, which are pinned at the Fermi edge. These As 4p states are mixed with the predominant M 3d states in the calculated conduction bands (Figure 4-8c in section 4.3.4 in Chapter 4).[141,142,180] The intensity of this peak diminishes on progressing from LaNiAsO to LaFeAsO, indicating a greater filling of As 4p states (fewer unoccupied As 4p states) and a more negative charge on the As atoms with greater M-to-As charge transfer. This observation confirms the interpretation above that ground state effects are largely responsible for the shift in As $3d_{5/2}$ BEs. Importantly, the intensity of this peak (relative to the high-energy background) is much weaker in the LaMAsO series than in FeAs, in which the As atoms have a charge of 1−.[8] That is, we deduce

that the charge of the As atoms in LaMAsO is more negative than 1–. In combination with the M charge of 1+, an overall negative charge on the [MAs] layer is now recovered, consistent with expectations.

In another XANES analysis on the F-doped LaFeAsO$_{1-x}$F$_x$ systems, this pre-edge peak has been proposed to have partial contributions from the dipole-forbidden transition of As 1s electrons into M 3d states, which are strongly hybridized with the As 4p states because of the covalent character of the M–As bonds.[178] If this contribution were significant in LaMAsO, one would expect that, as the M 3d band is depleted and there are more available empty M 3d conduction states to which the As 1s electrons can be excited in the progression from LaNiAsO to LaFeAsO, the pre-edge feature A should intensify, in contradiction with the observed trend. Thus, we can conclude that changes in the number of empty As 4p states are largely responsible for the trend in the intensity of this pre-edge feature.
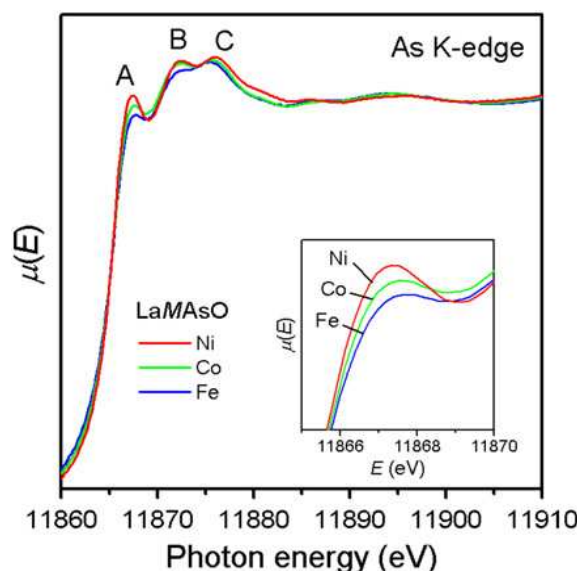
Figure 5-3 Normalized As K-edge (transmission mode) XANES spectra for LaMAsO (M = Fe, Co, Ni). Peak assignments (A, B, C) are discussed in the text. The inset highlights intensity changes in peak A.

The trend in the high-energy features marked B and C is more difficult to rationalize because there are several possibilities for their assignment. The calculated conduction bands, which have not been examined beyond ~6 eV, do not reveal any As 4p states past 3 eV above the Fermi edge.[136,141,142,180] These peaks may arise from the excitation of the As 1s electrons into M 4p and O 2p states, or hybridized As 4p and La 6p states, or some combination thereof.[190] However, because this region is also one where multiple scattering resonance (MSR) or EXAFS phenomena are likely occurring, we make no further attempts at interpretation.

5.3.3 La 3d XPS spectra

The La 3d XPS spectra for LaMAsO (M = Fe, Co, Ni) are essentially identical to each other and match well with the spectrum for a La_2O_3 standard (Figure 5-4a). The La $3d_{5/2}$ BE is higher in the arsenide oxides (834.8 eV) than in La_2O_3 (831.9 eV). For comparison, the La $3d_{5/2}$ BE is 834 eV in La_2S_3[191] and 836.1 eV in $LaFe_4P_{12}$.[120] In general, it is difficult to interpret La 3d BE shifts because they tend to be more sensitive to coordination environment and final state effects.[192] The more relevant observation is that the lineshapes are the same and indicative of La^{3+} species. The presence of trivalent La atoms is confirmed by the characteristic satellites found at higher BE (by about 4 eV) to each of the $3d_{3/2}$ and $3d_{5/2}$ core-line peaks. It is generally accepted that these satellites originate from a ligand-to-metal charge-transfer shake-up process where ligand valence electrons are promoted to the La 4f conduction states.[193-195] According to this model, the relative intensity of the satellite depends on the degree of orbital overlap between metal and ligand atoms and the electronegativity of the surrounding ligand atoms.[195] Thus, the

satellite intensities do vary between LaMAsO and La$_2$O$_3$ because the coordination environments around La atoms are different. However, as seen in spectra normalized to the 3d$_{5/2}$ core-line, the satellite intensities are the same among the three isostructural LaMAsO members (Figure 5-4b). Notwithstanding the arbitrary separation of the crystal structure into distinct layers, the La atoms are surrounded not only by four O atoms within the [LaO] layer, but also by four As atoms in the adjacent [MAs] layer. The observation that no changes occur in the La 3d spectra indicates that M substitution in the [MAs] layer exerts little influence on the La states, even though these are hybridized with the As states.[190]
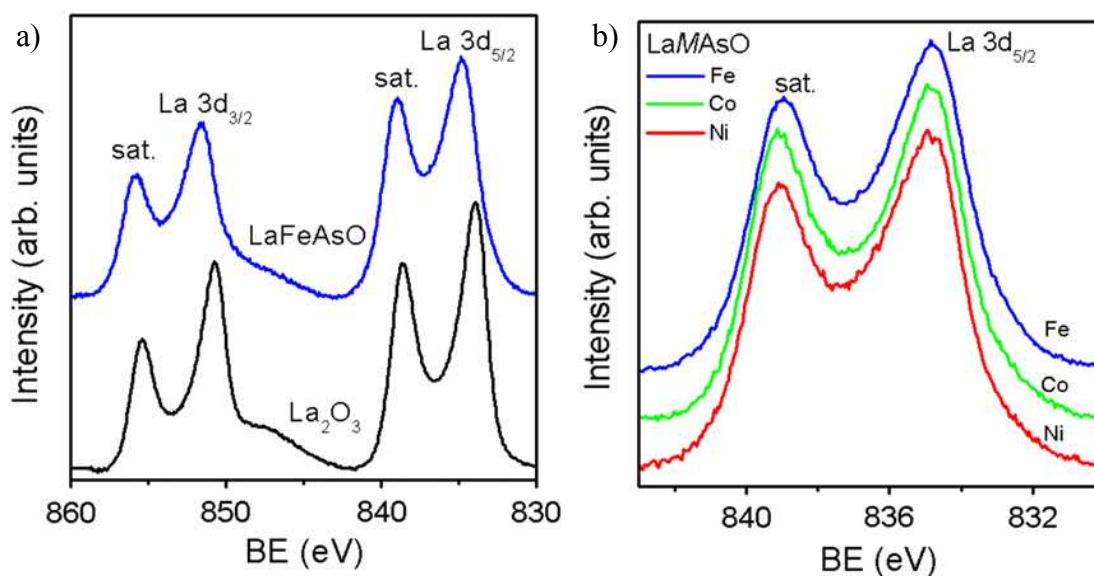
Figure 5-4 (a) Comparison of La 3d XPS spectra for LaFeAsO and La$_2$O$_3$. (b) La 3d$_{5/2}$ XPS spectra for LaMAsO (M = Fe, Co, Ni). The spectra are offset for clarity.

5.3.4 O 1s XPS spectra

As in the La spectra, the O 1s XPS spectra for LaMAsO (M = Fe, Co, Ni) are also identical to each other, with similar lineshapes and BEs. The O 1s peak is narrower (FWHM of

1 eV) in LaMAsO because only one O site is present, compared to the case of a La$_2$O$_3$ standard (FWHM of 1.4 eV) in which two different O sites are present (Figure 5-5). Both spectra show a second peak at higher BE that is attributed to residual surface water and hydroxide contaminants that could not be removed by Ar$^+$ ion sputter-cleaning; similar impurities plague the spectra of LaFeAsO$_{1-x}$F$_x$[180] and SmFeAsO$_{1-x}$F$_x$.[177]
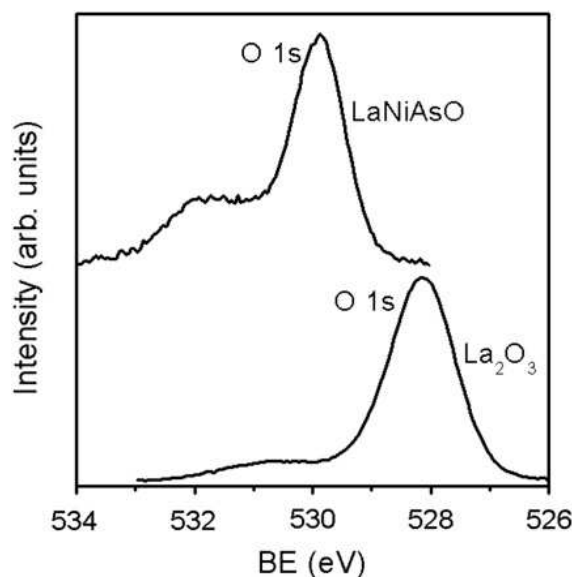
Figure 5-5 Comparison of O 1s XPS spectra for LaNiAsO and La$_2$O$_3$..

Assuming that ground state effects dominate, Barr has correlated O 1s BEs with the ionic character of metal–oxygen bonds in many simple oxides, which he classifies into three categories: semicovalent oxides (530.5–533.0 eV), normal ionic oxides (530.4–529.6 eV), and very ionic oxides (529.5–528.0 eV).[196,197] Accordingly, the higher O 1s BEs in LaMAsO (~529.9 eV) definitely indicate anionic O atoms but less ionic La–O bonds than in La$_2$O$_3$ (528.1 eV) In fact, the O 1s BEs in LaMAsO are similar to those in many transition-metal oxides.[196,197] The invariance of the O 1s spectra among the different LaMAsO members (Table 5-1) indicates

that M substitution within the [MAs] layer has little effect on the O states in the [LaO] layer, notwithstanding theoretical calculations that suggest hybridization between the O 2p and M 3d states.[136,190]

5.3.5 Valence band XPS spectra

The results from the core-line XPS spectra, taken at face value, present an inconsistency. The La 3d and O 1s XPS spectra do support the picture of strong ionic character in the [$La^{3+}O^{2-}$] layer, but the M 2p and As 3d spectra suggest charges that are much less extreme than implied by the formulation [$M^{2+}As^{3-}$]. For charge neutrality, an overall positive charge on the [LaO]$^{1+}$ layer must be compensated by a negative charge on the [MAs]$^{1-}$ layer. The charges deduced from correlations with BE shifts are close to 1+ for M and 1– for As, which do not sum to an overall negative charge. This conundrum stems from the difficulties in trying to assign an individual charge to these atoms participating in strongly covalent bonds. Moreover, there are idiosyncratic features in each core-line spectrum, such as the Co 2p satellite or the different BE correlations, that must be examined on a case-by-case basis. The analysis of the As K-edge XANES spectra does succeed in resolving the discrepancy in charge balance by recovering an As charge more negative than 1–.

To complement the core-line spectra, the valence band spectra can be examined as an alternative approach to determine the charge distribution of atoms in LaMAsO. Through a procedure developed previously to fit the valence band spectra with component peaks, it is possible to arrive at a partitioning of the electronic states even in solids with strong covalent

character.[3,6,119-121]   When the experimental valence band spectra for LaMAsO (M = Fe, Co, Ni) are compared to the calculated density of states (Figure 4-8c in section 4.3.4 of Chapter 4), it becomes apparent that there are three distinct regions: M 3d (0–3 eV), As 4p / O 2p (3–9 eV), and As 4s (9–13 eV) (Figure 5-6a-c).[46,134,135,137,141,144,145]   On the basis of this assignment, the valence band spectra were fitted to a minimum number of component peaks, labelled 1 to 6. By virtue of the tetrahedral coordination geometry around the metal atoms, the M 3d states undergo crystal field splitting into two sets, e and t_2, which are fitted to peaks 1–3. Peaks 2 and 3 correspond to the e states and are fitted as a spin-orbit-split doublet ($3d_{5/2}$ and $3d_{3/2}$) in a fixed intensity ratio of 3:2 and asymmetric lineshapes skewed towards higher BE as a result of the Doniach-Šunjić broadening process described earlier. Peak 1 corresponds to the $3d_{5/2}$ t_2 states (with the assumption that the corresponding $3d_{3/2}$ states are buried within the other peaks). As best observed when the spectra are overlapped (Figure 5-6d), the relative intensity of the M 3d signal grows most dramatically on progressing from LaFeAsO to LaNiAsO. Thus, it is assumed that the majority of M 3d states will be confined to this region. This increase in intensity can be related to the enhancement in photoelectron cross-section (Table 5-2) upon excitation with Al Kα X-rays as well as to the increase in the number of M 3d electrons.[94,95] In addition to the dominant d-band near the Fermi level, the M 3d states also contribute to the As 4p / O 2p region, as indicated in this and other band structure calculations.[46,134,135,137,141,144,145]   Peak 4, corresponding to the As 4p states, is much more intense than peak 5, corresponding to the O 2p states, because of the relative magnitudes of the photoelectron cross-sections.[94,95] Because the separation between the spin-orbit-split $np_{3/2}$ and $np_{1/2}$ states is small, only a single peak used for

fitting was justified. Peak 6 corresponds to the As 4s state. It should be noted that the relative photoelectron cross-sections of As 4s and 4p states, compared to those of M 3d states, determined on different scales exhibit the greatest discrepancies (Table 5-2).
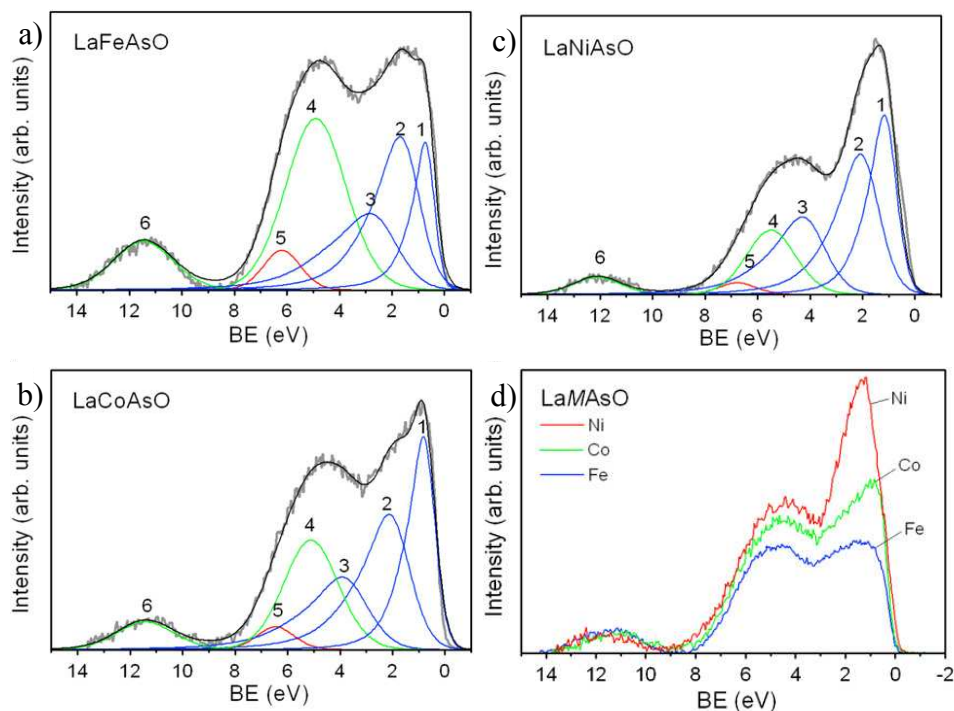
Figure 5-6 Comparison of fitted XPS valence band spectra for (a) LaFeAsO, (b) LaCoAsO, and (c) LaNiAsO. Assignments of peaks 1 to 6 are given in Table 5-3 and discussed in the text. The experimental spectra are shown by the grey lines and the fitted envelope by the thin black lines in (a)–(c). (d) XPS valence band spectra for LaMAsO (M = Fe, Co, Ni) normalized to the As 4s peak (9–13 eV) and overlapped to highlight the relative intensity differences in the 0–9 eV region arising from changes in the population of the M 3d states.

The integrated peak areas I, corrected for different photoelectron cross-sections (σ) and inelastic mean free paths (IMFP, λ), can be related to the fractional electron population of each state C_i according to:[88]

$$C_i = \frac{I_i/(\sigma_i \lambda_i)}{\sum_{j=1}^{n} I_i/(\sigma_i \lambda_i)}. \tag{5-1}$$

Table 5-2 Atomic photoelectron cross-sections, σ.

State	Ref. [95]	Ref. [94]
Fe 3d	0.08885	0.0022
Co 3d	0.1082	0.0037
Ni 3d	0.19895	0.0059
As 4s	0.1357	0.0018
As 4p	0.06045	0.0017
O 2p	0.00965	0.00024

[a] Values from Ref. [95] are proportional to the C 1s cross-section of 13,600 barns, whereas those from Ref. [94] are in units of megabarns.

Multiplying C_i by the total number of valence electrons per formula unit gives the electron population per state. Since all photoelectrons travel through the same medium with similar kinetic energies,[121] the IMFP can be assumed to be independent of the type of atom, simplifying this expression to:

$$C_i = \frac{I_i/\sigma_i}{\sum_{j=1}^{n} I_i/\sigma_i}.$$ (5-2)

Several assumptions were made in applying this analysis to LaMAsO, with the use of alternative sets of photoelectron cross-sections and two separate samples for each compound. First, since no La 4f states contribute to the valence band, the charge of La is taken to be 3+. Second, since O 2s states are located beyond the valence band well below the Fermi edge (at ~20 eV according to calculated density of states curves for LaFeAsO and LaZnAsO), at a BE similar to that for La 5p states as seen in spectra for binary rare-earth oxides, they are assumed to be completely filled

(i.e., $2s^2$).[139,140,198-200] In partitioning electrons within the component states in the valence band, we arrive at the calculated electron populations listed in Table 5-3. To perform this fitting, the population of As 4p and O 2p states (and the ratio between them) has been restrained to be relatively constant while the population of M 3d states has been allowed to vary more considerably among the LaMAsO members, in accordance with experimental observation (Figure 5-6d). This figure (normalized to the As 4s peak) reveals intensity differences not only in the 0–3 eV region, but also the 3–8 eV region. Because the As 4p and O 2p populations are assumed to be fixed among the LaMAsO members, the intensity differences in both regions are attributed to changes in the M 3d populations. Within these M 3d states, the difference in BE between the $3d_{5/2}$ and $3d_{3/2}$ peaks in the e set (peaks 2 and 3) becomes more pronounced on progressing from LaFeAsO to LaNiAsO, in accordance with the greater splitting between these spin-orbit final states with increasing atomic number and similar to previous observations in the transition-metal monophosphides MP.[6,86] The e states (peaks 2 and 3) were also set to be wider than the t_2 state (peak 1) as a result of the metal-metal bonding interactions involving the $3d_{x2-y2}$ orbitals.[134,144,145] The FWHM values and BEs for the O 1s and As 4p peaks were fixed to be roughly the same across the series. There is some variation in the individual atomic charges obtained, a result of the difficulty in deconvoluting the M 3d and As 2p states in the valence band because of their strong hybridization (covalent character in the M–As bonds). In the course of fitting an experimental valence band spectra, the goodness-of-fit was determined from the residual standard deviation (RSD), which is evaluated from the differences between the experimental and simulated spectra. Typically a fit was considered good when the RSD value

reduces to 2-3. Table 5-3 shows that there is a trend of increasing population of the t_2 states from LaFeAsO (1.2 e⁻) to LaNiAsO (2.8 e⁻), consistent with the expected electron configurations of low-spin divalent metal centres M^{2+} (i.e., Fe^{2+} ($e^4 t_2^2$) to Ni^{2+} ($e^4 t_2^4$)) in agreement with results from Mössbauer spectra.[201] A satisfying outcome of this experimental population analysis of the valence band is that we recover a charge distribution that agrees well with the formal charge assignment of $[La^{3+}O^{2-}][M^{2+}As^{3-}]$, with layers that are held together by ionic interactions, similar to the conclusions reached from a Bader analysis on LaFePO.[202]

Table 5-3 Electron population of valence states and charge distribution in LaMAsO (M = Fe, Co, Ni).

Compound	State	Sample 1		Sample 2	
	Cross-section reference	Ref. [95]	Ref. [94]	Ref. [95]	Ref. [94]
LaFeAsO	Fe 3d t_2 (peak 1)	1.0	1.0	1.4	1.4
	Fe 3d e (peaks 2, 3)	4.7	4.7	4.6	4.7
	As 4p (peak 4)	7.4	6.6	7.0	6.2
	O 2p (peak 5)	6.1	6.1	6.1	6.2
	As 4s (peak 6)	0.8	1.6	0.8	1.5
	Total no. of e⁻	20	20	20	20
	Fe charge	2.3+	2.3+	2.0+	1.9+
	As charge	3.2–	3.2–	2.8–	2.7–
	O charge	2.1–	2.1–	2.1–	2.2–
	Average charges	$[La^{3+}O^{2.1-}][Fe^{2.3+}As^{3.0-}]$			
LaCoAsO	Co 3d t_2 (peak 1)	2.4	2.2	2.4	2.2
	Co 3d e (peaks 2, 3)	4.7	4.4	5.0	4.7

	As 4p (peak 4)	6.9	6.4	7.1	6.6
	O 2p (peak 5)	6.2	6.5	5.7	6.0
	As 4s (peak 6)	0.8	1.5	0.8	1.5
	Total no. of e^-	21	21	21	21
	Co charge	1.9+	2.4+	1.6+	2.1+
	As charge	2.7–	2.9–	2.9–	3.1–
	O charge	2.2–	2.5–	1.7–	2.0–
	Average charges	$[La^{3+}O^{2.1-}][Co^{2.0+}As^{2.9-}]$			
LaNiAsO	Ni 3d t_2 (peak 1)	2.8	2.5	3.0	2.7
	Ni 3d e (peaks 2, 3)	5.6	5.0	5.2	4.7
	As 4p (peak 4)	6.9	6.5	7.3	7.0
	O 2p (peak 5)	5.9	6.4	5.7	6.1
	As 4s (peak 6)	0.8	1.6	0.7	1.5
	Total no. of e^-	22	22	22	22
	Ni charge	1.6+	2.5+	1.8+	2.6+
	As charge	2.7–	3.1–	3.0–	3.5–
	O charge	1.9–	2.4–	1.7–	2.1–
	Average charges	$[La^{3+}O^{2.0-}][Ni^{2.1+}As^{3.1-}]$			

5.3.6 Mixed-metal arsenide oxides LaFe$_{1-x}$$M'_x$AsO ($M'$ = Co, Ni)

Although the occurrence of M-to-As charge transfer has been confirmed from the As 3d XPS and K-edge XANES spectra described above, the presence of two dissimilar metals may entail additional charge transfer through metal-metal interactions (~2.8 Å) within square nets in

the [*M*As] layers, as suggested earlier.[175,190] The asymmetric lineshapes seen earlier in the Fe

and Co 2p spectra also seem to lend support for the delocalization of metal 3d electrons. To

acquire direct evidence for metal-metal charge transfer, the mixed-metal series LaFe$_{1-x}$$M'_x$AsO

(M' = Co, Ni) serves as a useful test system to examine. Interestingly, when their core-line

spectra were acquired (Figure A3-3 in Appendix 3), we observed no changes in the Co and Fe

2p$_{3/2}$ BEs, the Co 2p satellite intensity, or the As 3d$_{5/2}$ BE relative to the parent compounds.

Because next-nearest neighbour effects (to be discussed in detail in Chapter 8) imparted by the

partial substitution of M' for Fe atoms may be difficult to detect in XPS BE shifts, a different

approach is required.

Metal L- and K-edge XANES spectroscopy probes directly the occupation of 3d valence

states. The metal L-edge corresponds to a dipole-allowed transition of a 2p electron into

available empty 3d and possibly 4s conduction states ($\Delta l = \pm 1$). The Fe and Co L-edges for

various LaFe$_{1-x}$$M'_x$AsO members are split by spin-orbit coupling into L$_3$ (2p$_{3/2}$ $\rightarrow$ 3d) and L$_2$-

edges (2p$_{1/2}$ $\rightarrow$ 3d) (Figure 5-8a–b). In the Fe and Co K-edge spectra, the lowest-energy feature

is a pre-edge peak arising from a dipole-forbidden transition of a 1s electron into empty 3d

conduction states (mixed with 4p states) (Figure 5-8c–d).[178,203] (The higher-energy features

correspond to transitions of a 1s electron into empty metal 4p, As 4p, or O 2p states, or possibly

to MSR or EXAFS phenomena.) If metal-metal charge transfer were occurring, one would

expect to see differences in the intensities in the L-edge spectra and in the pre-edge in the K-edge

spectra, since both of these features are influenced by the occupation of metal 3d states. Because

metal substitution may cause some geometrical distortions, which might influence the K-edge

pre-edge feature in particular, we focus our attention only on the mixed-metal arsenide oxides at low doping levels.[7] The key observation is that the spectra for the M'-doped compounds show no changes relative to the parent LaMAsO compounds (Figure A3-4 in Appendix 3), indicating that metal-metal (M-to-M') charge transfer does not take place, or is too negligible to be detected because of the small differences in electronegativity and the low doping levels studied.

Figure 5-7 (a) Fe L-edge, (b) Co L-edge, (c) Fe K-edge, and (d) Co K-edge XANES spectra for mixed-metal arsenide oxides LaFe$_{1-x}$$M'$$_x$AsO (compared to the parent LaMAsO compounds). The L-edge spectra were measured in TEY mode and the K-edge spectra were measured in transmission mode. The spectra are offset for clarity.

5.4 Conclusions

This study has demonstrated some of the challenges in interpreting XPS and XANES spectra for the arsenide oxides LaMAsO (M = Fe, Co, Ni). Although the XPS spectra correctly reveal cationic character for the La and M atoms, and anionic character for the As and O atoms, further careful analysis is required to extract more detailed information. The La 3d and O 1s XPS spectra confirm significant ionic character implied by the formulation [La^{3+}O^{2-}]. The insensitivity of the O 1s BEs to substitution by M atoms indicates that any charge transfer within the conducting [MAs] layer has no effect on the insulating [LaO] layer. Changes in the M 2p and As 3d XPS spectra were more subtle, presenting greater difficulties in extracting individual atomic charges, primarily because of the strong covalent character within the [MAs] layer. On casual inspection, these XPS spectra suggest charges of M^{1+} and As^{1-}. However, analysis of the pre-edge feature in the As K-edge XANES spectra suggests that the true As charge is more negative than 1−. Moreover, shifts in the As 3d$_{5/2}$ BE do correlate with greater M-to-As charge transfer as the difference in electronegativity between these atoms is enhanced. An alternative approach involving fitting of the valence band XPS spectra to individual atomic states succeeds in recovering the formulation [LaO]$^{1+}$[MAs]$^{1-}$. Finally, the metal K- and L-edge spectra of the LaFe$_{1-x}M'_x$AsO series reveal that no significant metal-metal charge transfer takes place within these [MAs] layers.

A comparison of XPS and XANES spectra reveals profound differences that reflect the enhancement of covalent character on progressing from LaNiAsO to ZrCuSiAs. The [LaO] layer in LaNiAsO exhibits significant ionic character, as indicated by its O 1s BE which falls in the

range expected for normal oxides, whereas the [ZrSi] layer in ZrCuSiAs exhibits strongly covalent character, as indicated by its Si 2p BE which is nearly the same as in elemental Si and is consistent with the development of a polyanionic Si network. The [NiAs] layer in LaNiAsO and the [CuAs] layer in ZrCuSiAs are similar in nature, with As $3d_{5/2}$ BEs slightly lower than in elemental As, indicating the presence of anionic As atoms and highly covalent M–As bonds.

Chapter 6

Effects of rare-earth substitution in the arsenide oxides *RE*FeAsO (*RE* = Ce, Pr, Nd, Sm, Gd) and CeNiAsO by X-ray photoelectron and absorption spectroscopy*

6.1 Introduction

In Chapter 5, X-ray photoelectron spectroscopy (XPS) and X-ray absorption near-edge spectroscopy (XANES) were used to probe the electronic structure of several lanthanum transition-metal arsenide oxides La*M*AsO (*M* = Fe, Co, Ni). In the tetragonal ZrCuSiAs-type crystal structure of the arsenide oxides, which was previously discussed in Chapter 4, [LaO] and [*M*As] layers are stacked in an alternating fashion with the O and *M* atoms tetrahedrally coordinated by La and As atoms, respectively. The XPS and XANES study demonstrated that changing the [*M*As] layer modifies the degree of *M*-to-As charge transfer but has no electronic effect on the [LaO] layer. In this chapter, the effects of altering the [*RE*O] layer in the *RE*FeAsO (*RE* = Ce, Pr, Nd, Sm, Gd) series will be examined. High resolution core-line (*RE* 3d, Fe 2p, As 3d, and O 1s) and valence band XPS spectra will be analyzed. Supplementing this study will be an investigation of the nickel-containing compound CeNiAsO. The XPS (Ce 3d, Ni 2p, As 3d, O 1s) and XANES (Ce L$_3$-edge; Ni L- and M-edges) spectra for CeNiAsO were measured to allow a comparison to the previously studied compound LaNiAsO (Chapter 5).

6.2 Experimental

6.2.1 Synthesis and X-ray diffraction

All reagents, obtained from Alfa-Aesar, Cerac, or Hefa with purities generally better than 99.5%, were handled in an Ar-filled glove box. Binary arsenides REAs (RE = Ce, Pr, Nd, Sm, Gd) were prepared from stoichiometric reactions of elemental RE and As at 1050 °C for 2 days in evacuated fused silica tubes. Binary oxides CeO_2, RE_2O_3 (RE = Pr, Nd, Sm, Gd), Fe_2O_3, and NiO were dehydrated by heating at 900 °C for 2 days. The quaternary oxyarsenides REFeAsO and CeNiAsO were prepared from stoichiometric mixtures of the appropriate starting materials: CeFeAsO (from CeAs, CeO_2, FeAs, and Fe); PrFeAsO (from PrAs, Fe_2O_3, and Fe); NdFeAsO (from NdAs, Nd_2O_3, FeAs, and Fe_2As); SmFeAsO (from SmAs, Fe_2O_3, and Fe); GdFeAsO (from GdAs, Gd_2O_3, FeAs, and Fe); CeNiAsO (from CeAs and NiO). The mixtures were finely ground and loaded into alumina crucibles placed within fused-silica tubes, which were evacuated, sealed, and heated at 1250 °C for 3 days. The products were judged to be single-phase from their powder X-ray diffraction (XRD) patterns measured on an Inel powder diffractometer (Figure A4-1 in Appendix 4). Although the compound CeNiAsO has been reported, no structural information has been available.[204] With initial positions taken from the isotypic arsenide oxides, the crystal structure of CeNiAsO was refined with the full-profile Rietveld method with use of the program LHPM-Rietica.[25] The results are summarized in Table 6-1 and the fit to the powder XRD pattern is shown in Figure 6-1.

Table 6-1 Crystallographic data for CeNiAsO.

Rietveld refinement results

Formula	CeNiAsO
Formula mass (amu)	289.72
Space group	*P4/nmm* (No. 129)
a (Å)	4.0752(2)
c (Å)	8.1134(4)
V (Å^3)	134.74(1)
Z	2
ρ_{calcd} (g cm^{-3})	7.139
Radiation	Cu Kα_1, $\lambda = 1.54056$ Å
2θ range (deg.)	20.00–100.00
No. of data points	2759
No. of reflections	59
No. of variables	26
Residuals [a]	$R_B = 0.027$; $R_p = 0.039$; $R_{wp} = 0.054$
GOF	3.89

Positional and displacement parameters

Ce at 2c (1/4, 1/4, z)

Z	0.1481(4)
B_{iso} (Å^2)	0.28(6)

Ni at 2b (3/4, 1/4, 1/2)

B_{iso} (Å^2)	1.2(2)

As at 2c (1/4, 1/4, z)

Z	0.6479(8)
B_{iso} (Å^2)	1.4(1)
O at $2a$ (3/4, 1/4, 0)	
B_{iso} (Å^2)	3.2(9)

Interatomic distances (Å)

Ce–O (×4)	2.365(2)
Ce–As (×4)	3.323(5)
Ce–Ni (×4)	3.508(3)
Ni–As (×4)	2.365(3)
Ni–Ni (×4)	2.8816(1)

^{a} $R_B = \Sigma|I_o - I_c|/\Sigma I_o$; $R_p = \Sigma|y_o - y_c|/\Sigma y_o$; $R_{wp} = \left[\Sigma\left[w(y_o - y_c)\right]/\Sigma w y_o^2\right]^{1/2}$.

Figure 6-1 Rietveld refinement results for CeNiAsO. The observed profile is indicated by circles and the calculated profile by the solid line. Bragg peak positions are located by the vertical tick marks. The difference plot is shown at the bottom.

6.2.2 XPS analysis

XPS spectra for all compounds prepared were measured on a Kratos 165 spectrometer equipped with a monochromatic Al Kα X-ray source (14 mA, 15 kV) and a hybrid lens with a spot size of $700 \times 400 \ \mu m^2$. The samples are air-stable but to minimize exposure to air, they were handled in an Ar-filled glove box where they were finely ground, pressed into In foil, mounted on a Cu sample holder, and placed in a sealed container for transfer to the analysis chamber of the spectrometer. The pressure inside the XPS instrument was maintained between 10^{-8} and 10^{-9} Pa. Samples were sputter-cleaned with an Ar^+ ion beam (4 kV, 10 mA) until core-line peaks associated with surface oxides were no longer observed in the XPS spectra. A small shoulder in the As 3d XPS spectra indicated that a slight reduction of As occurred; however, the binding energies (BE) in these and other spectra were, within standard uncertainties, the same before and after the sputtering procedure (Table A4-1 in Appendix 4).

Survey spectra, collected with a BE range of 0–1100 eV, a pass energy of 160 eV, a step size of 0.7 eV, and a sweep time of 180 s, confirmed the expected chemical compositions (*RE*:*M*:As:O = 1:1:1:1) for the arsenide oxides. High-resolution core-line spectra were collected with an energy envelope of appropriate range (Ce 3d, 60 eV; *M* 2p, 50 eV; As 3d and O 1s, 20 eV), a pass energy of 20 eV, a step size of 0.05 eV, and a sweep time of 180 s. Although no charge correction was required because the samples are good conductors, the spectra were calibrated to the C 1s line at 284.8 eV arising from adventitious carbon. All spectra were analyzed with use of the CasaXPS software package.[128] The background arising from energy loss was removed by applying a Shirley-type function and the peaks were fitted to pseudo-Voigt (70% Gaussian and 30% Lorentzian) line profiles to take into account spectrometer and lifetime broadening effects. Table 6-2 lists all BE values expressed to two decimal places, with

uncertainties estimated at better than ±0.10 eV, as established by collecting multiple spectra (Table A4-1 in Appendix 4).

Table 6-2 Core-line BEs (eV) for *RE*FeAsO (*RE* = La–Nd, Sm, Gd) and *RE*NiAsO (*RE* = La, Ce).

Sample	*RE* 3d$_{5/2}$	Fe or Ni 2p$_{3/2}$ [a]	As 3d$_{5/2}$	O 1s
LaFeAsO [b]	834.88	707.11	41.18	529.94
CeFeAsO	881.76	707.16	41.14	530.04
PrFeAsO	not measured	707.09	41.14	530.09
NdFeAsO	not measured	707.16	41.10	530.13
SmFeAsO	not measured	707.10	41.13	530.17
GdFeAsO	not measured	707.08	41.13	530.31
LaNiAsO [b]	834.92	not measured	41.43	529.96
CeNiAsO	881.87	853.18	41.35	530.02

[a] For comparison, the 2p$_{3/2}$ BEs are 707.0 eV for Fe metal[6] and 852.7 eV for Ni metal.

[b] Values for LaFeAsO and LaNiAsO are taken from Table 5-1 of Chapter 5.

6.2.3 XANES analysis

Ni M-edge XANES spectra for CeNiAsO were collected on the variable line spacing plane grating monochromator (PGM) beamline at the Canadian Light Source (CLS) in Saskatoon, Saskatchewan. Finely ground samples were mounted on carbon tape and inserted into the vacuum chamber via a load lock. Spectra were measured from ~20 eV below to ~65 eV above the edge, with a step size of 0.1 eV through the edge. Spectra were collected in both total electron yield (TEY) and X-ray fluorescence yield (FLY) modes; however, because the Ni M-edge occurs at low energy and surface oxides become more apparent in the TEY spectra, only

the FLY spectra are presented. The spectra were calibrated to Ni metal, with the maximum in the first derivative of its M_3-edge set to 66.2 eV.[147]

RE L_3-edge XANES spectra for REFeAsO (RE = La–Nd, Gd) and CeNiAsO were collected on the bending magnet beamline (20BM) accessed through the Pacific Northwest Consortium / X-ray Operations and Research Collaborative Access Team (PNC/XOR-CAT), Sector 20 of the Advanced Photon Source (APS) at Argonne National Laboratory. Finely ground samples were sandwiched between Kapton tape and positioned at 45° to the X-ray beam. A silicon (111) double crystal monochromator provided a monochromatic photon flux of ~10^{11} photons/sec with a resolution of 1.4 eV at 10 keV and a beam size of approximately 1 × 4.5 mm. Spectra were measured in transmission mode with an ionization detector (filled with a 50:50 mixture of He and N_2 in the ionization chamber) and in fluorescence mode with a Canberra 13-element fluorescence detector. The step size was 0.1 eV through the absorption edge. Metal standards were placed behind the sample and measured concurrently in transmission mode. The RE L_3-edge spectra were calibrated to Cr (for RE = La–Nd) and Fe metal (for RE = Gd), with the maxima in the first derivatives of their K-edges set to 5989 and 7112 eV, respectively.[147] All XANES spectra were analyzed with use of the Athena software program.[147]

6.3 Results and discussion

6.3.1 [REO] layer

The general expectation is that the RE atoms within the [REO] layer of the arsenide oxides REMAsO are trivalent; however, there is a possibility that Ce can adopt other valence states. To this end, the Ce 3d XPS and L_3-edge XANES spectra for CeFeAsO and CeNiAsO

were collected (Figure 6-2). In general, the XPS BE shifts of rare-earth-containing compounds are relatively insensitive to changes in bonding character because of the increased nuclear screening provided by the 4f electrons.[119] However, the Ce 3d XPS lineshapes in CeFeAsO and CeNiAsO do resemble those in other trivalent cerium compounds (e.g. CeF_3, $CeFe_4P_{12}$, $CeFe_4Sb_{12}$), where characteristic satellite peaks are observed on the higher BE (by ~4 eV) side of each of the two core-line peaks representing the $3d_{5/2}$ and $3d_{3/2}$ spin-orbit-coupled final states (Figure 6-2a).[119,120] Relative to the core-line peaks, the intensity of these satellite peaks, which have been proposed to originate from various shake-up processes discussed in Chapter 5, is proportional to the degree of orbital overlap between the *RE* atom and its surrounding ligands (here, As and O atoms).[205-207] The satellite peaks have the same intensity in CeFeAsO and CeNiAsO, implying that changing the metal has no effect on the [CeO] layer, but they are more intense than in LaFeAsO and LaNiAsO (section 5.3.3 of Chapter 5), a reflection of the greater orbital overlap provided by the $4f^l$ state in trivalent cerium. In the Ce L_3-edge XANES spectra for CeFeAsO and CeNiAsO (Figure 6-2b), the occurrence of a single white line peak (labeled A), assigned as the dipole-allowed transition of a 2p electron into 6s or 5d states ($\Delta l = \pm 1$), indicates that only one valence state for Ce is present.[208,209] A second feature (labeled B) is interpreted as a continuum resonance associated with the shell of ligand atoms surrounding the absorbing atom.[210] The *RE* L_3-edge XANES spectra for other *RE*FeAsO members (*RE* = La, Pr, Nd, Gd) exhibit similar features (Figure A4-2 in Appendix 4). The confirmation of trivalent *RE* atoms has also been supported by previous *RE* M-edge XANES measurements on *RE*FeAsO (*RE* = La, Ce, Sm, Gd).[179]

Figure 6-2 (a) Ce 3d XPS and (b) Ce L$_3$-edge XANES spectra for CeFeAsO and CeNiAsO. The spectra are offset for clarity. The vertical dashed lines mark the Ce 3d$_{5/2}$ BE in (a) and the absorption edge energy in (b).

Representative O 1s XPS spectra are selected for comparison (Figure 6-3); spectra for the remaining compounds are also available (Figure A4-3 in Appendix 4). The O 1s BE values for these arsenide oxides range from 529.9 to 530.3 eV (Table 6-2). According to a classification scheme developed by Barr for correlating O 1s BEs to the degree of ionic character in metal-oxygen bonds (semicovalent oxides, 530.5–533.0 eV; normal ionic oxides, 529.6–530.4 eV; very ionic oxides, 528.0–529.5 eV), the arsenide oxides fall in the category of normal ionic oxides.[196,197]   In contrast, binary rare-earth oxides tend to have BEs associated with very ionic bonding.[196] Thus, the *RE*–O bond becomes less ionic as we progress from the binary rare-earth oxides to the rare-earth arsenide oxides. Interestingly, the O 1s BE is virtually the same for differently substituted transition metals (cf. 530.04 eV in CeFeAsO vs. 530.02 eV in CeNiAsO) (Figure 6-3a), consistent with the assertion above that the changes in the [*M*As] layer have little

effect on the [*RE*O] layer. The O 1s BE increases perceptibly upon substitution with a smaller *RE* metal (cf. 529.94 eV in LaFeAsO vs. 530.31 eV in GdFeAsO) (Figure 6-3b). One possible explanation might be that these BE shifts reflect changes in the degree of *RE*-to-O charge transfer, analogous to trends previously observed in the P $2p_{3/2}$ BE of metal phosphides as the electronegativity difference between component atoms is modified.[6] However, this explanation can be ruled out because the Allred-Rochow electronegativity difference between *RE* and O changes by less than 0.05 units upon substitution of La with Gd.[211] If ground state effects are assumed to be responsible for this trend, a more careful analysis requires consideration of the charge potential model, where the BE for an electron in an atom (E_i) is shifted relative to a reference energy (E_i^o) because of two factors:[183]

$$\Delta E_i = E_i - E_i^o = k\Delta q_i + \Delta \sum_{j \neq i} \frac{q_j}{r_{ij}} \qquad (6\text{-}1)$$

The first term describes intraatomic effects, which scale with changes in charge on a given atom i, whereas the second term (a Madelung potential) describes interatomic effects, which scale with changes in the coordination environment defined by the surrounding atoms j with charges q_{ij} at some distance r_{ij}. Since intraatomic effects are minimal (given the similar electronegativities of *RE* atoms), we attribute the BE shifts to interatomic effects in which changes in r_{ij} are significant. As expected, when the *RE* component becomes smaller (from La to Gd) and the *RE*–O distances decrease, the O 1s BE shifts to higher energy (Figure 6-4). Similar arguments have also been applied to account for the O 1s BE shifts in binary rare-earth oxides.[181]
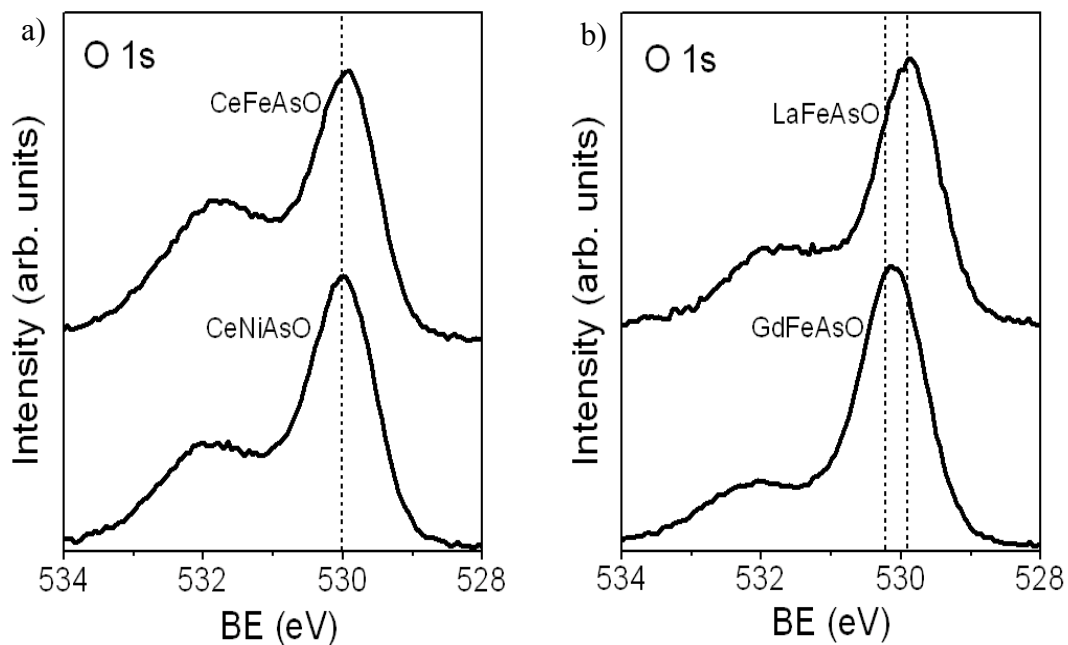
Figure 6-3 O 1s XPS spectra for (a) CeFeAsO vs. CeNiAsO and (b) LaFeAsO vs. GdFeAsO. The spectra are offset for clarity. The vertical dashed lines mark the O 1s BE. The second peak at higher BE is attributed to a surface contaminant.
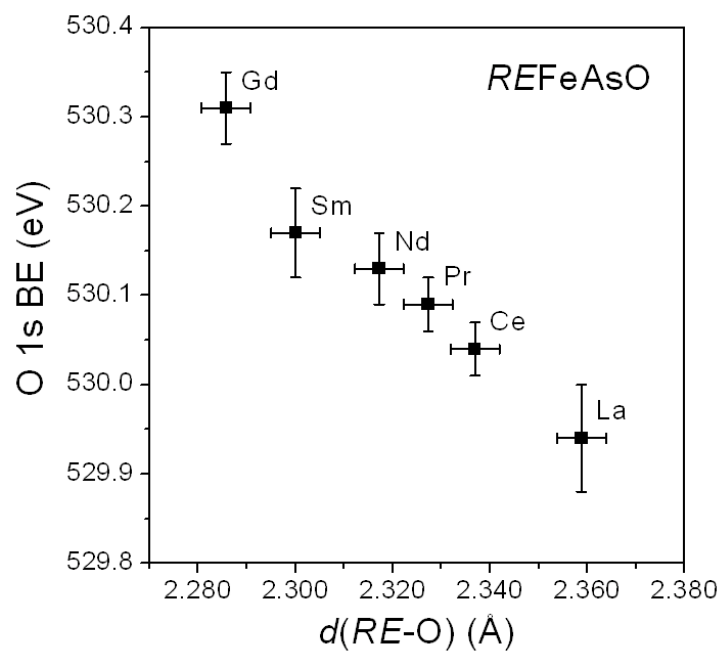
Figure 6-4 Plot of O 1s BE vs. *RE*–O distance in *RE*FeAsO (*RE* = La–Nd, Sm, Gd).

6.3.2 [*M*As] layer

It is generally accepted that electronic conduction in the arsenide oxides *REM*AsO takes place primarily within the [*M*As] layer. Evidence for this electronic delocalization can be sought through analysis of the *M* 2p XPS spectra (Figure A4-3 in Appendix 4). The most prominent feature, as seen in the representative spectra for CeFeAsO (Figure 6-5a) and CeNiAsO (Figure 6-5b), is the asymmetric lineshape exhibited by each of the $2p_{3/2}$ and $2p_{1/2}$ peaks, which are skewed towards higher BE. This asymmetry, attributed to the Doniach-Šunjić process described in Chapter 3, is indicative of the electronic delocalization found in metallic systems.[130] The linehape arises when valence electrons, interacting with the core-hole, are scattered into the continuum of conduction states above the Fermi edge. The electronic delocalization also causes the core electrons to experience significant nuclear screening such that the *M* 2p BEs are little shifted from those in the elemental metals. The shift in Fe 2p BE is barely discernible (cf. 707.1–707.2 eV in all *RE*FeAsO members vs. 707.0 eV in Fe metal)[6] whereas the shift in Ni 2p BE is somewhat more pronounced (cf. 853.2 eV in CeNiAsO vs. 852.7 eV in Ni metal, which will be discussed in Chapter 7). In both cases, the slightly higher BE (relative to the elemental metal) is consistent with the presence of cationic *M* atoms, but in a delocalized system such as this, the BE is not necessarily a reliable indicator.[6] Note, however, that a satellite peak is found on the higher BE side of the Ni $2p_{3/2}$ core-line peak in the spectrum of CeNiAsO (Figure 6-5b). The satellite feature is similar to that observed in the Co 2p XPS spectra (section 5.3.2 of Chapter 5), which has been proposed to arise from either the two-core-hole or plasmon model.[212,213] Support for an analogous mechanism occurring in the Ni-containing samples comes from REELS data on Ni metal, which reveal several peaks located at a similar separation from the main elastic line as the satellite peaks from the core-line peak in the Ni $2p_{3/2}$ XPS
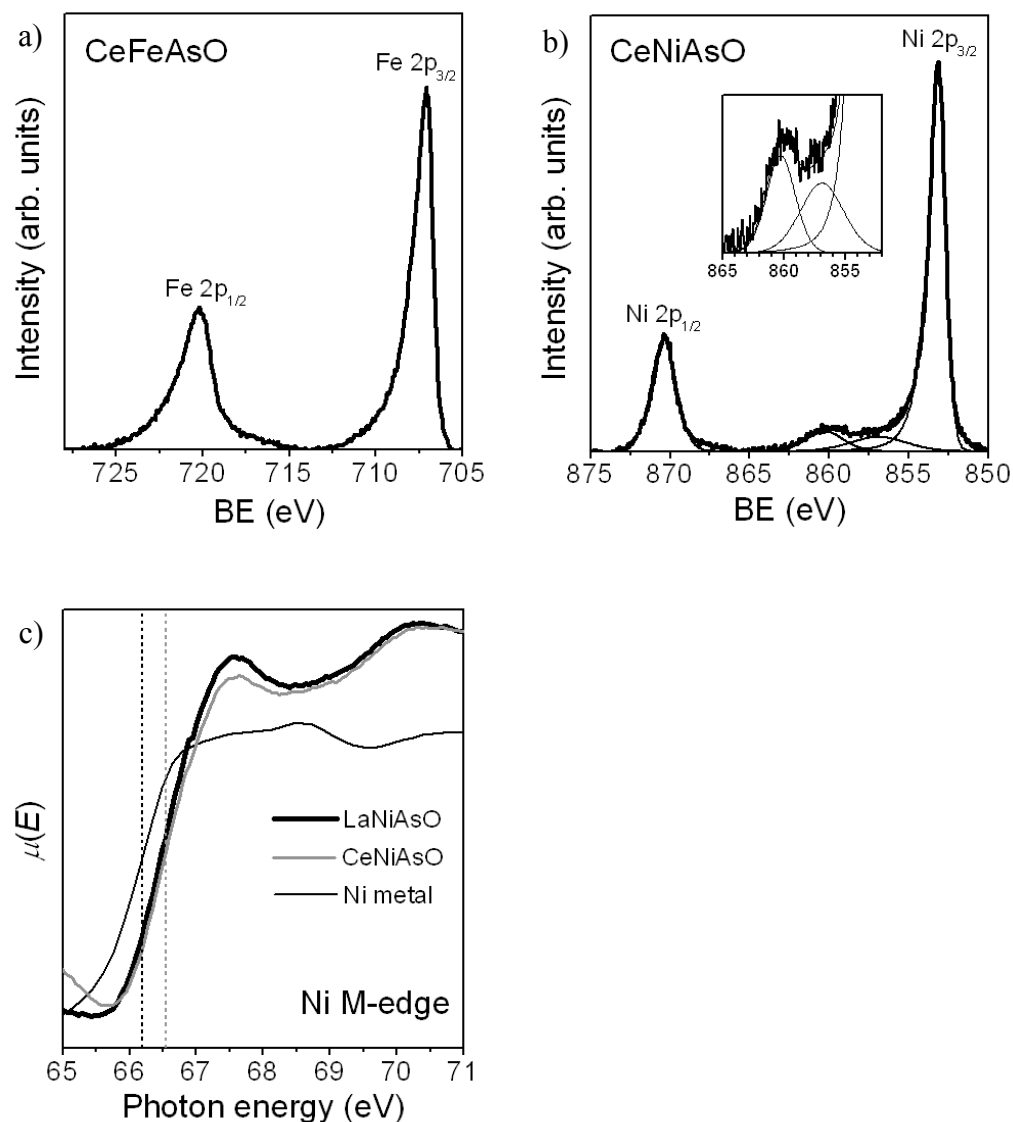
Figure 6-5 (a) Fe 2p XPS spectrum for CeFeAsO and (b) Ni 2p XPS spectrum for CeNiAsO. The inset in (b) highlights the satellite feature. (c) Ni M-edge XANES spectra (FLY mode) for LaNiAsO, CeNiAsO, and Ni metal, with the absorption edges marked by vertical dashed lines.

spectrum.[213]   Because photoionization does not occur in low-energy loss processes, as in the

REELS experiment, the two-core-hole explanation is unlikely. However, definitive confirmation

of the plasmon loss mechanism will require further REELS experiments on CeNiAsO.

Regardless, the satellite feature can be used to extract information about the Ni charge, with the

satellite intensity being proportional to the number of valence states.[120] If a plasmon loss model is assumed, the satellite peak can be fitted to two components representing bulk plasmon (higher energy) and surface plasmon (lower energy) processes. The normalized satellite intensity ($I_{satellite}/I_{core-line}$) is lower in CeNiAsO (0.27) than in elemental Ni (0.38), indicating the presence of fewer valence states and thus positively charged Ni atoms. Further evidence for the cationic nature of the Ni atoms is provided by the higher absorption edge energies in the Ni M-edge XANES spectra for LaNiAsO and CeNiAsO (66.5 eV), compared to that for Ni metal (66.2 eV) (Figure 6-5c). Spin-orbit splitting into the M_3-edge ($3p_{3/2} \rightarrow 3d$) and M_2-edge ($3p_{1/2} \rightarrow 3d$) is evident in Ni metal, but not in LaNiAsO and CeNiAsO, likely because of peak broadening effects. The higher energy peak at 70.3 eV is attributed to a surface oxide. The invariance of the Ni M-edge energy for LaNiAsO and CeNiAsO reaffirms the independence of the separate [*RE*O] and [*M*As] layers.

The As 3d XPS spectra for all members of the *RE*FeAsO series are similar (Figure A4-3 in Appendix 4). The spectra were fitted to two peaks corresponding to the $3d_{5/2}$ and $3d_{3/2}$ spin-orbit-coupled final states with a FWHM of 1.2–1.3 eV in an intensity ratio of 3:2. There is little difference in $3d_{5/2}$ BE values (41.1–41.2 eV), as expected because *RE* substitution has little effect on the [*M*As] layer. These BE values are lower than in elemental As (41.7(2) eV), consistent with the presence of anionic As atoms, but the small shift reflects considerable covalency in the *M*–As bonds.[101,121] Substitution of the *M* atoms, which are directly bonded to the As atoms, does lead to observable shifts in the As $3d_{5/2}$ BEs. Thus, for example, the As $3d_{5/2}$ BE is further lowered in CeFeAsO (41.1 eV) than in CeNiAsO (41.4 eV) relative to elemental As (Figure 6-6); the greater electronegativity difference between Fe and As leads to a more pronounced metal-to-As charge transfer and more negatively charged As atoms in CeFeAsO.
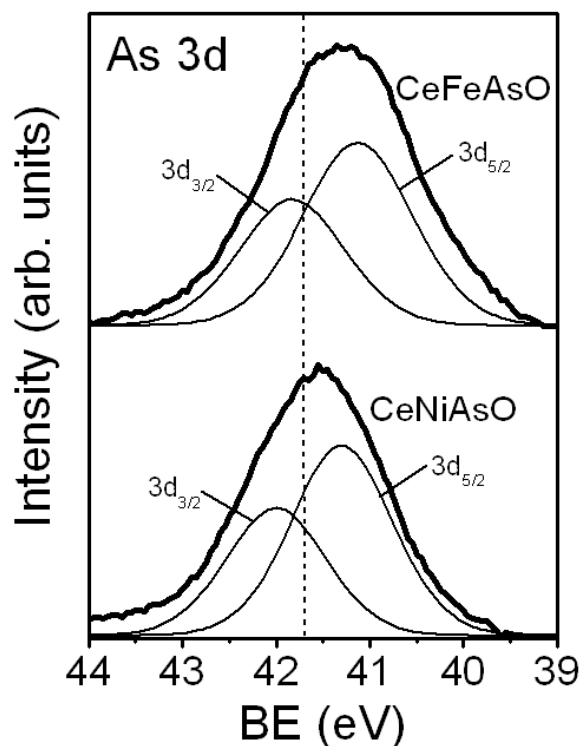
Figure 6-6 As 3d XPS spectra for CeFeAsO and CeNiAsO, fitted with $3d_{5/2}$ and $3d_{3/2}$ component peaks. The vertical dashed line at 41.7 eV marks the $3d_{5/2}$ BE for elemental As.

6.3.3 Valence band spectrum of CeNiAsO

The XPS and XANES spectra presented above confirm the expectations of largely ionic character in the [*RE*O] layer and largely covalent character in the [*M*As] layer. The discrepancy with the idealized formulation $[RE^{3+}O^{2-}][M^{2+}As^{3-}]$ arises because the charge transfer within the [*M*As] layer is not as extreme as implied by these charges. Indeed, if such BE correlations are taken at face value, the As $3d_{5/2}$ BE in these arsenide oxides corresponds to a charge closer to 1– than 3–.[101] One way to recover the chemically valuable concept of valence state is to interpret the experimental valence band spectra through an electron population analysis, as we have applied to the La*M*AsO (*M* = Fe, Co, Ni) series in Chapter 5. The procedure for this is explained in section 5.3.5 in Chapter 5 and is used to fit the spectrum of CeNiAsO.

The XPS valence band spectrum for CeNiAsO is shown in Figure 6-7a. By comparison to calculated band structures, in particular that of LaNiAsO (Figure 4-8c in section 4.3.4 of Chapter 4), the spectrum can be fitted to Ni 3d states at low BE, As 4p / O 2p states at intermediate BE, and As 4s states at high BE, with substantial mixing of the first two sets. In agreement with predictions that the Ce 4f states should lie near the Fermi edge, the valence band spectrum of CeNiAsO exhibits higher intensity at 1–2 eV when it is overlapped with that of LaNiAsO (Figure 6-7b).[214] These Ce 4f states are represented by peak 1. The Ni 3d states are split by a tetrahedral crystal field into t_2 ($3d_{5/2}$ as peak 2) and e sets ($3d_{5/2}$ and $3d_{3/2}$ as peaks 3 and 4, in a fixed intensity ratio of 3:2 and with somewhat greater FWHM because of metal-metal bonding interactions involving the $3d_{x^2-y^2}$ orbitals), with asymmetric lineshapes to higher BE to account for Doniach-Šunjić broadening.[134,145] The As 4p (peak 5) and O 2p (peak 6) states were each modeled as single peaks only because of the small energy difference between the $np_{3/2}$ and $np_{1/2}$ spin-orbit-split final states. The O 2p peak appears smaller because of its much lower photoionization cross-section.[94,95] The As 4s states (peak 7) account for the isolated region at high BE. The relative intensity and peak positions of these Ni, As, and O states in CeNiAsO were constrained to have similar values as in LaNiAsO (section 5.3.5 of Chapter 5). The O 2s states are located well below the Fermi edge and are assumed to be fully occupied.[139,140] The results of this fitting, applied to two separate samples and using two different sets of photoelectron cross-sections, are summarized in Table 6-3. The charge distribution obtained from this analysis, $[Ce^{2.9+}O^{2.0-}][Ni^{2.1+}As^{3.0-}]$, agrees well with the formal charge assignment based on the assumption of full electron transfer.

Table 6-3 Electron population (e⁻) of valence states and charge distribution in CeNiAsO.

Atomic photoelectron cross-section, σ	Sample 1		Sample 2	
	Ref. [95] [a]	Ref. [94] [b]	Ref. [95] [a]	Ref. [94] [b]
Electron population				
Ce 4f (peak 1)	1.0	0.8	1.4	1.2
Ni 3d t_2 (peak 2)	3.4	3.1	3.5	3.2
Ni 3d e (peaks 3, 4)	4.9	4.5	4.8	4.3
As 4p (peak 5)	7.1	6.8	6.4	6.0
O 2p (peak 6)	5.7	6.2	5.8	6.2
As 4s (peak 7)	0.8	1.6	1.1	2.2
Total no. of e⁻	23	23	23	23
Charge				
Ce	3.0+	3.2+	2.6+	2.8+
Ni	1.7+	2.4+	1.7+	2.5+
As	2.9–	3.4–	2.5–	3.2–
O	1.7–	2.2–	1.8–	2.2–
Average charges	$[Ce^{2.9+}O^{2.0-}][Ni^{2.1+}As^{3.0-}]$			

[a] Cross-section values, expressed relative to the C 1s cross-section of 13,600 barns, are: 0.06945 (Ce 4f), 0.19895 (Ni 3d), 0.06045 (As 4p), 0.1357 (As 4s), and 0.00965 (O 2p).
[b] Cross-section values, in units of megabarns, are: 0.0022 (Ce 4f), 0.0059 (Ni 3d), 0.0017 (As 4p), 0.0018 (As 4s), and 0.00024 (O 2p).
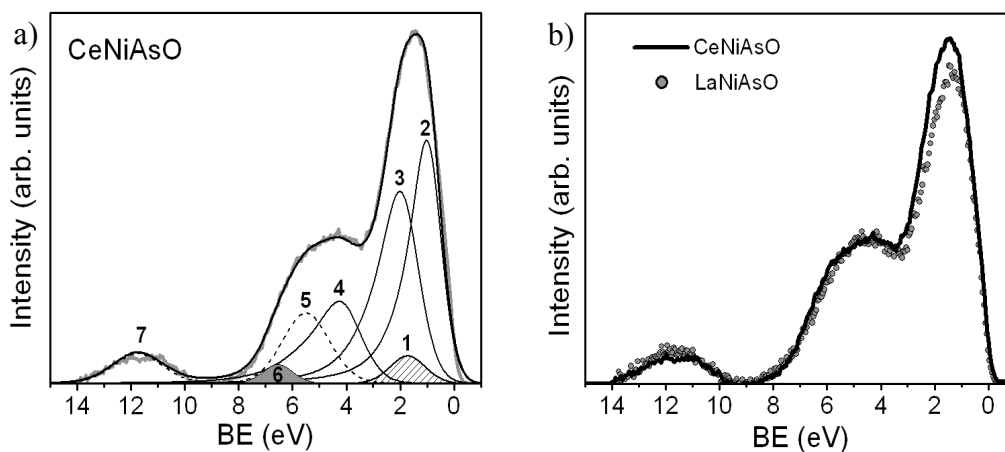
Figure 6-7 (a) XPS valence band spectrum for CeNiAsO, fitted to component peaks as assigned in Table 6-3. (b) Valence band spectra for LaNiAsO and CeNiAsO, overlapped to highlight the location of Ce 4f states.

6.4 Conclusions

A comparison of the XPS and XANES spectra of the *RE*FeAsO (*RE* = La–Nd, Sm, Gd) and *RE*NiAsO (*RE* = La, Ce) series reveals minimal changes in the [*M*As] layer but substantial ones in the [*RE*O] layer as the *RE* component is varied. However, the shifts in the O 1s BEs do not arise from intraatomic effects involving a change in charge, but rather from interatomic effects reflecting the change in the Madelung potential as the *RE*–O distances are modified. The As 3d BEs in the *RE*FeAsO series and of the Ni M-edge energy in the *RE*NiAsO series are insensitive to *RE* substitution, supporting the oft-made assertion that the [*RE*O] and [*M*As] layers can be treated independently. Although the As and O atoms are both found to be anionic, the shifts in the As 3d BEs are much less pronounced that those in the O 1s BEs, an indication of strong covalent character in the [*M*As] layer and strong ionic character in the [*RE*O] layer. The asymmetric lineshapes in the *M* 2p XPS spectra provide evidence for electronic delocalization within the [*M*As] layer. The presence of trivalent cerium is confirmed from the Ce 3d XPS and

L_3-edge XANES spectra of CeFeAsO and CeNiAsO. Furthermore, a Ce 4f component can be detected in the valence band spectrum of CeNiAsO.

Chapter 7

X-ray photoelectron and absorption spectroscopy of metal-rich phosphides M_2P and M_3P (M = Cr–Ni)[*]

7.1 Introduction

Binary metal-rich phosphides of the first-row transition metals form an important class of compounds long studied for their electrical and magnetic properties. For M = Cr–Ni, the M_2P phases adopt three closely related structures: orthorhombic Cr_2P-type (M = Cr),[215] hexagonal Fe_2P-type (M = Fe, Mn, Ni),[18,216] and orthorhombic Co_2P-type (M = Co).[217] A convenient way to relate these structures is to identify the common building blocks as M_6 trigonal prisms centred by P atoms; these prisms then form confacial columns extending along the short axis of the unit cell (Figures 7-1a-c). The Cr_2P-type structure is essentially a distorted variant of the Fe_2P-type structure, where the trigonal prisms share all three lateral edges to generate a hexagonal framework outlining channels that contain additional isolated columns. In the Co_2P-type structure, the trigonal prisms share two lateral edges to form corrugated slabs that stack along the c direction. Co_2P also has a high-temperature modification (Fe_2P-type)[218] and Fe_2P has a high-pressure modification (Co_2P-type).[219] The M_3P phases adopt the tetragonal Ni_3P-type structure for M = Cr, Mn, Fe, Ni.[5,18,220] Co_3P was initially believed to be nonexistent,[5] but has subsequently found to be metastable, also adopting the Ni_3P-type structure.[221] Although

considerably more complicated, this structure can also be described in terms of P-centred trigonal prisms but in this case grouped in tetrameric clusters in a densely packed arrangement (Figure 7-1d). Common to all these M_2P and M_3P structures, the trigonal prisms are capped on their quadrilateral faces by M atoms from neighbouring prisms, so that the coordination environment around each P atom consists of nine surrounding M atoms at distances of 2.2–2.5 Å.[5,18,216,217,220] On the other hand, the coordination environments around the M atoms are substantially different (Figure 7-2). In M_2P, one M site is surrounded by four P atoms in a tetrahedral geometry, and another by five P atoms in a square pyramidal geometry. In M_3P, there are three distinct M sites, each surrounded in a tetrahedral geometry but with neighbouring M atoms successively replacing P atoms. Although not depicted in Figure 7-1, strong metal-metal bonding interactions (~2.5 Å and longer) pervade these structures, consistent with the metal-rich compositions.

Despite the numerous applications of these metal-rich phosphides, detailed knowledge about their electronic structure has remained elusive. In earlier theoretical and magnetic studies on Fe$_2$P, Fe$_3$P, and Co$_2$P, backbonding was suggested to take place from the P to M atoms, to the extent that the P atoms become positively charged.[54,57,59] However, this proposal is contradicted by the observation of P 2p binding energies (BE) in Fe$_2$P, Co$_2$P, and Ni$_2$P that are lower than those for elemental phosphorus.[115,222,223] Because it is presumed that the catalytic activity of M_2P materials will depend on the occupancy of metal 3d states and the degree of P backbonding (which influences the ability of N- and S-containing molecules to adsorb on the (001) surface), managing the process to provide maximum efficacy will require a firmer understanding of the electronic structure and bonding of the system.[73] X-ray photoelectron spectroscopy (XPS) and X-ray absorption near-edge spectroscopy (XANES) are powerful techniques for directly probing

the electronic structure of solids, but their application to highly covalent systems has been hampered by difficulties in interpreting the small shifts in binding or absorption energies. Recently, however, we have demonstrated that trends in the energy shifts in transition-metal monophosphides MP[6] (and their mixed-metal, $M_{1-x}M'_xP$,[7] or mixed-pnicogen variants, $MAs_{1-y}P_y$[8]) can be related to ground-state effects involving nearest and next-nearest neighbour interactions.
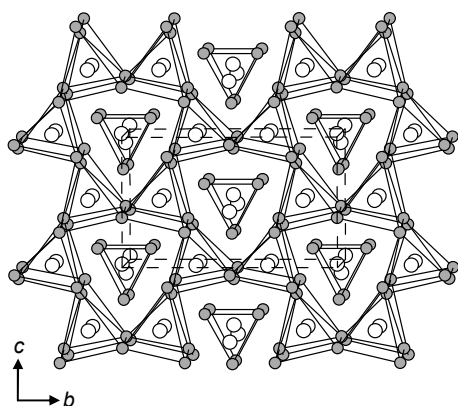
a) Cr_2P (*Imm2*)   b) M_2P (M = Mn, Fe, Ni) (*P-62m*)
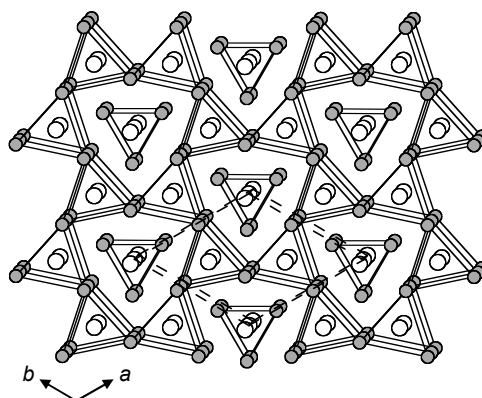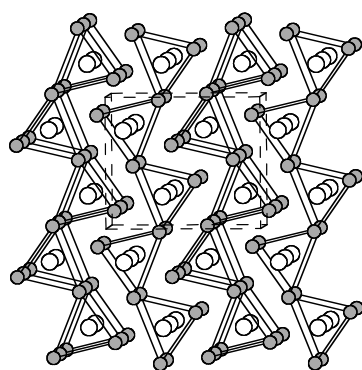
c) α-Co_2P (*Pnma*)   d) M_3P (M = Cr–Ni) (*I-4*)
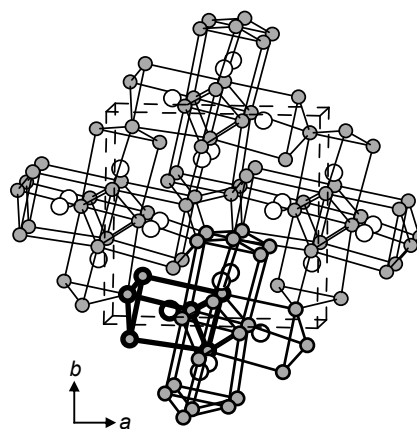
Figure 7-1 Structures of metal-rich phosphides M_2P and M_3P (M = Cr–Ni) in terms of P-centred M_6 trigonal prisms. The small shaded circles are M atoms and the large open circles are P atoms. The trigonal prisms are oriented with their threefold axes perpendicular to the page in M_2P (a–c), but parallel in M_3P (d), where one is highlighted with bold lines.

a) M_2P
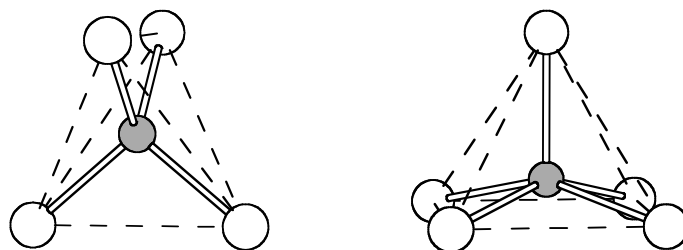
b) M_3P
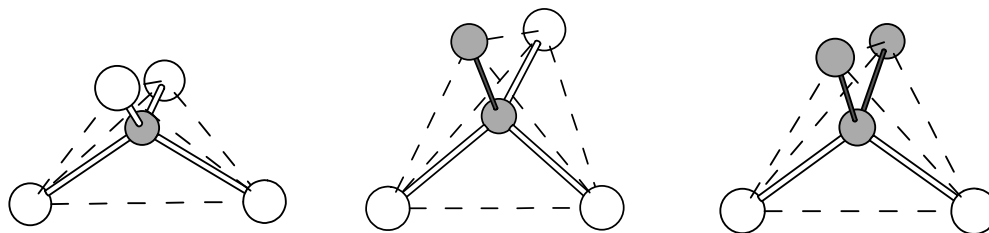
Figure 7-2 Coordination environments around M atoms in (a) M_2P and (b) M_3P, where M = Cr–Ni. The small shaded circles are M atoms and the large open circles are P atoms.

As an extension of our work on the monophosphides MP, we report herein high-resolution XPS and soft X-ray XANES measurements on the metal-rich phosphides M_2P and M_3P (M = Cr–Ni) with state-of-the-art instrumentation. The superior resolution achieved for these spectra enables clear trends to be discerned within these two series as M is varied, as well as within the progression MP, M_2P, and M_3P.

7.2 Experimental section

7.2.1 Synthesis

Starting materials were powders of the transition metals (Cr, 99.95%, Alfa-Aesar; Mn, 99.95%, Alfa-Aesar; Fe, 99.9%, Cerac; Co, 99.8%, Cerac; Ni, 99.9%, Cerac) and red phosphorus (99.995%, Cerac). Samples of M_2P (M = Cr–Ni) and M_3P (M = Cr, Mn, Fe, Ni) were prepared by combining M and P in stoichiometric proportions in evacuated fused-silica tubes, which were

heated to 1323 K over 48 h, kept at that temperature for 5 d, and quenched in water. In the case of Ni_2P and Ni_3P, the reactants were placed within an inner alumina crucible (to prevent deleterious reaction with the silica tube) and the tubes were heated for a longer period of 8 d (to ensure complete reaction). The products were confirmed to be single phases, according to their powder X-ray diffraction patterns (obtained on an Inel powder diffractometer equipped with a CPS 120 detector), in good agreement with those calculated from literature crystallographic data. All samples were isolated and stored in a glove box under argon. Co_3P could not be successfully synthesized using this procedure.

7.2.2 XPS analysis

Measurements were performed on a Kratos AXIS 165 spectrometer equipped with a monochromatic Al Kα X-ray source (14 mA, 15 kV) and a hybrid lens with a spot size of 700 × 400 μm². Samples were finely ground in a glove box, pressed into In foil, and mounted on a Cu sample holder. To minimize exposure to air, the sample holder was transferred within a sealed container to the analysis chamber of the XPS instrument, where the pressure was maintained at 10^{-7} to 10^{-9} Pa. The samples were sputter-cleaned with an Ar^+ ion beam (4 kV, 10 mA), to remove any surface oxides or phosphates, for different times depending on the degree of oxidation. This procedure resulted in a slight reduction of phosphorus as manifested by a small shoulder in the P 2p XPS spectra after sputtering, whereas no reduction was evident in the *M* 2p spectra. This sputtering causes no significant change, within standard uncertainties, in the P 2p BEs. Only a small amount of phosphate and unreacted phosphorus was visible in the high-resolution P 2p XPS spectra.

Survey spectra were collected with a BE range of 0–1100 eV, a pass energy of 160 eV, a step size of 0.7 eV, and a sweep time of 180 s. The expected chemical compositions of all samples were confirmed from these spectra. High-resolution spectra were collected with an energy envelope of 20 eV (P 2p peak) or 50 eV (M 2p$_{3/2}$ peak), a pass energy of 20 eV, a step size of 0.05 eV, and a sweep time of 180 s. No charge correction was required because these samples are good conductors. All high-resolution spectra were calibrated against the C 1s line at 284.8 eV arising from adventitious C. The CasaXPS software package was used to analyze the high-resolution spectra.[128] The background arising from energy loss was removed through a Shirley-type function and the peaks were fitted with a pseudo-Voigt (70% Gaussian, 30% Lorentzian; M 2p$_{3/2}$ peak) line profile. Multiple spectra were collected for each sample to yield a statistical average of the BE, with uncertainties better than ±0.1 eV (Table A5-1 in Appendix 5).

7.2.3 XANES analysis

Measurements were performed at the Canadian Light Source (CLS) in Saskatoon, Saskatchewan. Phosphorus K-edge and metal L-edge XANES spectra were collected on the spherical grating monochromator (SGM) undulator beamline (11-1D.1), and Ni M-edge XANES spectra were collected on the variable line spacing plane grating monochromator (VLS PGM) beamline (111D-2). Ground samples were mounted on carbon tape and loaded into the vacuum chamber via a load lock. Both total electron yield and X-ray fluorescence yield spectra were collected from ~20 eV below to ~65 eV above the edge (for P K-edge and metal L-edges) or from ~15 eV below to ~30 eV above the edge (for Ni M-edge). Because the P K-edge lies outside the design range of the SGM beamline, a dark current (a small pressure-dependent current that runs through the X-ray fluorescence detector in the absence of a radiation source)

correction was applied to the X-ray fluorescence yield spectra to alleviate the background. Absorption threshold energies were located from the maximum in the first derivative, and calibrated against $Na_4P_2O_7$ (peak maximum of P K-edge set at 2152.4 eV)[224] and the elemental metals (first derivative maxima of metal L_3-edges set at 574.1 eV (Cr), 638.7 eV (Mn), 706.8 eV (Fe), 778.1 eV (Co), 852.7 eV (Ni); Ni M-edge at 66.2 eV), obtained from the Hephaestus software program.[147] Multiple scans were collected for each sample, giving estimated uncertainties of ±0.1 eV for the absorption energies. All XANES spectra were analyzed using the Athena software program.[147]

Table 7-1 lists BE and absorption energies for all M_2P and M_3P (Cr–Ni) samples examined in this study. For comparison, values from the previously reported spectra for MP as well as from newly measured spectra for the elemental metals are provided. Representative spectra are chosen for the discussion below, with remaining spectra for other samples available as Supporting Information (Figures A5-1 – A5-4 in Appendix 5). In particular, discussion of the metal XANES spectra is limited to the Ni L- and M-edge data, which are the simplest to interpret among the M_2P and M_3P series.

7.3 Results and discussion

7.3.1 Phosphorus 2p XPS and K-edge XANES spectra

The P 2p XPS spectra for M_2P and M_3P show two characteristic peaks corresponding to the $2p_{3/2}$ and $2p_{1/2}$ spin-orbit coupled final states, which were fitted as components having a full-width at half-maximum (FWHM) of ~0.7 eV in an intensity ratio of 2:1 in accordance with theoretical expectations (Figure 7-3).[86] The spectra for the earliest (M = Cr) and latest (M = Ni)

Table 7-1 BE and absorption energies (eV) for M_2P and M_3P (M = Cr–Ni). [a]

Sample	P $2p_{3/2}$ BE	P K-edge	Metal $2p_{3/2}$ BE	Metal L_3-edge / M-edge [b]
CrP	129.11	2142.5	573.0	
MnP	129.18	2142.6	638.7	
FeP	129.34	2142.8	706.9	
CoP	129.49	2142.9	778.1	
Cr_2P	129.15	2142.5	574.0	
Mn_2P	129.25	2142.7	638.7	
Fe_2P	129.31	2142.7	706.8	
Co_2P	129.43	2142.8	778.3	
Ni_2P	129.45	2142.9	852.9	853.2 / 67.2
Cr_3P	129.24	2142.8	574.0	
Mn_3P	129.31	2142.9	638.6	
Fe_3P	129.43	2143.0	706.9	
Ni_3P	129.53	2143.1	852.7	852.9 / 66.7
Cr metal			574.1	
Mn metal			638.7	
Fe metal			707.0	
Co metal			778.1	
Ni metal			852.7	852.7 / 66.2

[a] Values for MP are from Ref. 8 and 7.
[b] Except for the Ni-containing samples, the XANES spectra exhibit complex lineshapes (L_3-edge (Figure A5-4)) or are of inadequate quality (M-edge) to permit absorption energies to be located accurately.
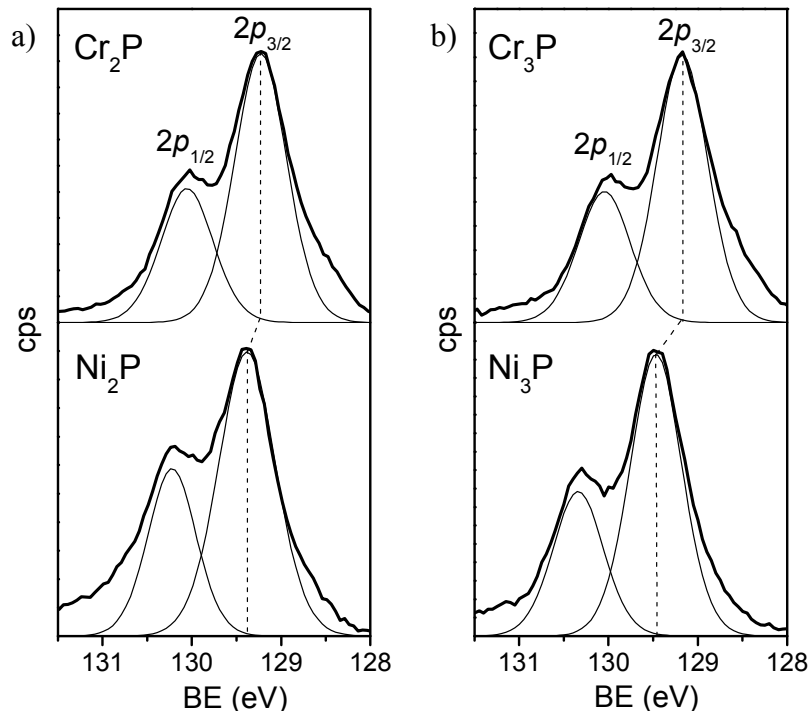
Figure 7-3 High-resolution P 2p XPS spectra for (a) M_2P and (b) M_3P (M = Cr, Ni), fitted with $2p_{3/2}$ and $2p_{1/2}$ component peaks. The $2p_{3/2}$ BEs are marked by vertical dashed lines.

transition-metal members in each series are shown here; the peaks for the other members appear

at intermediate BE between these extremes (Figure A5-1 in Appendix 5). These spectra are

superior to those previously reported for M_2P (M = Fe, Co, Ni) and Ni_3P, where the separation

between $2p_{3/2}$ and $2p_{1/2}$ peaks could not be resolved because of the use of a high pass energy or

where metal oxide impurities were present in the sample.[115,222] In general, the spectra for M_2P

and M_3P are similar to those for MP (with the MnP-type structure),[6] differing only in small shifts

in BE. Importantly, the P $2p_{3/2}$ BE values are systematically lower in M_2P and M_3P (by more

than 0.4 eV, well beyond the BE uncertainties) than in elemental phosphorus (129.9 eV),[101]

clearly establishing the presence of anionic P species even within these highly metal-rich

phosphides. As in the MP series, the charge on the P atoms in M_2P and M_3P can be estimated to

be close to 1–, if the same correlation holds in which the BE is assumed to be linearly proportional to P oxidation state in various series of phosphorus-containing compounds for fixed *M*, as tabulated in the NIST XPS database.[6,101]

The P XANES spectra for the end and middle members (*M* = Fe, Cr, Ni) for each of the M_2P and M_3P series are shown in Figure 7-4 to emphasize the shifts in absorption energy; remaining spectra are available in Supporting Information (Figure A5-2 in Appendix 5). The spectra reveal the K-edge absorption (A) corresponding to a dipole-allowed 1s → 3p transition, and a second feature at higher energy (B). These signals resemble those found in other Ni-rich phosphides, where peak B can be interpreted as multiple-scattering resonance, which is essentially a low-energy EXAFS phenomenon.[225] An alternative possibility for the interpretation of peak B, which appears within 10 eV of the absorption edge, is that it arises from a dipole-allowed transition of the 1s electron into conduction states involving mixing of P 3p and Ni 4p character.[226] In the case of Fe_2P, a pre-edge feature (C) is visible below the edge onset, arising from mixing of P 2p and unoccupied metal 3d states. A similar mechanism has been invoked to explain the pre-edge peaks in the O K-edge EELS spectra[227] of metal oxides and the P and S K-edge XANES spectra in phosphates and sulphates,[228] respectively. Pre-edge peaks were not seen in the other metal phosphides, but they may well be buried in the background or in the broader absorption edge, as occurs in $MnSO_4$ and $Mn_3(PO_4)_2$.[228,229] This feature persisted in multiple scans in the spectra of Fe_2P, eliminating the possibility that it arises from instrumental noise.

Although the shifts in BE and absorption energy are small (~0.5 eV) through the M_2P or M_3P series as *M* is varied from Cr to Ni, they are well above the uncertainty in individual energies (better than ±0.1 eV). Plots of the P $2p_{3/2}$ BEs and K-edge absorption energies show a marked dependence with the difference in Allred-Rochow electronegativity,[168] $\Delta\chi = \chi_P - \chi_M$,
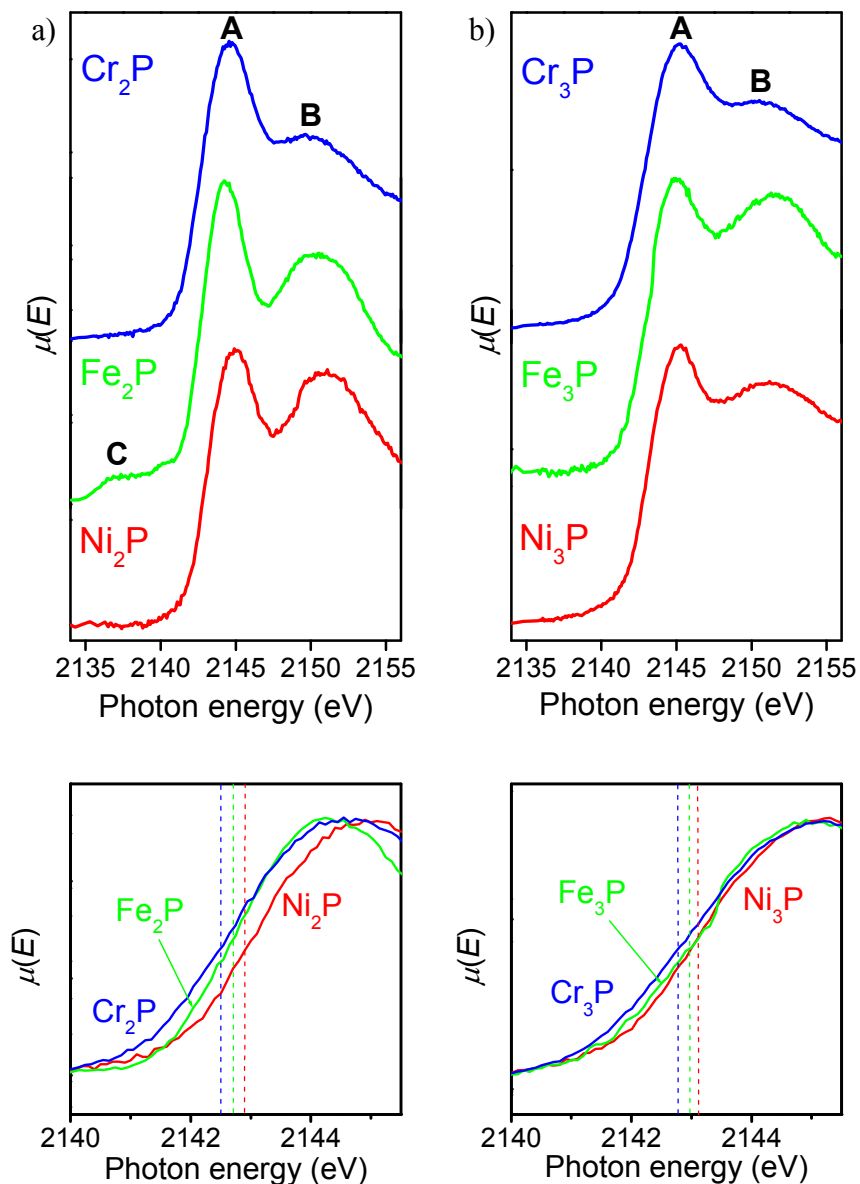
Figure 7-4 P K-edge XANES spectra for (a) M_2P and (b) M_3P (M = Cr, Fe, Ni), measured in fluorescence mode. The bottom panels highlight the absorption edges (located from the maximum in the first derivative), marked by vertical dashed lines. Assignments of features A, B, and C are discussed in the text.

within the M_2P and M_3P series, as well as the previously studied MP series (which was examined

on the same instruments as here) (Figure 7-5).[6] Although XPS is primarily regarded as a surface

characterization technique, the trends in BE parallel those in absorption energies measured by

XANES, which probes the bulk of the solid. Thus, we can be confident that these energy shifts are intrinsic to the solid. Moreover, because XANES involves the excitation of a core electron into an unoccupied bound state so that relaxation processes (which may modify final-state energies) are less likely to occur, these energy shifts can be interpreted in terms of ground-state effects with the use of the charge potential model.[148,183] In this model, which was introduced in Chapter 6 to explain the shifts in the O 1s BE for the arsenide oxides REFeAsO, the BE or absorption energy E_i is shifted from a reference energy $E_i°$ according to the following equation:[183]

$$\Delta E_i = E_i - E_i^o = k\Delta q_i + \Delta\sum_{j\neq i}\frac{q_j}{r_{ij}} \tag{6-1}$$

The first term represents intraatomic effects, which scale with the change in charge Δq_i on a given atom i by a nonlinear constant k that depends on the valence charge and degree of ionization. The second term, a Madelung potential, represents interatomic effects, which scale with the change in the coordination environment, comprising various surrounding atoms j of charge q_j, each at some interatomic distance r_{ij} around the given atom i. Both intraatomic and interatomic effects influence shifts in BE and absorption energy by altering the screening of the nuclear charge experienced at atom i. Intraatomic effects generally dominate these shifts, but in the case of the M_2P and M_3P series, interatomic effects should also be considered given the extended nature of the bonding in these compounds.

Within each of the MP, M_2P, or M_3P series, the P $2p_{3/2}$ BE or K-edge absorption energies decrease with greater $\Delta\chi$. According to the charge potential model, this observation implies that intraatomic effects dominate as M is varied within a series: with greater ionic character of the M–P bond, the enhanced electron transfer from M to P results in a more negative charge on the P

atoms (more negative Δq_i term), consistent with the negative energy shift relative to elemental phosphorus. Note also that the BE or absorption energies are generally slightly higher for M_3P than for M_2P or MP, implying that the P atoms in M_3P are slightly less negatively charged. This is understandable given that the M atoms in M_3P participate in more extensive metal-metal bonding, which tends to diminish the degree of metal-to-phosphorus electron transfer. Interatomic effects also play an important role in these metal-rich phosphides because the presence of more metal atoms in the coordination environment around each P atom induces a more positive Madelung potential, resulting in a positive shift in BE or absorption energies.
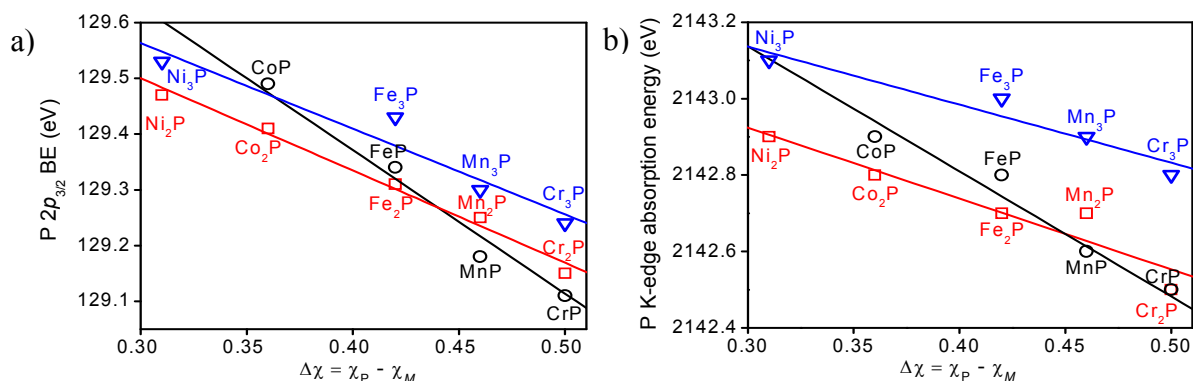
Figure 7-5   Dependence of (a) P $2p_{3/2}$ BE and (b) P K-edge absorption energy on electronegativity difference for MP ($\circ$) (Ref. 6), M_2P ($\square$), and M_3P ($\triangledown$). For MP, the line of best fit has been extrapolated below $\Delta\chi = 0.36$.

Although the slopes of the plots in Figure 7-5 are similar for M_3P and M_2P, they are significantly more pronounced for MP. This observation can again be related to the difference in coordination environment around each P atom, which is surrounded by nine M atoms in M_2P and M_3P, in contrast to only six M atoms in MP (with the MnP-type structure).[230] Moreover, two additional P atoms (at 2.6–2.7 Å), forming part of a zigzag phosphorus-phosphorus bonding network, surround each P atom in MP.[230] Anionic P atoms enhance, whereas cationic M atoms in the coordination environment diminish, the screening experienced at the photoemission or

absorption centre. These competing factors then act to lower or raise the BE and absorption energies (as negative or positive contributions to the $\Delta \sum_{j \neq i} \dfrac{q_j}{r_{ij}}$ term), respectively, as a secondary perturbation to the main effect of the metal-to-phosphorus charge transfer described above. The similar slopes in the BE dependence on $\Delta\chi$ for the M_3P and M_2P series imply that interatomic effects are similar in these two series, whereas the more prominent negative energy shifts with $\Delta\chi$ in the MP series can be traced primarily to the presence of additional P atoms in the coordination environment. The similarity in the behaviour for M_3P and M_2P may seem surprising at first glance, given that M is less positively charged in M_3P than M_2P, but it should not be forgotten that the more extended coordination environment (*next*-nearest neighbours) also plays a contributing role to the interatomic effects.

7.3.2 Metal 2p$_{3/2}$ XPS spectra

Unlike the P 2p spectra, all the M 2p$_{3/2}$ XPS spectra for M_2P and M_3P resemble each other, and those of the MP series and the elemental metal for a given M, with hardly any shift in BE for the main core-line (Figure 7-6 and Table 7-1). The spectra for the Co- and Ni-containing members, where satellites are present, are highlighted here; remaining spectra are available in Appendix 5. The asymmetric lineshape to higher BE, a signature of the electronic delocalization characteristic of metallic solids, arises from the Doniach-Šunjić process discussed in detail in Section 3.3.3 of Chapter 3.[130] As a result of the electronic delocalization within the metal-metal bonding networks present in the structures of MP, M_2P, and M_3P, the electrons on the metal photoemission centre experience, on average, greater nuclear screening to the extent that the BE becomes similar to that in the elemental metal. Because significant final state effects are operative here, the charge potential model cannot be applied to analyze the shifts in M 2p$_{3/2}$ BEs.
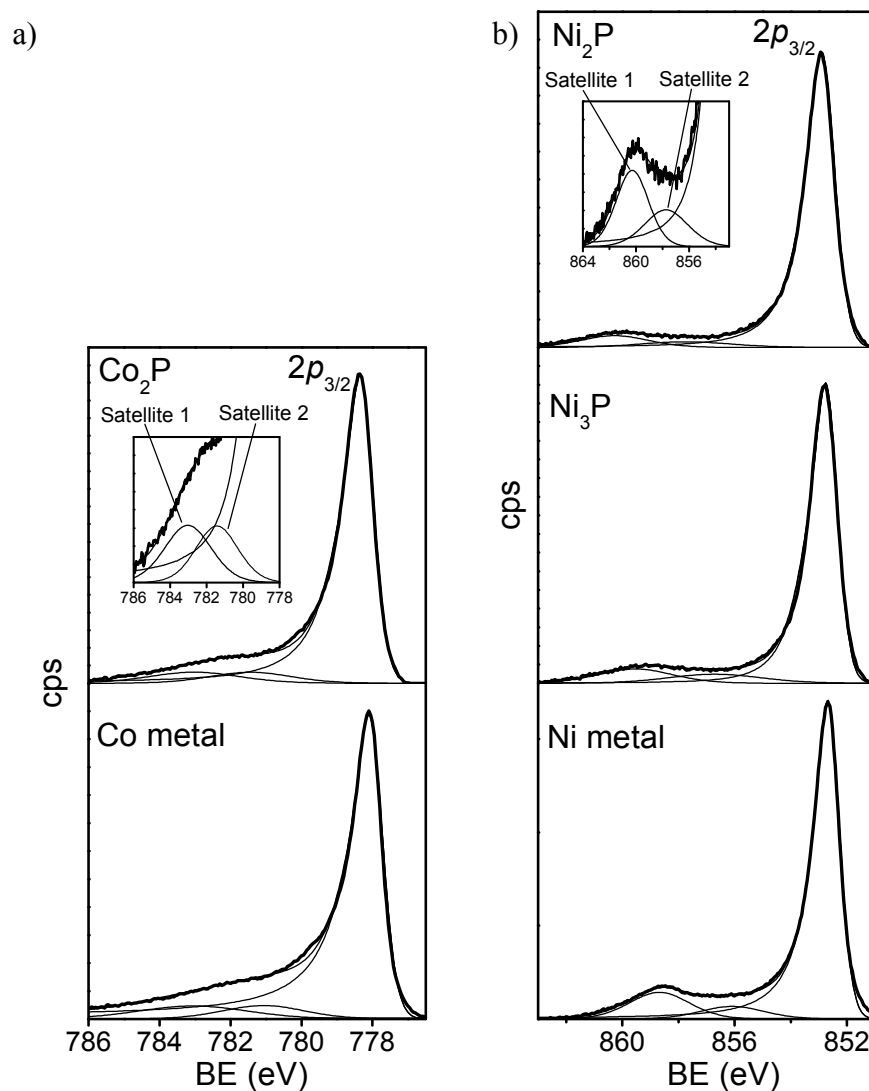
Figure 7-6 High-resolution M 2p$_{3/2}$ XPS spectra for M_3P, M_2P, and M metal for (a) $M = $ Co and (b) $M = $ Ni, with satellite structure enlarged in insets.

In the case of Co$_2$P, Ni$_2$P, and Ni$_3$P, the M 2p$_{3/2}$ spectra reveal an additional satellite structure that is relatively broad (FWHM of 2.9–3.7 eV). The origin of these satellites, either the plasmon loss processes or two-core-hole final state effects, has previously been discussed in Chapter 5 and Chapter 6.[184,185] Here, the plasmon loss process is used to explain these satellite peaks and the spectra are fitted to two satellite peaks, BEs of which are listed in Table 7-2.

These peaks can be attributed to bulk (higher energy) and surface (lower energy) plasmon loss processes, which involve the interaction of photoelectrons with atoms located below and near the surface, respectively. Satellite features were not observed in the spectra of the other M_2P and M_3P compounds, but they could well be buried within the more intense core-line peak.

Table 7-2 BE and intensities of satellite peaks in Metal 2p$_{3/2}$ XPS spectra of M_2P and M_3P (M = Co, Ni). [a]

Sample	Satellite 1 BE (eV)	Satellite 2 BE (eV)	$I_{satellite}/I_{core\text{-}line}$ [b]
CoP	783.0	781.4	0.13
Co$_2$P	782.8	781.5	0.24
Co metal	783.1	781.1	0.32
Ni$_2$P	860.0	857.1	0.17
Ni$_3$P	859.5	856.7	0.28
Ni metal	858.8	855.3	0.35

[a] Values for MP are from Ref. 6.
[b] $I_{satellite}$ is the sum of the intensities for the bulk and surface plasmon loss satellite peaks.

In the plasmon loss processes, an excited photoelectron loses kinetic energy (KE) (which is manifested by an increase in BE) to the collective oscillation of delocalized valence electrons belonging to other metal atoms.[184,213] The energies of the surface plasmon oscillations relative to those of the bulk plasmon oscillations are in good agreement (to within 20%) with the expected ratio of $1/\sqrt{2}$.[231] Because the cross-section for these processes is proportional to the density of valence electrons, the satellite intensity provides information about the charge on the M atoms.[120] The core-hole model, in a similar manner, would also predict that the cross-section of the two core-hole states is proportional to the number of valence states.[120] The normalized intensity of

the satellite peaks ($I_{satellite}/I_{core-line}$) gradually increases as the samples become more metal-rich in the Co- and Ni-containing phosphides and is highest in the elemental metals (Table 7-2 and Figure 7-7). From this, we can infer that Co and Ni atoms within the transition-metal phosphides do not contain as many valence electrons as in the elemental metals (i.e., they are definitely cationic). Relative to MP, where charges of $M^{1+}P^{1-}$ have been previously proposed, the metal atoms have more valence electrons and become less positively charged on proceeding to M_2P, as indicated by comparing CoP with Co$_2$P.[6] Similarly, the metal atoms become less positively charged on proceeding from M_2P to M_3P, as indicated by comparing Ni$_2$P with Ni$_3$P. If the P atoms are assumed to be approximately 1− in all three series of phosphides, then this trend is consistent with the M charge predicted from simple charge balancing: $M^{1+}P^{1-}$, $(M^{0.5+})_2P^{1-}$, and $(M^{0.33+})_3P^{1-}$. Unlike the MnP-type structure adopted by the MP series, there are actually several crystallographically inequivalent M sites with different coordination environments in both the M_2P or M_3P series. The relative charges extracted in this manner thus only represent an average, and clearly the inequivalent M sites cannot be resolved in the M 2p$_{3/2}$ spectra.
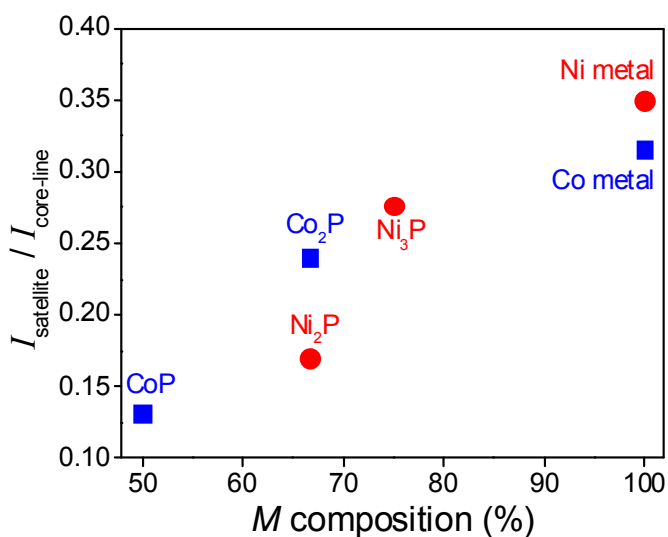
Figure 7-7 Plot of normalized satellite intensity ($I_{satellite}/I_{core-line}$) vs M composition in Co and Ni phosphides, and the elemental metals.

7.3.3 Nickel L- and M-edge XANES spectra

Although XANES spectra were measured for the entire M_2P and M_3P series (Figure A5-4 in Appendix 5), only the Ni L- and M-edge spectra for Ni_2P and Ni_3P are presented here because they exhibit the most prominent shifts relative to Ni metal (Figure 7-6). The Ni L-edge spectra reveal transitions of 2p electrons into unoccupied 3d and possibly 4s states, in accordance with dipole selection rules ($\Delta l = \pm 1$). The L-edge is split by spin-orbit coupling into a lower-energy L_3-edge ($2p_{3/2} \to 3d$) and a higher-energy L_2-edge ($2p_{1/2} \to 3d$). The L_3-edge appears sharper and better resolved than the L_2-edge, consistent with the longer lifetime of the excited state in this transition, which is inversely proportional to the peak width.[232] In principle, the lineshape of the L_3-edge reveals information about the coordination environment of the Ni atoms (since unoccupied 3d states are being probed), but its interpretation is hampered by the fact that these environments differ substantially in Ni_2P vs Ni_3P. Moreover, the intensity of these edges should reflect the charge on the Ni atoms, but line broadening in different compounds can be influenced by changes in site symmetry, rendering an intensity analysis somewhat problematic.[233] Qualitatively, however, there does appear to be an increase in the L-edge peak areas on progressing from Ni metal to Ni_3P and Ni_2P (Figure 7-8a), implying more unoccupied Ni-based conduction states and lending support to the presence of cationic Ni in these compounds.

The Ni L-edge XANES spectra here do show noticeable shifts in absorption energy, unlike the Ni $2p_{3/2}$ XPS spectra, where no BE shifts were apparent. The absorption energy of the Ni L_3- and L_2-edges increases slightly (by $\sim 0.5-1.0$ eV) on progressing from Ni metal to Ni_3P and then to Ni_2P, indicative of the Ni charge becoming more positive and consistent with the earlier analysis of satellite intensity in the Ni $2p_{3/2}$ XPS spectra. Within the M_2P or M_3P series,
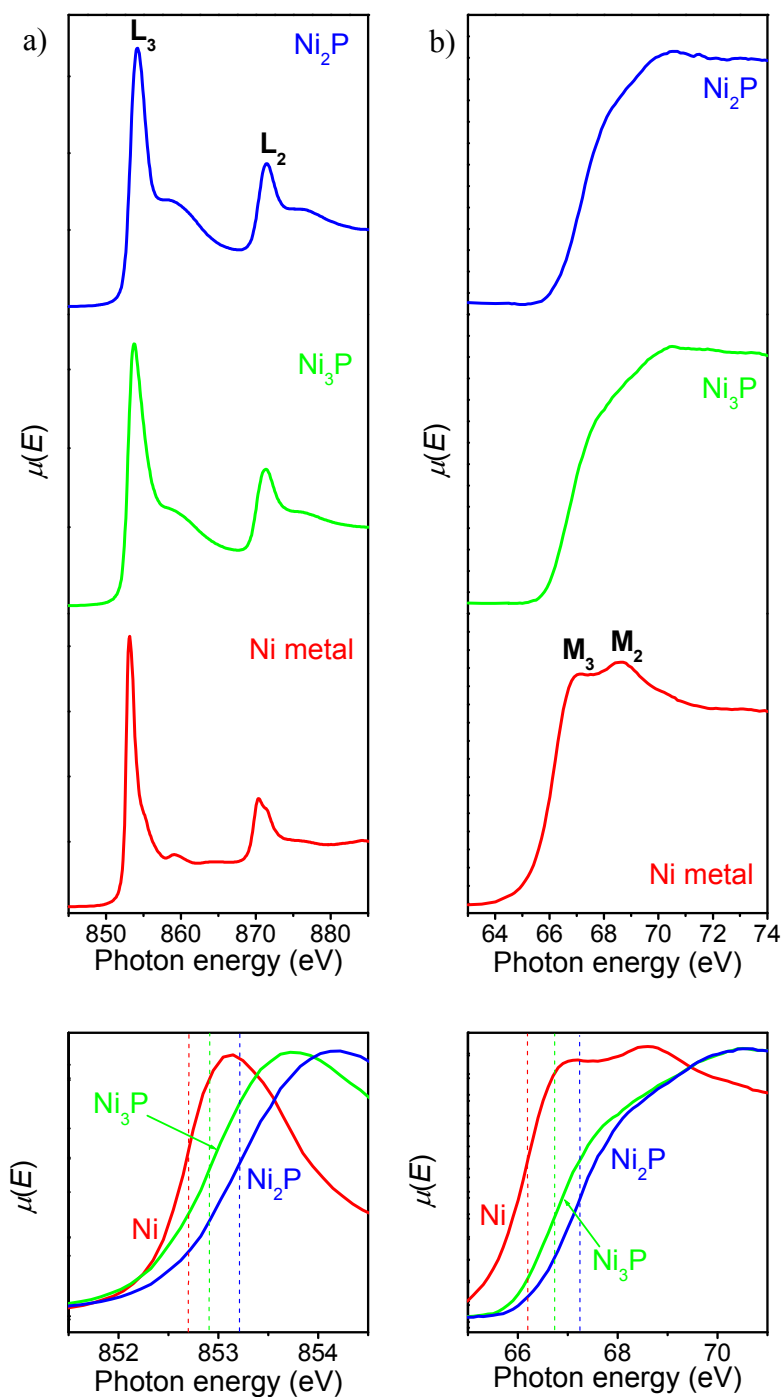
Figure 7-8 (a) Ni L-edge (transmission mode) and (b) M-edge XANES spectra (fluorescence mode) for Ni_2P, Ni_3P, and Ni metal. The bottom panels highlight the absorption edges (located from the maximum in the first derivative), marked by vertical dashed lines.

the Ni-containing members correspond to the greatest d-electron count, so that the empty conduction bands to which core electrons are excited are narrower than for the other M-containing members. This is reflected in the relatively thin L_3-edges in Ni_2P and Ni_3P compared to the other compounds. The narrowness of the Ni-based conduction states also accounts for the greater sensitivity of the L-edge energies to changes in the electronic structure.

The Ni M-edge XANES spectra, presented in X-ray fluorescence mode because of its better resolution compared to total electron yield mode, reveal dipole-allowed transitions of 3p electrons into unoccupied 3d and 4s states (Figure 7-8b). The splitting of the M-edge arising from spin-orbit coupling (M_3-edge, $3p_{3/2} \rightarrow 3d$; M_2-edge, $3p_{1/2} \rightarrow 3d$) is visible in Ni metal but not in Ni_2P and Ni_3P. As in the L-edge spectra, the onset of the M-edge clearly shifts to higher energy from Ni metal to Ni_3P and then to Ni_2P, lending further support to the Ni charge becoming more positive in this progression.

7.4 Conclusion

The metal-rich phosphides M_2P and M_3P exhibit a linear decrease in the phosphorus $2p_{3/2}$ BE and K-edge absorption energy as the electronegativity difference $\Delta\chi$ increases, reflecting an enhanced charge transfer from M to P. Relative to elemental phosphorus, the BE shifts to lower energy, implying the presence of anionic P atoms, with a charge estimated as 1−, similar to that found in the monophosphide series MP. This conclusion contradicts theoretical proposals that significant backbonding takes place from P to M in the M_2P and M_3P series, and forces a re-evaluation of standard explanations for the catalytic activity of compounds such as Ni_2P. Through a charge potential model, smaller differences in the P $2p_{3/2}$ BE can be rationalized in terms of interatomic effects, which are modified by changes in the coordination environment

around the P atom in the MP, M_2P, and M_3P series. This suggests that the catalytic activity of M_2P and M_3P compounds could be modified through tuning of the electron count, most simply through the evaluation of mixed-metal compounds. The valence electrons on the metal atoms are highly delocalized, through an extensive metal-metal bonding network, which acts to enhance the screening felt by metal photoelectrons such that little shift in the M 2p$_{3/2}$ BE is seen within these series. However, the M 2p$_{3/2}$ XPS spectra of the Co- and Ni-containing compounds reveal a satellite structure which can be accounted for by either a plasmon loss or a two-core-hole model, and which provides an indirect measure of the charge on the M atoms. These satellites become more intense on progressing from MP to M_2P and then to M_3P, indicating that the M atoms become less positively charged. This trend was confirmed in the case of Ni$_2$P and Ni$_3$P through shifts in the absorption energy in the Ni L- and M-edge XANES spectra.

Chapter 8

Effects of metal substitution in transition-metal phosphides $(Ni_{1-x}M_x)_2P$ (M = Cr, Fe, Co) studied by X-ray photoelectron and absorption spectroscopy[*]

8.1 Introduction

As previously discussed in Chapter 1, one of the most exciting developments in transition-metal phosphides lies in their potential as catalysts for hydrodesulphurization and hydrodenitrogenation processes.[68] Of these, Ni_2P has been identified as the most promising. Its high activity is attributed to the ability of N- and S-containing molecules to adsorb onto the (001) surface.[73] The catalytic activity is improved when Ni_2P is doped with Co, suggesting that it is influenced by the occupancy of the metal 3d band. Further improvements thus demand a more detailed understanding of the electronic effects of metal substitution in this and related systems.

Ni_2P adopts the well-known hexagonal Fe_2P-type structure (Figure 7-1a in Chapter 7).[18] Mixed-metal phosphides $(M_{1-x}M'_x)_2P$ (where M' is more electronegative M) are also known; in particular, the Ni-containing mixed-metal series $(Ni_{1-x}M_x)_2P$ have been prepared for M = Cr,[234] Fe,[235] Co and $0 \leq x \leq 1$.[236] In the $(Ni_{1-x}Cr_x)_2P$ and $(Ni_{1-x}Co_x)_2P$ series, the structure adopted eventually transforms from the hexagonal Fe_2P-type to the orthorhombic Co_2P-type (Figure 7-1c in Chapter 7) when the degree of substitution, x, exceeds a critical value.[234,236] Nevertheless, the local environments around metal and P atoms remain similar in both structure types. The metal

---

atoms are coordinated by P atoms in two types of environments (tetrahedral (CN4) and square pyramidal (CN5)) (Figure 7-2a in Chapter 7) and participate in an extensive metal-metal bonding network. In the mixed-metal phosphides $(M_{1-x}M'_x)_2P$, the more electronegative metal M' preferentially occupies the tetrahedral sites and the more electropositive metal M' the square pyramidal sites.[235,237,238] In turn, the P atoms are nine-coordinate, residing at the centres of trigonal prisms formed by the metal atoms, with three additional capping metal atoms provided by neighbouring trigonal prisms.

In this chapter, X-ray photoelectron spectroscopy (XPS) and X-ray absorption near-edge spectroscopy (XANES) will be used to probe the electronic structure of mixed-metal phosphides. The phosphorus $2p_{3/2}$ binding energy (BE) and K-edge absorption energy, as well as satellite features in the metal spectra, are sensitive to changes in charge of a given atom and its local environment, in which not only the nearest neighbours but also the next-nearest neighbours may be important. Evidence for charge transfer between two dissimilar metals M and M' has been found in the mixed-metal series $M_{1-x}M'_xP$ with the MnP-type structure.[8] In the case of the Ni-containing phosphides $(Ni_{1-x}M_x)_2P$, only the series with $M =$ Fe has been previously examined by K-edge XANES analysis and, to our knowledge, no corresponding analysis of the metal L-edge XANES has been completed.[226] We present herein high-resolution metal and phosphorus XPS and XANES spectra of the three series $(Ni_{1-x}M_x)_2P$ ($M =$ Cr, Fe, Co; $0 \leq x \leq 1$), making use of these results to evaluate the degree of charge transfer that takes place between the different components.

8.2 Experimental section

8.2.1 Synthesis

Starting materials were powders of the metal (Cr, 99.95%, Alfa-Aesar; Fe, 99.9%, Cerac; Co, 99.8%, Cerac; Ni, 99.9%, Cerac) and red P (99.995%, Cerac). All samples were manipulated and stored in a glove box under Ar. Products were identified by their powder X-ray diffraction (XRD) patterns collected on an Inel powder diffractometer equipped with a CPS 120 detector.

Binary phosphides M_2P (M = Cr, Fe, Co, Ni) were prepared by reacting stoichiometric mixtures of the elements sealed in evacuated fused-silica tubes. For Cr_2P, Fe_2P, and Co_2P, the tubes were heated to 1323 K over a 48-h period, held at that temperature for 5 d, and then quenched in water. For Ni_2P, the reactants were also placed in an inner alumina crucible within the tube and the heating period at 1323 K was lengthened to 9 d. Mixed-metal phosphides ($Ni_{1-x}M'_x)_2P$ (M' = Cr, Fe, Co; x = 0.2, 0.5, 0.7–0.8) were prepared by reacting stoichiometric mixtures of the appropriate binary phosphides M_2P placed within evacuated fused-silica tubes. The homogeneity of the products, as gauged by examining the powder XRD patterns, was optimized by grinding and reheating (1323 K for 5 d); this procedure was repeated three times. In cases where single crystals were found in the products, windowless energy-dispersive X-ray (EDX) analysis performed on a Hitachi S-2700 scanning electron microscope confirmed the absence of oxygen and gave approximate elemental compositions in good agreement with expectations (e.g., observed Ni/Fe ratios of 1.05(4) in $(Ni_{0.5}Fe_{0.5})_2P$ and 0.25(1) in $(Ni_{0.2}Fe_{0.8})_2P$).

8.2.2 XPS analysis

Phosphorus 2p and metal 2p$_{3/2}$ XPS spectra were measured on a Kratos AXIS 165 spectrometer equipped with a monochromatic Al Kα X-ray source (14 mA, 15 kV) and a hybrid lens with a spot size of 700 × 400 μm^2. To minimize exposure to air, samples were finely ground under Ar in a glove box, pressed into In foil, mounted on a Cu sample holder, and transferred within a sealed container to the analysis chamber of the XPS instrument, where the pressure was maintained at 10^{-7} to 10^{-9} Pa. To remove surface oxides, samples were sputter-cleaned with an Ar$^+$ ion beam (4 kV, 10 mA) for varying times depending on the degree of oxidation until core-line peaks associated with phosphorus- and iron-containing surface oxides were no longer observed in the XPS spectra. A small shoulder in the P 2p XPS spectra indicated that a slight reduction of P occurred, whereas no evidence of reduction was observed in the metal 2p spectra.

Survey spectra were collected with a BE range of 0–1100 eV, a pass energy of 160 eV, a step energy of 0.7 eV, and a sweep time of 180 s. The chemical compositions determined from these survey spectra agreed well with the expectations for each sample. High-resolution spectra were collected with an energy envelope of 20 eV (P 2p peak) or 50 eV (metal 2p$_{3/2}$ peak), a pass energy of 20 eV, a step size of 0.05 eV, and a sweep time of 180 s. No charge correction was required because these compounds are good conductors. The high-resolution spectra, referenced to the C 1s line at 248.8 eV, were analyzed with the CasaXPS software package.[128] The background arising from energy loss was removed by applying a Shirley-type function, and peaks were fitted to either Gaussian (P 2p) and pseudo-Voigt (metal 2p) lineshapes. Multiple spectra of each sample were analyzed to establish a precision of BE values, estimated to be better than ±0.10 eV.

8.2.3 XANES analysis

Measurements were performed at the Canadian Light Source (CLS) in Saskatoon, Saskatchewan. Phosphorus K- and metal L-edge XANES spectra were collected with the spherical grating monochromator (SGM) undulator beamline (11-1.D1). Powder samples were mounted on carbon tape and inserted into the vacuum chamber via a load lock. Spectra were collected from ~20 eV below to ~65 eV above the edge using both total electron yield (TEY) and X-ray fluorescence yield (FLY) modes. Because the P K-edge lies outside the design range of the SGM beamline, a dark current (a small pressure-dependent current that runs through the XRF detector in the absence of a radiation source) correction was applied to the XRF yield P K-edge spectra to suppress the background. The phosphorus spectra were calibrated against $Na_4P_2O_7$ with the peak maximum of the K-edge set to 2152.4 eV.[224] The metal spectra were calibrated against the elemental metals, with the maxima in the first derivatives of the L_3-edges set to 574.1 eV (Cr), 706.8 eV (Fe), 778.1 eV (Co), and 852.7 eV (Ni).[147] All edge energies reported were located from the maxima in the first derivatives.

Nickel K-edge XANES spectra were collected on the hard X-ray microanalysis (HXMA) superconducting wiggler beamline (06ID-1). Powder samples were sandwiched between Kapton tape and positioned in front of the X-ray beam. A silicon (220) crystal monochromator provided a monochromatic flux of ~6×10^{11} photons/sec, with a resolution of 1 eV at 10 keV and a beam size of 100×500 μm^2. Spectra were collected in transmission mode with a N_2-filled ion chamber detector, and in fluorescence mode with a Lytle detector.[182] The spectra were calibrated against the literature values for elemental metal standards, whose spectra were measured simultaneously in transmission mode. All XANES spectra were analyzed with the Athena software program.[147]

8.2.4 Band structure calculations

Interpretation of the Ni K-edge XANES spectrum was aided with tight-binding linear muffin tin orbital band structure calculations for Ni_2P (Fe_2P-type structure) within the local density and atomic sphere approximations using the Stuttgart TB-LMTO program.[127] Contributions from the Ni 3d, Ni 3p, and P 3p orbitals to the density of states were extracted.

8.3 Results and discussion

Samples of binary phosphides M_2P (M = Cr, Fe, Co, Ni) and mixed-metal phosphides $(Ni_{1-x}M_x)_2P$ (M = Cr, Fe, Co; x = 0.2, 0.5, 0.7–0.8) were found to be phase-pure as ascertained by their powder XRD patterns. Representative XRD patterns for a series with fixed composition, $(Ni_{0.8}M_{0.2})_2P$ (M = Cr, Fe, Co), and a solid solution series, $(Ni_{1-x}Cr_x)_2P$ ($0 \leq x \leq 1$), are shown in Figure A6-1 (Appendix 6). Consistent with previous studies, the mixed-metal phosphides adopt the hexagonal Fe_2P-type structure of the parent Ni_2P end-member, except for the Cr- and Co-rich members $(Ni_{0.5}Cr_{0.5})_2P$, $(Ni_{0.3}Cr_{0.7})_2P$, and $(Ni_{0.2}Co_{0.8})_2P$, which adopt the orthorhombic Co_2P-type structure. Table A6-1 (Appendix 6) lists the cell parameters, which do not follow Vegard's law, as previously noted, because of preferential occupation by metal atoms on the tetrahedral vs square pyramidal sites. Table 8-1 summarizes the BE and absorption energies for all samples examined here, with additional literature data provided for comparison. Representative XPS and XANES spectra are shown for the discussion below, with remaining spectra available in Appendix 6 (Tables A6-2–A6-3; Figures A6-2–A6-5).

Table 8-1 BE and absorption energies (eV) for elemental metals, M_2P, and $(Ni_{1-x}M_x)_2P$.

Sample	Structure type	P $2p_{3/2}$ BE	P K-edge	Ni $2p_{3/2}$ BE / M $2p_{3/2}$ BE
Cr metal	Bcc			574.1
Mn metal	α-Mn			638.7
Fe metal	Bcc			707.0
Co metal	Hcp			778.1
Ni metal	Fcc			852.73
Cr_2P	Cr_2P-type	129.15	2142.5	574.00
Mn_2P	Fe_2P-type	129.25	2142.7	638.65
Fe_2P	Fe_2P-type	129.31	2142.7	706.82
Co_2P	Co_2P-type	129.43	2142.8	778.28
Ni_2P	Fe_2P-type	129.45	2142.9	852.89
$(Ni_{0.8}Cr_{0.2})_2P$	Fe_2P-type	129.41	2142.7	852.94 / 574.04
$(Ni_{0.5}Cr_{0.5})_2P$	Co_2P-type	129.35	2142.7	853.14 / 574.05
$(Ni_{0.3}Cr_{0.7})_2P$	Co_2P-type	129.25	2142.6	853.16 / 574.04
$(Ni_{0.8}Fe_{0.2})_2P$	Fe_2P-type	129.41	2142.8	852.87 / 706.66
$(Ni_{0.5}Fe_{0.5})_2P$	Fe_2P-type	129.44	2142.8	853.01 / 706.87
$(Ni_{0.2}Fe_{0.8})_2P$	Fe_2P-type	129.36	2142.4	853.07 / 706.80
$(Ni_{0.8}Co_{0.2})_2P$	Fe_2P-type	129.46	2142.9	852.98 / 778.12
$(Ni_{0.5}Co_{0.5})_2P$	Fe_2P-type	129.42	2142.8	852.91 / 778.14
$(Ni_{0.2}Co_{0.8})_2P$	Co_2P-type	129.41	2142.8	853.01 / 778.27

8.3.1 P 2p XPS and K-edge XANES spectra

The phosphorus component in Ni_2P and related transition-metal phosphide HDS and HDN catalysts has been proposed to play several roles, including stabilizing the metal d levels to assist in the dissociation of substrates and acting as a base to abstract protons. Thus, it is of interest to identify what effects can be observed in the P BE and absorption energies as different metal atoms are doped into Ni_2P, and whether phosphidic (anionic) species are present. The P 2p XPS spectra reveal two peaks corresponding to the $2p_{1/2}$ and $2p_{3/2}$ spin-orbit coupled final states, as exemplified for Ni_2P and $(Ni_{0.3}Cr_{0.7})_2P$ (Figure 8-1a). The spectra were fitted to these components, which are separated by 0.9 eV, using a full-width at half-maximum (FWHM) of 0.7–0.8 eV and an intensity ratio of 2:1 ($2p_{3/2}$:$2p_{1/2}$), consistent with theoretical expectations.[87] In general, the P $2p_{3/2}$ BE decreases as more of the Ni atoms are replaced by M atoms in $(Ni_{1-x}M_x)_2P$. A similar shift is seen in the P K-edge XANES spectra for Ni_2P and $(Ni_{0.3}Cr_{0.7})_2P$ (Figure 8-1b), in which the absorption arises from the dipole-allowed transition of a 1s electron into unoccupied 3p states. Figure 8-2 shows plots of the P $2p_{3/2}$ BE and the P K-edge absorption energy for these $(Ni_{1-x}M_x)_2P$ phosphides versus the difference in Allred-Rochow electronegativity ($\Delta\chi$) between phosphorus and metal, with a weighted average assigned to the latter ($(1-x)\chi_M + x\chi_{M'}$) because of the mixing. The correlation of these energy shifts with $\Delta\chi$ is strong, as indicated by the good linear fits for the BE ($R^2 = 0.95$) and absorption energy ($R^2 = 0.84$). Although XPS is normally considered to be a surface-sensitive technique, the similar trends seen in the absorption energies measured by XANES, which is a bulk-sensitive technique, imply that these shifts are intrinsic to the solid.

A simple interpretation is that, as $\Delta\chi$ is increased, the metal atoms transfer more electrons to the phosphorus atoms which become increasingly anionic, as reflected by their lower binding
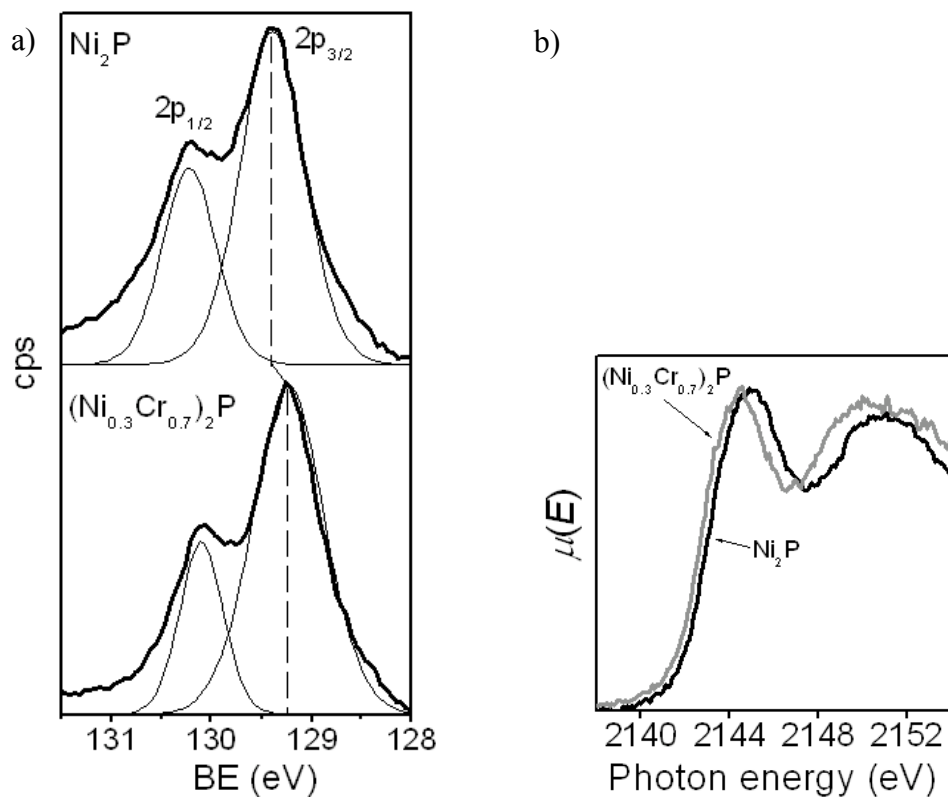
Figure 8-1 (a) High-resolution P 2p XPS and (b) P K-edge XANES spectra (measured in fluorescence mode with a dark current correction) for Ni_2P and $(Ni_{0.3}Cr_{0.7})_2P$.
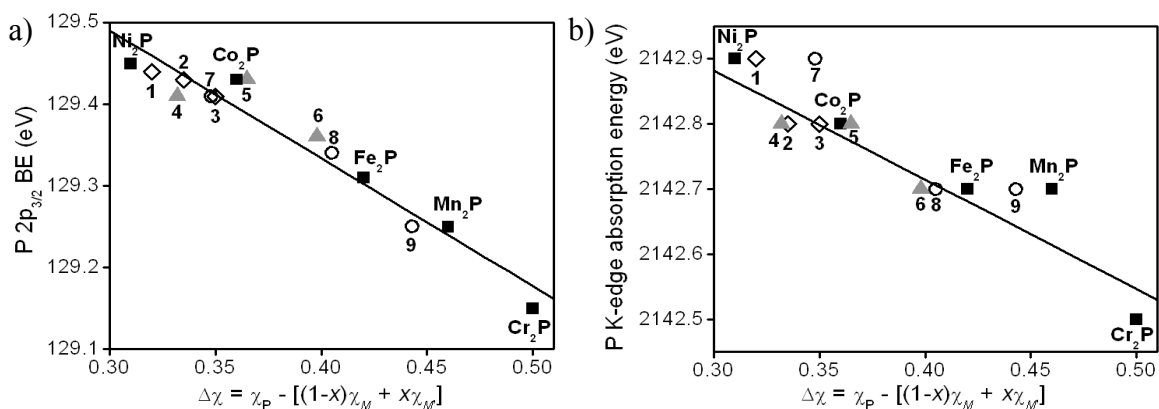
Figure 8-2 Dependence of (a) P $2p_{3/2}$ BE and (b) P K-edge absorption energy on the weighted electronegativity difference $\Delta\chi$ for binary phosphides M_2P (■) and ternary phosphides $(Ni_{1-x}M_x)_2P$ (M = Co ($\diamond$), Fe (▲), Cr (○); **1** = $(Ni_{0.8}Co_{0.2})_2P$, **2** = $(Ni_{0.5}Co_{0.5})_2P$, **3** = $(Ni_{0.2}Co_{0.8})_2P$, **4** = $(Ni_{0.8}Fe_{0.2})_2P$, **5** = $(Ni_{0.5}Fe_{0.5})_2P$, **6** = $(Ni_{0.2}Fe_{0.8})_2P$, **7** = $(Ni_{0.8}Cr_{0.2})_2P$, **8** = $(Ni_{0.5}Cr_{0.5})_2P$, **9** = $(Ni_{0.3}Cr_{0.7})_2P$).

and absorption energies. However, a thorough analysis must take into account that the BE is really the difference between the initial (ground) state and the final (excited) state of the ionized atom resulting from the photoionization process. Various relaxation mechanisms may alter the final state energy. For example, the core hole that remains after photoionization acts as a positive charge adiabatically attracting the remaining electrons thereby imparting a greater nuclear screening, which would result in a negative shift in BE.[91] As well, the presence of less electronegative nearest neighbour atoms in a fixed coordination environment around a P atom would tend to increase relaxation, also lowering the BE.[187,188] Although this trend is observed in the BEs as more M atoms substitute for Ni atoms in $(Ni_{1-x}M_x)_2P$ (e.g., 129.45 eV in Ni_2P vs. 129.25 eV in $(Ni_{0.3}Cr_{0.7})_2P$), we do not consider this relaxation mechanism to be the main contributor to the BE shifts in this case because similar shifts are found in the P K-edge absorption energy. Unlike the XPS experiment, where electrons are ionized into the vacuum, the XANES experiment is less sensitive to final state effects because it involves excitation of electrons into unoccupied bound conduction states which remain associated with the atom.[148] The similar trends in BE and absorption energies therefore confirm that ground state effects are chiefly responsible for the energy shifts in the phosphorus spectra.

If ground state effects are assumed to dominate, these energy shifts can be understood by applying the charge potential model (first introduced in Chapter 6):[183]

$$\Delta E_i = E_i - E_i^o = k\Delta q_i + \Delta \sum_{j \neq i} \frac{q_j}{r_{ij}}. \tag{8-1}$$

Thus the BE or absorption energy E_i for an electron in an atom i is shifted (ΔE_i) relative to a reference energy E_i° because of two contributing factors. The first term ($k\Delta q_i$) describes intraatomic effects resulting from a change in charge on an atom and the second term describes interatomic effects (a Madelung potential) which result from a change in the chemical

environment defined by all other surrounding atoms j with charges q_j at some distance, r_{ij}. According to this model, intraatomic effects would lead to a negative shift in phosphorus BE and absorption energy as the concentration of more electropositive M atoms increases in $(Ni_{1-x}M_x)_2P$, because the core electrons of P atoms experience greater nuclear screening and acquire a more negative charge (Δq_i is negative, relative to elemental phosphorus as the reference) as a result of the enhanced electron transfer. On the other hand, interatomic effects would lead to a positive shift in phosphorus BE and absorption energy because the surrounding metal atoms acquire a more positive charge ($\Delta \sum_{j \neq i} \dfrac{q_j}{r_{ij}}$ is positive). The observed trends seen in Figure 8-2, where the energy shifts for the mixed-metal series $(Ni_{1-x}M_x)_2P$ do not deviate much from the linear fit to those for the parent binary phosphides M_2P, imply that intraatomic effects are more important than interatomic effects, as is usual. This behaviour differs from the metal-poorer $M_{1-x}M'_xP$ (MnP-type) series examined previously, where significant deviations from a linear fit were attributed to next-nearest neighbour contributions to the interatomic effects, involving a secondary metal-metal (M-to-M') charge transfer taking place.[7] To probe more directly whether any metal-metal charge transfer takes place in the metal-richer $(Ni_{1-x}M_x)_2P$ series, it is helpful to examine the metal-based spectra.

8.3.2 Metal 2p$_{3/2}$ XPS spectra

In phosphide HDS and HDN catalysts such as Ni_2P, it is assumed that the primary sites to which substrate molecules adsorb are the transition-metal atoms. In principle, the metal XPS spectra may be useful in providing information about the electronic structure of these metal sites, but as we have shown earlier on the simpler monophosphides MP and their mixed-metal variants,

the energy shifts are quite small. It is thus important to develop techniques for analyzing these spectra for eventual application to real catalytic systems and to understand what factors affect the appearance of these spectra. The metal $2p_{3/2}$ XPS spectra for all M_2P and $(Ni_{1-x}M_x)_2P$ samples reveal an asymmetric lineshape, as exemplified for the Ni $2p_{3/2}$ peaks in Ni_2P and $(Ni_{0.3}Cr_{0.7})_2P$ (Figure 8-3). If an electron transfer from M to Ni takes place, one might expect to see shifts to higher M and lower Ni $2p_{3/2}$ BEs as the M concentration increases in $(Ni_{1-x}M_x)_2P$. However, the measured BEs either change little or do not follow this expectation (Table 8-1). The inability to relate the charges of the metal atoms with BEs indicates that the charge potential model is inapplicable here because of the failure in the assumption that ground state effects dominate. In fact, the asymmetric lineshape in the metal $2p_{3/2}$ XPS spectra is a signature of important final state effects in which valence electrons, interacting with the core hole generated after photoionization, are excited into the continuum of empty conduction states near the Fermi edge (Doniach-Šunjić process).[130] The lower probability of electrons occupying conduction states at higher energies leads to the asymmetric tail. Such a feature is characteristic of the delocalization of valence electrons, which provide greater nuclear screening in the final state around the metal atoms, consistent with the extensive metal-metal bonding network present in the structures of these metal-rich phosphides. Because of these final state effects, other approaches are required to extract information about metal charges in the metal-rich phosphides.

An interesting trend is observed in the $(Ni_{1-x}M_x)_2P$ series in which the Ni $2p_{3/2}$ BE generally shifts to higher energy with increasing concentration of M atoms (Table 8-1). This trend is opposite to expectations, since greater electron transfer from M to Ni should lead to a more negative charge on Ni and shift its $2p_{3/2}$ BE to lower energy, as occurs in the $M_{1-x}M'_xP$ series. These shifts in energy are likely a manifestation of a next-nearest neighbour effect. In
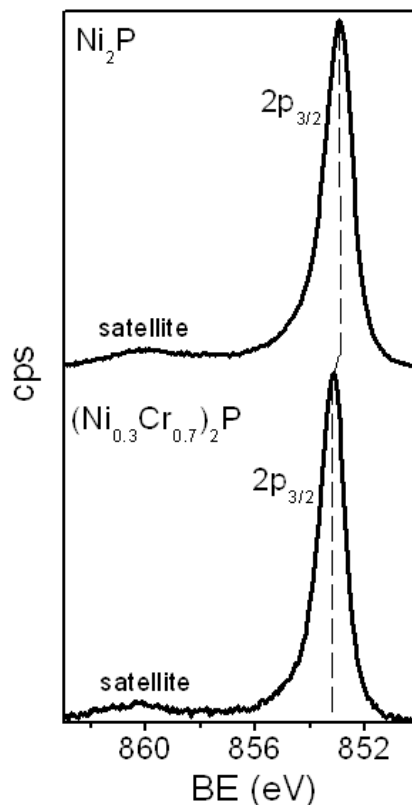
Figure 8-3 Ni $2p_{3/2}$ XPS spectra for Ni_2P and $(Ni_{0.3}Cr_{0.7})_2P$.

the metal-richer $(Ni_{1-x}M_x)_2P$ series, each metal atom is generally surrounded by more metal atoms and fewer P atoms than in the $M_{1-x}M'_xP$ series. As Ni is progressively substituted by the more electropositive M atoms, each Ni atom is surrounded by a greater number of positively charged M atoms, thereby raising the Madelung potential. This effect becomes particularly noticeable at high M concentrations, when Ni atoms preferentially occupy the tetrahedral sites. At this stage, each Ni atom will then be surrounded by only four P atoms in the first coordination sphere and six M atoms (in the square pyramidal sites) in the second coordination sphere.[19]

A satellite feature has been previously observed at about 3.9 or 5.3 eV above the main peak in the Co and Ni $2p_{3/2}$ XPS spectra, respectively, of the elemental metals[6] and metal phosphides discussed in Chapter 7. As seen in Figure 8-3, the Ni $2p_{3/2}$ XPS spectra for the Ni-

containing phosphides examined here also exhibit the same feature. Two explanations, a two-core-hole or a plasmon loss model, have been advanced to account for the origin of these satellites, as has been described in detail elsewhere in this thesis (Chapter 5). The two-core-hole model proposes that the core hole initially generated after photoionization draws conduction states below the Fermi edge into the valence band, which results in two possible final states, depending on whether the conduction state was occupied (corresponding to the main core line) or empty (generating the second hole and corresponding to the satellite peak).[212] The plasmon loss model proposes that the ejected photoelectron loses kinetic energy as it interacts with valence electrons, causing them to oscillate and produce a satellite peak that appears at higher BE.[184] Although some controversy still exists about which model is applicable, both provide useful information about the charge of the metal atoms to the extent that the cross-section of two-core-hole states or the degree of plasmon oscillations is proportional to the number of valence electrons.[120] Figure 8-4 shows a plot of the normalized satellite intensity ($I_{satellite}/I_{core\text{-}line}$) versus the difference in electronegativity between the metals ($\chi_{Ni} - \chi_{M'}$) for Ni_2P and the three $(Ni_{1-x}M_x)_2P$ (M = Cr, Fe, Co) series examined. Relative to Ni metal, the satellite intensity in the Ni-containing phosphides is always lower, indicating less electron density and thus the presence of positively charged Ni atoms. On proceeding from Ni_2P to $(Ni_{1-x}M_x)_2P$, the intensity increases slightly as the electronegativity difference between the metals grows, evidence of the greater electron transfer from M to Ni. Admittedly, the trend is weak because the analysis is somewhat hampered by partial overlap of the satellite peak with the core-line peak, particularly in the $(Ni_{1-x}Co_x)_2P$ series. However, the satellite structure is quite prominent in the $(Ni_{1-x}Cr_x)_2P$ series, where an increase in Cr concentration x also leads to a more intense satellite peak (Figure 8-4),

consistent with expectations of a greater Cr-to-Ni electron transfer and less positively charged Ni atoms.
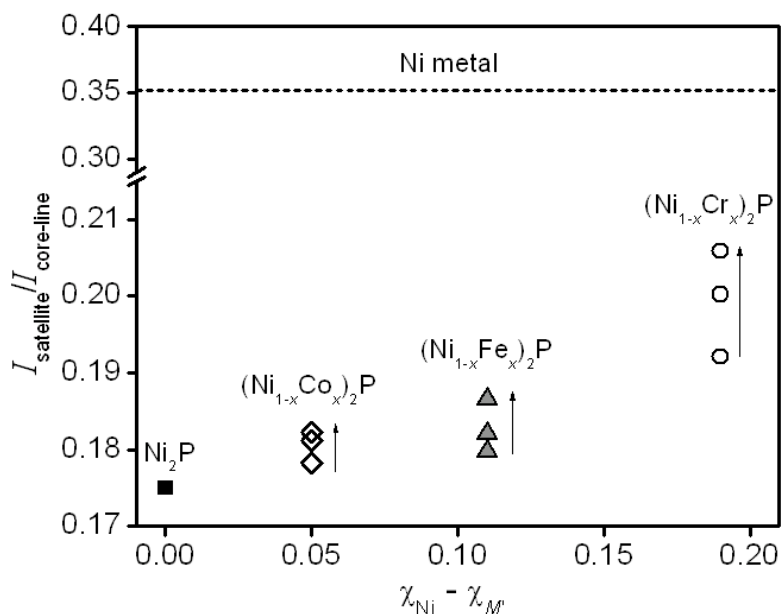
Figure 8-4 Plot of normalized satellite intensity versus the difference in electronegativity between Ni and M for Ni_2P and $(Ni_{1-x}M_x)_2P$ (M = Cr, Fe, Co), with x increasing according to the arrows in each series. The horizontal dashed line corresponds to the satellite intensity for Ni metal.

8.3.3 Metal L- and K-edge XANES spectra

Further evidence for the proposed metal-metal charge transfer may be gained from an examination of the metal L- and K-edge XANES spectra. The metal L-edge corresponds to the dipole-allowed transition of a 2p electron into unoccupied 3d and possibly 4s states ($\Delta l = \pm 1$), with spin-orbit coupling causing a splitting into an L_3- ($2p_{3/2} \rightarrow 3d$) and L_2-edge ($2p_{1/2} \rightarrow 3d$). The L_3-edge is generally sharper and more detailed because of the longer lifetime of the excited state, to which the peak width is inversely proportional.[232] The lineshape is influenced by the metal coordination environment and the intensity by the number of conduction states.[239-241] Although there are two different metal coordination environments in this metal phosphide series,

they cannot be resolved and we present only a qualitative interpretation of the spectra. Moreover, we compare spectra only for those mixed-metal phosphides $(Ni_{1-x}M_x)_2P$ that adopt the same structure type as the parent binary phosphides.

The Ni L-edge spectra for Ni_2P and $(Ni_{0.8}M_{0.2})_2P$ (where any metal-metal charge transfer will be most extreme in each series and adopting the same Fe_2P-type structure) are shown in Figure 8-5a. The intensity (especially clear in the L_3-edge) gradually diminishes through the progression Ni_2P, $(Ni_{0.8}Co_{0.2})_2P$, $(Ni_{0.8}Fe_{0.2})_2P$, and $(Ni_{0.8}Cr_{0.2})_2P$, consistent with the presence of fewer Ni-based conduction states and less positively charged Ni atoms resulting from increasing M-to-Ni electron transfer, confirming the trend seen earlier. Correspondingly, one expects that the M atoms will become more positively charged in the mixed-metal phosphides relative to the parent binary phosphides. The Fe L-edge spectra for Fe_2P and $(Ni_{0.2}Fe_{0.8})_2P$ (both Fe_2P-type structure; Figure 8-5b), and the Co L-edge spectra for Co_2P and $(Ni_{0.2}Co_{0.8})_2P$ (both Co_2P-type structure; Figure 8-5c) reveal that the L_3-edge intensity grows upon increased substitution by Ni, consistent with the presence of more M-based conduction states and more positively charged M atoms. (Cr L-edge spectra were not analyzed because no samples in the $(Ni_{1-x}Cr_x)_2P$ series adopt the same structure as Cr_2P.) Although the spectra exhibit fine structure that may originate from crystal field splitting, identifying which states gain or lose electron density is complicated by the energy overlap of states arising from the mix of tetrahedral and square pyramidal metal sites. For example, the intensities of the two peaks in the Fe L_3-edge are very different between Fe_2P and $(Ni_{0.2}Fe_{0.8})_2P$. The Ni atoms preferentially substitute into the tetrahedral sites, which in turn are surrounded by Fe atoms in the square pyramidal sites. Thus, the largest intensity change in the Fe L_3-edge most likely reflects a change in the charge of those Fe atoms within square pyramidal sites.
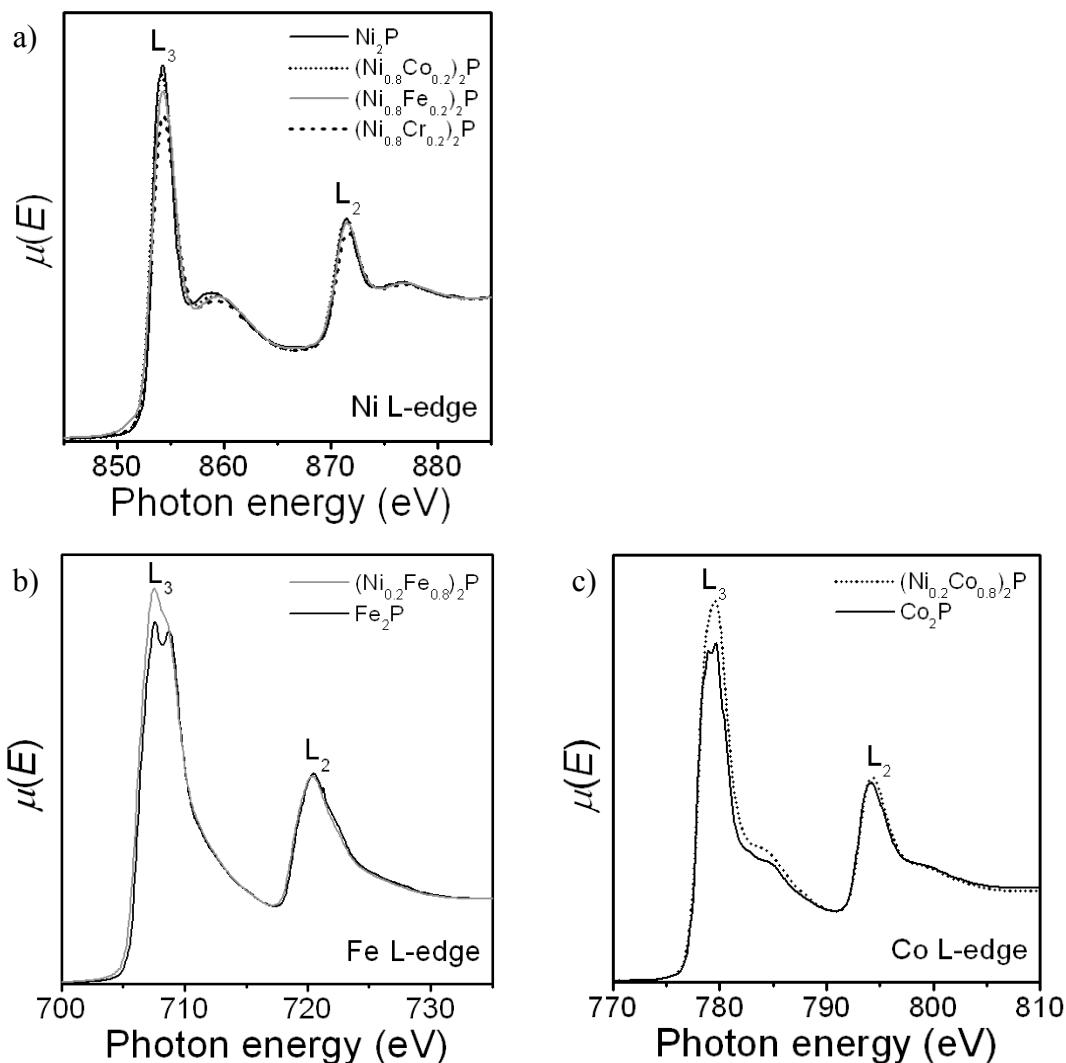
Figure 8-5 Normalized total electron yield (a) Ni, (b) Fe, and (c) Co L-edge XANES spectra for various metal phosphides.

Ni K-edge spectra have been previously measured for Ni_2P and $(Ni_{1-x}Fe_x)_2P$. However, most of these studies have focused primarily on changes to features in the extended X-ray absorption fine structure (EXAFS) during HDS and HDN processes.[116,118] Here, we compare the Ni K-edge spectra of Ni_2P to that of $(Ni_{0.8}Cr_{0.2})_2P$, selected because this contrast should exhibit the most prominent metal-metal charge transfer among the three mixed-metal series while still retaining the same Fe_2P-type structure (Figure 8-6a). The calculated conduction states in the
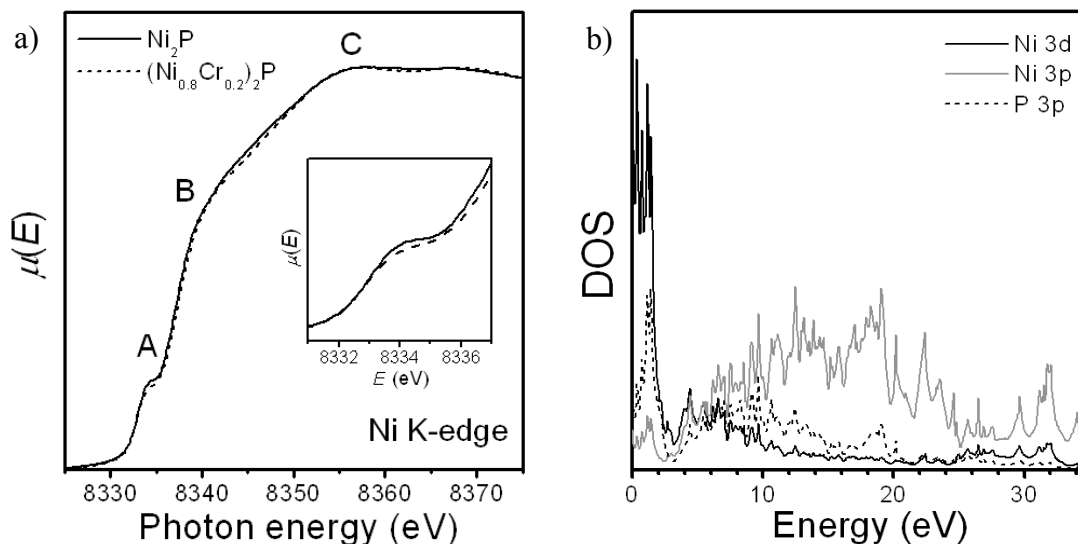
Figure 8-6 (a) Normalized Ni K-edge XANES spectra (measured in transmission mode) for Ni_2P and $(Ni_{0.8}Cr_{0.2})_2P$, with peak assignments (A, B, C) discussed in the text. (b) Orbital projections of the calculated conduction states in the band structure of Ni_2P, with the Fermi edge set to 0 eV.

band structure of Ni_2P (Figure 8-6b) assist in the interpretation. Analogous to the metal K-edge spectra in other metal phosphides, peak A is assigned to be a pre-edge peak, involving a quadrupolar transition of a Ni 1s electron into unoccupied states just above the Fermi edge with predominantly Ni 3d and some P 3p character. At higher absorption energy are two broader peaks that can be assigned as dipole-allowed transitions of a Ni 1s electron into Ni 4p / P 3p (peak B) or mostly Ni 3p states (peak C). Although weaker than the dipolar transitions, the quadrupolar transition corresponding to the pre-edge peak of the Ni K-edge spectra provides similar information as the Ni L-edge spectra above in that both interrogate the unoccupied Ni 3d states.[242] Relative to Ni_2P, the pre-edge peak is less intense in $(Ni_{0.8}Cr_{0.2})_2P$, consistent with an increase in occupied Ni valence states and with the earlier conclusions for the charge transfer from Cr to Ni atoms. This intensity change is less pronounced than that in the Mn K-edge XANES spectra for the P-richer $Mn_{1-x}Co_xP$ and $Mn_{1-x}V_xP$ series,[7] whose MnP-type structure

accommodates octahedral metal sites in contrast to the tetrahedral and square pyramidal sites in the Fe_2P-type structure of Ni_2P and $(Ni_{0.8}Cr_{0.2})_2P$. The pre-edge feature in Figure 8-6a may be assigned as largely a dipole-allowed 1s-to-4p transition, because complexes containing metal atoms in tetrahedral and square pyramidal coordination have been shown to exhibit Ni 4p character in this feature, unlike those in octahedral coordination.[243]

8.3.4 Comparison between $M_{1-x}M'_xP$ and $(Ni_{1-x}M_x)_2P$

Compared to the metal-poorer $M_{1-x}M'_xP$ series reported previously,[7] a key difference in the metal-richer $(Ni_{1-x}M_x)_2P$ series studied here is the lesser degree of metal-metal charge transfer taking place, as manifested by the lack of next-nearest neighbour effects in the P 2p BEs (Figure 8-2), as well as smaller changes in satellite intensity in the Ni $2p_{3/2}$ XPS spectra (Figure 8-4) and in L-edge intensity in the metal L-edge XANES spectra. In both cases, a P charge of about 1– can be estimated based on comparison of the P $2p_{3/2}$ BEs to other phosphorus-containing compounds in various oxidation states. To a first approximation, then, the average charge of the metal atoms will start out less extreme in the metal-richer binary phosphides M_2P (with the formulation "$(M^{0.5+})_2(P^{1-})$" as determined in the previous chapter) than in the monophosphides MP (with the formulation "$M^{1+}P^{1-}$").[6,7] Furthermore, at low levels of substitution in $(Ni_{1-x}M_x)_2P$, the electropositive M atoms preferentially occupy one (square pyramidal) of the two possible metal sites. With less metal-metal charge transfer and smaller changes in the absolute charge on the metal atoms, these factors in turn lead to smaller changes in the Madelung potential $\Delta\sum_{j\neq i}\dfrac{q_j}{r_{ij}}$ that influence the P BEs. Only in the $(Ni_{1-x}Cr_x)_2P$ series,

which exhibits the greatest difference in electronegativity between the dissimilar metal atoms, do significant changes begin to be detected in the metal XANES spectra.

8.4 Conclusion

Unlike the $M_{1-x}M'_xP$ series, next-nearest neighbour effects imparted by the presence of two different metal atoms around a P atom do not play an important role in influencing the shifts in P $2p_{3/2}$ BE and K-edge absorption energy in the metal-richer $(Ni_{1-x}M_x)_2P$ (M = Cr, Fe, Co) series, because of the relatively smaller magnitudes of the metal charges. However, metal-metal charge transfer (from M to Ni) continues to operate, as evidenced by changes in the satellite intensity of the Ni $2p_{3/2}$ XPS spectra and in the metal L- and K-edge XANES spectra. Establishing these trends allows an application to the evaluation of changes in the electronic structure of different and mixed metal phosphides which can be used as catalysts. In particular, enhanced catalytic activity of the binary phosphides Fe_2P and Ni_2P in the course of HDS and HDN processes can be correlated with an increase in P $2p_{3/2}$ BE and K-edge absorption energy.[68] On the other hand, the $(Ni_{1-x}Co_x)_2P$ series exhibits no increase in BE or absorption energy with increasing Co concentration even though there is apparently an enhancement of the catalytic activity for Co-doped Ni_2P.[74] It appears that the support used in these catalytic studies may be something to be considered more closely. In fact, analysis of the P 2p XPS spectra of silica-supported cobalt phosphides suggests that greater metal-to-phosphorus charge transfer takes place in CoP/SiO_2 than in Co_2P/SiO_2.[71] This observation differs from our previous studies which indicate approximately the same charge for P atoms in these compounds. The SiO_2 support may alter the electronic properties of the metal phosphides, perhaps by favouring the deposition of a

preferred orientation of the catalyst, such as the (001) surface of Ni_2P, which exposes a greater

concentration of metal atoms than the bulk average.[73]

Chapter 9

Conclusion

X-ray spectroscopy is an effective experimental technique for probing the electronic structure of solids. Although XPS and XANES have been applied in the past to study metal pnictides, extensions to more complex systems or solid solutions (mixed cation or mixed anion) is more difficult particularly because shifts in BE and absorption energies are very small, sometimes less than 0.1 eV between members in a series. These small shifts, however, reflect the degree of electron transfer and provide information about the bonding character in these compounds. To gain further information about the electronic structure, more advanced interpretation can be made by comparing intensities of satellite peaks, fitting the valence band spectra, and analyzing the fine-structure in XANES. Table 9-1 summarizes the type of electronic information obtained from these analyses.

Table 9-1 Electronic information obtained from XPS and XANES analysis.

Compound	Charge formulation from XPS	Electron transfer	Metallic	3-D/2-D bonding	Agrees with Theory	Interatomic effects
$Zr(Ge_xAs_{1-x})As$			Yes		Yes	
$ZrCuSiPn$		Yes	Yes	3-D	No	
$REMAsO°$	$RE^{3+}M^{2+}As^{3-}O^{2-\,a}$	Yes	Yes	2-D	No	Yes
$(M_{1-x}M'_x)_2P$	$(M_{1-x}M'_x)^{0.5+}_2P^{1-\,b}$	Yes	Yes	3-D	No	Yes
M_3P	$M^{0.33+}_3P^{1-\,b}$	Yes	Yes	3-D	No	Yes

[a] Determined from the fitting of the valence XPS spectra.
[b] Determined from shifts in the P $2p_{3/2}$ BE and Co/Ni $2p_{3/2}$ satellite intensity.

9.1 PbCl$_2$-type compounds

Within the pseudobinary ZrAs$_2$-ZrGe$_2$ system, it has been found that ZrAs$_2$ is a true binary phase (not a Si-stabilized ternary phase) and Zr(Ge$_x$As$_{1-x}$)As, a partially ordered solid solution, adopts the PbCl$_2$-type structure for $0 \leq x \leq 0.4$. No ternary PbFCl-type phase forms, unlike the corresponding Zr(Si$_x$As$_{1-x}$)As series. If the end members of Zr(Ge$_x$As$_{1-x}$)As are simplified as ZrAs$_2$ and Zr(Ge$_{0.5}$As$_{0.5}$)As, their bonding can be rationalized through the Zintl concept, giving the formulations Zr^{2+}As^{0}As^{2-} and Zr$^{2.5+}$(Ge$^{1-}_{0.5}$As$^0_{0.5}$)As^{2-}, respectively. The Zr $3d_{5/2}$ BE suggests that Zr 4d states are occupied, indicating that the Zr atoms are not 4+, whereas the As 3d BE reveals an average oxidation state of 1- for both As atoms. Although two peaks (for As^0 and As^{2-}) would have been expected in the As 3d XPS spectra based on the Zintl approximation, they cannot be resolved. As the FWHM of the As 3d core-line peaks were similar to those in other compounds presented in this thesis, it is likely that the two As atoms have the same oxidation state.

9.2 ZrCuSiAs-type compounds

The ability of X-ray spectroscopy to distinguish between ionic and covalent bonding character is best illustrated in the analysis of the ZrCuSiAs-type compounds, which may be viewed in a first approximation as consisting of alternating [ZrSi] and [Cu*Pn*] layers in ZrCuSi*Pn*, and alternating [*RE*O] and [*MPn*] layers in *REMPn*O. The charge formulation of Zr^{4+}Cu^{1+}Si^{2-}*Pn*$^{3-}$ was shown by XPS and XANES analysis to be too simplistic. Similar to the case in Zr(Ge$_{1-x}$As$_x$)As, the Zr $3d_{5/2}$ BE is smaller than predicted for Zr^{4+}. Likewise, the Si $2p_{3/2}$, As $3d_{5/2}$, and P $2p_{3/2}$ BEs shifted less than expected. These small BE shifts are attributed to strong covalency between [ZrSi] and [Cu*Pn*] layers. Further evidence of interlayer bonding is

shown in the Cu K-edge and Zr K/L-edge XANES spectra. Replacing As with P resulted in greater Cu-to-*Pn* and Zr-to-*Pn* charge transfer, a strong indication that bonding in ZrCuSi*Pn* is 3-dimensional.

In contrast, The [*RE*O] and [*M*As] layers in *REM*AsO are separated by more than 3 Å, and the charge formulation $RE^{3+}M^{2+}As^{3-}O^{2-}$ is proposed. The [*RE*O] layer contains RE^{3+} (as found in the *RE* 3d XPS) and O^{2-} (as found by O 1s BE), with considerable ionic character. The [*M*As] layer contain cationic *M* (as found from satellites), and anionic As atoms (as found from As $3d_{5/2}$ BE) but they are not as highly charged as expected. The asymmetric line shape of the *M* 2p XPS spectra confirms the presence of delocalized valence electrons. Thus there is considerable covalent, delocalized bonding in the [*M*As] layer. The DOS curves also reveal that the M and As states are much broader than the La and O states. To our knowledge, this is the first demonstration of distinctly different bonding character for the substructure of a complex solid through X-ray spectroscopy.

Chapter 5 and Chapter 6 explored the effects of altering bonding in the [*RE*O] layer (substituting the *RE* atom) and [*M*As] layer (substituting the *M* atom), respectively. Shifts in the As $3d_{5/2}$ and O 1s BEs were explained using the charge potential model. Intraatomic effects (change in As charge) dominated the shifts in the As 3d core-line XPS spectra, whereas interatomic effects (change in *RE* size) dominated the shifts in the O 1s core-line XPS spectra. Interestingly, altering the electronic structure of one layer has no effect on the other, confirming the two-dimensionality of the *REM*AsO structure, which is believed to be critical to its superconducting properties. In general, it has been found that the critical temperature (T_C) increases in the Fe*Pn*-based superconductors as the distance between [Fe*Pn*] layers increases, suggesting that T_C is tunable.[244] Given that Fe 3d levels are believed to be the superconducting

states, greater delocalization of valence electrons near the Fermi edge may enhance their movement along the surface, inducing superconductivity.[41] It is possible that greater covalency in the [MAs] layer may result in a larger T_C.

9.3 M_2P- and M_3P-type compounds

The analysis of the metal-rich phosphides (M_2P, ($M_{1-x}M'_x$)$_2$P, and M_3P; M, M' = Cr-Ni) extends previous work on the monophosphides (MP, $M_{1-x}M'_x$P).[7,8] The XPS and XANES spectra support the formulations ($M^{0.5+}$)$_2$P^{1-} and ($M^{0.33+}$)$_3$P^{1-}, with the P 2p$_{3/2}$ BE and K-edge absorption energy decreasing as M becomes more electronegative, an indication of increasing ionic character in the M–P bond. In contrast to the monophosphides, for which the shifts in P BEs and absorption edge energies agree well with the formulation M^{1+}P^{1-} derived from the Zintl concept,[6] the more metal-rich phosphides M_2P and M_3P experience additional interatomic effects that induce secondary variations in the BE and absorption energy shifts. The strong delocalization of valence electrons arising from M–M bonding in these metal-rich phosphides is confirmed by the lineshape in the M 2p XPS spectra.

These spectroscopic results lead to interesting implications about the catalytic mechanism of Ni$_2$P doped with other metals, such as Co, in HDS and HDN processes.[74] It has been proposed that the catalytic activity increases as the M–P bond becomes more covalent, enhancing the backbonding of P to the C atoms of the S- or N-containing substrate in the HDS and HDN mechanism.[73] However, our results show that Co-substituted Ni$_2$P does not significantly enhance the covalent character of the M–P bond. Although we initially suggested that charge transfer between the metal phosphides and the silica substrate may play a role in the catalytic process, a recent study by Bussell and co-workers has shown that the P 2p$_{3/2}$ BEs in (Ni$_{1-x}$Fe$_x$)$_2$P

are similar in the bulk as well as when they are supported on silica.[245] The electronic effects of the substrate may still well be negligible. Rather, as shown by XPS and XANES analysis on the mixed-metal phosphides $(Ni_{1-x}M_x)_2P$, the Ni atoms may be gaining electron density through a metal-metal interaction from other M atoms. That is, the enhanced catalytic activity of Co-doped Ni_2P may likely be arising from a Co-to-Ni charge transfer.

9.4 Co and Ni 2p satellite features

A recurring feature that illustrates the complexities of interpreting XPS spectra is the satellite peak always found in conjunction with the Co or Ni 2p core-line peak. This satellite peak was exploited to extract information about the charge of the Co or Ni atoms in various compounds analyzed in this thesis, even when the BE of the core-line peak itself undergoes no apparent shift. The physical origin of this satellite has been much debated in the literature, and two competing explanations have emerged: a two-core-hole or a plasmon loss model (section 5.3.1). For many years, the two-core-hole model was generally accepted. However, Grosvenor and co-workers recently observed plasmon features in the REELS spectra of Ni and Co metal,[6,213] suggesting that the plasmon loss model could provide a viable alternative explanation of the satellite peaks. The satellite peak can be fitted to two components corresponding to surface and bulk plasmon oscillations at energies in the expected ratio of $1:\sqrt{2}$.[231] Subsequently, Oppeneer and co-workers have revealed a satellite peak above the 1s core-line in the hard X-ray photoelectron spectrum of Ni metal.[246] The shift in BE of the satellite relative to its core-line peak is less in 1s than in 2p.[246] This observation is consistent with the two-core-hole model (since a 1s core-hole has less influence than a 2p core-hole on the valence electrons and thus is less effective in pulling 3d conduction states below the Fermi edge). It is not consistent

with the plasmon loss model (since the number of valence electrons scattering the photoelectron is the same and the satellite BE is independent of the core-shell).

Comparison of the Co and Ni 2p satellites in most samples studied in this thesis (Co metal, Ni metal, Co_2P, Ni_2P, LaCoAsO, CeNiAsO) presents conflicting evidence for both models. The general observation is that the difference in BE between the core-line and its satellite is smaller for Co 2p than for Ni 2p. This is consistent with the plasmon loss model (since fewer valence electrons in Co cause less scattering of the photoelectron, increasing its KE and lowering the BE) but not with the two-core-hole model (since fewer valence electrons in Co would reduce screening of the core-hole, allowing more conduction states to fall below the Fermi edge, thereby raising the BE of the Co 2p satellite). In the special case of the Ni-rich phosphides (Ni_2P and Ni_3P), the observation is that the BE of the satellite relative to the Ni 2p core-line follows an opposite trend with decreasing valence electrons: Ni metal < Ni_3P < Ni_2P. Here, surprisingly, the plasmon loss model fails (fewer valence electrons result in the photoelectron having a higher KE and thus lower BE) but the two-core-hole model works (fewer valence electrons provide reduced screening of the core-hole, allowing more conduction states to fall below the Fermi edge and increasing the BE)! Finally, no BE shifts were observed in the Co 2p satellites for any of the Co-containing compounds. All these observations tend to suggest that other factors, such as shake-up processes and crystal structure differences, may well play important roles, but these remain poorly understood.

In the plasmon loss model, a further distinction can be made between intrinsic and extrinsic mechanisms. When this model has been applied in this thesis, it has been assumed that the plasmon loss is extrinsic, as the photoelectron undergoes inelastic scattering and interactions with the valence band. But the possibility must also be allowed that the plasmon loss can be

intrinsic, as the core-hole can also interact with the valence electrons. Extrinsic plasmon loss tends to dominate in both the bulk and surface, whereas intrinsic plasmon loss occurs more often in the surface, as shown in several theoretical studies on Al metal.[247] Although we have not carried out similar calculations for the contributions of extrinsic vs intrinsic plasmon loss for the Co and Ni 2p satellites, we note that these satellites generally exhibit a symmetrical lineshape consistent with extrinsic plasmon loss. (In contrast, an asymmetric lineshape arises from intrinsic plasmon loss because of the Doniach-Šunjić process.[248]) However, competing evidence for intrinsic plasmon loss is shown by no change in intensity in the angle-resolved XPS spectrum of Co metal (not shown); the plasmon intensity should be independent of the take-off angle since intrinsic plasmon loss does not depend on scattering of the outgoing photoelectron.

The discussion above indicates that one model alone is insufficient to explain the Co and Ni 2p satellite features in all instances (Table 9-2). It is likely that the satellites result from various degrees of mixing of plasmon loss (both extrinsic and intrinsic) and a two-core-hole final state. Given the difference in lineshape and BE shifts of these satellites, the degree of mixing probably differs in Co and Ni metal. In this thesis, we have related the charge in the metal atom to the satellite intensity, which is predicted to be proportional to the valence electron concentration in either model (including extrinsic and intrinsic plasmon loss).[120,248] That is, the same information about the metal charge can be extracted no matter which model is applied.

9.5 Limitations of XPS and XANES

XPS and XANES are powerful techniques that can be used to extract important information about the electronic structure of solids, providing experimental evidence for bonding type, oxidation state, metallic behaviour, and charge transfer effects. However, they do have

Table 9-2. A summary of the feature of the Co and Ni 2p satellite that supports plasmon loss model and two-core-hole fin al state.

Observation	Plasmon loss model	Two-core-hole final state
REELS on Co and Ni metal	✓	✗
Comparison of Ni 1s and Ni 2p satellites	✗	✓
Comparson of Co 2p and Ni 2p satellites	✓	✗

some limitations when applied to intermetallic phases, which have bonding character that is highly metallic (i.e., delocalized) or polar covalent. The chief difficulty is that the charge on an atom is not trivially related to the BE shift. For the phosphides and arsenides examined, it is true that the core-line peaks shift to lower BE (relative to the element), confirming the presence of anionic P or As atoms. In the phosphides M_2P and M_3P, the correct relative charges of P are obtained if a linear relationship to BE is assumed. In the arsenide oxides, REMAsO, however, similar assumptions lead to As^{3-} if the As K-edge XANES and valence band XPS spectra are analyzed but As^{1-} if the As $3d_{5/2}$ BE is analyzed. This apparent discrepancy illustrates the care that must be taken in interpreting energy shifts. Core-line XPS BEs measure how energy levels are influenced by the screening that an atom experiences in a specific environment; as such, they reflect the polarity of the bonds formed by this atom, that is, the degree of ionic vs. covalent character. As illustrated for the P $2p_{3/2}$ and As $3d_{5/2}$ BEs (Figure 9-1), larger shifts are experienced by the more electronegative P atoms, which are able to participate in more polar bonds.

a)

Covalent
Bonding

Ionic
Bonding

Decreasing P 2p$_{3/2}$ BE

b)

Covalent
Bonding

Ionic
Bonding

Decreasing As 3d$_{5/2}$ BE
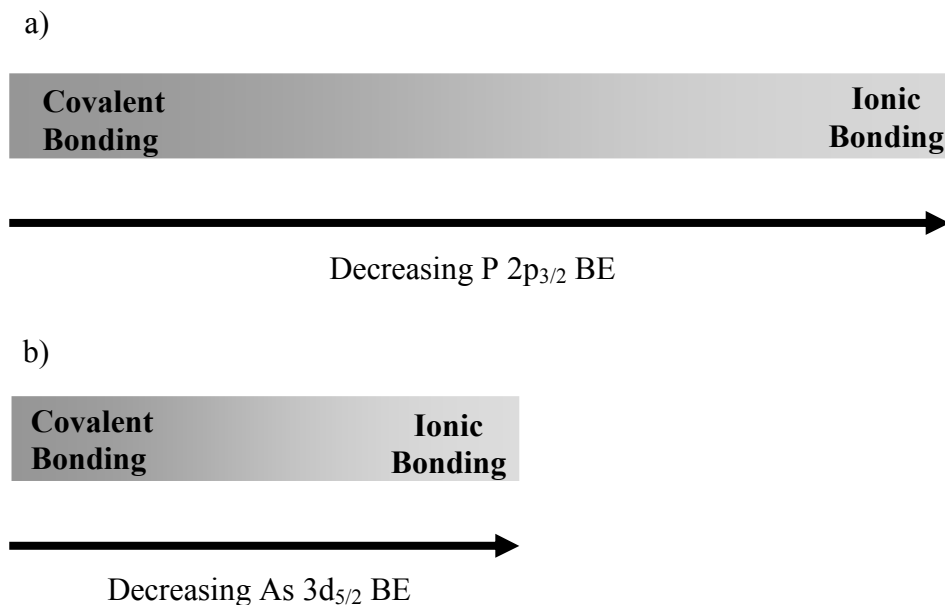
Figure 9-1 Correlation between bonding character and (a) P 2p$_{3/2}$, and (b) As 3d$_{5/2}$ BE shifts.

X-ray spectroscopy can be used to detect subtle charge transfer effects. This was first demonstrated in the transition-metal phosphides MP and their mixed-metal counterparts $M_{1-x}M'_xP$ (M' is more electronegative than M),[6,7] where the expected M-to-P and M-to-M' charge transfers were observed. The more metal-rich phosphides M_2P and M_3P also show evidence of M-to-P charge transfer (Figure 9-2a), but the smaller shifts imply less polar character in the M–P bonds. In even more complex phases studied in this thesis, XANES analysis indicated Zr-to-Pn and Cu-to-Pn charge transfer in ZrCuSiPn (Figure 9-2b), and M-to-As (and possibly RE-to-O) charge transfer in $RE M$AsO (Figure 9-2c). The small shifts (<0.3 eV) in the O 1s and As 3d$_{5/2}$ BEs refect the smaller electronegativity difference with the RE atoms and the more covalent character of the M–As bonds. The [REO] and [MAs] substructures are essentially isolated in $RE M$AsO, whereas the [ZrSi] and [CuPn] substructures interact through Zr–Pn bonds in ZrCuSiPn.

a) M_2P, M_3P, $(M_{1-x}M'_x)_2P$

M　　　**P**　　　**M′**

b) ZrCuSi*Pn*

Si　　　**Zr**　　　***Pn***　　　**Cu**

c) *REM*AsO

O　　　***RE***　　　**As**　　　**M**
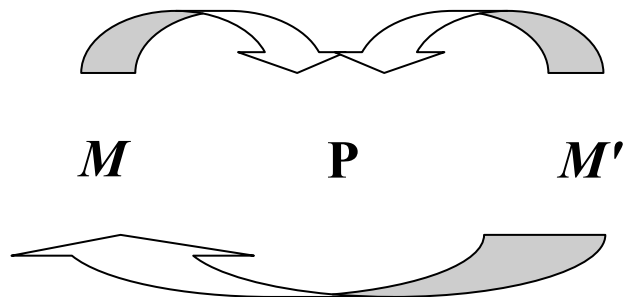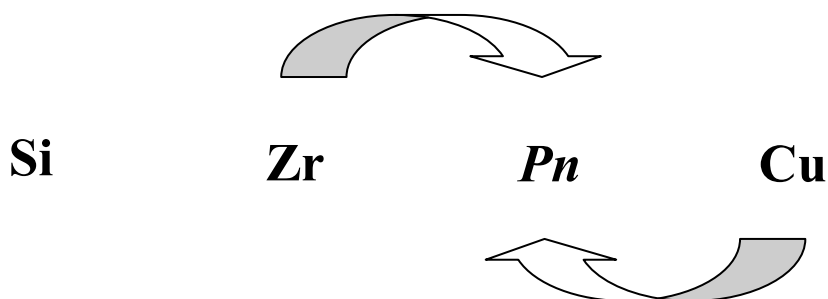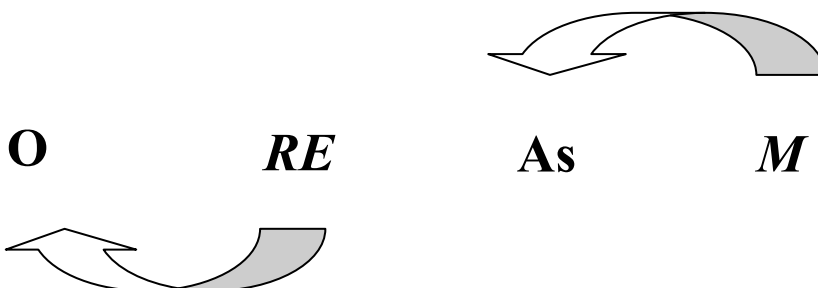
Figure 9-2 Charge transfer effects that are observed in (a) ZrCuSi*Pn*, (b) *REM*AsO, and (c) M_2P, M_3P, and $(M_{1-x}M'_x)_2P$.

Mixed-metal systems present the possibility for a secondary electron transfer between two different metal atoms. Unlike the monophosphides $M_{1-x}M'_xP$, where interatomic effects (M-to-M' charge transfer) arising from the difference in electronegativity between M and M' lead to shifts in the P $2p_{3/2}$ BE and K-edge absorption energy,[7] similar next-nearest neighbour effects

were not observed in $(M_{1-x}M'_x)_2P$ and $REM_{1-x}M'_xAsO$. For $(M_{1-x}M'_x)_2P$, only intraatomic effects are needed to account for the shifts in BE and absorption energy, notwithstanding the evidence of M-to-M' charge transfer from the Ni K/L-edge XANES spectra. This apparent absence of next-nearest neighbour effects may be attributed to the smaller magnitude of charges on the M and M' atoms, and possibly preferential occupation of these atoms. For $REM_{1-x}M'_xAsO$, extensive electron delocalization within the [MAs] layer likely reduces M-to-M' charge transfer. In general, we conclude that next-nearest neighbour effects are much less prominent in intermetallic phases that exhibit high electronic delocalization and significant metallic bonding.

Finally, it is important to distinguish between the charges determined from X-ray spectroscopic analysis and those derived from simple electron-counting schemes. In the Zintl concept, full electron transfer is assumed from the electropositive component to the electronegative component; charges are necessarily integral and always overestimated relative to the true values. In intermetallic phases, electronic delocalization tends to lead to intermediate, less extreme charge distributions. Analysis of the valence band spectra, which can be fitted to states of component atoms, is a way to recover charges that correspond to expectations from the Zintl concept, as was shown earlier for MP.[6] However, this procedure becomes increasingly more difficult for compounds with significant covalency, for which the component atomic states in the valence band will be much broader, a reflection of the greater electronic delocalization, as demonstrated in the fitting of the valence band XPS spectra for REMAsO. An important general conclusion is that charges obtained from core-line XPS BEs are influenced by screening effects of delocalized valence electrons, whereas charges obtained by fitting valence band spectra to component states are derived from the number of valence electrons associated with each atom.

9.6 Future studies

The results presented here have highlighted the successful application of X-ray spectroscopy to resolve questions about bonding and electronic structure in solid-state chemistry. In particular, even complex intermetallic phases can be analyzed through detailed interpretation of these spectra. Several systems merit further investigation. For example, although the effects of metal substitution in M_2P have now been clarified through the study of $(M_{1-x}M'_x)_2$P, the corresponding effects of pnicogen substitution through the study of $M_2(As_{1-y}P_y)$ are still not well understood. Unlike the monopnictides, $MAs_{1-y}P_y$, which contain an extensive Pn–Pn bonding network,[8] the more metal-rich pnictides, $M_2As_{1-y}P_y$, lack Pn–Pn bonds. Furthermore, given that there are two metal sites in $M_2As_{1-y}P_y$, it is not known how Pn substitution will affect M-to-Pn charge transfer. Eventually, these studies could lead to investigation of more complicated quaternary systems ($(M_{1-x}M'_x)_2As_{1-y}P_y$) where M and Pn substitution will allow us to "tune" the electronic properties of these materials.

Among the quaternary ZrCuSiAs-type materials, only three silicide pnicitides are known so far.[13,132] Given their potential applications as high temperature superconductors, it is wothwhile to attempt the preparation of related compounds. On the basis of different combinations of quaternary phases in the (Ti, Zr, Hf)-(Cu-Ag)-(Si-Ge-Sn)-(P-As-Sb) system, there are potentially 51 new compounds that could form this structure type. Altering the size of the atoms in these compounds may destroy the 3-dimensional bonding network and possibly affect the electronic structure of these materials. Recent efforts by an undergraduate student (Alyson Baergen) in our group have resulted in the discovery of ZrCuGeAs and HfCuGeAs, with electronic properties very similar to those of ZrCuSiAs.

The more numerous "layered" representatives of the ZrCuSiAs-type phases present attractive opportunities to explore the relationship between structure and electronic properties. From our results, it is clear that the distance between the two layers influences the bonding character (ionic vs. covalent) and possibly the superconducting behaviour of the pnictide oxides *REMPn*O. Several related layered Fe-containing pnictides that do not adopt the ZrCuSiAs-type structure (such as Li_xFeAs, $BaFe_2As_2$, $Sr_4Sc_2Fe_2P_2O_6$) exhibit superconductivity. Given that T_C increases as the [Fe*Pn*] layers become further apart,[244] we propose that covalent character also increases within their layers. This correlation could be probed through appropriate X-ray spectroscopic experiments.

References

(1)   Pauling, L. *The Nature of the Chemical Bond, 3rd ed*; Cornell University Press; Ithaca: NY, 1960.

(2)   Sauthoff, G. *Intermetallics*; VCH: Wienheim, 1995.

(3)   Grosvenor, A.P.; Cavell, R.G.; Mar, A. *Structure and Bonding* **2009**, *133*, 41-92.

(4)   Jeitschko, W.; Braun, D.J. *Acta Cryst.* **1978**, *B34*, 3196-3201.

(5)   Rundqvist, S. *Acta. Chem. Scand.* **1962**, *16*, 1-19.

(6)   Grosvenor, A.P.; Wik, S.D.; Cavell, R.G.; Mar, A. *Inorg. Chem.* **2005**, *44*, 8988-8996.

(7)   Grosvenor, A.P.; Cavell, R.G.; Mar, A. *J. Solid State Chem.* **2007**, *180*, 2702-2712.

(8)   Grosvenor, A.P.; Cavell, R.G.; Mar, A. *J. Solid State Chem.* **2008**, *181*, 2549-2558.

(9)   Müller, U. *Inorganic structural chemistry*, 2nd ed; Wiley: C*hichester*, 2007.

(10)   Kauzlarich, S.M., Ed. *Chemistry, Structure, and Bonding in Zintl Phases and Ions;* VCH Publishers: New York, 1996.

(11)   Gaultois, M.W.; Grosvenor, A.P.; Blanchard, P.E.R.; Mar, A. *J. Alloys Compd.* **2009**, *492*, 19-25.

(12)   Papoian, G.A.; Hoffmann, R. *Angew. Chem. Int. Ed.* **2000**, *39*, 2408-2448.

(13)   Johnson, V.; Jeitschko, W. *J. Solid State Chem.* **1974**, *11*, 161-166.

(14)   Huheey, J.E.; Keiter, E.A.; Keiter, R.L. *Inorganic Chemistry: Principles of Structure and Reactivity,* 4th Ed; Harper Collins: New York, 1993.

(15)   Hoffmann, R. *Angew. Chem. Int. Ed. Engl.* **1987**, *26*, 846-878.

(16)   Dronskowski, R. *Computational Chemistry of Solid State Materials*; Wiley-VCH: Weinheim, 2005.

(17)   Andersen, O.K. *Phys. Rev. B* **1975**, *12*, 3060-3083.

(18)   Rundqvist, S. *Acta. Chem. Scand.* **1962**, *16*, 992-998.

(19)   Pecharsky, V.K.; Zavalij, P.Y. *Fundamentals of Powder Diffraction and Structural Characterization of Materials*; Kluwer Academic Publishers: Boston, 2004.

(20)   Glusker, J.P.; Trueblood, K.N. *Crystal Structure Analysis: A Primer*, 3rd Ed.; Oxford University Press: New York, 2010.

(21)   Sheldrick, G.M. *SHELXTL, version 6.12*, Burker AXS Inc., Madison, WI, 2001.

(22)   Massa, W. *Crystal Structure Determination*, 2nd Ed.; Springer-Verlag: Berlin, 2004.

(23)   Rietveld, H. *J. Appl. Crystallogr.* **1969**, *2*, 65-71.

(24)   Rodriguez-Carvajal, J. *Phys. B* **1993**, *55*, (www.ccp14.ac.uk/tutorial/fullprof/index.html).

(25)   Hunter, B. *LHPM-Rietica,* version 1.7.7, International Union of Crystallography Commission on Powder Diffration Newsletter, no. 20 (summer), 1998 (www.rietica.org).

(26)   Reehuis, M.; Jeitschko, W. *J. Phys. Chem. Solids.* **1990**, *51*, 961-968.

(27)   Zimmer, B.I.; Jeitschko, W.; Albering, J.H.; Glaum, R.; Reehuis, M. *J. Alloys Compd* **1995**, *229*, 238-242.

(28)   Kamihara, Y.; Hiramatsu, H.; Hirano, M.; Kawamura, R.; Yanagi, H.; Kamiya, T.; Hosono, H. *J. Am. Chem. Soc.* **2006**, *128*, 10012-10013.

(29)   Yanagi, H.; Watanabe, T.; Kodama, K.; Iikubo, S.; Shamoto, S.I.; Kamiya, T.; Hirano, M.; Hosono, H. *J. Appl. Phys.* **2009**, *105*, 093916/1-093916/8.

(30)   Yanagi, H.; Kawamura, R.; Kamiya, T.; Kamihara, Y.; Hirano, M.; Nakamura, T.; Osawa, H.; Hosono, H. *Phys. Rev. B* **2008**, *77*, 224431/1 - 224431/7.

(31)   Takahashi, H.; Igawa, K.; Arii, K.; Kamihara, Y.; Hirano, M.; Hosono, H. *Nature* **2008**, *453*, 376-378.

(32)   West, A. R. *Basic Solid State Chemistry*, 2nd ed.; Wiley: New York, 1999 .

(33)   Watanabe, T.; Yanagi, H.; Kamiya, T.; Kamihara, Y.; Hiramatsu, H.; Hirana, M.; Hosono, H. *Inorg. Chem.* **2007**, *46*, 7719-7721.

(34)   Li, Z.; Chen, G.F.; Dong, J.; Li, G.; Hu, W.Z.; Wu, D.; Su, S.K.; Zheng, P.; Xiang, T.; Wang, N.L.; Luo, J.L. *Phys. Rev. B* **2008**, *78*, 060504/1 - 060504/4.

(35)   Bardeen, J.; Cooper, L.N.; Schrieffer, J.R. *Phys. Rev.* **1957**, *108*, 1175-1204.

(36)   Boeri, L.; Dolgov, O.V.; Golubov, A.A. *Phys. Rev. Lett.* **2008**, *101*, 026403/1-026403/4.

(37)   Bednorz, J.G.; Müller, K.A. *Z. Physik, B* **1986**, *64*, 189-193.

(38)   Chu, C.W.; Gao, L.; Chen, F.; Huang, Z.J.; Meng, R.L.; Xue, L.L. *Nature* **1993**, *365*, 323-325.

(39)   Kamihara, Y.; Hirano, M.; Yanagi, H.; Kamiya, T.; Saitoh, Y.; Ikenaga, E.; Kobayashi, K.; Hosono, H. *Phys. Rev. B* **2008**, *77*, 214515/1 - 214515/9.

(40)   Randeria, M.; Trivedi, N. *J. Phys. Chem. Solids* **1998**, *59*, 1754-1758.

(41)   Sato, T.; Nakayama, K.; Sekiba, Y.; Arakane, T.; Terashima, K.; Souma, S.; Takahashi, T.; Kamihara, Y.; Hirano, M.; Hosono, H. *J. Phys. Soc. Jpn. Suppl. C* **2008**, *77*, 65-68.

(42)   Ikeda, H. *J. Phys. Soc. Jpn.* **2008**, *77*, 123707/1-123707/4.

(43)   Ishida, Y.; Shimojima, T.; Ishizaka, K.; Kiss, T.; Okawa, M.; Togashi, T.; Watanabe, S.; Wang, X.; Chen, C.; Kamihara, Y.; Hirano, M.; Hosono, H.; Shin, S. *J. Phys. Jpn. Suppl. C* **2008**, *77*, 61-64.

(44)   Lu, D. H.; Yi. M.; Mo, S.K.; Erickson, A.S.; Analytis, J.; Chu, J.H.; Singh, D.J.; Hussain, Z.; Geballe, T.H.; Fisher, I.R.; Shen, Z.X. *Nature* **2008**, *455*, 81-84.

(45)   Mazin, I.I.; Singh, D.J.; Johannes, M.D.; Du, M.H. *Phys. Rev. Lett.* **2008**, *101*, 057003/1-057003/4.

(46)   Wang, C.; Li, L.; Chi, S.; Zhu, Z.; Ren, Z.; Li, Y.; Wang, Y.; Lin, X.; Luo, Y.; Jiang, S.; Xu, X.; Cao, G.; Xu, Z. *Europhys. Lett.* **2008**, *83*, 67006/1 - 67006/4.

(47)   Ma, Y.W.; Gao, Z.S.; Wang, L.; Qi, Y.P.; Wang, D.L.; Zhang, X.P. *Chin. Phys. Lett.* **2009**, *26*. 037401/1 - 037401/4.

(48)   Ren, Z.A.; Yang, J.; Lu, W.; Yi, W.; Che, G.C.; Dong, X.L.; Sun, L.L.; Zhao, Z.X. *Mater. Res. Innovations* **2008**, *12*, 105-106.

(49)   Ren, Z. A.; Yang, J.; Lu, W.; Yi, W.; Shen, X.L.; Li, Z.C.; Che, G.C.; Dong, X.L.; Sun, L.L.; Zhou, F.; Zhao, Z.X. *Europhys. Lett.* **2008**, *82*, 57002/1 - 57002/4.

(50)   Cheng, P.; Fang, L.; Yang, H.; Zhu, X.; Mu, G.; Luo, H.; Wang, Z.; Wen, H.. *Sci. China Ser. G* **2008**, *51*, 719-722.

(51)   Wen, H.H.; Mu, G.; Fang, L.; Yang, H.; Zhu, X. *EPL* **2008**, *82*, 17009/1=17009/6.

(52)   Wang, C.; Li, Y.K.; Zhu, Z.W.; Jiang, S.; Lin, X.; Luo, Y.K.; Chi, S.; Li, L.J.; Ren, Z.; He, M.; Chen, H. Wang, Y.T.; Tao, Q.; Cao, G.H.; Xu, Z.A. *Phys. Rev. B* **2009**, *79*, 054521/1 - 054521/9.

(53)   Yessik, M. *Phil. Mag.* **1978**, *17*, 623.

(54)   Bailey, R.E.; Duncan, J.F. *Inorg. Chem.* **1967**, *6*, 1444-1447.

(55)   Meyer, A.J.P.; Cadeville, M.C. *J. Phys. Soc. Jpn.Suppl. B* **1962**, *17*, 223-225.

(56)   Chiba, S. *J. Phys. Soc. Jpn.* **1960**, *15*, 581-585.

(57)   Fujii, H.; Hōkabe, T.; Kamigaichi, T.; Okamoto, T. *J. Phys. Soc. Jpn.* **1977**, *43*, 41-46.

(58)   Fujii, H.; Komura, S.; Takeda, T.; Okamoto, T.; Ito, Y.; Akimitsu, J. *J. Phys. Soc. Jpn.* **1979**, *46*, 1616-1621.

(59)   Fujii, S.; Ishida, S.; Asano, S. *J. Phys. F: Met. Phys.* **1988**, *18*, 971-980.

(60)   Bacmann, M.; Fruchart, D.; Chenevier, B.; Fruchart, R.; Puertolas, J.A.; Rillo, C. *J. Magn. Magn. Mater.* **1990**, *83*, 313-314.

(61)   Fujii, H.; Hōkabe, T.; Fujiwara, H.; Okamoto, T. *J. Phys. Soc. Jpn.* **1978**, *44*, 96-100.

(62)   Cam Thanh, D.T.; Brück, E.; Tegus, O.; Klaasse, J.C.P.; Buschow, K.H.J. *J. Magn. Magn. Mater.* **2007**, *310*., e1012-e1014

(63)   Tegus, O.; Brück, E.; Buschow, K.H.J.; de Boer, F.R. *Nature* **2002**, *415*, 150-152.

(64)   Gschneidner Jr., K.A.; Pecharsky, V.K. *Ann. Rev. Mater. Sci.* **2000**, *30*, 387-429.

(65)   Brück, E. *J. Phys. D: Appl. Phys.* **2005**, *38*, R381-R391.

(66)   Pecharsky, V.K.; Gschneidner Jr., K.A. *Phys. Rev. Lett.* **1997**, *78*, 4494-4497.

(67)   Balli, M.; Fruchart, D.; Gignoux, D.; Tobola, J.; Hlil, E.K.; Wolfers, P.; Zach, R. *J. Magn. Magn. Mater.* **2007**, *316*, 358-360.

(68)   Oyama, S.T. *J. Catal* **2003**, *216*, 343-352.

(69)   Chen, J.; Zhou, S.; Ci, D.; Zhang, J.; Wang, R.; Zhang, J. *Ind. Eng. Chem. Res.* **2009**, *48*, 3812-3819.

(70)   Stinner, C.; Prins, R.; Weber, T. *J. Catal.* **2001**, *202*, 187-194.

(71)   Burns, A.W.; Layman, K.A.; Bale, D.H.; Bussell, M.E. *Appl. Catal. A: Gen.* **2008**, *343*, 68-76.

(72)   Zuzaniuk, V.; Prins, R. *J. Catal.* **2003**, *219*, 85-96.

(73)   Lui, P.; Rodriguez, J.A.; Asakura, T.; Gomes, J.; Nakamura, K. *Phys. Chem. B* **2005**, *109*, 4575-4583.

(74) Abu, I.I.; Smith, K.J. *J. Catal.* **2006**, *241*, 356-366.

(75) Sawhill, S.J.; Layman, K.A. Van, D.R. *J. Catal.* **2005**, *215*, 300-313.

(76) Lee, Y.K.; Oyama, S.T. *Stud. Surf. Sci. Catal.* **2006**, *159*, 357-360.

(77) Henkes, A.E.; Vasquez, Y.; Schaak, R.E. *J. Am. Chem. Soc.* **2007**, *129*, 1896-1897.

(78) Chiang, R.K.; Chiang, R.T. *Inorg. Chem.* **2007**, *46*, 369-371.

(79) Liu, X.; Chen, J.; Zhang, *Catal. Commun.* **2007**, *8*, 1905-1909.

(80) Landau, M.V.; Herskowitz, M.; Hoffman, T.; Fuks, D.; Liverts, E.; Vingurt, D.; Froumin, N. *Ind. Eng. Chem. Res.* **2009**, *48*, 5239-5249.

(81) Zuzaniuk, V.; Stinner, C.; Prins, R.; Weber, Th. *Stud. Surf. Sci. Catal.* **2000**, *143*, 247-255.

(82) Pfeiffer, H.; Tancret, F.; Brousse, T. *Mater. Chem. Phys.* **2005**, *92*, 534-539.

(83) Hou, K.H.; Jeng, M.C.; Ger, M.D. *J. Alloys Compd.* **2007**, *437*, 289-297.

(84) Moretzki, O.; Morgenroth, W.; Skála, R.; Szymanski, A.; Wendschuh, M.; Geist, V. *J. Synchrotron Radiat.* **2005**, *12*, 234-240.

(85) Gambino, R.J.; McGuire, T.R.; Nakamura, Y. *J. Appl. Phys.* **1967**, *38*, 1253-1255.

(86) Briggs, D.; Seah, M.P., Eds. *Practial Durface Analysis Volume 1: Auger and X-ray Photoelectron Spectroscopy,* 2nd Ed.; Wiley: Chichester, 1990.

(87) Briggs, D. *Surface Analysis of Polymers by XPS and Static SIMS*; Cambridge University Press: Cambridge, 2005.

(88) Watts, J.F.; Wolstenholme, J. *An Introduction to Surface Analysis by XPS and AES*; Wiley: Rexdale, 2003.

(89) Carlson, T.A. *Photoelectron and Auger Spectroscopy*; Plenum Press, New York, 1975.

(90) Wagner, C.D.; Gale, L.H.; Raymond, R.H. *Anal. Chem.* **1979**, *51*, 466-482.

(91) Moretti, G. *J. Electron Spectrosc. Relat. Phenom.* **1998**, *95*, 95-144.

(92) Reinert, F.; Hüfner, S. *New J. Phys.* **2005**, *7*, 97/1-91/35.

(93) Heber, M.; Grünert, W. *Topics im Catal.* **2000**, *15*, 3-11.

(94) Yeh, J.J.; Lindau, I. *At. Data Nucl. Data Tables* **1985**, *32*, 1-155.

(95) Scofield, J.H. *J. Electron Spectrosc. Relat. Phenom.* **1976**, *8*, 129-137.

(96) Tougaard, S. *QUASES-IMFP-TPP2M: Database for Calculation of IMFPs by TPP2M Formula, version 2.1*; QUASES-Tougaard Inc.: Odense, Denmark, 2000 (www.quases.com).

(97) Fadley, C.S. *Prog. Surf. Sci.* **1984**, *16*, 275-388.

(98) Shirley, D.A. *Phys. Rev. B* **1972**, *5*, 4709-4714.

(99) Castle, J.E.; Chapman-Kpodo, H.; Proctor, A.; Salvi, A.M. *J. Electron Spectrosc. Relat. Phenom.* **2000**, *106*, 65-80.

(100) Grosvenor, A.P.; Kobe, B. A.; Biesinger, M.C.; McIntyre, N.S. *Surf. Interface Anal.* **2004**, *36*, 1564-1574.

(101) Wagner, C.D.; Naumkin, A.V.; Kraut-Vass, A.; Allison, J.W.; Powell, C.J.; Rumble Jr., J.R., *NIST X-ray Photoelectron Spectroscopy Database, version 3.5 (web version)*; National Institute of Standards and Technology: Gaithersburg, MD, 2007, (srdata.nist.gov/xps).

(102) Trudeau, M.L.; Tschöpe, A.; Ying, J.Y. *Surf. Interface. Anal.* **1995**, *23*, 219-226.

(103) Iwanowski, R.J.; Heinonen, M.H.; Janik, E. *Chem. Phys. Lett.* **2004**, *387*, 110-115.

(104) Sokolov, A.A.; Ternov, I.M. *Izvestiya. VUZ. Fizika* **1967**, *10*, 66-82.

(105) Sham, T.K.; Rivers, M.L. *Rev. Miner. Geochem.* **2002**, *49*, 117-147.

(106) Blewett, J.P. *J. Synchrotron Radiat.* **1998**, *5*, 135-139.

(107) Thompson, A.; Attwood, D.; Gullikson, E.; Howells, M.; Kim, K.J.; Kirz, J.; Kortright, J.; Lindau, I.; Peanetta, P.; Robinson, A.; Scofield, J.; Underwood, J.; Vaughan, D.; Williams, G.; Winick, H. *X-ray Data Booklet*; Lawrence Berkeley National Laboratory, University of California: Berkeley, 2001.

(108) Winick, H. *Synchrotron Radiation Source - A Primer*; World Scientific Publishing: London, 1994.

(109) Newville, M. "Fundamentals in XAFS," Consortium for Advanced Radiation Sources, University of Chicago: Chicago, 2004.

(110) Fleet, M.E. *Can. Miner.* **2005**, *43*, 1811-1838.

(111)   Farges, F.; Brown, J., G.E.; Rehr, J.J. *Phys. Rev. B* **1997**, *56*, 1809-1819.

(112)   Rehr, J.J.; Albers, R.C. *Rev. Mod. Phys.* **2000**, *72*, 621-654.

(113)   Penner-Hahn, J.E. *Coord. Chem. Rev* **1999**, *190-192*, 1101-1123.

(114)   Schroeder, S.L.M.; Moggridge, G.D.; Rayment, T.; Lambert, R.M. *J. Mol. Catal. A: Chem.* **1997**, *119*, 357-365.

(115)   Nemoshkalenko, V.V.; Didyk, V.V.; Krivitskii, V.P.; Senkevich, A.I. *Russ. J. Inorg. Chem.* **1983**, *28*, 1239-1241; Transl. *Zh. Neorg. Mater.* **1983**, *28*, 2182-2186.

(116)   Oyama, S.T.; Wang, X.; Lee, Y.K.; Bando, K.; Requejo, F.G. *J. Catal.* **2002**, *210*, 207-217.

(117)   Shu, Y.; Lee, Y.K.; Oyama, S.T. *J. Catal.* **2005**, *236*, 112-121.

(118)   Kawai, T.; Bando, K.K.; Lee, Y.K.; Oyama, S.T.; Chun, W.J.; Asakura, K.J. *J. Catal.* **2006**, *241*, 20-24.

(119)   Grosvenor, A.P.; Cavell, R.G.; Mar, A. *Chem. Mater.* **2006**, *18*, 1650-1657.

(120)   Grosvenor, A.P.; Cavell, R.G.; Mar, A. *Phys. Rev. B* **2006**, *74*, 125102/1 - 125102/10.

(121)   Grosvenor, A.P.; Cavell, R.G.; Mar, A.; Blyth, R.I.R. *J. Solid State Chem.* **2007**, *180*, 2670-2681.

(122)   Soheilnia, N.; Assoud, A.; Kleinke, H. *Inorg. Chem.* **2003**, *42*, 7319-7325.

(123)   Lam, R.; Mar, A. *J. Solid State Chem.* **1997**, *134*, 388-394.

(124)   Trzebiatowski, W.; Weglowski, S.; Lukaszewicz, K. *Rocz Chem.* **1956**, *30*, 353-354.

(125)   Trzebiatowski, W.; Weglowski, S.; Lukaszewicz, K. *Rocz. Chem.* **1958**, *32*, 189-201.

(126)   Gelato, M.W.; Parthé, E. *J. Appl. Crystallogr.* **1987**, *20*, 139-143.

(127)   Tank, R.; Jepsen, O.; Burkhardt, A.; Andersen, O.K. *TB-LMTO-ASA Program,* version 4.7. Max Planck institut Fur Festkorperforschung. Stuttgart. Germany. 1998.

(128)   Fairley, N. *CasaXPS. version 2.3.9.* Casa Software Ltd., Teighnmouth, Devon, UK. 2003, (www.casaxps.com).

(129)   Landrum, G.A.; Hoffmann, R.; Evers, J.; Boysen, H. *Inorg. Chem.* **1998**, *37*, 5754-5763.

(130)   Doniach, S.; Šunjić, M. *J. Phys. C: Solid State Phys.* **1970**, *3*, 285-291.

(131) Siokou, A.; Kalyva, M.; Yannopoulos, S.N.; Frumar, M.; Němec, P. *J. Phys.; Condens. Matter* **2006**, *18*, 5525-5534.

(132) Abe, H.; Yoshii, K. *J. Solid State Chem.* **2002**, *165*, 372-375.

(133) Pöttgen, R.; Johrendt, D.*Z. Naturforsch.* **2008**, *63*, 1135-1148.

(134) Anisimov, V.I.; Kurmaev, K.Z.; Moewes, A.; Izyumov, I.A. *Physica C* **2009**, *469*, 442-447.

(135) Nekrasov, I.A.; Pchelkina, Z.V.; Sadovskii, M.V. *JETP Lett.* **2008**, *87*, 560-564.

(136) Kroll, T.; Bonhommeau, S.; Kachel, T.; Dürr, H.A.; Werner, J.; Behr, G.; Koitzsch, A.; Hübel, R.; Leger, S.; Schönfelder, R.; Ariffin, A.K.; Manzke, R.; de Groot, F.M.F.; Fink, J.; Eschrig, H.; Büchner, B.; Knupfer, M. *Phys. Rev. B* **2008**, *78*, 220502/1 - 220502/4.

(137) Xu, G.; Ming, W.; Yao, Y.; Dai, X.; Zhang, S.C.; Fang, Z. *Europhys. Lett.* **2008**, *82*, 67002/1 - 67001/4.

(138) Giovannetti, G.; Kumar, S.; van der Brink, J. *Physica B* **2008**, *403*, 3653-3657.

(139) Chen, N.; Li, Y. *Open Condens. Matter Phys.J.* **2008**, *1*, 13-18.

(140) Bannikov, V.V.; Shein, I.R.; Ivanovskii, A.L. *arXiv:0810.2606* **2008**, 13 pp.

(141) Ishibashi, S.; Terakura, K.; Hosono, H. *J. Phys. Soc. Jpn.* **2008**, *77*, 053709/1 - 053709/4.

(142) Sadovskii, M.V. *Phy. Usp.* **2008**, *51*, 1201-1227.

(143) Haule, K.; Shim, J.H.; Kotliar, G. *Phys. Rev. Lett.* **2008**, *100*, 226402/1-226402/4.

(144) Singh, D.J.; Du, M.H. *Phys. Rev. Lett.* **2008**, *100*, 237003/1-237003/4.

(145) Shorikov, A.O.; Korotin, M.A.; Streltsov, S.V.; Korotin, D.M.; Anisimov, V.I.; Skornyakov, S. I. *arXiv:0804.3283v2* **2008**, 4pp.

(146) Canning, G.; Kasrai, M.; Bancroft, G.M.; Andrew, D. *J. Synchrotron Radiat.* **1999**, *6*, 740-742.

(147) Ravel, B.; Newville, M. *J. Synchrotron Radiat.* **2005**, *12*, 537-541.

(148) Opila, R.L.; Wilk, G.D.; Alam, M.A.; van Dover, R.B.; Busch, B.W. *Appl. Phys. Lett.* **2002**, *81*, 1788-1790.

(149) Li, D.; Bancroft, G.M.; Kasrai, M.; Fleet, M.E.; Feng, X.H.; Tan, K.H.; Yang, B.X. *Solid State Commun.* **1993**, *87*, 613-617.

(150) Kasrai, M.; Lennard, W.N.; Brunner, R.W.; Bancroft, G.M.; Bardwell, J.A.; Tan, K.H. *Appl. Surf. Sci.* **1996**, *99*, 303-312.

(151) Rosencwaig, A.; Wertheim, G.K. *J. Electron Spectrosc. Relat. Phenom.* **1972/73**, *1*, 493-496.

(152) Roberts, A.; Engelberg, D.; Liu, Y.; Thompson, G.E.; Alexander, M.R. *Surf. Interface Anal.* **2002**, *33*, 697-703.

(153) Frost, D.C.; Ishitani, A.; McDowell, C.A. *Mol. Phys.* **1972**, *24*, 861-877.

(154) Ghodselahi, T.; Vesaghi, M.A.; Shafiekhani, A.; Baghizadeh, A.; Lameii, M. *Appl. Surf. Sci.* **2008**, *255*, 2730-2734.

(155) Werfel, F.; Heinonen, M.; Suoninen, E.*Z. Phys. B: Condens. Matter* **1988**, *70*, 317-322.

(156) Vasquez, R.P. *Surf. Sci. Spectra* **1993**, *2*, 149-154.

(157) Vasquez, R.P. *Surf. Sci. Spectra* **1993**, *2*, 144-148.

(158) Chawla, S.K.; Sankarraman, N.; Payer, J.H. *J. Electron Spectrosc. Relat. Phenom.* **1992**, *61*, 1-18.

(159) Kowalczyk, A.; Toliński, T.; Reiffers, M.; Pugaczowa-Michalska, M.; CheŁkowska, G.; Gažo, E. *J. Phys.: Conden. Matter* **2008**, *20*, 255252/1-255252/7.

(160) Healy, P.C.; Myhra, S.; Stewart, A.M. *Jpn. J. Appl. Phys.* **1987**, *26*, L1884-L1887.

(161) Ishii, H.; Koshizawa, T.; Hanyu, T.; Yamaguchi, S. *Jpn. J. Appl. Phys.* **1993**, *32*, 1070-1076.

(162) Sugiyama, J.; Itti, R.; Yamauchi, H.; Koshizuka, N.; Tanaka, S. *Phys. Rev. B* **1992**, *45*, 4952-4956.

(163) Vasquez, R.P.; Siegal, M.P.; Overmyer, D.L.; Ren, Z.F.; Lao, J.Y.; Wang, J.H. *Phys. Rev. B* **1999**, *60*, 4306-4319.

(164) Steiner, P.; Kinsinger, V.; Sander, I.; Siegwart, B.; Hüfner, S.; Politis, C.*Z. Phys. B: Condens. Matter* **1987**, *67*, 19-23.

(165) Bianconi, A.; Congiu Castellano, A.; De Santis, M.; Rudolf, P.; Lagarde, P.; Flank, A. M.; Marcelli, A. *Solid State Commun.* **1987**, *63*, 1009-1013.

(166) Choy, J.H.; Choi, S.H.; Byeon, S.H.; Chun, S.-\H.; Hong, S.T.; Jung, D.Y.; Choe, W.Y.; Park, Y.W. *Bull. Korean Chem. Soc.* **1988**, *9*, 289-291.

(167) Pattrick, R.A.D.; van der Laan, G.; Charnock, J.M.; Grguric, B.A. *Am. Miner.* **2004**, *89*, 541-546.

(168) Allred, A.L.; Rochow, E.G. *J. Inorg. Nucl. Chem.* **1958**, *5*, 264-268.

(169) Farges, F.; Rossano, S. *Eur. J. Miner.* **2000**, *12*, 1093-1107.

(170) Brown, J.M.; Powers, L.; Kincaid, B.; Larrabee, J.A.; Spiro, T.G. *J. Am. Chem. Soc.* **1980**, *102*, 4210-4216.

(171) Chattopadhyay, T.; Chetal, A. R. *J. Phys. C: Solid State Phys.* **1985**, *18*, 5373-5378.

(172) Grosvenor, A.P.; Greendan, J.E. *J. Phys. Chem. C* **2009**, *113*, 11366-11372.

(173) Koitzsch, A.; Inosov, D.; Fink, J.; Knupfer, M.; Eschrig, H.; Borisenko, S.V.; Behr, G.; Köhler, A.; Werner, J.; Büchner, B.; Follath, R.; Dürr, H. A. *Phys. Rev. B* **2008**, *78*, 180506/1-180506/4.

(174) Pandey, S.K.; Khalid, S.; Pimpale, A.V. *J. Phys.: Condens. Matter* **2007**, *19*, 036212/1 - 036212/16.

(175) Quebe, P.; Terbüchte, L.J.; Jeitschko, W. *J. Alloys Comp.* **2000**, *302*, 70-74.

(176) Kurmaev, E.Z.; Wilks, R.G.; Moewes, A.; Skorikov, N.A.; Izyumov, Yu.A.; Finkelstein, L.D.; Li, R.H.; Chen, X.H. *Phys. Rev. B.* **2008**, *78*, 220503/1 - 220503/4.

(177) Zhang, Y.; Chen, Y. L.; Cui, Y.J.; Cheng, C.H.; Zhang, H.; Zhao, Y. *Supercond. Sci. Technol.* **2009**, *22*, 015007/1 - 015007/6.

(178) Ignatov, A.; Zhang, C.L.; Vannucci, M.; Croft, M.; Tyson, T.A.; Kwok, D.; Qin, Z.; Cheong, S. W. *arxiv:0808.2134v2* **2008**, 12pp.

(179) Kroll, T.; Roth, F.; Koitzsch, A.; Kraus, R.; Batchelor, D.R.; Werner, J.; Behr, G.; Büchner, B.; Knupfer, M. *New J. Phys.* **2009**, *11*, 025019/1 - 025019/4.

(180) Malaeb, W.; Yoshida, T.; Kataoka, T.; Fujimori, A.; Kubota, M.; Ono, K.; Usui, H.; Kuroki, K.; Arita, R.; Aoki, H.; Kamihara, Y.; Hirano, M.; Hosono, H. *J. Phys. Soc. Jpn.* **2008**, *77*, 093714/1 - 093714/4.

(181) Uwamino, Y.; Ishizuka, Y.; Yamatera, H.*J. Electron Spectrosc. Relat. Phenom.* **1984**, *34*, 67-78.

(182) Jiang, D.T.; Crozier, E.D. *Can. J. Phys.* **1998**, *76*, 621-643.

(183) van der Heide, P.A.W. *J. Electron Spectrosc. Relat. Phenom.* **2006**, *151*, 79-91.

(184) Egerton, R.F.; Malac, M.*J. Electron Spectrosc. Relat. Phenom.* **2005**, *143*, 43-50.

(185) Hüfner, S. *Photoelectron Spectroscopy*; Springer-Verlag: Berlin, 1995.

(186) Raaen, S. *Solid State Commun.* **1986**, *60*, 991-993.

(187) Cavell, R G.; Sodhi, R.N.S. *J. Electron Spectrosc. Relat. Phenom.* **1986**, *41*, 1-24.

(188) Cavell, R.G.; Sodhi, R.N.S. *J. Electron Spectrosc. Relat. Phemon.* **1986**, *41*, 25-35.

(189) Pfeiffer, G.R.; Rehr, J.J.; Sayers, D. E. *Phys. Rev. B* **1995**, *51*, 804-810.

(190) Shein, I.R.; Ivanovskii, A.L. *Physica C* **2009**, *469*, 15-19.

(191) Kačiulis, S.; Latišenka, A.; Plešanovas, A. *Surf. Sci.* **1991**, *251-252*, 330-335.

(192) Grünert, W.; Sauerlandt, U.; Schlögl, R.; Karge, H. G. *J. Phys. Chem.* **1993**, *97*, 1413-1418.

(193) Tatsumi, K.; Tsutsui, M.; Beall, G.W.; Mullica, D.F.; Milligan, W.O. *J. Electron Spectrosc. Relat. Phenom.* **1979**, *16*, 113-118.

(194) Ikeda, T.; Okada, K.; Ogasawara, H.; Kotani, A. *J. Phys. Soc. Jpn* **1990**, *59*, 622-630.

(195) Niu, C.J.; Jia, Y.Q. *Spectrochim. Acta, Part A* **1993**, *49*, 947-951.

(196) Barr, T.L. *The Principles and Practices of X-Ray Photoelectron Spectroscopy;* CRS Press: Boca Raton, FL, 1994.

(197) Dimitrov, V.; Komatsu, T. *J. Solid State Chem.* **2002**, *163*, 100-112.

(198) Kuwata, Y.; Suga, S.; Imada, S.; Sekiyama, A.; Ueda, S.; Iwasaki, T.; Harada, H.; Muro, T.; Fukawa, T.; Ashida, K.; Yoshioka, H.; Terauchi, T.; Sameshima, J.; Kuwahara, H.; Moritomo, Y.; Tokura, Y. *J. Electron Spectosc. Relat. Phenom.* **1998**, *88-91*, 281-285.

(199) Kowalczyk, A.; Baszyćski, J.; Szajek, A.; Ślebarski, A.; Toliński, T. *J. Phys.: Condens. Matter* **2001**, *13*, 5519-5526.

(200) Konno, H.; Tachikawa, H.; Furusaki, A.; Furuichi, R. *Anal. Sci.* **1992**, *8*, 641-646.

(201) Nowik, I.; Felner, I.; Awana, V.P.S.; Vajpayee, A.; Kishan, H. *J. Phys.: Condens. Matter* **2008**, *20*, 292201/1-292201/5.

(202) Lebégue, S. *Phys. Rev. B* **2007**, *75*, 035110/1-035110/5.

(203) Westre, T.E.; Kennepohl, P.; DeWitt, J.G.; Hedman, B.; Hodgson, K.O.; Solomon, E.I. *J. Am. Chem. Soc.* **1997**, *119*, 6297-6314.

(204) Chen, G.F.; Li, Z.; Wu, D.; Dong, J.; Li, G.; Hu, W.Z.; Zheng, P.; Luo, J.L.; Wang, N.L. *Chin. Phys. Lett.* **2008**, *25*, 2235-2238.

(205) Fuggle, J.C.; Campagna, M.; Zolnierek, Z.; Lässer, R.; Platau, A. *Phys. Rev. Lett.* **1980**, *45*, 1597-1600.

(206) Berthou, H.; Jørgensen, C.K.; Bonnelle, C. *Chem. Phys. Lett.* **1976**, *38*, 199-206.

(207) Novosselov, A.; Talik, E.; Pajaczkowska, A. *J. Alloys Compd.* **2003**, *351*, 50-53.

(208) Kaindl, G.; Schmiester, G.; Sampathkumaran, E.V.; Wachter, P. *Phys. Rev. B* **1988**, *38*, 10174-10177.

(209) Hormes, J.; Pantelouris, M.; Balazs, G.B.; Rambabu, B. *Solid State Ionics* **2000**, *136-137*, 945-954.

(210) Jeon, Y.; Lu, F.; Jhans, H.; Shaheen, S.A.; Liang, G.; Croft, M.; Ansari, P.H.; Ramanujachary, K.V.; Hayri, E.A.; Fine, S.M.; Li, S.; Feng, X.H.; Greenblatt, M.; Greene, L.H.; Tarascon, J.M. *Phys. Rev. B* **1987**, *36*, 3891-3894.

(211) Little Jr., E.J.; Jones, M.M. *J. Chem. Educ.* **1960**, *37*, 231-233.

(212) Nesbitt, H.W.; Legrand, D.; Bancroft, G.M. *Phys. Chem. Miner.* **2000**, *27*, 357-366.

(213) Grosvenor, A.P.; Biesinger, M.C.; Smart, R.S.; MnIntyre, N.S. *Surf. Sci.* **2006**, *600*, 1771-1779.

(214) Miyake, T.; Pourovskii, L.; Vildosola, V.; Biermann, S.; Georges, A. *J. Phys. Soc. Jpn.* **2008**, *77*, 99-102.

(215) Artigas, M.; Bacmann, M.; Fruchart, D.; Fruchart, R. *J. Solid State Chem.* **1996**, *123*, 306-312.

(216) Rundqvist, S.; Jellinek, F. *Acta. Chem. Scand.* **1959**, *13*, 425-432.

(217) Rundqvist, S. *Acta. Chem. Scand.* **1960**, *14*, 1961-1979.

(218) Ellner, M.; Mittemeijer, E.J. *Z. Anorg. Allg. Chem.* **2001**, *627*, 2257-2260.

(219) Senateur, J.P.; Rouault, A.; Fruchart, R.; Capponi, J.J.; Perroux, M. *Mater. Res. Bull.* **1976**, *11*, 631-635.

(220) Rundqvist, S.; Hassler, E.; Lundvik, L. *Acta. Chem. Scand.* **1962**, *16*, 242-243.

(221) Bashev, V.F.; Miroshnichenko, I.S. *Izv. Akad. Nauk SSSR, Neorg. Mater.* **1983**, *19*, 860-862.

(222) Kanama, D.; Oyama, S.T.; Otani, S.; Cox, D.F. *Surf. Sci.* **2004**, *552*, 8-16.

(223) Elsener, B.; Atzei, D.; Krolikowski, A.; Rossi, A. *Surf. Interface Anal.* **2008**, *40*, 919-926.

(224) Engemann, C.; Kohring, G.; Pantelouris, A.; Hormes, J.; Grimme, S.; Peyerimhoff, S.D.; Clade, J.; Frick, F.; Jansen, M. *Chem. Phys.* **1997**, *221*, 189-198.

(225) Franke, R. *Spectrochim Acta, Part A* **1997**, *53*, 933-941.

(226) Ma, C.Y.; Cui, M.Q.; Zhang, L.Y.; Xiang, W.; Zhou, K.J.; Wu, Z.Y.; Xing, C.; Zhao, Y.D.; Lei, Z. *Acta Phys. Sin.* **2008**, *57*, 3868-3874.

(227) Sefat, A.S.; Amow, G.; Wu, M.Y.; Botton, G.A.; Greedan, J.E. *J. Solid State Chem.* **2005**, *178*, 1008-1016.

(228) Okude, N.; Nagoshi, M.; Noro, H.; Baba, Y.; Yamamoto, H.; Sasaki, T.A. *J. Electron Spectrosc.Relat. Phenom.* **1999**, *101-103*, 607-610.

(229) Franke, R.; Hormes, J. *Physica B* **1995**, *216*, 85-95.

(230) Rundvist, S.; Nawapong, P.C. *Axta. Chem. Scand.* **1965**, *19*, 1006-1008.

(231) Ashcroft, N.W.; Mermin, N.D. *Solid State Physics;* Saunders: Philadelphia, 1976.

(232) Weigel, C.; Calas, G.; Cormier, L.; Galoisy, L.; Henderson, G.S. *J. Phys. C: Condens. Matter* **2008**, *20*, 135219/1-135219/8.

(233) Chang, C.L.; Chern, G.; Chen, C.L.; Hsieh, H.H.; Dong, C.L.; Pong, W.F.; Chao, C.H.; Chien, H.C.; Chang, S.L. *Solid State Commun.* **1999**, *109*, 599-604.

(234) Iwata, N.; Matsushima, T.; Fujii, H.; Okamoto, T. *J. Phys. Soc. Japn.* **1981**, *50*, 729-731.

(235) Drábek, M. *Eur. J. Miner.* **2006**, *18*, 545-550.

(236) Fruchart, R.; Roger, A.; Sénateur, J.P. *J. Appl. Phys.* **1969**, *40*, 1250-1257.

(237) Kumar, S.; Chander, S.; Krishnamurthy, A.; Srivastava, B.K. *J. Magn. Magn. Mater.* **2001**, *237*, 135-142.

(238) Chenevier, B.; Soubeyroux, J.L.; Bacmann, M.; Fruchart, D.; Fruchart, R. J. *Solid State Comm.* **1987**, *64*, 57-61.

(239)   Sammynaiken, R.; Kuhn, M.; Sham, T.K. *Physica B* **1995**, *208-209*, 371-372.

(240)   Sham, T.K.; Hiraya, A.; Watanabe, M. *Phys. Rev. B* **1997**, *55*, 7585-7592.

(241)   Hsieh, H.H.; Chang, Y.K.; Pong, W.F.; Pieh, J.Y.; Tseng, P.K.; Sham, T.K.; Coulthard, I.; Naftel, S.J.; Lee, J.F.; Chung, S.C.; Tsang, K.L. *Phys. Rev. B* **1998**, *57*, 15204-15210.

(242)   Gilbert, B.; Frazer, B.H.; Belz, A.; Conrad, P.G.; Nealson, K.H.; Haskel, D.; Lang, J.C.; Srajer, G.; De Stasio, G. *J. Phys. Chem. A* **2003**, *107*, 2839-2847.

(243)   Yamamoto, T. *X-ray Spectrom.* **2008**, *37*, 572-584.

(244)   Wang, G.; Liang, Y.; Zheng, L.; Yang, Z. *J. Phys.:Condens. Matter* **2009**, *21*, 415702/1-415702/5.

(245)   Gaudette, A.F.; Burns, A.W.; Hayes, J.R.; Smith, M.C.; Bowker, R.H.; Seda, T.; Bussell, M. E. *J. Catal.* **2010**, *272*, 18-27.

(246)   Karis, O.; Svensson, S.; Rusz, J.; Oppeneer, P.M.; Gorgoi, M.; Schäfers, F.; Braun, W.; Eberhardt, W.; Mårtensson, N. *Phys. Rev. B* **2008**, *78*, 233105/1-233105/3.

(247)   van Attekum, P.M.Th.M.; Trooster, J.M. *Phys. Rev. B* **1979**, *20*, 2335-2340.

(248)   Moslemzadeh, N.; Beamson, G.; Tsakiropoulos, P.; Watts, J.F.; Haines, S.R.; Weightman, P. *J. Electron Spectrosc. Relat.* **2006**, *152*, 129-133.

Appendix 1

Supplementary Data for Chapter 3

Table A1-1 Cell parameters for $Zr(Ge_xAs_{1-x})As$.

Loading composition	a (Å)	b (Å)	c (Å)	V (Å^3)	Remarks
$ZrGe_{0.1}As_{1.9}$	6.779(5)	3.688(3)	9.051(6)	226.3(2)	Single phase
$ZrGe_{0.2}As_{1.8}$	6.772(3)	3.685(1)	9.068(3)	226.3(1)	Single phase
$ZrGe_{0.3}As_{1.7}$	6.749(2)	3.673(1)	9.079(3)	225.1(1)	Single phase
$ZrGe_{0.4}As_{1.6}$	6.753(4)	3.675(2)	9.087(5)	225.5(1)	Single phase
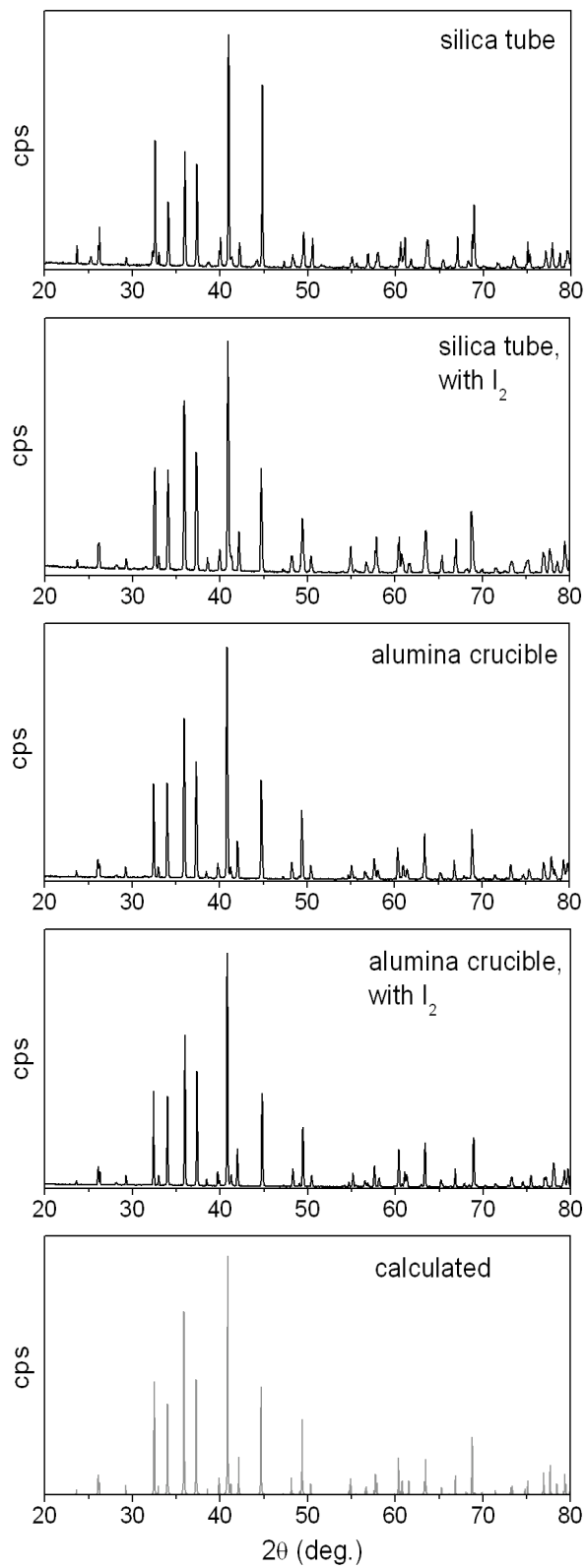
Figure A1-1 Powder XRD patterns for samples of $ZrAs_2$ prepared under different conditions.
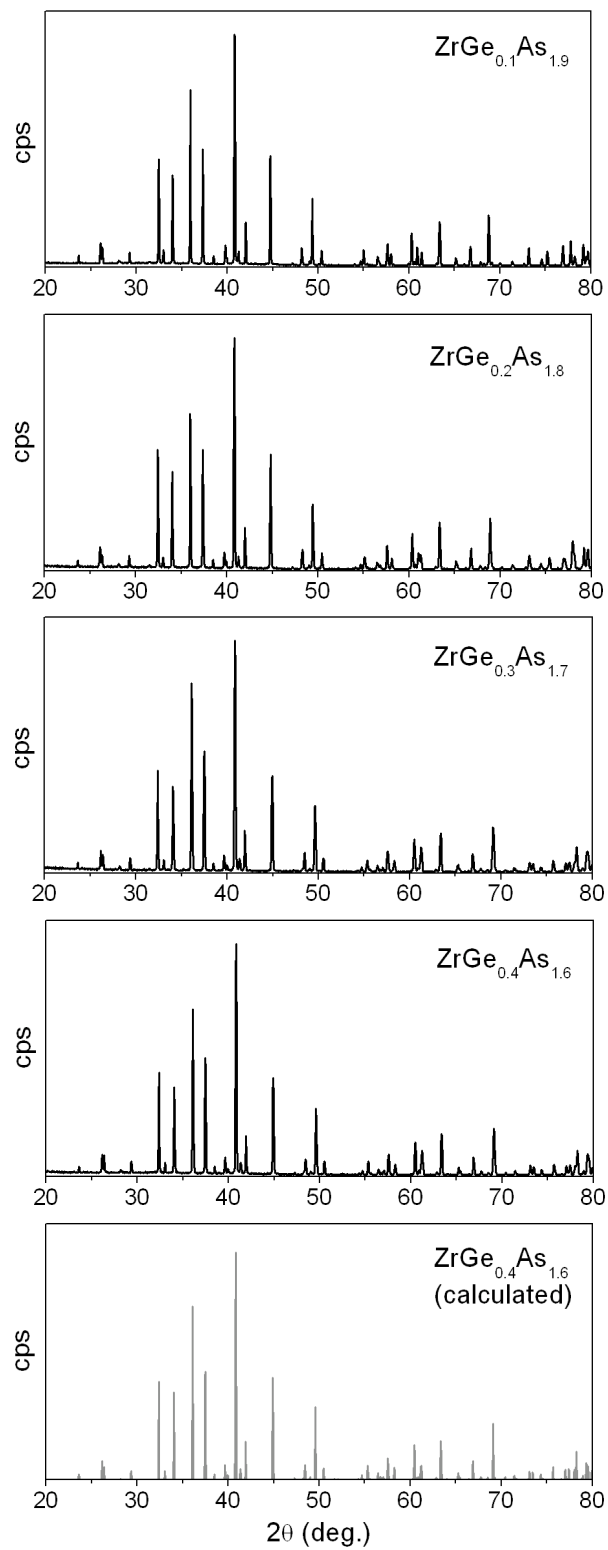
Figure A1-2 Powder XRD patterns for different members of $Zr(Ge_xAs_{1-x})As$.

Appendix 2

Supplementary Data for Chapter 4

Table A2-1. BEs (eV) for separate samples, or same sample measured at different times.

Sample	Run 1	Run 2	Run 3
ZrCuSiP			
Zr $3d_{5/2}$	179.71	179.66	179.62
Cu $2p_{3/2}$	933.72	933.64	933.75
Si $2p_{1/2}$	99.46	99.38	99.36
P $2p_{3/2}$	128.87	128.76	128.82
ZrCuSiAs			
Zr $3d_{5/2}$	179.62	179.65	
Cu $2p_{3/2}$	933.65	933.70	
Si $2p_{1/2}$	99.43	99.38	
As $3d_{5/2}$	41.08	41.17	
Zr metal			
Zr $3d_{5/2}$	178.89	178.93	
Cu metal			
Cu $2p_{3/2}$	932.89	932.83	
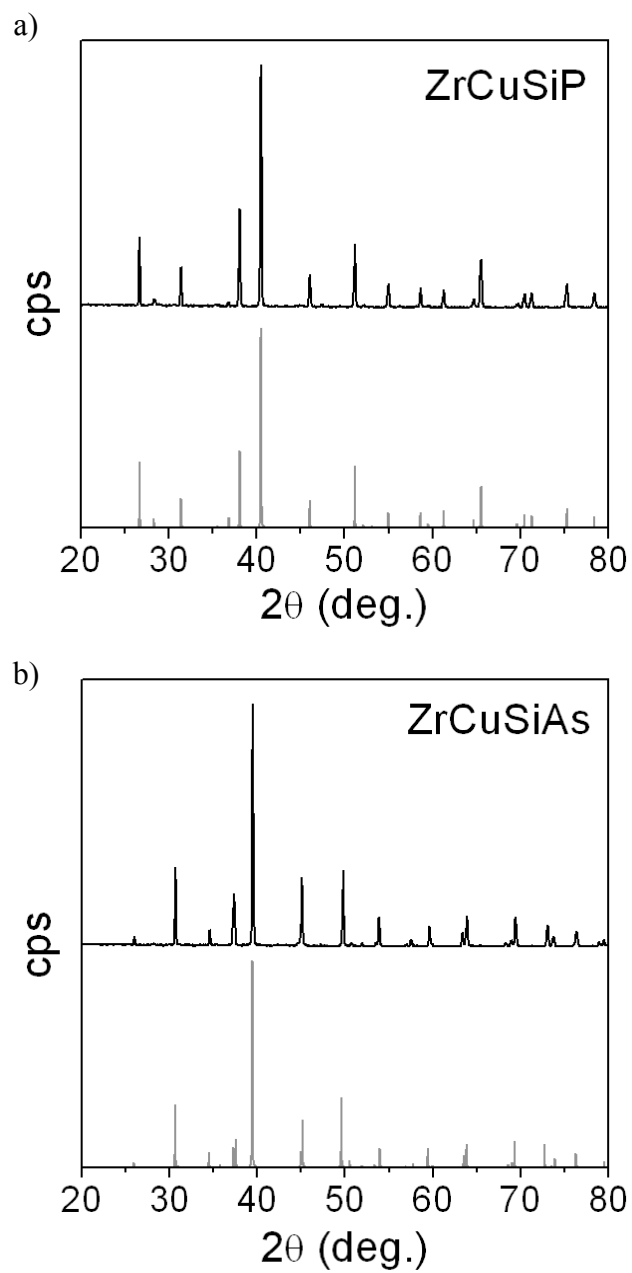
Figure A2-1 Powder XRD patterns for ZrCuSiP and ZrCuSiAs.

Appendix 3

Supplementary Data for Chapter 5

Table A3-1 Cell parameters for LaMAsO (M = Fe, Co, Ni) and LaFe$_{1-x}M'_x$AsO (M' = Co, Ni) samples.[a]

Sample	a (Å)	c (Å)	V (Å^3)
LaFeAsO	4.054(1)	8.791(4)	144.5(1)
LaCoAsO	4.063(2)	8.532(9)	140.9(2)
LaNiAsO	4.148(2)	8.247(6)	141.9(1)
LaFe$_{0.9}$Co$_{0.1}$AsO	4.055(2)	8.757(4)	144.0(1)
LaFe$_{0.8}$Co$_{0.2}$AsO	4.056(2)	8.701(4)	143.1(1)
LaFe$_{0.4}$Co$_{0.6}$AsO	4.058(1)	8.642(7)	142.3(1)
LaFe$_{0.2}$Co$_{0.8}$AsO	4.060(3)	8.591(8)	141.6(2)
LaFe$_{0.8}$Ni$_{0.2}$AsO	4.062(2)	8.756(3)	144.5(1)
LaFe$_{0.7}$Ni$_{0.3}$AsO	4.076(2)	8.689(5)	144.4(2)
LaFe$_{0.4}$Ni$_{0.6}$AsO	4.096(3)	8.547(1)	143.4(2)

[a] ZrCuSiAs-type structure: space group $P4/nmm$ (no. 129); atomic positions La 2c (1/4, 1/4, ~0.14), M/M' 2b (3/4, 1/4, 1/2), As 2c (1/4, 1/4, ~0.66), O 2a (3/4, 1/4, 0) taken from Ref 13.

Table A3-2 As $3d_{5/2}$ BEs (eV) for separate LaMAsO (M = Fe, Co, Ni) and LaFe$_{1-x}M'_x$AsO (M' = Co, Ni) samples, or same sample measured at different times.[a]

Sample	Run 1	Run 2	Run 3
LaFeAsO	41.17	41.15 [a]	41.23
LaCoAsO	41.26	41.28 [a]	41.33
LaNiAsO	41.43	41.39 [a]	41.47
LaFe$_{0.9}$Co$_{0.1}$AsO	41.11	41.16	
LaFe$_{0.8}$Co$_{0.2}$AsO	41.14	41.22	
LaFe$_{0.4}$Co$_{0.6}$AsO	41.25	41.19	
LaFe$_{0.2}$Co$_{0.8}$AsO	41.32	41.27	
LaFe$_{0.8}$Ni$_{0.2}$AsO	41.26	41.30	
LaFe$_{0.7}$Ni$_{0.3}$AsO	41.32	41.29	
LaFe$_{0.4}$Ni$_{0.6}$AsO	41.41	41.37	

[a] Obtained before Ar$^+$-ion sputter-cleaning.

Table A3-3 Fe and Co 2p$_{3/2}$ BEs (eV) for separate LaMAsO (M = Fe, Co) and LaFe$_{1-x}M'_x$AsO (M' = Co, Ni) samples, or same sample measured at different times. [a]

Sample	Fe 2p$_{3/2}$			Co 2p$_{3/2}$		
	Run 1	Run 2	Run 3	Run 1	Run 2	Run 3
LaFeAsO	707.16	707.12 [a]	707.05			
LaCoAsO				778.55	778.51 [a]	778.59
LaFe$_{0.9}$Co$_{0.1}$AsO	707.04	707.09		778.58	778.49	
LaFe$_{0.8}$Co$_{0.2}$AsO	707.08	707.03		778.62	778.56	
LaFe$_{0.4}$Co$_{0.6}$AsO	707.13	707.16		778.38	778.45	
LaFe$_{0.2}$Co$_{0.8}$AsO	707.21	707.14		778.41	778.44	
LaFe$_{0.8}$Ni$_{0.2}$AsO	707.09	707.15				
LaFe$_{0.7}$Ni$_{0.3}$AsO	707.15	707.06				
LaFe$_{0.4}$Ni$_{0.6}$AsO	707.13	707.09				

[a] Obtained before Ar$^+$-ion sputter-cleaning.

Table A3-4 La $3d_{5/2}$ and O 1s BEs (eV) for separate LaMAsO (M = Fe, Co, Ni) and LaFe$_{1-x}M'_x$AsO (M' = Co, Ni) samples, or same sample measured at different times. [a]

Sample	La $3d_{5/2}$			O 1s		
	Run 1	Run 2	Run 3	Run 1	Run 2	Run 3
LaFeAsO	834.85	834.94 [a]	834.94	529.94	529.88 [a]	529.99
LaCoAsO	834.91	834.83 [a]	834.81	529.83	529.93 [a]	529.92
LaNiAsO	834.92	834.95 [a]	834.89	529.98	529.89 [a]	530.01
LaFe$_{0.9}$Co$_{0.1}$AsO	834.93	834.89		529.91	529.94	
LaFe$_{0.8}$Co$_{0.2}$AsO	834.78	834.83		529.84	529.88	
LaFe$_{0.4}$Co$_{0.6}$AsO	834.91	834.96		529.89	529.93	
LaFe$_{0.2}$Co$_{0.8}$AsO	834.74	834.80		529.94	529.91	
LaFe$_{0.8}$Ni$_{0.2}$AsO	834.82	834.75		530.01	529.93	
LaFe$_{0.7}$Ni$_{0.3}$AsO	834.99	834.91		529.96	530.03	
LaFe$_{0.4}$Ni$_{0.6}$AsO	834.87	834.84		530.04	529.98	

[a] Obtained before Ar^+-ion sputter-cleaning.
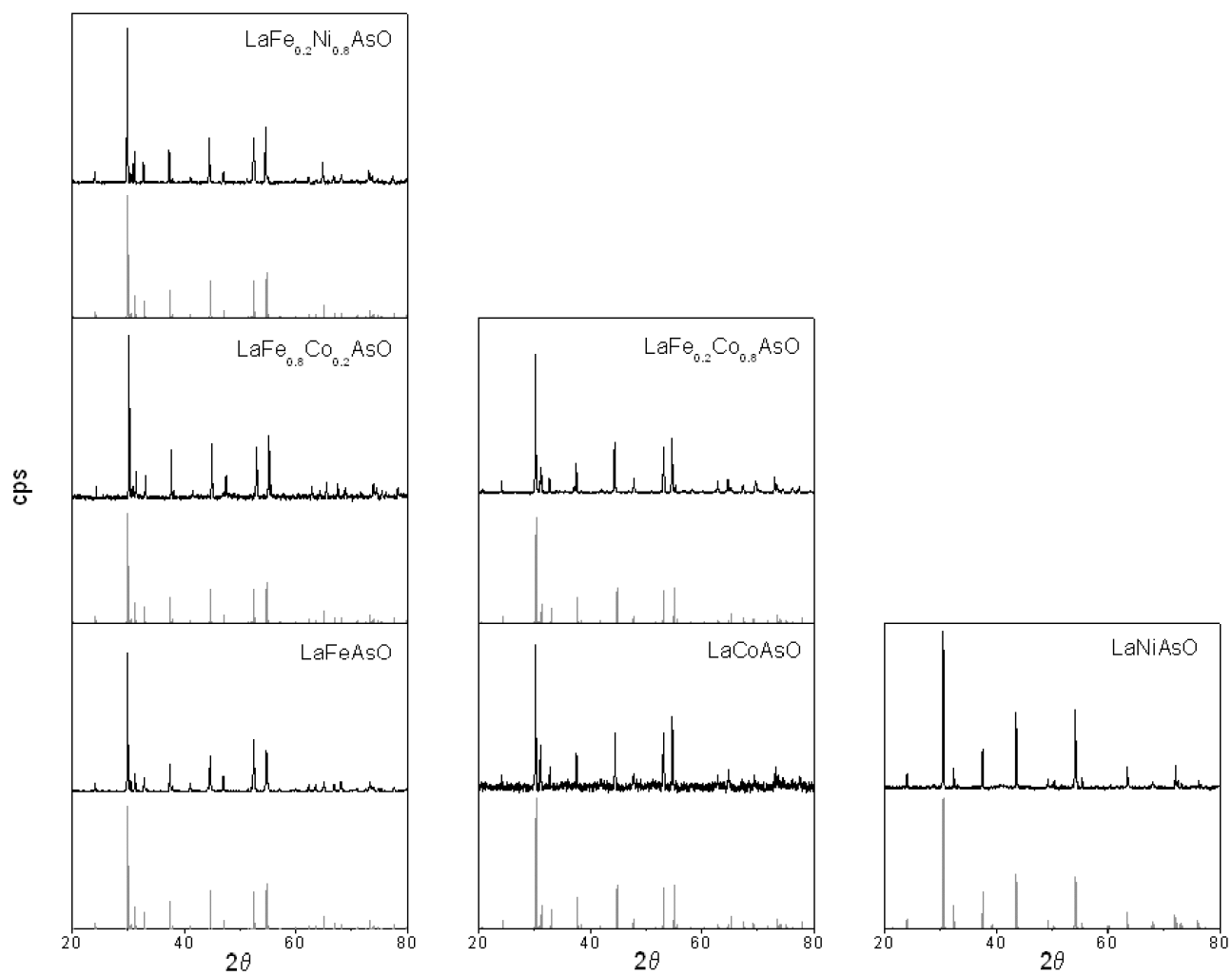
Figure A3-1 Powder XRD patterns for La*M*AsO (*M* = Fe, Co, Ni) and representative members of LaFe$_{1-x}$*M*′$_x$AsO (*M*′ = Co, Ni).
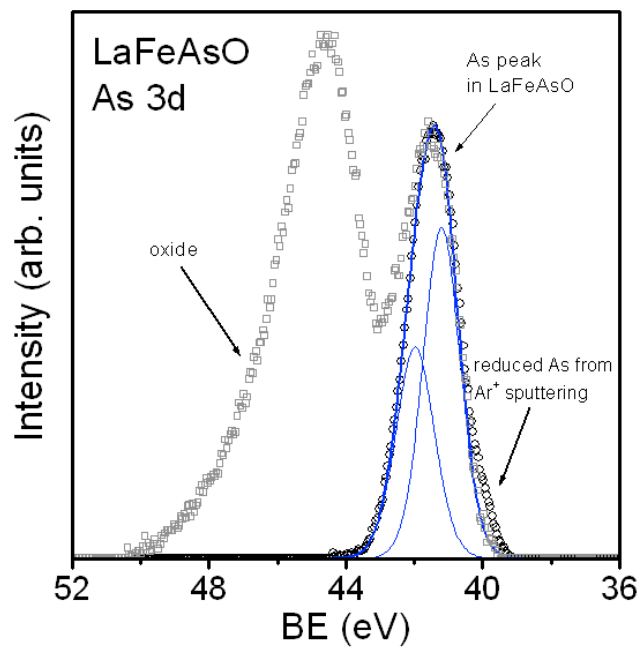
Figure A3-2 As 3d XPS spectra of LaFeAsO before (grey squares) and after (black circles) Ar$^+$ ion sputtering. The fitted envelope and the component peaks are in blue.
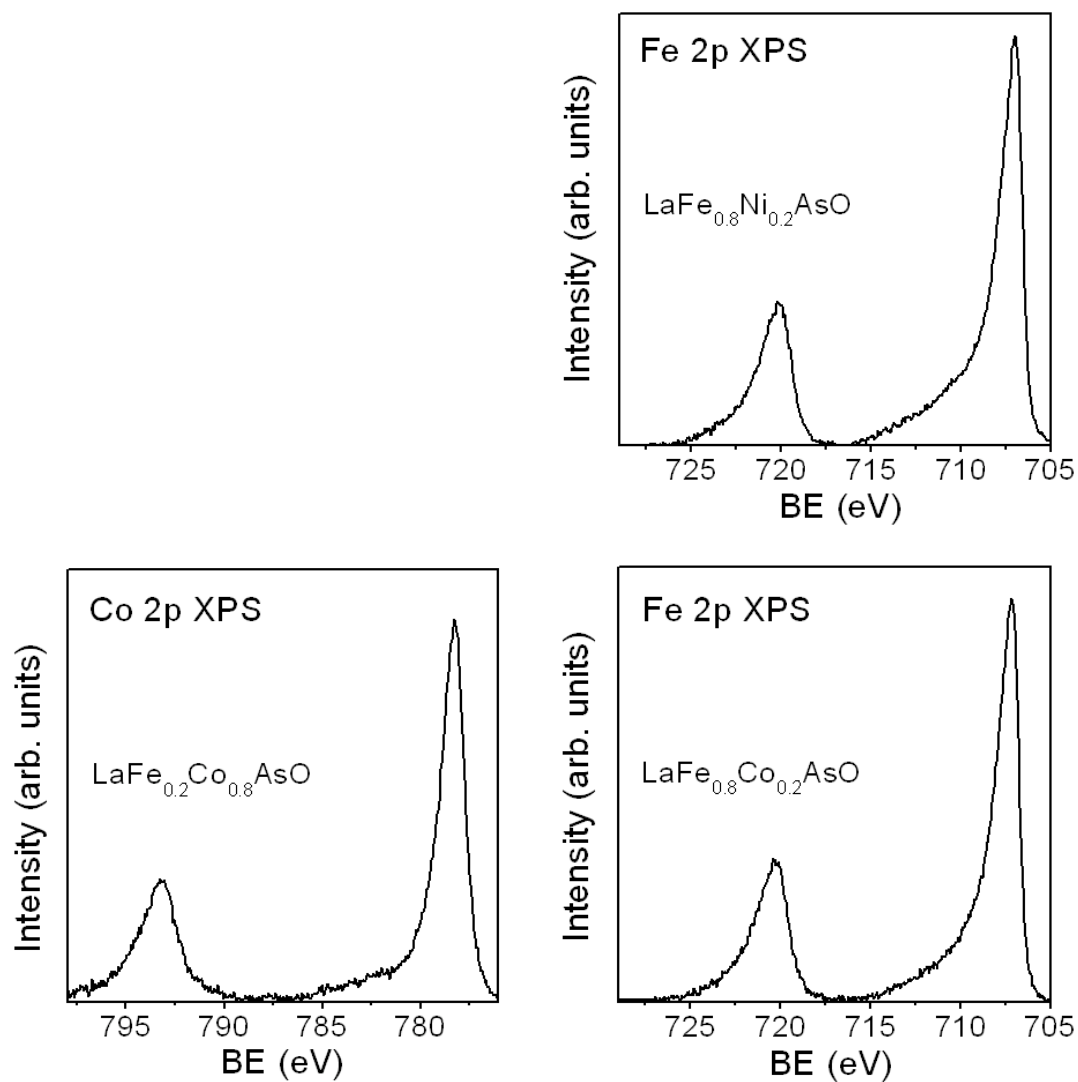
Figure A3-3 Fe 2p and Co 2p XPS spectra for some members of LaFe$_{1-x}$$M'_x$AsO ($M'$ = Co, Ni).
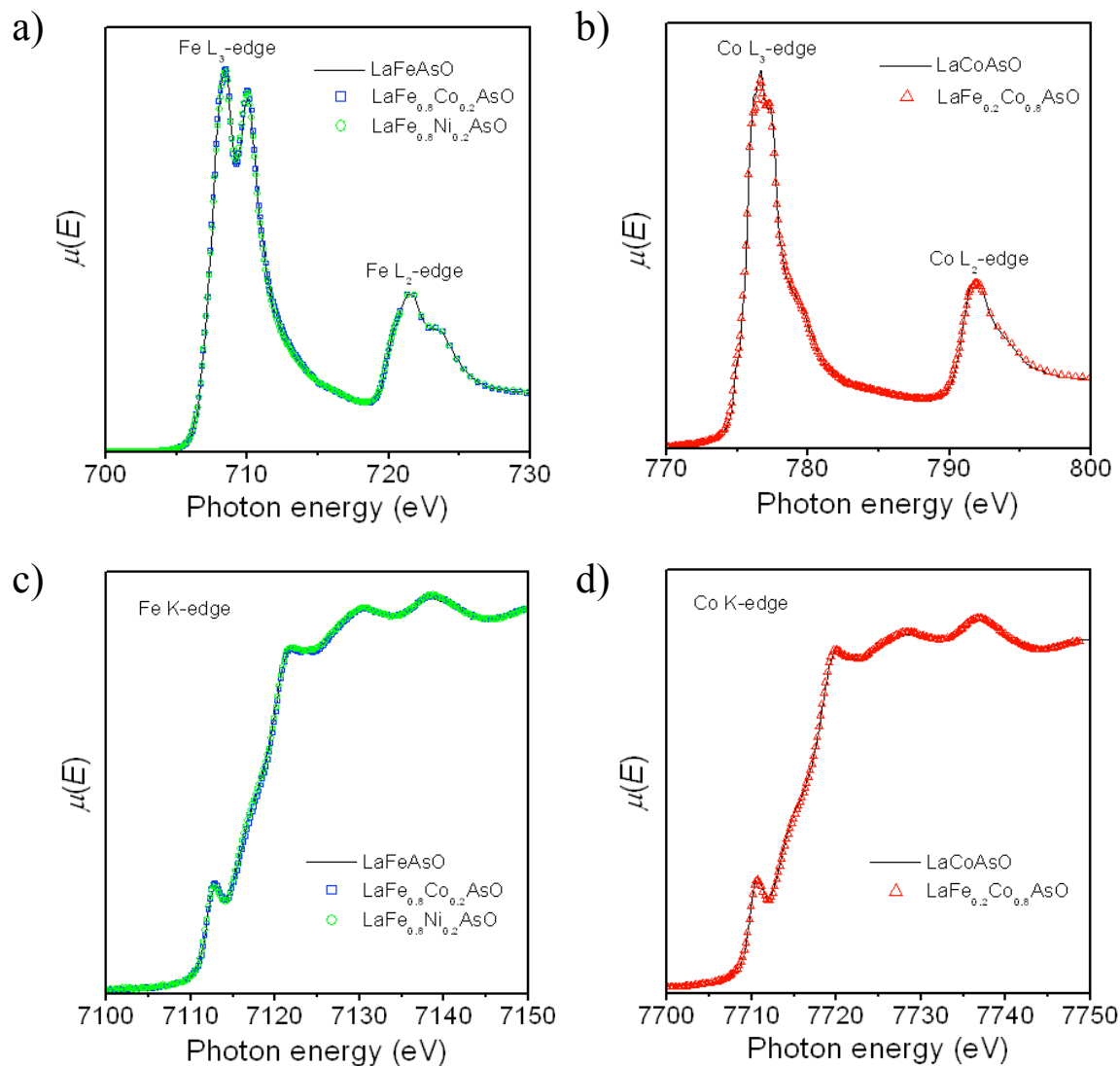
Figure A3-4 (a) Fe L-edge. (b) Co L-edge, (c) Fe K-edge, and (d) Co K-edge XANES spectra for mixed-metal arsenide oxides LaFe$_{1-x}M'_x$AsO (compared to the parent LaMAsO compounds). The spectra are overlapped to emphasize their similarity.

.

Appendix 4

Supplementary Data for Chapter 6

Table A4-1 BEs (eV) for separate REFeAsO (RE = Ce, Pr, Nd, Sm, Gd) and CeNiAsO samples, or same sample measured at different times.

Sample	Run 1	Run 2	Run 3
Ce 3d$_{5/2}$			
CeFeAsO	881.71	881.80 [a]	
CeNiAsO	881.83	881.90 [a]	
Fe 2p$_{3/2}$			
CeFeAsO	707.20	707.15 [a]	707.12
PrFeAsO	707.09	707.12 [a]	707.06
NdFeAsO	707.12	707.16	707.19
SmFeAsO	707.12	707.07	
GdFeAsO	707.14	707.06	707.04
Ni 2p$_{3/2}$			
CeNiAsO	853.15	853.18 [a]	853.22
As 3d$_{5/2}$			
CeFeAsO	41.14	41.16 [a]	41.11
PrFeAsO	41.10	41.14 [a]	41.18
NdFeAsO	41.08	41.16	41.07
SmFeAsO	41.09	41.16	
GdFeAsO	41.12	41.17	41.09
CeNiAsO	41.35	41.38 [a]	41.32
O 1s			
CeFeAsO	530.04	530.06 [a]	530.01
PrFeAsO	530.12	530.09 [a]	530.07
NdFeAsO	530.17	530.12	530.09
SmFeAsO	530.20	530.14	
GdFeAsO	530.32	530.26	530.35
CeNiAsO	530.07	530.01 [a]	529.99

[a] Obtained before Ar^+-ion sputter-cleaning.
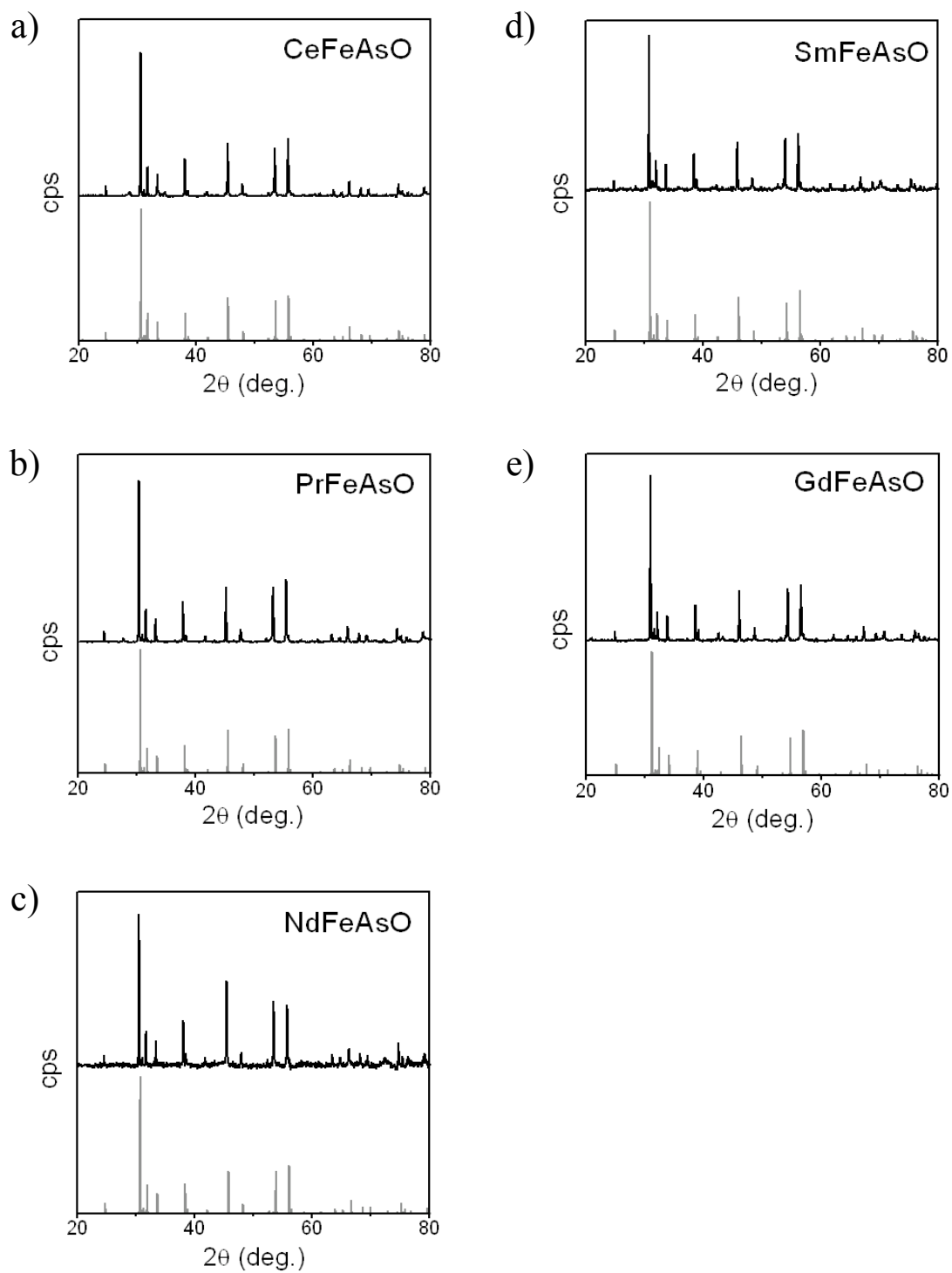
Figure A4-1 Powder XRD patterns for *RE*FeAsO.
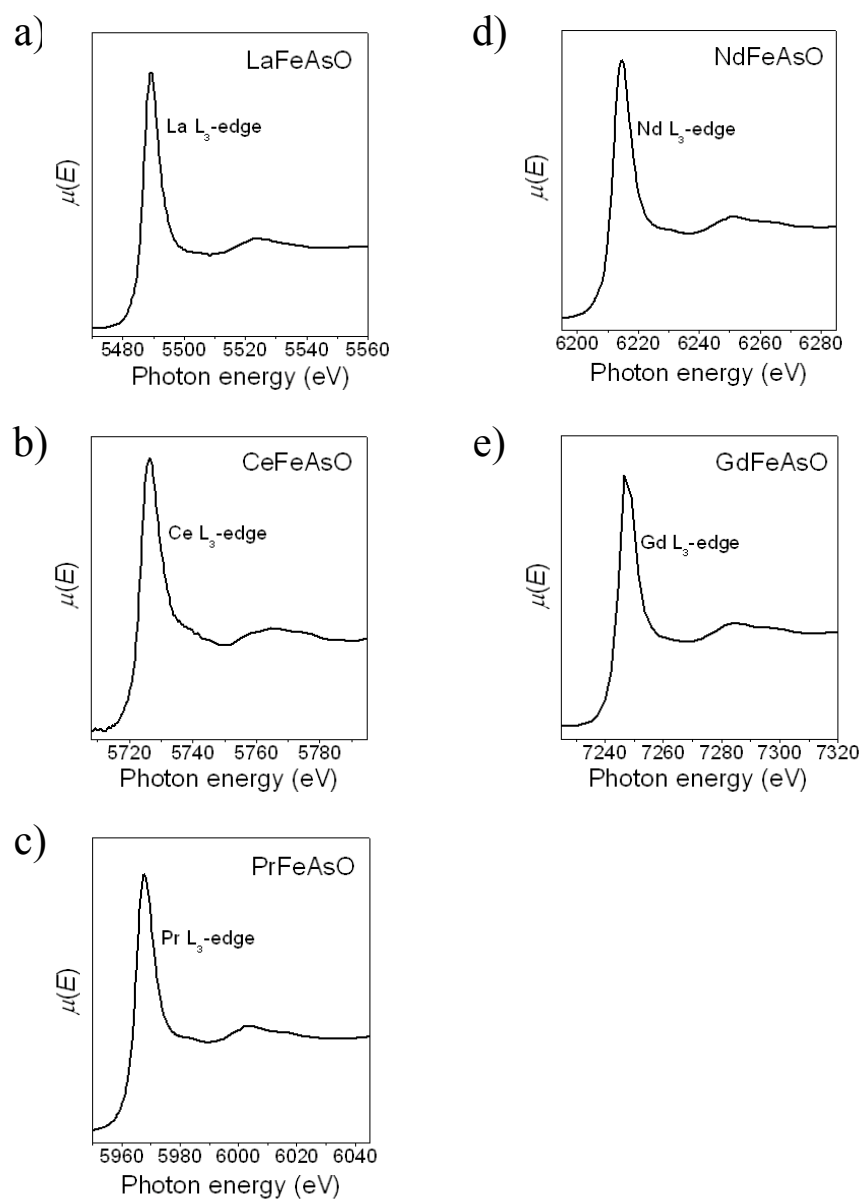
Figure A4-2 *RE* L$_3$-edge XANES spectra for *RE*FeAsO. (The spectrum for SmFeAsO was not measured.)
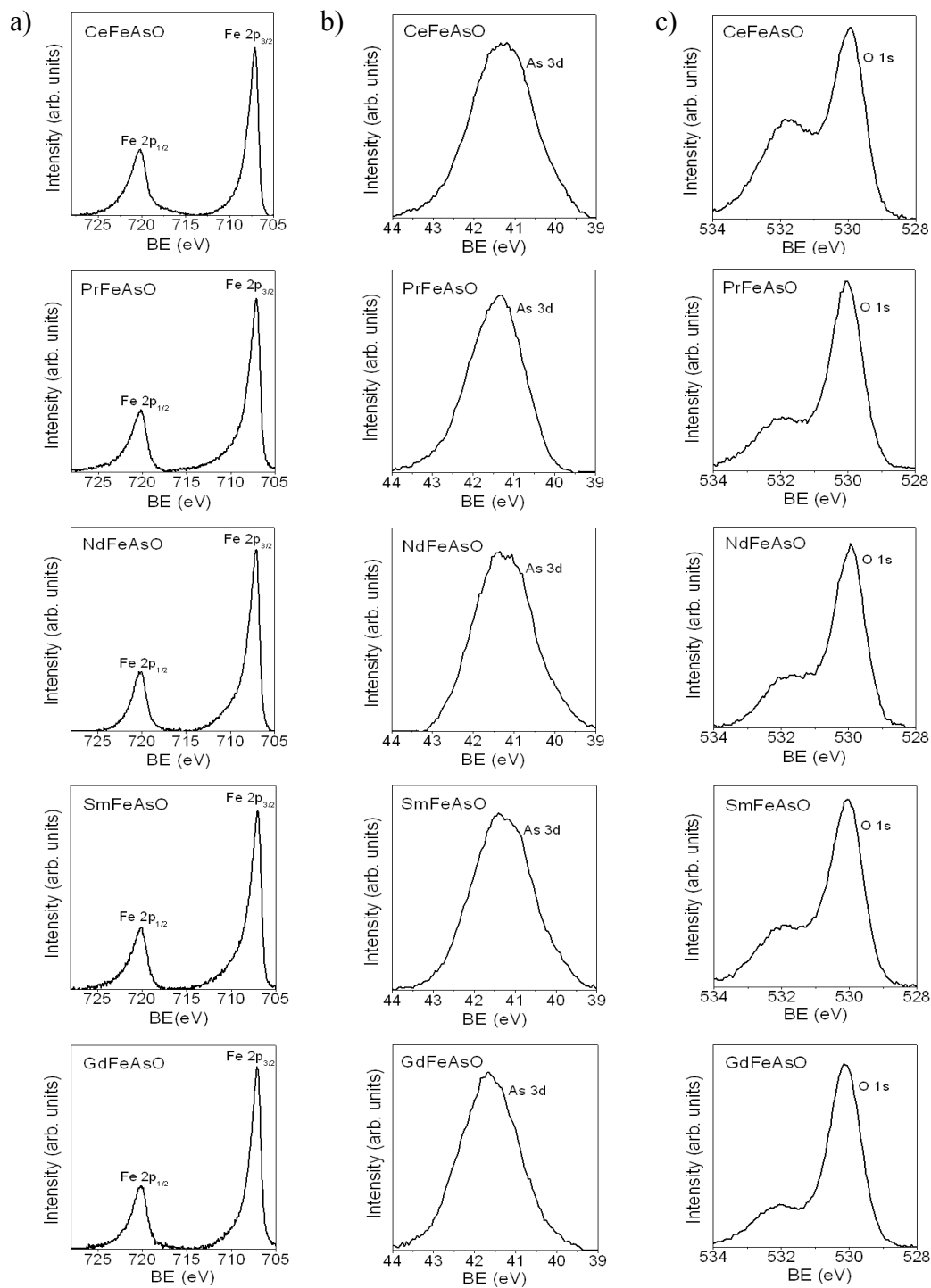
Figure A4-3 (a) Fe 2p, (c) As 3d, and (d) O 1s XPS spectra for *RE*FeAsO.

Appendix 5

Supplementary Data for Chapter 7

Table A5-1 P $2p_{3/2}$ BEs (eV) for separate M_2P and M_3P (M = Cr–Ni) samples, or same sample measured at different times.

Sample	Run 1	Run 2	Run 3
Cr_2P	129.13	129.17	
Mn_2P	129.27	129.22	129.26
Fe_2P	129.38	129.25	129.29 [a]
Co_2P	129.44	129.41	129.39
Ni_2P	129.46	129.43	129.51 [a]
Cr_3P	129.26	129.21	
Mn_3P	129.30	129.31	129.28
Fe_3P	129.47	129.41	129.44
Ni_3P	129.50	129.56	129.52

[a] Obtained before Ar^+-ion sputter-cleaning.
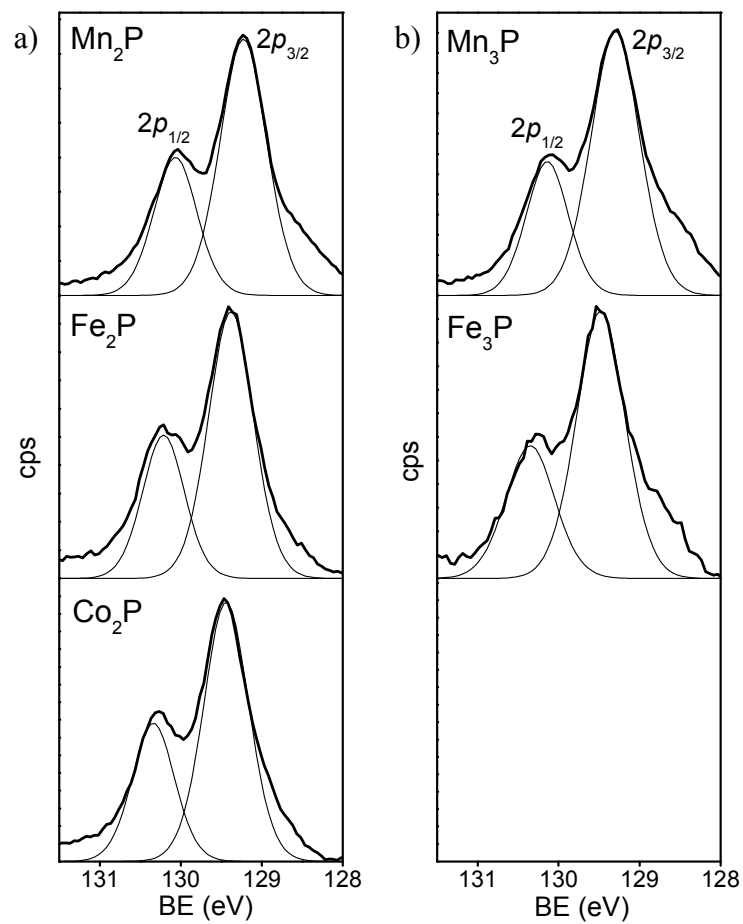
Figure A5-1 P 2p XPS spectra for (a) M_2P and (b) M_3P (M = Mn, Fe, Co).
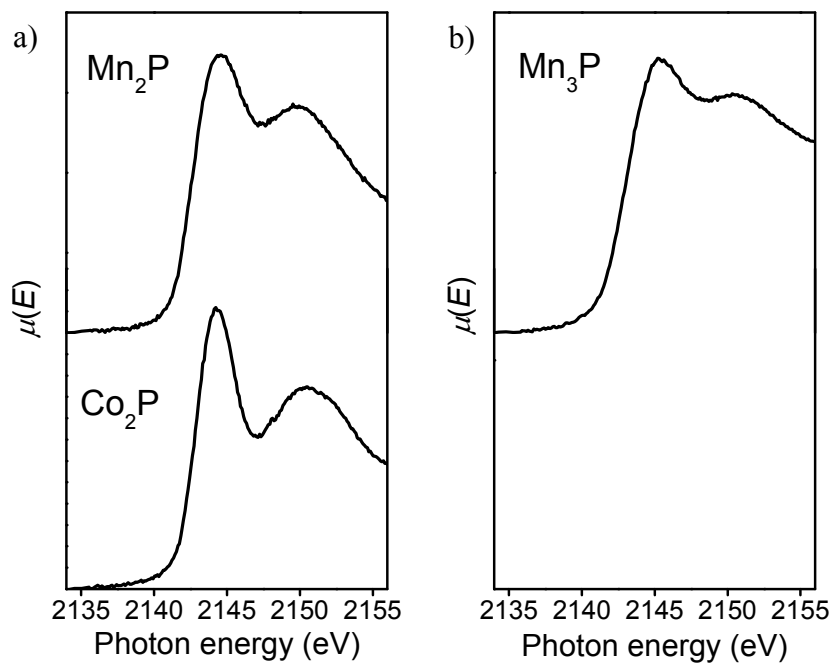
Figure A5-2 P K-edge XANES spectra for (a) M_2P (M = Mn, Co) and (b) Mn₃P.
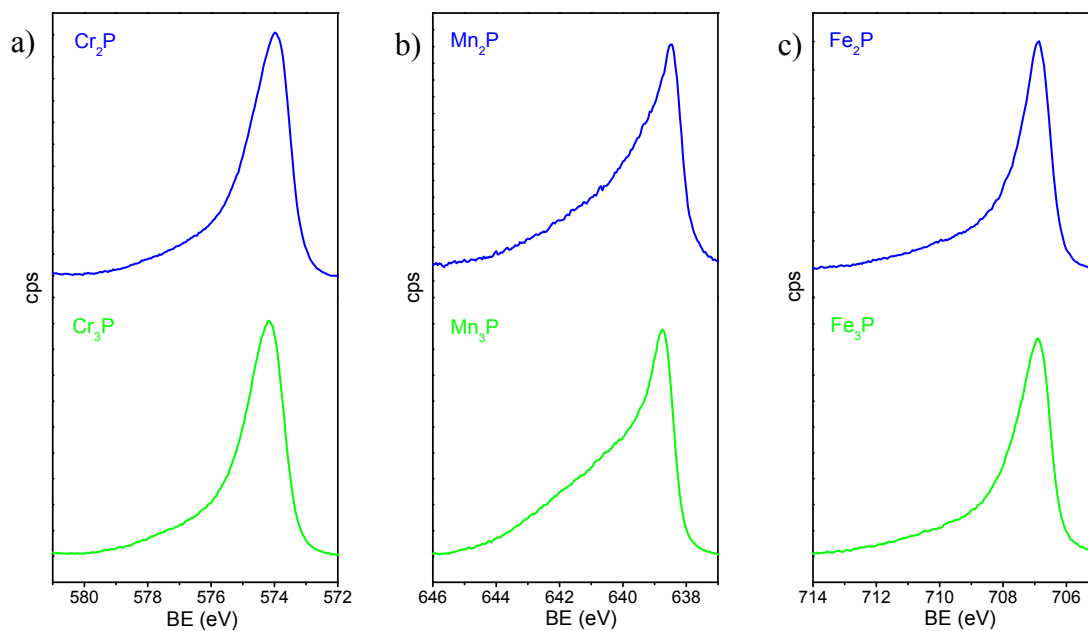
Figure A5-3 M 2p$_{3/2}$ XPS spectra for M_2P and M_3P (M = (a) Cr, (b) Mn, (c) Fe).
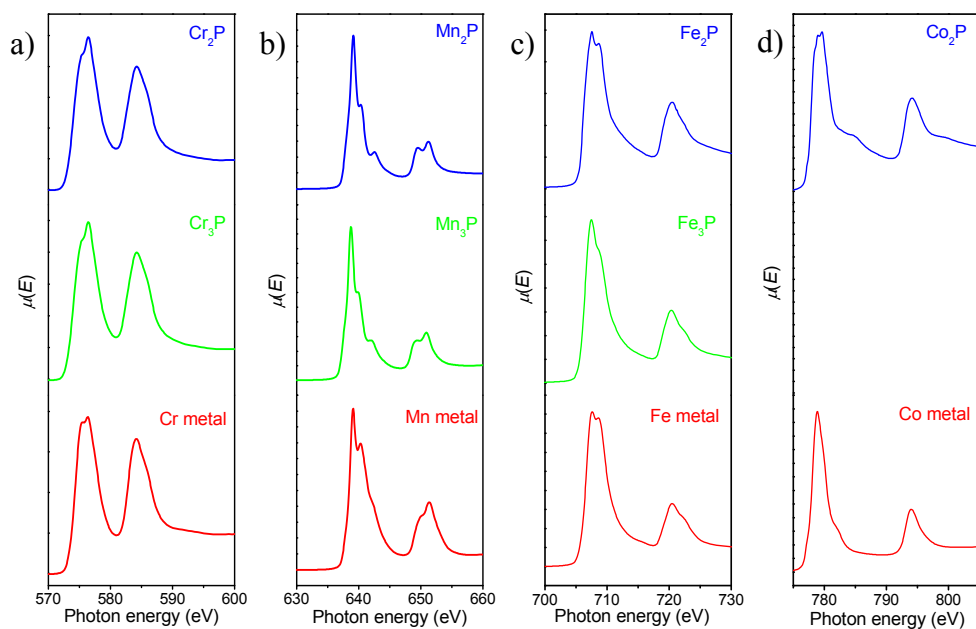
Figure A5-4 M L-edge XANES spectra for M_2P, M_3P, and M metal (M = (a) Cr, (b) Mn, (c) Fe, (d) Co).

Appendix 6

Supplementary Data for Chapter 8

Table A6-1 Cell parameters for $(Ni_{1-x}M_x)_2P$ (M = Cr, Fe, Co) samples.

Sample	Structure type [a]	a (Å)	b (Å)	c (Å)	V (Å^3)
Cr_2P	Cr_2P-type	6.648(2)	10.458(2)	6.371(1)	443.0(1)
Fe_2P	Fe_2P-type	5.894(1)		3.478(3)	104.64(8)
Co_2P	Co_2P-type	5.674(1)	3.5290(9)	6.6387(8)	132.93(3)
Ni_2P	Fe_2P-type	5.893(4)		3.402(6)	102.3(2)
$(Ni_{0.8}Cr_{0.2})_2P$	Fe_2P-type	5.886(3)		3.396(5)	101.9(2)
$(Ni_{0.5}Cr_{0.5})_2P$	Co_2P-type	5.854(2)	3.555(1)	6.874(3)	142.8(1)
$(Ni_{0.3}Cr_{0.7})_2P$	Co_2P-type	5.878(2)	3.570(1)	6.912(2)	145.07(5)
$(Ni_{0.8}Fe_{0.2})_2P$	Fe_2P-type	5.896(1)		3.367(3)	101.36(7)
$(Ni_{0.5}Fe_{0.5})_2P$	Fe_2P-type	5.878(2)		3.451(3)	103.26(7)
$(Ni_{0.2}Fe_{0.8})_2P$	Fe_2P-type	5.881(2)		3.479(5)	104.2(1)
$(Ni_{0.8}Co_{0.2})_2P$	Fe_2P-type	5.886(2)		3.401(3)	102.0(3)
$(Ni_{0.5}Co_{0.5})_2P$	Fe_2P-type	5.851(6)		3.394(4)	100.6(4)
$(Ni_{0.2}Co_{0.8})_2P$	Co_2P-type	5.701(3)	3.5076(2)	6.6363(6)	132.72(6)

[a] Cr_2P-type, space group $Imm2$; Fe_2P-type, space group $P\bar{6}2m$; Co_2P-type, space group $Pnma$.

Table A6-2 P 2p$_{3/2}$ BEs (eV) for separate (Ni$_{1-x}$M$_x$)$_2$P (M = Cr, Fe, Co) samples, or same sample measured at different times.

Sample	Run 1	Run 2	Run 3
(Ni$_{0.8}$Co$_{0.2}$)$_2$P	129.45	129.47	
(Ni$_{0.5}$Co$_{0.5}$)$_2$P	129.44	129.42	129.39 [a]
(Ni$_{0.2}$Co$_{0.8}$)$_2$P	129.41	129.39	129.42 [a]
(Ni$_{0.8}$Fe$_{0.2}$)$_2$P	129.43	129.39	129.42 [a]
(Ni$_{0.5}$Fe$_{0.5}$)$_2$P	129.39	129.49	129.43 [a]
(Ni$_{0.2}$Fe$_{0.8}$)$_2$P	129.42	129.33	129.32 [a]
(Ni$_{0.8}$Cr$_{0.2}$)$_2$P	129.44	129.37	
(Ni$_{0.5}$Cr$_{0.5}$)$_2$P	129.37	129.32	
(Ni$_{0.3}$Cr$_{0.7}$)$_2$P	129.23	129.26	

[a] Obtained before Ar$^+$-ion sputter-cleaning.

Table A6-3 Metal $2p_{3/2}$ BEs (eV) for separate $(Ni_{1-x}M_x)_2P$ (M = Cr, Fe, Co) samples, or same sample measured at different times.

Sample	Ni $2p_{3/2}$			M' $2p_{3/2}$		
	Run 1	Run 2	Run 3	Run 1	Run 2	Run 3
$(Ni_{0.8}Co_{0.2})_2P$	852.93	853.02		778.10	778.14	
$(Ni_{0.5}Co_{0.5})_2P$	852.91	852.88	852.94[a]	778.14	778.17	778.11[a]
$(Ni_{0.2}Co_{0.8})_2P$	852.96	853.03	853.05[a]	778.23	778.30	778.28[a]
$(Ni_{0.8}Fe_{0.2})_2P$	852.91	852.86	852.85[a]	706.62	706.64	706.71[a]
$(Ni_{0.5}Fe_{0.5})_2P$	853.05	853.01	852.98[a]	706.86	706.83	706.92[a]
$(Ni_{0.2}Fe_{0.8})_2P$	853.09	853.04	853.08[a]	706.74	706.84	706.81[a]
$(Ni_{0.8}Cr_{0.2})_2P$	852.92	852.96		573.98	574.09	
$(Ni_{0.5}Cr_{0.5})_2P$	853.11	853.16		574.01	574.09	
$(Ni_{0.3}Cr_{0.7})_2P$	853.20	853.12		574.08	573.99	
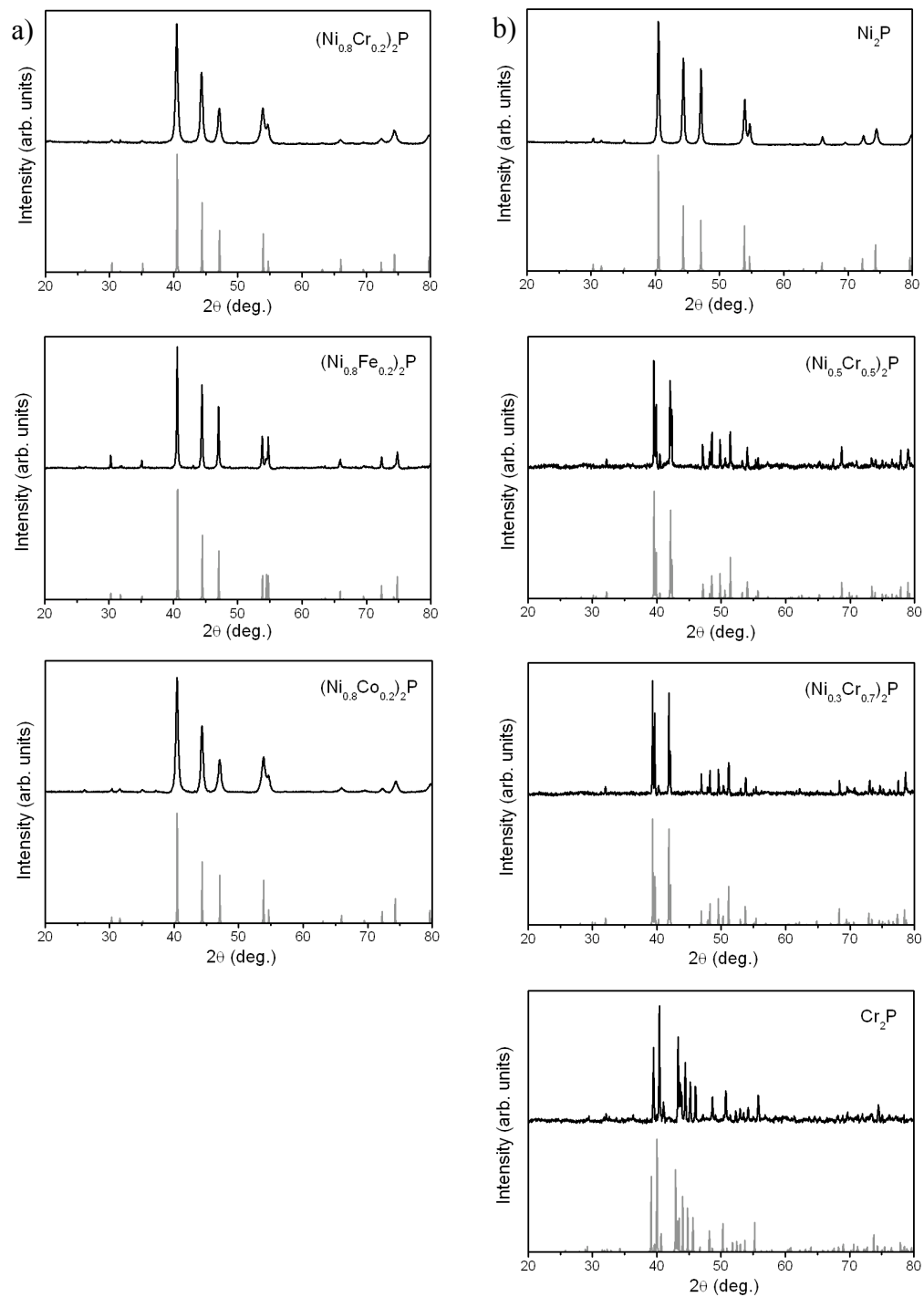
Figure A6-1 Powder X-ray diffraction patterns for (a) $(Ni_{0.8}M_{0.2})_2P$ (M = Cr, Fe, Co) and (b) $(Ni_{1-x}Cr_x)_2P$ (x = 0, 0.5, 0.7, 1).
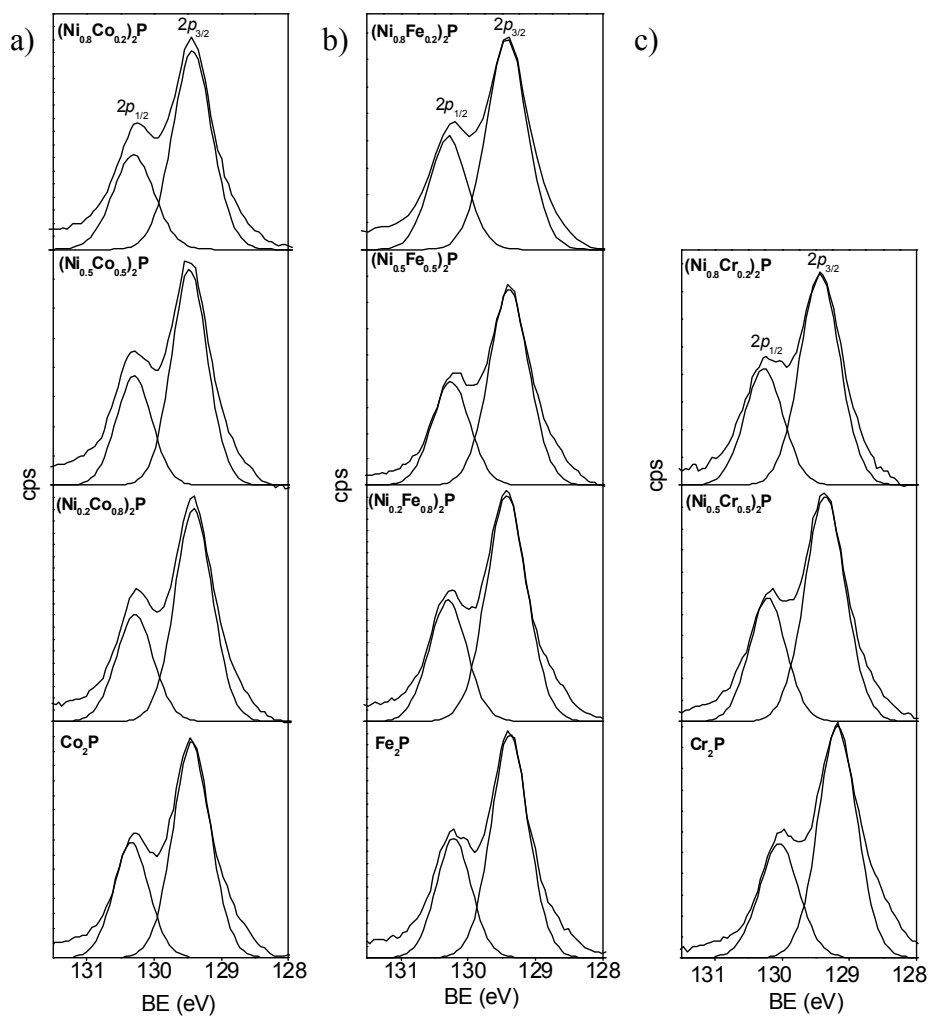
Figure A6-2 P 2p XPS spectra for (a) $(Ni_{1-x}Co_x)_2P$, (b) $(Ni_{1-x}Fe_x)_2P$, and (c) $(Ni_{1-x}Cr_x)_2P$.
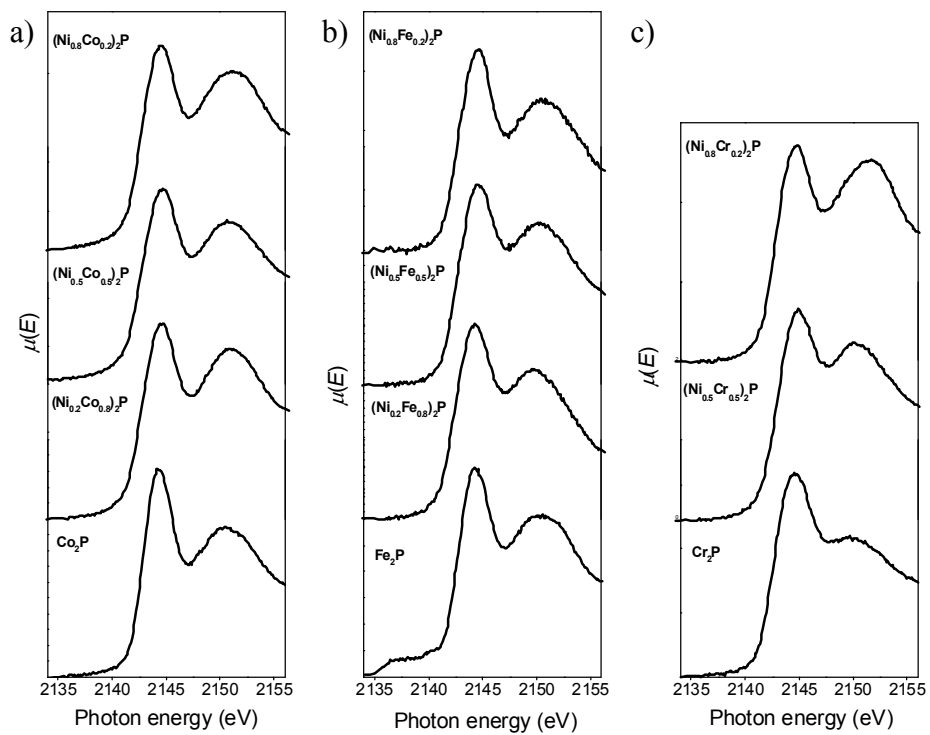
Figure A6-3 P K-edge XANES spectra for (a) $(Ni_{1-x}Co_x)_2P$, (b) $(Ni_{1-x}Fe_x)_2P$, and (c) $(Ni_{1-x}Cr_x)_2P$.

a)

Ni 2p$_{3/2}$ XPS

$(Ni_{0.2}Co_{0.8})_2P$

$(Ni_{0.5}Co_{0.5})_2P$

$(Ni_{0.8}Co_{0.2})_2P$

cps

BE (eV)

Co 2p$_{3/2}$ XPS

$(Ni_{0.8}Co_{0.2})_2P$

$(Ni_{0.5}Co_{0.5})_2P$

$(Ni_{0.2}Co_{0.8})_2P$

Co_2P

cps

BE (eV)

b)

Ni 2p$_{3/2}$ XPS

(Ni$_{0.2}$Fe$_{0.8}$)$_2$P

(Ni$_{0.5}$Fe$_{0.5}$)$_2$P

(Ni$_{0.8}$Fe$_{0.2}$)$_2$P

cps

861 858 855 852

BE (eV)

Fe 2p$_{3/2}$ XPS

(Ni$_{0.8}$Fe$_{0.2}$)$_2$P

(Ni$_{0.5}$Fe$_{0.5}$)$_2$P

(Ni$_{0.2}$Fe$_{0.8}$)$_2$P

Fe$_2$P

cps

714 712 710 708 706

BE (eV)
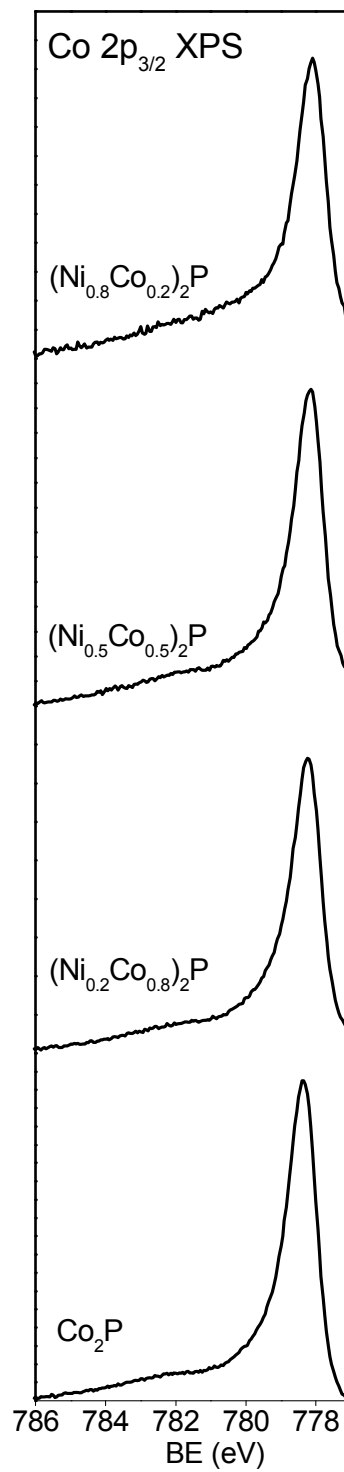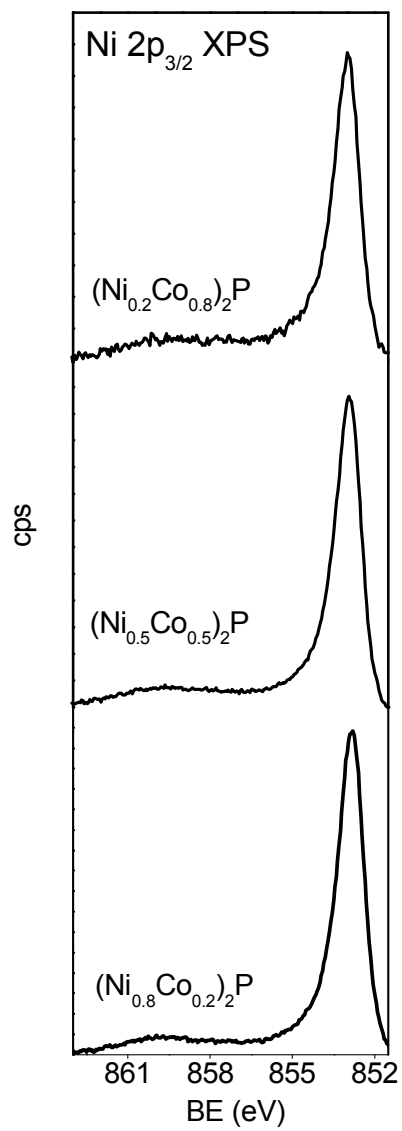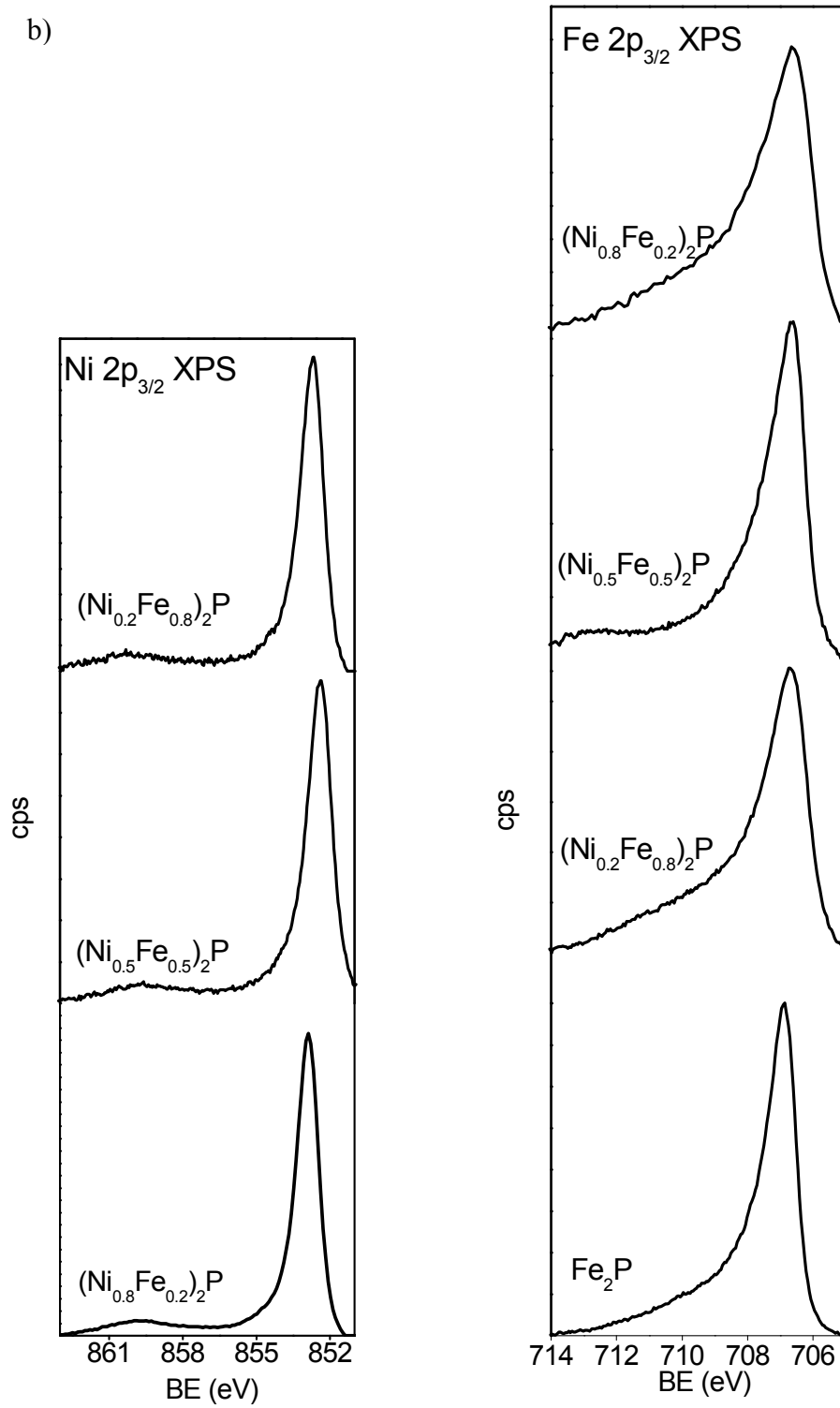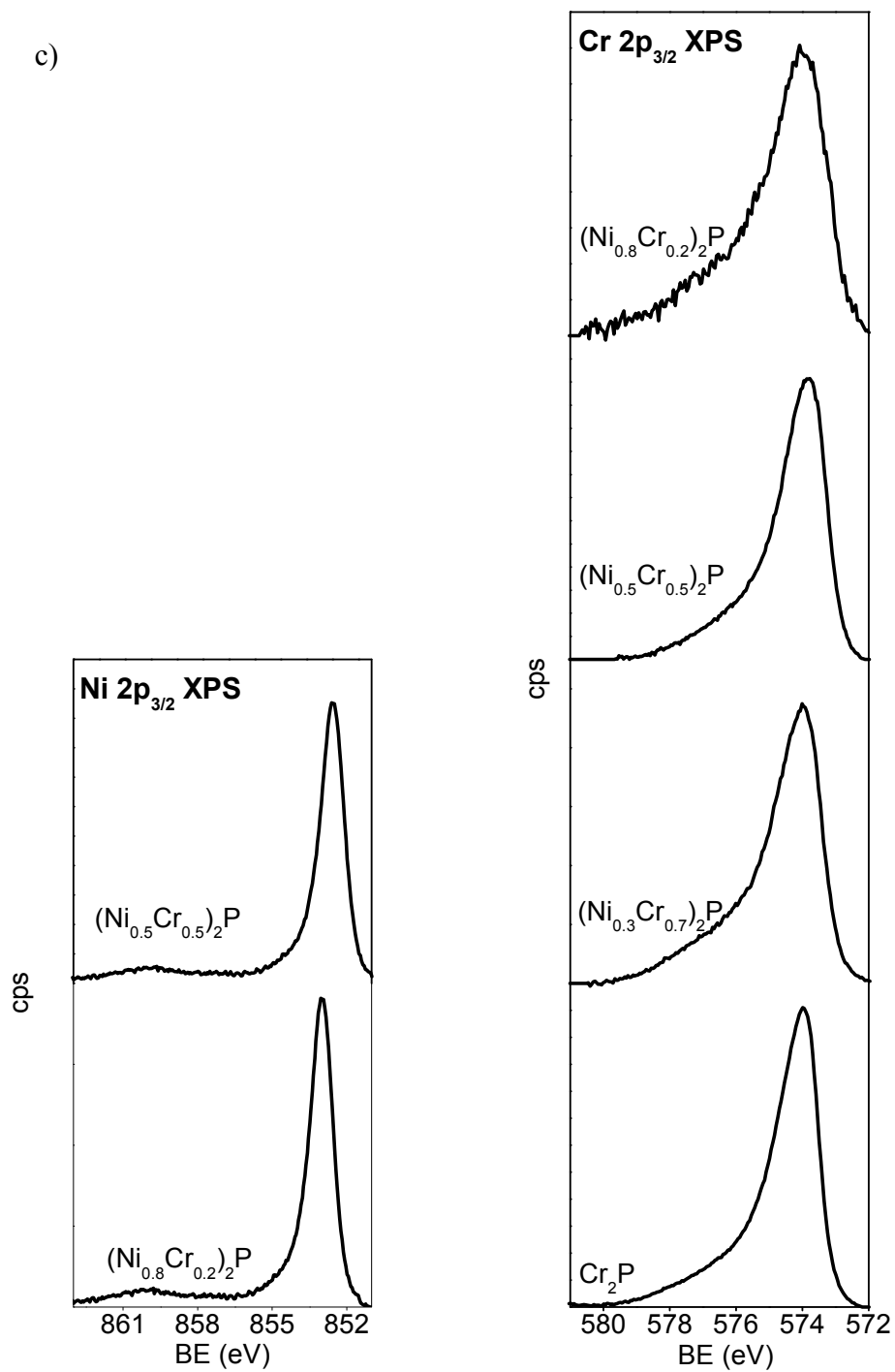
Figure A6-4 Metal 2p$_{3/2}$ XPS spectra for (a) $(Ni_{1-x}Co_x)_2P$, (b) $(Ni_{1-x}Fe_x)_2P$, and (c) $(Ni_{1-x}Cr_x)_2P$.
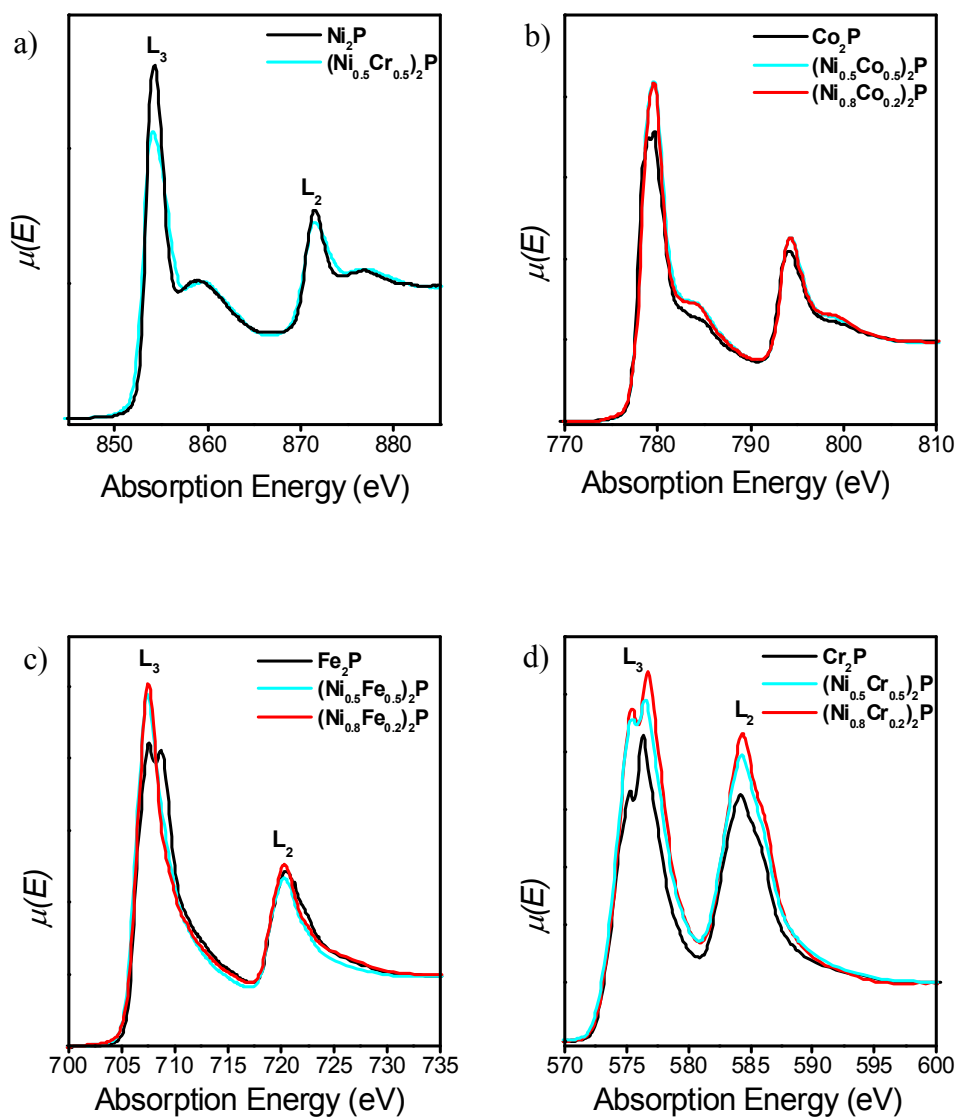
Figure A6-5 Normalized TEY (a) Ni, (b) Co, (c) Fe, and (d) Cr L-edge XANES spectra for $(Ni_{1-x}M_x)_2P$ ($M = Cr$, Fe, Co).